



# Hybrid modeling and control of mechatronic systems using a piecewise affine dynamics approach

---

Philipp Pasolli

---



**Philipp Pasolli**

**Hybrid modeling and control of mechatronic systems  
using a piecewise affine dynamics approach**

Doctoral Dissertation for the Degree *Philosophiae Doctor (PhD)* at  
the Faculty of Engineering and Science, Specialisation in Mechatronics

University of Agder  
Faculty of Engineering and Science  
2020

Doctoral Dissertation at the University of Agder 273

ISSN: 1504-9272

ISBN: 978-82-7117-974-8

©Philipp Pasolli, 2020

Printed by Media 07

Kristiansand



# Acknowledgments

First and foremost, I would like to thank my supervisor Michael Ruderman for his support throughout my PhD studies, in particular his supervision and quick turnaround times.

A huge thank you is also due to the University of Agder for providing a dynamic and family-like work environment, making it easy to interact and get to know people.

I would also like to extend my gratitude to the faculty's laboratory staff for always providing me with help for any issues I had with the infrastructure and setting up my testbench. I want to especially thank Jan Andreas Holm, who played a vital role in getting the test setup up and running.

While I am very grateful for having had the opportunity to pursue a PhD in the first place, it would not have been the same without the many colleagues and friends I made during this time. It was a pleasure to share an office with Andreas Klausen, Sondre Tørdal, Sondre Nordås and Rune Husveg which provided a quiet work environment with the occasional pleasant distraction. A special thanks goes to Andreas Klausen for being my mentor and seemingly having an answer to any Latex and Matlab-related question I could think of.

As to the many hours spent at Apotekergaarden, I would like to thank Shaun Falconer, Reyn O'Born, Rolf Kjellby and Yvonne Murray for joining me there, Sissel Kristensen for always having an open ear, Ingvild Brattestad for making me a 'dogfather' to Molly and Sondre Larsen for being a true Norwegian friend.

I would also like to thank my Austrian friends for constantly reminding me that Austria has better skiing resorts than Norway and staying in close contact with me despite the distance, making me feel like I was never really gone.

Finally, to my parents, Andreas and Eveline, and my sister and brother, Vanessa and Alexander: thank you for your unconditional support and love throughout my PhD studies and always being there whenever I needed you!

# Abstract

Every physical system contains non-linear characteristics. When the system becomes increasingly complex, the number of non-linearities rises accordingly, which makes operating the system as desired a challenge. Thus finding a suitable control structure, tuning controller gains and evaluating the system with regard to response and stability requires a high level of in-depth knowledge about the system itself as well as the topology of modeling, identification and control. One approach to simplify this process is to linearize the system around a specified operational point. However, this will result in a model which is only representative of the physical system in the vicinity of said operation point and therefore accurately represents only a small subset of the system's operational state-space. On the other side of the spectrum are models with high complexity, in future referred to as full-order models. These include full-order dynamics, non-linearities, etc., all of which require explicit knowledge of the system – including its characteristics and internal states – which might not be feasible to obtain. If generated, these models provide a highly accurate system representation.

Introducing the topology of hybrid systems in recent years, especially its subclass of piecewise affine (PWA) systems, appears to be one class of systems capable of representing the middle ground with respect to complexity between a model linearized around an operational point and a full-order model. It allows for a linearization of a non-linear characteristic at several points, resulting in the characteristic being expressed as a combination of different cells defined by linear functions. The compliance between linearized and actual characteristics can also be easily customized by adjusting the number and locations of linearization points.

This thesis investigates the topic of modeling and control of PWA systems based on two experimental cases of an electrical and hydraulic nature with varying complexity that were also built, instrumented and evaluated. A full-order model has been created for both systems, including all dominant system dynamics and non-linearities. The unknown parameters and characteristics have been identified via an extensive parameter identification. In the following, the non-linear characteristics are linearized at several points, resulting in PWA models for each respective setup.

Regarding the closed loop control of the generated models and corresponding experimental setups, a linear control structure comprised of integral error, feed-forward and state-feedback control has been used. Additionally, the hydraulic setup has been controlled in an autonomous hybrid position/force control mode, resulting in a switched system with each mode's dynamics being defined by the previously derived PWA-based model in combination with the control structure and respective mode-dependent controller gains. The autonomous switch between control modes has been defined by a switching event capable of consistently switching between modes in a deterministic manner despite the noise-afflicted measurements. Several methods were used to obtain suitable controller gains, including optimization routines and pole placement. Validation of the system's fast and accurate response was obtained through simulations and experimental evaluation.

The controlled system's local stability was proven for regions in state-space associated with operational points by using pole-zero analysis. The stability of the hybrid control approach was proven by using multiple Lyapunov functions for the investigated test scenarios.

# Publications

The following listed articles have been published or submitted for publication in peer reviewed international conference proceedings and journals.

**Paper A** P. Pasolli, M. Ruderman. Design and Analysis of non-linear Circuit with Tunnel Diode for Hybrid Control Systems. *Proceeding of IEEE 15th International Workshop on Advanced Motion Control (AMC2018)*, 181-186, 2018.

doi: 10.1109/AMC.2019.8371084.

**Paper B** P. Pasolli, M. Ruderman. Design, Control, and Analysis of Nonlinear Circuits with Tunnel Diode with Piecewise Affine Dynamics. *IEEJ Journal of Industry Applications*, Vol.8 No.2 pp.280-249, 2018. doi: 10.1541/ieejia.8.240.

**Paper C** P. Pasolli, M. Ruderman. Linearized Piecewise Affine in Control and States Hydraulic System: Modeling and Identification. *IECON 2018-44th Annual Conference of the IEEE Industrial Electronics Society*, pp. 4537-4544, 2018. doi: 10.1109/IECON.2018.8591572.

**Paper D** P. Pasolli, M. Ruderman. Hybrid State Feedback Position-Force Control of Hydraulic Cylinder. *2019 IEEE International Conference on Mechatronics (ICM)*, Vol. 1, pp. 54-59, 2019. doi: 10.1109/ICMECH.2019.8722829.

**Paper E** P. Pasolli, M. Ruderman. Hybrid Position/Force Control for Hydraulic Actuators. Under review at *IEEE Transactions on Industrial Electronics*.

The following article was written and published during the course of this work but is not included in this thesis.

**Paper F** M. Ruderman, L. Fridman, P. Pasolli. Virtual sensing of load forces in hydraulic actuators using second- and higher-order sliding modes. *Control Engineering Practice*, Volume 92, 2019. doi: 10.1016/j.conengprac.2019.104151.

# Contents

<b>1</b>	<b>Introduction</b>	<b>1</b>
1.1	Background . . . . .	1
1.2	State of the Art . . . . .	2
1.2.1	Hybrid Systems - An Overview . . . . .	2
1.2.1.1	Hybrid System Requirements . . . . .	4
1.2.1.2	Model of Hybrid Systems . . . . .	5
1.2.1.3	Survey of Hybrid Systems . . . . .	6
1.2.1.4	Hybrid System Phenomena . . . . .	10
1.2.2	Piecewise Affine Systems . . . . .	12
1.2.2.1	Modeling . . . . .	12
1.2.2.2	Control . . . . .	13
1.2.2.3	Stability Analysis . . . . .	15
1.3	Contributions . . . . .	17
1.4	Test Setup Overview . . . . .	20
1.5	Outline . . . . .	20
<b>2</b>	<b>Modeling of Dynamical Systems</b>	<b>23</b>
2.1	State-Space Modeling - Linear Time Invariant Systems . . . . .	23
2.2	Non-linear Systems . . . . .	25
2.2.1	Electric Setup . . . . .	25
2.2.2	Hydraulic Setup . . . . .	26
2.3	Parameter Identification . . . . .	31
2.4	Linearisation of Dynamic Systems . . . . .	33
<b>3</b>	<b>Hybrid Control System Design</b>	<b>37</b>
3.1	Integral, Feed-Forward, State-Feedback Control . . . . .	37
3.2	Control Signal Filtering . . . . .	39
3.3	Static Compensator . . . . .	39
3.4	Switching Event . . . . .	40

3.5	Control Parameter Adjustment . . . . .	43
3.5.1	Optimal State Feedback . . . . .	43
3.5.2	Pole Placement . . . . .	45
<b>4</b>	<b>Stability Analysis</b>	<b>47</b>
4.1	Stability Analysis of Linear Systems . . . . .	47
4.2	Stability Analysis of Non-linear Systems . . . . .	48
<b>5</b>	<b>Concluding Remarks</b>	<b>51</b>
5.1	Conclusions . . . . .	51
5.2	Potential for Future Works . . . . .	52
	<b>References</b>	<b>53</b>
	<b>Appendices</b>	<b>61</b>
<b>A</b>	<b>Design and Analysis of non-linear Circuit with Tunnel Diode for Hybrid Control Systems</b>	<b>63</b>
A.1	Introduction . . . . .	65
A.2	Modeling of Non-linear Circuit . . . . .	66
A.3	Test Setup and Experiment . . . . .	67
A.4	Measuring of Diode Characteristic . . . . .	70
A.5	Transient Response and Circuit Analysis . . . . .	73
A.6	Open Loop Control . . . . .	75
A.7	Summary and Outlook . . . . .	79
	References . . . . .	80
<b>B</b>	<b>Design, Control, and Analysis of Nonlinear Circuits with Tunnel Diode with Piecewise Affine Dynamics</b>	<b>83</b>
B.1	Introduction . . . . .	85
B.2	Modeling of Nonlinear Circuit . . . . .	87
B.3	Experimental Setup . . . . .	88
B.4	Identification of Diode Characteristics . . . . .	91
B.5	Analysis of Transient and Steady-State Response . . . . .	94
B.6	Controlled Closed-loop Behavior of Circuit with Reference-dependent Limit Cycles . . . . .	96
B.6.1	Integral-State-Feedback Controller . . . . .	96
B.6.2	Simulation Results . . . . .	97
B.6.3	Experimental Results . . . . .	98

B.7	Piecewise Affine (PWA) Model Formulation . . . . .	100
B.8	Formal verification . . . . .	105
B.9	Conclusions . . . . .	105
	References . . . . .	108
<b>C</b>	<b>Linearized Piecewise Affine in Control and States Hydraulic System: Modeling and Identification</b>	<b>113</b>
C.1	Introduction . . . . .	115
C.2	Full-Order Model . . . . .	117
C.2.1	Servo Valve Approximation . . . . .	117
C.2.2	Orifice and Continuity Equations . . . . .	118
C.2.3	Mechanical Sub-Model of Cylinder . . . . .	119
C.3	Model Reduction . . . . .	119
C.4	Non-linear System Affine in Control and States . . . . .	120
C.5	Experimental Setup . . . . .	122
C.6	Parameter Identification . . . . .	123
C.6.1	Servo Valve . . . . .	124
C.6.2	Dead-zone . . . . .	126
C.6.3	Stribeck Friction . . . . .	126
C.7	Model Evaluation . . . . .	127
C.8	Summary . . . . .	130
	References . . . . .	134
<b>D</b>	<b>Hybrid State Feedback Position-Force Control of Hydraulic Cylinder</b>	<b>139</b>
D.1	Introduction . . . . .	141
D.2	System Modeling . . . . .	142
D.3	Control Design . . . . .	143
D.3.1	Static Dead-zone Compensation . . . . .	143
D.3.2	Integral Error State-Feedback Control . . . . .	144
D.3.3	Filtering of Control Signal . . . . .	147
D.3.4	Event-based Switching . . . . .	147
D.3.5	Optimal State Feedback . . . . .	148
D.4	Experimental Evaluation . . . . .	150
D.5	Summary . . . . .	153
	References . . . . .	155
<b>E</b>	<b>Hybrid Position/Force Control for Hydraulic Actuators</b>	<b>157</b>
E.1	Introduction . . . . .	159

E.2	System Description . . . . .	161
E.2.1	Hydraulic Actuator Setup . . . . .	161
E.2.2	System Modeling . . . . .	162
E.2.2.1	Servo valve model . . . . .	162
E.2.2.2	Orifice equations . . . . .	163
E.2.2.3	Continuity equations . . . . .	164
E.2.2.4	Mechanical subsystem . . . . .	164
E.3	Control Design . . . . .	165
E.3.1	Hybrid Control Structure . . . . .	166
E.3.2	Dead-zone Compensation . . . . .	168
E.3.3	Filtering of Control Signal . . . . .	168
E.3.4	Event-based Switching . . . . .	169
E.3.5	Determining of Control Gains . . . . .	169
E.3.6	Stability Analysis . . . . .	173
E.4	Experimental Evaluation . . . . .	174
E.4.1	Hard-stop Environment . . . . .	174
E.4.2	Dynamic Environment . . . . .	175
E.5	Summary . . . . .	177
	References . . . . .	179
<b>F</b>	<b>Hydraulic Test Setup</b>	<b>183</b>
F.1	Hydraulic/Mechanical components . . . . .	184
F.1.1	Overview . . . . .	184
F.1.2	Component specification overview . . . . .	185
F.2	Electric Cabinet . . . . .	187
F.3	Real-Time Target . . . . .	188
F.4	Interfaces . . . . .	189
F.5	Wiring Schematic . . . . .	192



# List of Figures

- 1.1 Hybrid model of a thermostat . . . . . 3
- 1.2 Autonomous state jump . . . . . 5
- 1.3 Schematic of hybrid automata with three discrete states . . . . . 6
- 1.4 Comparison of switching schemes between piecewise affine and discretely controlled continuous systems . . . . . 9
- 1.5 Simulation of stable subsystems and unstable switched system . . . . . 10
- 1.6 Bouncing ball . . . . . 11
- 1.7 Chattering of switched system . . . . . 12
- 1.8 Sensitivity of hybrid systems . . . . . 12
- 1.9 Electric circuit including a non-linear tunnel diode . . . . . 20
- 1.10 Schematic of hydraulic test setup . . . . . 21
  
- 2.1 Linear time invariant mass spring damper system . . . . . 24
- 2.2 Subsystems of hydraulic setup . . . . . 26
- 2.3 Schematic cross-section of over lapped valve . . . . . 27
- 2.4 Generalized dead-zone, saturation characteristic of a hydraulic valve . . . . . 28
- 2.5 Hydraulic differential cylinder schematic . . . . . 29
- 2.6 Averaging of signals experiencing initial transient behavior between two chosen start/end points . . . . . 32
- 2.7 Highly distorted signal due to low signal to noise ratio and filtered signal . . . . . 33
- 2.8 Diode characteristic with its linearization . . . . . 34
- 2.9 Non-linear damping function and its linearization . . . . . 35
  
- 3.1 Integral error, feed-forward, state-feedback control structure . . . . . 38
- 3.2 Linearized dead-zone and compensator . . . . . 40
- 3.3 Relay function . . . . . 41
- 3.4 Automaton for adapted time-delayed relay function . . . . . 42
- 3.5 Simulation of adapted version of the time-delayed relay function . . . . . 42
- 3.6 Hysteresis relay . . . . . 43
  
- 4.1 Pole-zero plot of controlled hydraulic model for both control modes . . . . . 48

A.1	Characteristic curve of tunnel diode . . . . .	68
A.2	Electrical diagram for experimental setup of complete circuit . . . . .	69
A.3	Experimental setup . . . . .	70
A.4	Diode characteristic - raw voltage and current measurement . . . . .	71
A.5	Diode characteristic - Fast Fourier Transform . . . . .	72
A.6	Diode characteristic curve with characteristic points from data sheet . . . . .	73
A.7	Transient response of diode, numeric simulation as in Table A.1 . . . . .	74
A.8	Simulation and experiment response according to Table A.4 . . . . .	74
A.9	Bode plot of the circuit . . . . .	76
A.10	Measured input-output hysteresis curve of diode . . . . .	76
A.11	Open loop control structure . . . . .	77
A.12	Measured input voltage and system response at amplitude of $5V$ , offset $5V$ with pulse-width of $32\%$ . . . . .	78
A.13	Measured input voltage and system response at amplitude of $5V$ , offset $5V$ with pulse-width of $18\%$ . . . . .	78
A.14	Measured input voltage and system response at amplitude of $3.4V$ , offset $4.2V$ with pulse-width of $32\%$ . . . . .	78
A.15	Measured input voltage and system response at amplitude of $3.4V$ , offset $4.2V$ with pulse-width of $18\%$ . . . . .	79
B.1	Laboratory experimental setup of circuits with amplifier unit and real-time control board . . . . .	90
B.2	Differential operational amplifier . . . . .	90
B.3	Circuit diagram of experimental setup including differential operational amplifier (red) and measurement points . . . . .	91
B.4	Measured diode data: raw voltage measurement above and raw current measurement below . . . . .	92
B.5	FFT transformed diode measurements: voltage spectrum above and cur- rent spectrum below . . . . .	93
B.6	Diode characteristic measurement including characteristic points from datasheet	93
B.7	Numerically simulated transient response of the circuit with parameter values from Table B.1 . . . . .	94
B.8	Simulation and experiment of the circuit pulse response for different $R$ , $C$ , $L$ values, as in Table B.4 . . . . .	95
B.9	Simulated FRF of the entire circuit . . . . .	96
B.10	Simulated closed-loop response of the output voltage $x_1$ to the $0.025V$ reference . . . . .	98

B.11 Simulated closed-loop response to the $0.2V$ reference: output voltage above and phase portrait below . . . . .	99
B.12 Simulated closed-loop response of the output voltage $x_1$ to the $0.5V$ reference	100
B.13 Measured closed-loop response of the output voltage $x_1$ to the $0.025V$ ref- erence . . . . .	100
B.14 Measured closed-loop response to the $0.2V$ reference: output voltage above and phase portrait below . . . . .	101
B.15 Measured closed-loop response of the output voltage $x_1$ to the $0.5V$ reference	101
B.16 Linearization of the diode characteristics . . . . .	102
B.17 Simulink and PWLTool trajectories for $r = 0.025V$ . . . . .	106
B.18 Simulink and PWLTool trajectories for $r = 0.2V$ . . . . .	106
B.19 Simulink and PWLTool trajectories for $r = 0.5V$ . . . . .	107
B.20 Simulink and PWLTool simulated trajectories for an instable system with $r = 0.2V$ and $k_i = -30000$ . . . . .	107
C.1 $\hat{C}_q$ coefficient and its linearization . . . . .	121
C.2 $\hat{C}_{qp}$ coefficient and its linearization . . . . .	122
C.3 Experimental hydraulic setup (laboratory view) . . . . .	123
C.4 Schematic representation of experimental setup . . . . .	124
C.5 Measured FRFs versus linear model fit . . . . .	125
C.6 Experimental test of the dead-zone and linearization . . . . .	126
C.7 Cylinder position measurements over normed time for all Stribeck curve measurements, 46 measurements for retracting and 45 measurements for extending motion . . . . .	127
C.8 Measured data points and fitted Stribeck model . . . . .	128
C.9 Measured supply pressure at sinusoidal input . . . . .	128
C.10 Measurement and simulation for sinusoidal input with 20% valve opening and 1Hz frequency . . . . .	130
C.11 Measurement and simulation for sinusoidal input with 60% valve opening and 1Hz frequency . . . . .	130
C.12 Measurement and simulation for sinusoidal input with 20% valve opening and 3Hz frequency . . . . .	131
C.13 Measurement and simulation for sinusoidal input with 60% valve opening and 3Hz frequency . . . . .	131
D.1 Static dead-zone compensation . . . . .	144
D.2 Control Structure . . . . .	145
D.3 Cost and gain value convergence for position control from (D.15) . . . . .	149

D.4	Cost and gain value convergence for force control from (D.16) . . . . .	149
D.5	Experimental setup of two cylinders in a antagonistic setup . . . . .	150
D.6	Measured cylinder position and reference for ramp with 0.03m/s slope . . .	151
D.7	Measured load force and reference for 3500N . . . . .	151
D.8	Measured cylinder position and reference for ramp with 0.07m/s slope . . .	152
D.9	Outtake of measured position and reference of ramp with slope of 0.07m/s	152
D.10	Measured load force and reference for 7000N . . . . .	153
E.1	Experimental setup of hydraulic actuators . . . . .	162
E.2	Block-diagram of the hybrid position/force control . . . . .	167
E.3	Pole-zero diagram of closed-loop controls versus plant . . . . .	172
E.4	Bode diagram of designed closed-loop controls . . . . .	172
E.5	Multiple Lyapunov function for position (red solid line) and force (blue dashed line) controls at periodic switching . . . . .	173
E.6	Reference and measured position control response . . . . .	175
E.7	Reference and measured force control response . . . . .	175
E.8	Mean values and standard deviations of position error . . . . .	176
E.9	Mean values and standard deviations of force error . . . . .	176
E.10	Reference and measured position control response . . . . .	177
E.11	Reference and measured force control response . . . . .	177
E.12	Mean values and standard deviations of position error . . . . .	177
E.13	Mean values and standard deviations of force error . . . . .	178
F.1	Experimental hydraulic test setup . . . . .	184
F.2	Testbench schematic . . . . .	184
F.3	Electric cabinet . . . . .	187
F.4	RT Target and interface terminal . . . . .	189
F.5	Connector port layout - cabinet mounted view . . . . .	190

# List of Tables

A.1	Initial components configuration . . . . .	68
A.2	Diode characteristic points . . . . .	68
A.3	Configuration of diode characteristic measurement values . . . . .	71
A.4	Components' configurations . . . . .	75
A.5	Amplitude, offset and pulse-width settings for experiments and correspond- ing figure references . . . . .	77
B.1	Circuit components' values . . . . .	89
B.2	Diode characteristic points . . . . .	89
B.3	Diode characteristic measurement configurations . . . . .	92
B.4	Component values for rise time simulation . . . . .	95
B.5	Closed-loop system parameters . . . . .	97
B.6	Cells and boundary constants of piecewise affine model . . . . .	102
C.1	Installed components of experimental system . . . . .	124
C.2	Servo valve second-order model parameters . . . . .	125
C.3	Simulation Parameters . . . . .	132
C.4	Values for linearized dead-zone and saturation . . . . .	132
C.5	Values for linearized Stribeck friction . . . . .	132
C.6	Values for $k_o$ for linearized $C_q$ . . . . .	132
C.7	Values for $d_o$ for linearized $C_q$ . . . . .	133
C.8	Values for $k_n$ for linearized $C_{qp}$ . . . . .	133
C.9	Values for $d_n$ for linearized $C_{qp}$ . . . . .	133
D.1	Optimized gain values for position and force control . . . . .	150
D.2	Numerical Indicators . . . . .	153
E.1	Hardware components of experimental setup . . . . .	162
E.2	Control gain parameters . . . . .	172
F.1	Pressure relief/reduction valve . . . . .	185
F.2	Hydraulic and Mechanical Components . . . . .	186

F.3 Component input/output voltages and currents . . . . . 186

F.4 List of electric components in cabinet . . . . . 188

F.5 Connerctors: Binder - Ordering Numbers . . . . . 190

F.6 4-pin wiring layout . . . . . 190

F.7 8-pin wiring layout for servo valve . . . . . 191

F.8 8-pin wiring layout for force gauge . . . . . 191

F.9 24-pin wiring layout for real-time-interface . . . . . 192

# Nomenclature

Scalar variables are described by letters as in  $x$  and vectors being defined as lower case bold letters, e.g.  $\mathbf{x}$ . Matrices are represented in capital, bold letters e.g.  $\mathbf{A}$  and sets in caligraphic letters e.g.  $\mathcal{S}$ .

<b>Abbreviations</b>		$\bar{\mathbf{f}}$	extended affine vector
BDCV	bidirectional control valve	$\bar{\mathbf{x}}$	extended state vector
FFT	fast fourier transformation	$\bar{A}$	average cross section
FRF	frequency response function	$\delta, \chi$	Stribeck shaping parameters
LMI	linear matrix inequality	$\dot{e}$	control error
LPF	low pass filter	$\gamma$	hyperbolic tangent transition coefficient
LTI	linear time invariant	$\nu$	spool position
MPC	model predictive control	$\omega_0$	valve natural frequency
PLC	programmable logic controller	$\phi(\cdot)$	function for kinetic energy
PRV	pressure relief/reduction valve	$\psi(\cdot)$	function for potential energy
PWA	piecewise affine	$\sigma$	viscous friction coefficient
RT	real-time	$\mathbf{A}$	dynamic matrix
<b>Variables</b>		$\mathbf{b}$	input vector
$(\cdot)^*$	linearization points	$\mathbf{c}$	output vector
$\bar{\mathbf{A}}$	extended dynamic matrix	$\mathbf{f}$	affine vector
$\bar{\mathbf{b}}$	extended input vector	$\mathbf{x}$	state vector
$\bar{\mathbf{c}}$	extended output vector	$\zeta$	valve damping

$A$	cross section	$m$	discrete time
$d$	offset of linear function	$P$	pressure
$e$	integrated control error	$P_L$	load pressure
$F_c$	Coulomb friction	$Q$	hydraulic flow
$F_L$	external load force	$q$	discrete state
$F_s$	stiction coefficient	$t$	continuous time
$h$	control mode	$u_c$	control input
$i_L$	inductance current	$u_D$	diode voltage
$k$	gradient of linear function	$W$	Lyapunov coefficients
$K_i$	integral gain	$x_{1,\dots,n}$	system states
$K_{1,\dots,n}$	state-feedback gains	FF	feed-forward controller gain



# Chapter 1

## Introduction

### 1.1 Background

Machines and appliances are built with a specific purpose in mind which they are supposed to fulfill. In many cases this implies that the system is controlled in one way or the other. To develop a suitable control structure, it is highly recommended to have an in-depth understanding of the system in order to be able to identify and tune control parameters accordingly. Even today, the PID controller, consisting of proportional, integral and derivative control [1], is overly prominent due to its simplicity, leading to many situations where the parameters are manually tuned because of how this machine operates. As history has proven, this is a viable method that has proven successful. However, if high performance requirements are placed on systems, relying solely on experience is not sufficient, especially if new systems are developed. So to create a suitable control structure and tune the parameters accordingly, an in-depth analysis of the system is necessary, out of which a model can be created. The highest degree of congruence between model and physical system can be achieved by deriving a full-order model which, if modeled in a sufficient level of detail, will most likely include one or more non-linearities, thereby possibly becoming rather complex. The usual approach to simplifying these models is to determine the system's operational point in its state-space around which the respective non-linearities may be linearized. While simulations in the vicinity of this operational point may be fairly compliant with the physical system, larger deviations from this point might result in an ample error, restricting viable simulations to a small subset of the system's overall operational state-space.

The rise of hybrid systems [2, 3], these being a combination of discrete and continuous time domains, resulted, among other things, in the development of piecewise affine (PWA) systems [4, 5, 6, 7] which allow a system to be linearized at several chosen points, resulting in a simplified model compared to a full-order model. Yet this model still manages to

yield promising simulation results with a certain degree of accuracy while at the same time being able to cover the entire system's state-space.

The topology of hybrid systems also resulted in a framework which allows the description of more complex e.g. switched control structures [8, 9, 10, 11, 12, 13]. A classical control approach for a combined position and force control is a cascaded control structure where the inner loop represents force control and the outer one position control, resulting in deficiencies in either or both controllers. In this particular case a switched system approach may be introduced that results in increased performance for either control mode without it being necessary to change the underlying control structure between control modes. In the following the state of the art of hybrid systems – with a focus on PWA systems – is described.

## 1.2 State of the Art

In this chapter the reader will be introduced to the underlying topics of this thesis and given a brief summary of their current state. While the topics under discussion cover a wide spectrum of approaches and methods, all of which are relevant to the respective fields, this chapter will try to give a general overview.

### 1.2.1 Hybrid Systems - An Overview

Hybrid systems are dynamic models or systems which have both continuous and discrete dynamics. While the respective fields are individually well known and extensively researched, their combination is a somewhat relatively new topic of investigation, which raises several methodological questions about modeling, analysis and design [2, 12, 14, 15, 16, 17]. Continuous dynamic systems are well understood at this point and may be expressed by the use of differential and difference equations, while discontinuous systems facilitate the use of automata [18] and Petri nets [19] to be modeled. Nowadays, almost every system having a high level of complexity uses a combination of continuous and discrete dynamics in one form or another to accomplish the tasks for which it has been designed. However, this also applies to much simpler mechanics like the backlash of a gearbox, dead-zones, friction models distinguishing between stick and slip. It even applies to examples as simple as a bouncing ball that changes its dynamic upon impact. For all these kinds of scenarios, mathematical models are necessary to describe the evolution of the dynamic states of the model's continuous and discrete parts.

To demonstrate the interaction between continuous and discrete dynamics, consider the simple example of regulating the temperature in a house [2, 3]. In its simplest form a heating system is either working at full power or turned off. This means the system

can operate at two different modes, namely *on* and *off*. In each mode  $q \in \{on, off\}$  the evolution of the temperature  $T$  can be expressed by a differential equation. The nodes or circles in Fig. 1.1 represent the *on* and *off* states of the system, including the differential equation describing the temperature's evolution over time. The circle's edges indicate the discrete state transitions that are possible. This system may be classified as a hybrid system, since the evolution of the temperature is dependent of both states  $(T, q)$  where  $q$  refers to the discrete state being either *on* or *off* and the temperature  $T$  being a state of the continuous time domain.

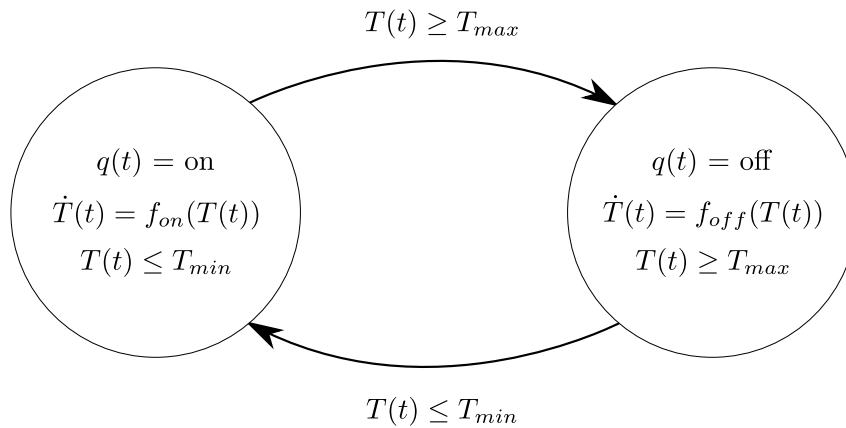


Figure 1.1: Hybrid model of a thermostat [2]

Based on this example, the main features of a hybrid system may already be determined:

- The thermostat is a hybrid system consisting of both a discrete state  $q$  and a continuous state  $T$ .
- The system's continuous behavior describing the evolution of temperature  $T$  is dependent on the discrete state  $q$  being *on* or *off*.
- Changes in the discrete state  $q$  are dependent on the continuous state  $T$  with  $T \leq T_{min}$  triggering a switch from the discrete state *off* to *on* and  $T \geq T_{max}$  triggering a switch from *on* to *off*.

In the previous example, the change in the discrete state is directly dependent on the continuous state; however, this does not necessarily have to be the case, as in more integrated systems, a switch of discrete state may be triggered by the model's other external factors not directly related to the system's output. An example of this is an automated gearbox whose input as well as output is revolutions per minute and torque, but the change of gears could be triggered by flooring the gas pedal, which, as seen from a car's perspective, is an external input not related to the output of the submodel of the gearbox.

While the discrete states are usually piecewise constant, the continuous states can change either continuously or discontinuously, the latter being referred to as jumps or resets [3]. These jumps can happen at transition times, at which point the discrete state changes its value, triggering a sudden change in the continuous state's value, e.g. a change of gains in a switched controlled system.

### 1.2.1.1 Hybrid System Requirements

On a bigger scheme, there are four phenomena [17] which are required as an extension to a purely continuous system so it can be classified as a hybrid system:

- autonomous switching of the dynamics
- autonomous state jumps
- controlled switching of the dynamics
- controlled state jumps

**Autonomous switching of the dynamics** occurs if the vector field  $f^{as}$  defining the evolution of the continuous state changes discontinuously [17]. This type of change can be invoked by the time if the vector field  $f^{as}$  is dependent on it.

$$\dot{x}(t) = f^{as}(x(t), t). \quad (1.1)$$

Another way of triggering a switch between vector fields is the continuous state  $x(t)$  reaching a *switching set*  $\mathcal{S}$  with  $x(t) \in \mathcal{S}$ , which is referred to as an *event driven* switch. An example of this is the thermostat example from above where the state  $T$  reaches the value of  $T_{max}$  while in a discrete state *on*, triggering a switch of discrete state to *off*.

**Autonomous state jumps** occur when at a certain time  $t$  and a jump from state value  $x(t_-)$  to  $x(t_+)$  occurs [17], cf. Fig. 1.2. For example, consider the behavior of the bouncing ball where the velocity of the ball has a discontinuous change in value when hitting the floor at time  $t$ . Where the state jumps to, upon reaching a switching set  $\mathcal{S}$ , is defined by a *reset map*  $\mathcal{R}$ , with the reset map possibly being dependent on the previous discrete state  $q(t_-)$ , and may be written as:

$$(x(t_-), x(t_+)) \in \mathcal{R}(q(t_-)), \quad \text{for } x(t) \in \mathcal{S}. \quad (1.2)$$

**Controlled switching** occurs when there is a discrete input  $v_{dis}$  which is used to switch between continuous dynamics [17]. If there is a change in the discrete input at time  $\bar{t}$  then the vector field  $f^{csw}(x(t), v_{dis}(t))$  changes abruptly at time  $\bar{t}$  as well.

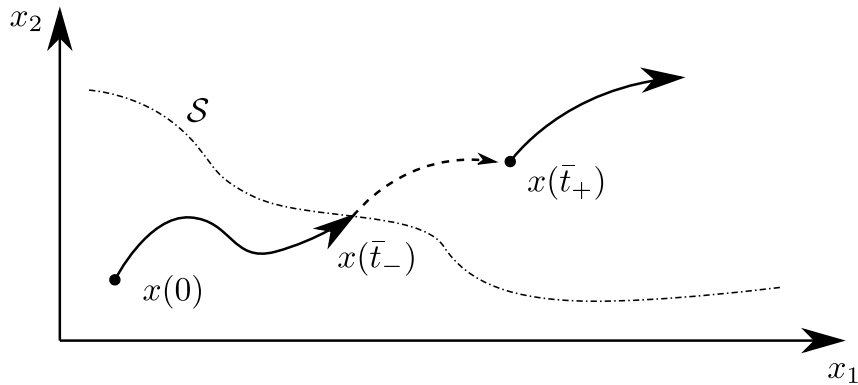


Figure 1.2: Autonomous state jump [2]

**Controlled state jumps** is a phenomenon where a continuous state experiences a discontinuity when the discrete state changes, e.g. based upon a control command [17]. The previously mentioned automated gearbox may be named as an example of this phenomenon.

### 1.2.1.2 Model of Hybrid Systems

As demonstrated above, there are several different ingredients necessary to define a hybrid system. While different formalisms were introduced in the past to describe a hybrid system, the main modeling formalism in hybrid systems theory remains the hybrid automaton, which is an 8-tuple [2, 3] and may be defined as:

$$H = (\mathcal{Q}, \mathcal{X}, \mathbf{f}^{hyb}, Init, Inv, \mathcal{E}, \mathcal{G}, \mathcal{R}) \quad (1.3)$$

where

- $\mathcal{Q} = \{q_1, \dots, q_k\}$  is a finite set of discrete states
- $\mathcal{X}$  represents the continuous state-space for which often  $\mathcal{X} = \mathbb{R}^n$  holds
- $\mathbf{f}^{hyb} : \mathcal{Q} \times \mathbb{R}^n \rightarrow \mathbb{R}^n$  is a vector field
- $Init$  is a set of initial conditions
- $Inv : \mathcal{Q} \rightarrow 2^{\mathbb{R}^n}$  defines the invariants of the locations
- $\mathcal{E} \subseteq \mathcal{Q} \times \mathcal{Q}$  is the transition relation
- $\mathcal{G} : \mathcal{E} \rightarrow 2^{\mathbb{R}^n}$  is the guard condition
- $\mathcal{R} : \mathcal{E} \rightarrow 2^{\mathbb{R}^n} \times 2^{\mathbb{R}^n}$  is the reset map

To elaborate on the above,  $2^{\mathbb{R}^n}$  describes the collection of subsets of  $\mathcal{X}$ .  $Inv$  and  $\mathcal{G}$  have similar roles, where  $\mathcal{G}$  represents a region in state-space called guard region in which a change in discrete state *may* occur. This region may be seen as an "enabling" condition for a discrete state change, while invariants ( $Inv$ ) describe when a change *must* take place.  $\mathcal{E}$  defines from which to which discrete state the automata switches [2, 3]. A schematic representation of a hybrid automata is given in Fig. 1.3.

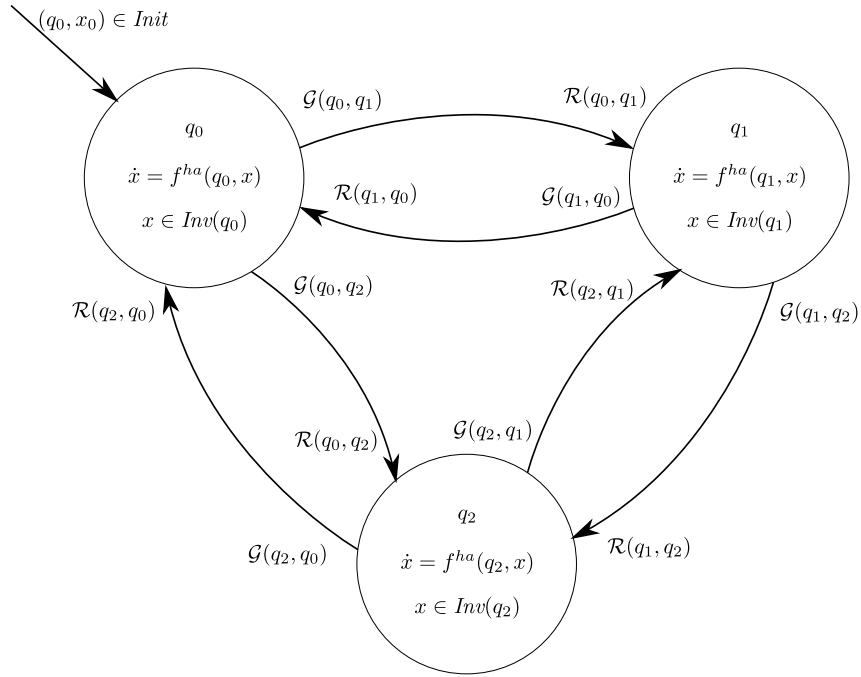


Figure 1.3: Schematic of hybrid automata with three discrete states, where each circle represents a mode associated with the respective differential equations. Arrows indicate possible transitions between discrete states [2]

### 1.2.1.3 Survey of Hybrid Systems

As mentioned above, the hybrid automaton is by far the most common method of describing a hybrid system. In this section a brief overview of alternative formalism and model structures is given [2]. The following list is by no means complete, but covers the most well-known classes:

- Hybrid automata
- Switched systems
- Piecewise affine models
- Mixed logical dynamical models

- Complementary systems
- Discretely controlled continuous systems
- Timed automata
- Hybrid inclusions

**Hybrid automata** may be seen as an extension to the finite-state machine where each discrete state is associated with differential equations, and thereby vector fields, along which the continuous states evolve over time. How to formulate this type of hybrid system has already been described above; however, it is worth mentioning that rewriting a physical system to fit the description of a hybrid automata is non-trivial, especially when considering the definition of reset maps, invariants and guards [2, 14, 16, 20, 21].

**Switched systems** as described in the literature [2, 8, 9, 10, 11, 12, 13] are a very general class of hybrid systems in which the continuous state evolves according to the vector field of the differential equation, and the switch between vector fields may be triggered based on either the state at a certain time or external signals. It can even contain memory. For example, consider

$$\dot{\mathbf{x}}(t) = \mathbf{f}_q^{\text{ss}}(\mathbf{x}(t)), \quad (1.4)$$

where  $\mathbf{x} \in \mathbb{R}^n$  describes the state vector and  $q : \mathbb{R}_+ \rightarrow \{1, \dots, N\}$  represents the switching signal defining the active vector field  $\mathbf{f}_q^{\text{ss}}$  with  $q \in \{1, \dots, N\}$ . Assuming the system is switching between two dynamics separated by a hypersurface  $\Phi(\mathbf{x}) = 0$  the dynamics can be written as:

$$\dot{\mathbf{x}}(t) = \mathbf{f}^{\text{ss}}(\mathbf{x}(t)) = \begin{cases} \mathbf{f}_-^{\text{ss}}(\mathbf{x}(t)), & \text{if } \Phi(\mathbf{x}(t)) < 0, \\ \mathbf{f}_+^{\text{ss}}(\mathbf{x}(t)), & \text{if } \Phi(\mathbf{x}(t)) > 0. \end{cases} \quad (1.5)$$

**Piecewise affine systems** is the class of hybrid systems on which this thesis will focus. These discontinuous dynamic systems have affine dynamics associated to each region which in respect are polytopic. This class was well-studied in the past and remains under investigation due to its flexibility, as it may be used in both discrete and continuous time [4, 5, 6, 7]. It is also the "simplest" extension of linear systems that allow modeling non-linearities with a high level of accuracy depending on the linearisation; moreover, it can cover simple hybrid phenomena. The continuous form of PWA is given by [2] as:

$$\begin{aligned} \dot{\mathbf{x}}(t) &= \mathbf{A}_q \mathbf{x}(t) + \mathbf{B}_q \mathbf{u}(t) + \mathbf{f}_q \\ \mathbf{y}(t) &= \mathbf{C}_q \mathbf{x}(t) + \mathbf{D}_q \mathbf{u}(t) + \mathbf{g}_q \end{aligned} \quad \text{for } \begin{bmatrix} \mathbf{x}(t) \\ \mathbf{u}(t) \end{bmatrix} \in \mathcal{C}_q, \quad (1.6)$$

with the discrete state  $q \in \{1, \dots, N\}$ ,  $\{\mathcal{C}_1, \dots, \mathcal{C}_N\}$  describing the non-overlapping convex polyhedra in the state-space.  $\mathbf{x}(t)$ ,  $\mathbf{y}(t)$  and  $\mathbf{u}(t)$  represent the state, output and input of the system respectively at time  $t$ .

**Mixed logical dynamical systems** is a class of hybrid systems in which dynamics, logic and constraints are combined in one description [2, 22, 23, 24, 25]

$$\mathbf{x}(m+1) = \mathbf{A}\mathbf{x}(m) + \mathbf{B}_1\mathbf{x}(m) + \mathbf{B}_2\Delta(m) + \mathbf{B}_3\mathbf{z}(m), \quad (1.7)$$

$$\mathbf{y}(m+1) = \mathbf{C}\mathbf{x}(m) + \mathbf{D}_1\mathbf{x}(m) + \mathbf{D}_2\Delta(m) + \mathbf{D}_3\mathbf{z}(m), \quad (1.8)$$

$$\mathbf{E}_1\mathbf{x}(m) + \mathbf{E}_2\mathbf{u}(m) + \mathbf{E}_3\Delta(m) + \mathbf{E}_4\mathbf{z}(m) \leq \mathbf{g}_5 \quad (1.9)$$

where  $\mathbf{A}$ ,  $\mathbf{B}$ ,  $\mathbf{C}$ ,  $\mathbf{D}$ ,  $\mathbf{E}$ , are matrices associated with the system,  $\mathbf{g}_5$  is a vector of the inequality,  $\mathbf{x}(m)$  can have boolean as well as real values (similar structure for  $\mathbf{u}(m)$  and  $\mathbf{y}(m)$ ).  $\mathbf{z}(m)$  and  $\Delta(m)$  are real-valued and boolean auxiliary variables, respectively, and the inequality (1.9) has to be interpreted component wise.

**Complementarity systems** combine differential equations of the form

$$\dot{\mathbf{x}}(t) = \mathbf{f}^{cs}(\mathbf{x}(t), \mathbf{w}(t), \mathbf{u}(t)), \quad (1.10)$$

$$\mathbf{z}(t) = \mathbf{g}^{cs}(\mathbf{x}(t), \mathbf{w}(t), \mathbf{u}(t)) \quad (1.11)$$

with complementarity conditions like

$$0 \leq \mathbf{z}(t) \perp \mathbf{w}(t) \geq 0 \quad (1.12)$$

where  $\mathbf{x}(t)$  is the state,  $\mathbf{u}(t)$  is the input and  $\mathbf{w}(t), \mathbf{z}(t)$  are complementarity variables. The inequality above indicates that  $\mathbf{z}(t)$  and  $\mathbf{w}(t)$  are perpendicular to each other, i.e.  $\mathbf{z}(t)^T \mathbf{w}(t) = 0$ . In other words  $z_i(t) = 0$  or  $w_i(t) = 0$  for each  $i \in \{1, \dots, j\}$  resulting in  $2^j$  modes of the system where each mode is characterized by an active index set  $J \subseteq \{1, \dots, j\}$  and  $z_i = 0$  for  $i \in J$  and  $w_i = 0$  for  $i \in J^c$  with  $J^c := \{1, \dots, n\} \setminus J$  [2, 26, 27, 28].

**Discretely controlled continuous systems** is a class of hybrid systems where the switching signal is dependent on the state vector  $\mathbf{x}(t)$  and the control input  $q(t)$  is a discrete signal switching between the plant's operation modes [2, 29, 30, 31, 32].

While the description is similar to the previously mentioned PWA system, the key difference is as follows: In a PWA system the state-space is partitioned into sets  $\mathcal{C}_q (q \in \mathcal{Q})$ . The evolution of the continuous states  $\mathbf{x}(t)$  is defined by the respective vector field associated with the set in which the state currently resides, e.g. if the state  $\mathbf{x}(t)$  is within the partition  $\mathcal{C}_2$ , its evolution is governed by the vector field  $\mathbf{f}_2^{pwa}$ . After crossing into



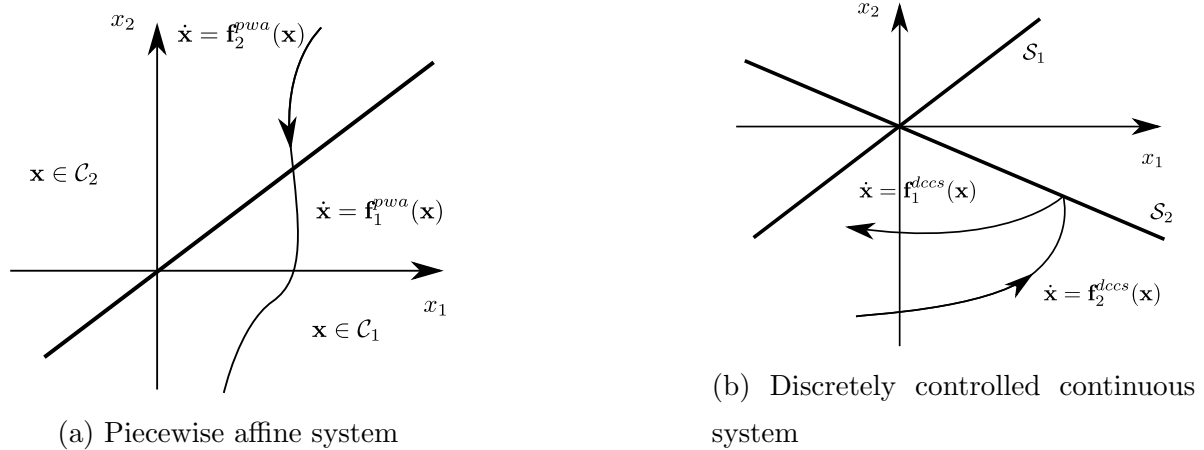


Figure 1.4: Comparison of switching schemes between piecewise affine and discretely controlled continuous systems [2]

another partition/set, e.g.  $\mathcal{C}_1$  the evolution of the state is then governed by vector field  $\mathbf{f}_1^{pwa}$ .

Contrary to the above, in discretely controlled continuous systems the switching between modes is usually defined by switching surfaces or hyperplanes in the state-space. If the state trajectory crosses a switching surface, a change of mode is triggered. The vector field that will become active at the time of crossing is dependent on the mode which becomes active. It is possible that while the states are passing through a region on one vector field, after crossing the switching surface they continue in the same region yet with a different vector field. A side-by-side comparison of PWA and discretely controlled continuous systems and how the state evolution might appear is shown in Fig. 1.4.

**Timed automata** have simple continuous dynamics of the form  $\dot{x} = 1$  with the invariants, guards, etc. being compared to constants. This limits the capability of timed automata with regard to modeling physical systems. At the same time it makes them very attractive for modeling timing constraints of the form: event  $A$  must take place at least 2s after event  $B$  but not more than 5s after event  $C$  [2, 18, 33, 34, 35, 36, 37].

**Hybrid inclusion** are an extension of differential inclusions  $\dot{\mathbf{x}} \in \mathcal{F}^{hi}(\mathbf{x})$  adding invariants, resets and guards. The inclusions are given by the flow set  $\mathcal{C}^{hi}$  and jump set  $\mathcal{D}^{hi}$  with the set-valued mappings  $\mathcal{F}^{hi} : \mathcal{C}^{hi} \rightarrow \mathbb{R}^n$  and  $\mathcal{G}^{hi} : \mathcal{D}^{hi} \rightarrow \mathbb{R}^n$  whereas the hybrid inclusion is then written as:

$$\begin{aligned} \dot{\mathbf{x}} &\in \mathcal{F}^{hi}(\mathbf{x}) && \text{if } \mathbf{x} \in \mathcal{C}^{hi}, \\ \mathbf{x}_+ &\in \mathcal{G}^{hi}(\mathbf{x}) && \text{if } \mathbf{x} \in \mathcal{D}^{hi}, \end{aligned} \tag{1.13}$$

which provides the user with a compact and well structured model and is suitable for many hybrid phenomena [2, 38, 39, 40, 41].

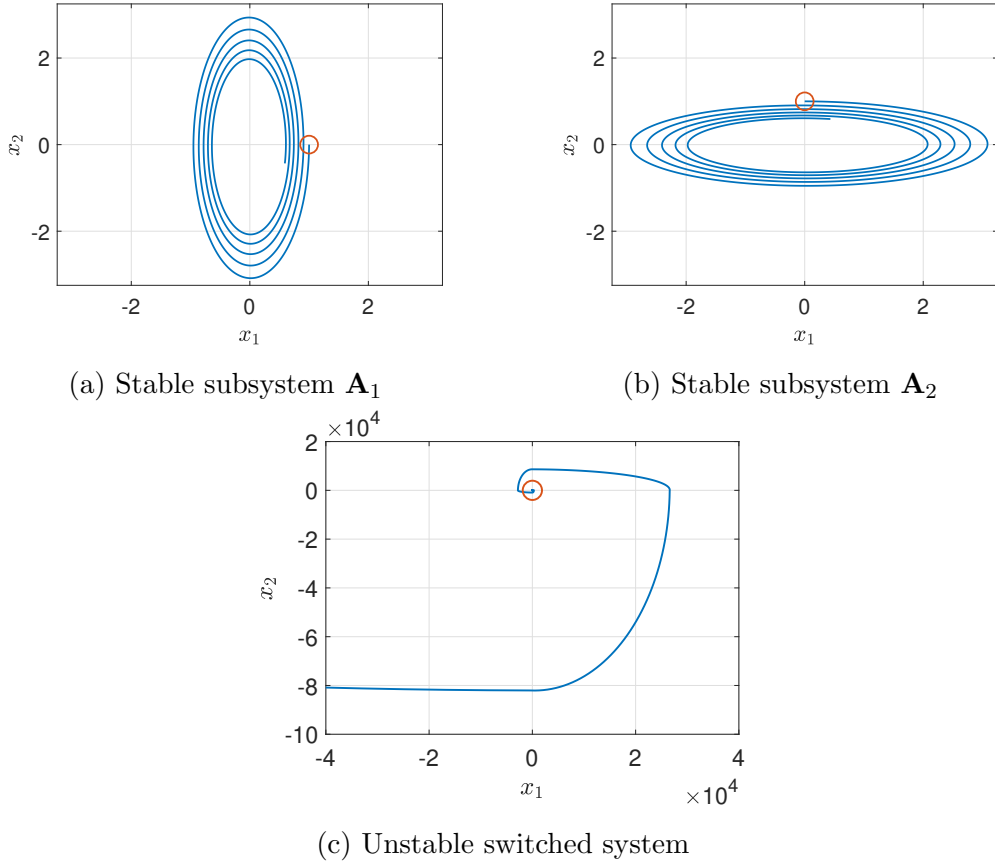


Figure 1.5: Simulation of stable subsystems and unstable switched system. The dots indicate initial condition [9]

#### 1.2.1.4 Hybrid System Phenomena

**Instability due to switching** is a phenomenon which may occur in some hybrid systems [9]. In such cases it is insufficient to just study the respective subsystems individually and prove their stability because the switching between them has to be taken into account as well. This may be illustrated by the following example of a switched system. Let us assume we have a hybrid system with two operation modes

$$\dot{\mathbf{x}} = \begin{cases} \mathbf{A}_1 \mathbf{x} & \text{if } x_1 x_2 \leq 0, \\ \mathbf{A}_2 \mathbf{x} & \text{if } x_1 x_2 > 0, \end{cases} \quad (1.14)$$

with

$$\mathbf{A}_1 = \begin{bmatrix} -1 & 10 \\ -100 & -1 \end{bmatrix} \quad \text{and} \quad \mathbf{A}_2 = \begin{bmatrix} -1 & 100 \\ -10 & -1 \end{bmatrix}. \quad (1.15)$$

From the eigenvalues of the two system matrices  $\mathbf{A}_1$  and  $\mathbf{A}_2$  which are approximately  $-1 \pm 31.62j$  for both, it may be seen that the single systems are stable, as further shown in Figs. 1.5a and 1.5b, but the switched system in Fig. 1.5c shows instability. The opposite effect may also be attained where two unstable systems are combined into a hybrid system with

the switching condition stabilizing the system. This can be illustrated by using the time-reversed version of the system described above. Switching is an additional uncertainty factor in system analysis that does not only have to be taken into account during stability analysis but also influences observability, controllability, etc.

**Zeno behavior** is another phenomenon that may be observed, which means that within finite time, an infinite amount of events occur for a given dynamic system [42]. An example of a system experiencing zeno behavior is the bouncing ball where the ball's position trajectory  $x_1$  is defined by the continuous dynamics. Upon ground impact an event takes place, changing the ball's velocity  $x_2(t_+) = -ax_2(t_-)$  with  $0 < a < 1$ , resulting in a constant overall decrease in the ball's height, cf. Fig. 1.6. This hybrid system leads to an infinite number of events taking place in finite time in order to get the ball to its idle state. Zeno behavior possibly influences the well-posedness of a system since it can affect the existence of a global solution [2].

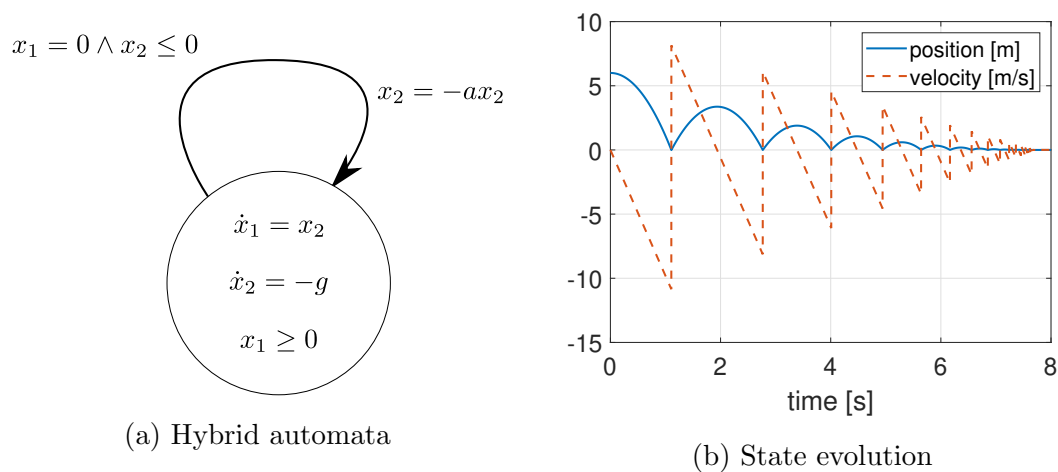


Figure 1.6: Bouncing ball [2]

**Chattering** is a side effect of hybrid systems that can occur if vector fields, which define the continuous dynamics, are divided by a hyperplane and point toward this hyperplane, cf. Fig. 1.7. While in some instances this kind of behavior is not desired and results in a possible systemic deadlock, sliding mode control uses this phenomenon to its advantage by defining a hyperplane  $\mathcal{S}$ , along which the continuous state is intended to propagate [43].

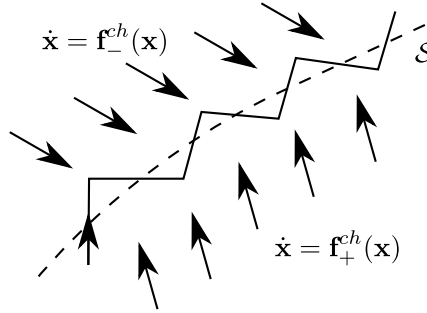


Figure 1.7: Chattering of switched system

**Nondeterminism** with respect to hybrid systems means that the system is sensitive to even minor changes in the initial continuous state, resulting in the sequence of discrete states being non-deterministic [2, 44]. The evolution of continuous states is governed by the vector field and depending on it, a state trajectory might lead to e.g. a switching surface  $\mathcal{S}$  where a discrete state change is triggered, or remain in the same set of the state-space, cf. 1.8a. In another scenario shown in Fig. 1.8b, two of the state trajectories tend toward the switching surfaces  $\mathcal{S}_1$  and  $\mathcal{S}_2$  where state jumps are triggered, after which the states continue in different sets associated with their jump. However, what happens if the trajectory ends up at the intersection of the two switching surfaces is not defined.

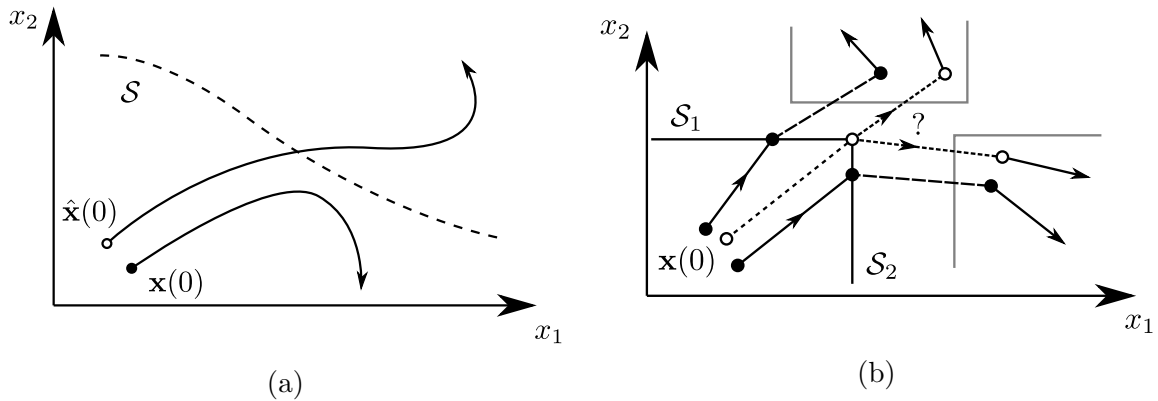


Figure 1.8: Sensitivity of hybrid systems [2]

## 1.2.2 Piecewise Affine Systems

### 1.2.2.1 Modeling

PWA systems allow for not only modeling a broad spectrum of physical systems but also allowing the expression of non-linearities around several operation points via multiple linearizations. They may therefore be seen as the middle ground between a full-order model and a model linearized around one operational point. The reproductive accuracy of the non-linearity by means of multiple linearizations is of course dependent on how

many linearizations are performed. A higher level of accuracy in reproduction is usually achieved with an increasing number of linearizations. However, it should be obvious that the model's accuracy is also dependent on how and at which points linearizations are performed. Further, the model's complexity increases with the number of linearizations performed, possibly making it more difficult to analyze the system properly with respect to stability [5].

Additionally, PWA systems are versatile due to them being able to be used in both continuous and discrete time domains. PWA systems are expressed by means of extended state-space equations

$$\begin{aligned} \dot{\mathbf{x}}(t) &= \mathbf{A}_q \mathbf{x}(t) + \mathbf{B}_q \mathbf{u}(t) + \mathbf{f}_q \\ \mathbf{y}(t) &= \mathbf{C}_q \mathbf{x}(t) + \mathbf{D}_q \mathbf{u}(t) + \mathbf{g}_q \end{aligned} \quad \text{for } \begin{bmatrix} \mathbf{x}(t) \\ \mathbf{u}(t) \end{bmatrix} \in \mathcal{C}_q. \quad (1.16)$$

The standard state-space formulation describes the evolution of the system's states  $\mathbf{x}(t)$  by means of  $\mathbf{A}$  describing the system's dynamics,  $\mathbf{B}$  describing the relation between input signal  $\mathbf{u}(t)$  and system dynamics alongside an output term  $\mathbf{C}$  and a feed through terms  $\mathbf{D}$  defining the system's output  $\mathbf{y}(t)$ .

In the above equation, one can see that the standard state-space format was extended by the vectors  $\mathbf{f}_q$  and  $\mathbf{g}_q$ . These vectors may be seen as constant offsets. In a PWA system some or all vectors and matrices are dependent on the currently active discrete state  $q \in \{1, \dots, n\}$  and differ in value between discrete states, therefore describing different vector fields to which the states' evolution is tied. Each discrete state relates to a set  $\mathcal{C}_q$  representing a convex polyhedra with the polyhedras not overlapping each other. If  $\mathbf{f}_q$  and  $\mathbf{g}_q$  are null, the system is considered to be piecewise linear with the associated set  $\mathcal{C}_q$  usually containing the system's equilibrium point [5]. Determining which discrete state is active depends on the combination of one or several states, possibly also including the input signal, e.g. actuator saturation.

### 1.2.2.2 Control

Over the past centuries, ever increasing knowledge in fields like mathematics and physics has enabled us to further examine and model systems as well as develop control structures, during which terms like controllability, stabilizability, observability and detectability have arisen. These play an important role in modern control theory. For example, Kalman was a pioneer in the field of controllability, which was further extensively studied in the field of finite-dimensional linear systems, nonlinear systems, infinite-dimensional systems, hybrid systems and behavioral systems [45]. Outside of the linear context, however, global controllability is hard to prove, even for smooth non-linear systems [2].

As regards hybrid systems, controllability and stabilizability remain a topic of investigation. For instance, while no general algorithm applicable to hybrid systems has yet been found [2], for specific classes, amongst which are PWA systems, results have been generated for both controllability [5, 46, 47] and observability/detectability [5, 48, 49].

Generally speaking, while controllability merely describes the ability of moving the system's states around in state-space according to a defined reference trajectory by manipulating its system inputs, choosing a suitable control structure to fulfill the requirements imposed is essential. The most common control structure is feedback control, which has a long history in various fields of application dating all the way back to antiquity. Recently, more elaborate control strategies/structures for more complex systems have been developed [50]. One of the most common and widespread control techniques is probably the well-known PID controller consisting of proportional, integral and derivative control [1]. While PID control might be sufficient for many application cases, more elaborate control strategies have been developed to further enhance a system's performance and tailor its response to the respective requirements.

In the following a short overview of various common control strategies is given, beginning with adaptive control [51] using online identification of process parameters and modification of controller gains for establishing robustness. Hierarchical control [52] is another way of controlling more complex systems where the system is split up in e.g. sub-systems which are controlled individually nested under e.g. an overall controller design. More recently, due to the rise of artificial intelligence (AI), intelligent control [53, 54] has become more prominent using artificial neural networks, fuzzy logic, machine learning, genetic algorithms, etc. Optimal controllers [55] are widely used to control a system based on a defined "cost index" that is to be minimized. The cost function can be related not only to common characteristics like settling time, overshoot, etc. but can also be more complex e.g. minimizing fuel consumption for an airplane flight. This group of controllers also include Model Predictive Control (MPC) [56] and linear-quadratic-Gaussian control (LQG) [57]. Especially when there are uncertainties prevalent between the model used to design a controller and the actual system, robust controllers [58] are used. This class of controllers include techniques like H-infinity [59] and sliding mode control (SMC) [43].

As it seems the overly dominant control strategy used for PWA systems was and is still MPC and certain variations of it [5, 60, 61, 62, 63, 64]. This control approach uses a model to predict the state trajectories for a given time horizon  $N$  based on the current states  $\mathbf{x}(m)$  and control inputs  $\hat{\mathbf{u}}$ , generated by a cost function

$$\hat{\mathbf{u}}(\mathbf{x}(m)) = \arg \min_{\mathbf{u}} \sum_{i=0}^{N-1} f^{MPC}(\mathbf{x}(m+i), \mathbf{u}(m+i)) \quad (1.17)$$

which is to be minimized. Only the first value of the generated control values is then

used in the following system iteration where the new states are measured again and the process repeated.

Other research has been conducted on synthesizing control laws based on linear algebra and reach-set computations [65], piecewise affine state-feedback [66] and moving horizon estimation [24].

In order to be able to control a system, one or more of its states has to be measurable. The limited number of states available/measurable often restricts the design of a proper control structure; therefore, having more states which can be used for control is beneficial. However, since in most physical systems not all states within the system can be measured, observers remain a topic of interest to hybrid and therefore PWA systems, where the remaining unknown states are estimated based on the observer's system model. One can imagine that creating a suitable observer turns out to be relatively complicated if the current discrete state  $q$  is unknown and cannot be reconstructed directly by the known system output  $\mathbf{y}(t)$  and system input  $\mathbf{u}(t)$ . Another level of difficulty associated with state estimation is added when resets of the continuous states are present. Works which are concerned with observer design for PWA systems are e.g. [67, 68, 69, 70, 71, 72, 73].

### 1.2.2.3 Stability Analysis

For linear time invariant (LTI) systems mathematical techniques in the frequency domain like Laplace transform, Fourier Transform, Z-Transform, Bode plot, root locus and Nyquist stability criterion can be applied to determine stability [1]. However, since all real world systems contain non-linearities and if analyzed in depth so will the models, other stability criteria are necessary to evaluate a system. Such criteria include but are not limited to limit cycle theory [74], Poincaré maps [75], Lyapunov stability theorem [76] and Popov criterium [77].

Since this thesis focuses on stability analysis using pole-zero plots, which are well known, and the Lyapunov theorem, only the latter approach will be further elaborated on in more detail, specific for PWA Systems. The pioneer of stability analysis for dynamical systems was Lyapunov [76] with his theorem being based on the conservation of energy in the sense that if the energy in a system decreases over time it must come to rest independent of its initial state. This means that the energy of a system  $L(\mathbf{x}(t))$  for a motion  $\mathbf{x}(t)$  is proper in the sense of  $L(0) = 0$  and

$$L(\mathbf{x}) > 0 \quad \forall \mathbf{x} \neq 0. \quad (1.18)$$

Further  $L(\mathbf{x}) \rightarrow \infty$  when  $\|\mathbf{x}\| \rightarrow \infty$ . That the energy of the system  $\dot{\mathbf{x}} = \mathbf{f}^{ya}(\mathbf{x})$  is to constantly decrease along all trajectories is defined by the requirement

$$\dot{L}(\mathbf{x}) = \frac{\partial L(\mathbf{x})}{\partial \mathbf{x}} \mathbf{f}^{ya}(\mathbf{x}) < 0 \quad \forall \mathbf{x} \neq 0. \quad (1.19)$$

The function  $L(\mathbf{x})$  is called a Lyapunov function and represents an abstract measure of the energy stored in the system. One might be able to determine a Lyapunov function based on the knowledge of the modeled system but as should be clear, finding an appropriate function is not trivial [15].

By fulfilling the above mentioned Lyapunov conditions a system is considered to be asymptotically stable. For linear systems the Lyapunov equation was defined as  $L(\mathbf{x}) = \mathbf{x}^T \mathbf{P} \mathbf{x}$  for a continuous linear system  $\dot{\mathbf{x}} = \mathbf{A} \mathbf{x}$  leading to the inequalities

$$\mathbf{P} > 0 \quad \mathbf{A}^T \mathbf{P} + \mathbf{P} \mathbf{A} < 0, \quad (1.20)$$

where the system is considered to be asymptotically stable if the matrix  $\mathbf{P}$  is positive definite.

While this method can be applied to linear systems which use standard state-space representation, the inequalities had to be expanded to accommodate for the additional affine vector  $\mathbf{f}_q$  of PWA systems resulting in *piecewise quadratic Lyapunov functions* [78, 79]. The state vector is extended to

$$\bar{\mathbf{x}}(t) = \begin{bmatrix} \mathbf{x}(t) \\ 1 \end{bmatrix} \quad (1.21)$$

with the dynamics of the system defined as

$$\dot{\bar{\mathbf{x}}} = \begin{bmatrix} \dot{\mathbf{x}} \\ 0 \end{bmatrix} = \begin{bmatrix} \mathbf{A}_q & \mathbf{f}_q \\ 0_{1 \times n} & 0 \end{bmatrix} \bar{\mathbf{x}} = \bar{\mathbf{A}}_q \bar{\mathbf{x}} \quad (1.22)$$

Since  $\bar{\mathbf{A}}_q$  describes the evolution of the continuous state only for the discrete state  $q$  and therefore only for a subset of the overall state-space, cell boundaries have to be established limiting the validity of the above mentioned linear matrix inequalities (LMI's) to the respective polyhedra. This is done by introducing the *polyhedral cell bounding matrix*  $\bar{\mathbf{E}}_q = [\mathbf{E}_q, \mathbf{e}_q]$  with the condition

$$\bar{\mathbf{E}}_q \bar{\mathbf{x}}(t) \succeq 0 \quad \text{for } \mathbf{x}(t) \in \mathcal{X}_q \quad (1.23)$$

and

$$\mathbf{e}_q = 0 \quad \text{for } q \in I_0, \quad (1.24)$$

where the polyhedra or cell  $I_0$  contains the origin and all other cells are denoted as  $I_1$ . To further ensure continuity between the different polyhedra/cells dividing the state-space, a *continuity matrix*  $\bar{\mathbf{F}}_q = [\mathbf{F}_q, \hat{\mathbf{f}}_q]$  is needed for cell  $\mathcal{X}_q$  with the condition that

$$\bar{\mathbf{F}}_q \bar{\mathbf{x}}(t) = \bar{\mathbf{F}}_{q^+} \bar{\mathbf{x}}(t) \quad \text{for } \mathbf{x}(t) \in \mathcal{X}_q \cap \mathcal{X}_{q^+}, \quad (1.25)$$

again with the condition that

$$\hat{\mathbf{f}}_q = 0 \quad \text{for } q \in I_0. \quad (1.26)$$



Using the knowledge about the LMI's of continuous linear systems combined with the extensions made for PWA systems, piecewise quadratic stability can be proven with

$$\begin{aligned}\mathbf{P}_q &= \mathbf{F}_q^T \mathbf{T} \mathbf{F}_q & q \in I_0, \\ \bar{\mathbf{P}}_q &= \bar{\mathbf{F}}_q^T \mathbf{T} \bar{\mathbf{F}}_q & q \in I_1,\end{aligned}\tag{1.27}$$

when the following LMI's are satisfied

$$\begin{cases} 0 > \mathbf{A}_q^T \mathbf{P}_q + \mathbf{P}_q \mathbf{A}_q + \mathbf{E}_q^T \mathbf{U}_q \mathbf{E}_q \\ 0 < \mathbf{P}_q - \mathbf{E}_q^T \mathbf{W}_q \mathbf{E}_q \end{cases} \quad q \in I_0,\tag{1.28}$$

$$\begin{cases} 0 > \bar{\mathbf{A}}_q^T \bar{\mathbf{P}}_q + \bar{\mathbf{P}}_q \bar{\mathbf{A}}_q + \bar{\mathbf{E}}_q^T \mathbf{U}_q \bar{\mathbf{E}}_q \\ 0 < \bar{\mathbf{P}}_q - \bar{\mathbf{E}}_q^T \mathbf{W}_q \bar{\mathbf{E}}_q \end{cases} \quad q \in I_1,\tag{1.29}$$

The symmetric matrices  $\mathbf{T}$ ,  $\mathbf{U}_q$  and  $\mathbf{W}_q$  are to be determined with  $\mathbf{U}_q$  and  $\mathbf{W}_q$  containing only non-negative entries.

This is merely a brief summary of the extensions to the original Lyapunov theorem that have been made to adopt the formalism to PWA systems, outlining the required key components and conditions to be fulfilled.

## 1.3 Contributions

This thesis is based on five papers that have been published or submitted for publication during the PhD study.

### 1.3.1 Paper A: Design and Analysis of non-linear Circuit with Tunnel Diode for Hybrid Control Systems

**Summary:** In this paper an electric circuit containing a non-linear tunnel diode is investigated. A test setup was built based on a model of the circuit, which was created containing two differential equations, including a non-linear term representing the tunnel diode's characteristic. Measurements were performed to characterize the diode and obtain the parameters for the non-linear term. The system's transient response was evaluated and the circuit analyzed, including the hysteresis behavior of the diode followed by an open loop control where the diode switches between its high and low states based on a pulsed input signal.

**This paper has been published as:**

P. Pasolli, M. Ruderman. Design and Analysis of non-linear Circuit with Tunnel Diode for Hybrid Control Systems. *Proceeding of IEEE 15th International Workshop on Advanced*

*Motion Control (AMC2018)*, 181-186, 2018.

doi: 10.1109/AMC.2019.8371084.

### **1.3.2 Paper B: Design, Control, and Analysis of Nonlinear Circuits with Tunnel Diode with Piecewise Affine Dynamics**

**Summary:** This paper expands upon the previous Paper A. A closed loop control structure in the form of an integral error, state-feedback controller is added. Further, a series of simulations and experiments are performed to validate the closed loop system where the diode is controlled toward its high and low states. A third simulation/experiment is conducted with a reference controlling the system to a section with a negative gradient on the diode's characteristic, resulting in a limit cycle behavior. The non-linearity is linearized, resulting in four cells, each of which is associated with a linear characteristic and results in a PWA model with four discrete states. A formal verification of the model is performed by using the PWLTool toolbox and compared to Simulink-based simulation results.

**This paper has been published as:**

P. Pasolli, M. Ruderman. Design, Control, and Analysis of Nonlinear Circuits with Tunnel Diode with Piecewise Affine Dynamics. *IEEJ Journal of Industry Applications*, Vol.8 No.2 pp.280-249, 2018. doi: 10.1541/ieejia.8.240.

### **1.3.3 Paper C: Linearized Piecewise Affine in Control and States Hydraulic System: Modeling and Identification**

**Summary:** A hydraulic test setup was built consisting of two cylinders in antagonistic setup which can be controlled individually and connected via a force gauge. A full-order model of the right cylinder-valve combination is created that includes several non-linearities followed by a model reduction. A series of tests are performed to identify the parameters and characteristics of the respective subsystems and non-linearities. The non-linear terms are then linearized at multiple points upon which a PWA model of the hydraulic system is created. A series of simulations and experiments are performed where the results from experimentally measured data, full-order model, reduced-order model and PWA model simulations are compared to one another.

**This paper has been published as:**

P. Pasolli, M. Ruderman. Linearized Piecewise Affine in Control and States Hydraulic System: Modeling and Identification. *IECON 2018-44th Annual Conference of the IEEE*

*Industrial Electronics Society*, pp. 4537-4544, 2018. doi: 10.1109/IECON.2018.8591572.

### 1.3.4 Paper D: Hybrid State Feedback Position-Force Control of Hydraulic Cylinder

**Summary:** This paper is part of a natural evolution of Paper C where the previously derived PWA model of the hydraulic setup is expanded upon by introducing a hybrid, closed loop control circuit capable of controlling the cylinder in both position and force control mode. The closed loop structure includes an integral error, state-feedback controller alongside a static dead-zone compensator for the valve and a low pass filter (LPF) for the control signal. The switching between control modes is triggered by a hysteresis relay. Optimal state feedback gains are established by the use of non-linear, least-squares optimization. Experiments and simulations are performed to verify the controller's performance based on a position- to force-control test scenario.

**This paper has been published as:**

P. Pasolli, M. Ruderman. Hybrid State Feedback Position-Force Control of Hydraulic Cylinder. *2019 IEEE International Conference on Mechatronics (ICM)*, Vol. 1, pp. 54-59, 2019. doi: 10.1109/ICMECH.2019.8722829.

### 1.3.5 Paper E: Hybrid Position/Force Control for Hydraulic Actuators

**Summary:** Paper E expands upon Paper D by establishing a position-force-position control approach based on the previously derived PWA model. To improve performance, the control structure is changed to an integral error, feed-forward, state-feedback controller, including a static dead-zone compensator and LPF. Controller gains are determined by the use of the standard pole placement method based on the linearized PWA model, further confirming local stability. A multiple Lyapunov function-based stability analysis is performed to verify the stability of the switched system, including the event-based switching of the hysteresis relay. Two test scenarios are presented simulating a hard stop and a dynamic environment, both triggering one or multiple cycles of switching from position to force control and back. Several experimental measurements for each respective scenario are performed to evaluate repeatability, the results of which are presented.

**This paper has been submitted as:**

P. Pasolli, M. Ruderman. Hybrid Position/Force Control for Hydraulic Actuators. Under review at *IEEE Transactions on Industrial Electronics*.

## 1.4 Test Setup Overview

During the course of this thesis two test setups were built with the first one being an electric circuit based on [80]. The circuit contains a voltage source  $u$  in series with a resistor  $R$  and an inductance  $L$ . In parallel to this two paths are added with the first one containing a capacitance  $C$  and the other one a non-linear tunnel diode. A schematic of the circuit is shown in Fig. 1.9. A more detailed description, including the components and instrumentation used, may be found in Papers A and B.

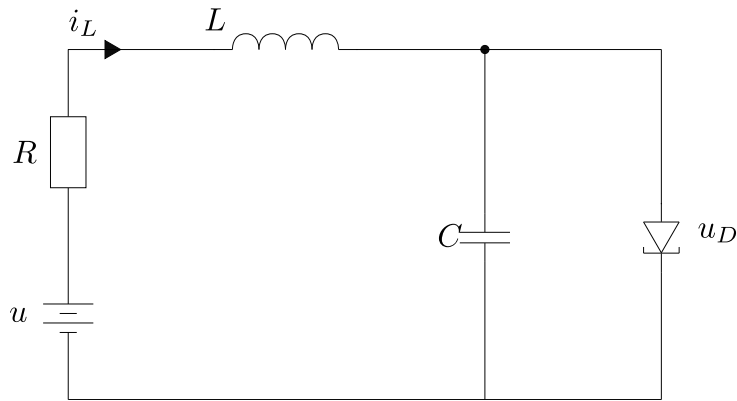


Figure 1.9: Electric circuit including a non-linear tunnel diode

The second test setup is a hydraulic system with increased complexity in comparison to the electrical one. The setup consists of two cylinders arranged in an antagonistic setup, coupled together via a force gauge. The left cylinder is connected to a bidirectional control valve (BDCV) which is only used to change the direction of the flow with a pressure relief/reduction valve (PRV) connected to it, adjusting the line's pressure. The right cylinder is connected to a servo valve that is to be controlled. All pressures in the system are measured as well as the servo valve's spool position and right cylinder's position. The models created are based on the right cylinder-valve combination (marked with dashed box), cf. Fig. 1.10. The uncontrolled system includes several unknown parameters which were identified alongside three non-linearities. A more detailed technical description of the setup, including components and instrumentation, may be found in appendix F.

## 1.5 Outline

Since detailed information is given in the respective papers listed in the appendix, which will be referred to in the following chapters, the rest of the thesis' main section focuses on the methodology used. Examples and information from the papers are occasionally used for illustration purposes. The remainder of this thesis is divided into three main chapters. In Chapter 2 the modeling methodology for dynamic systems, parameter identification and

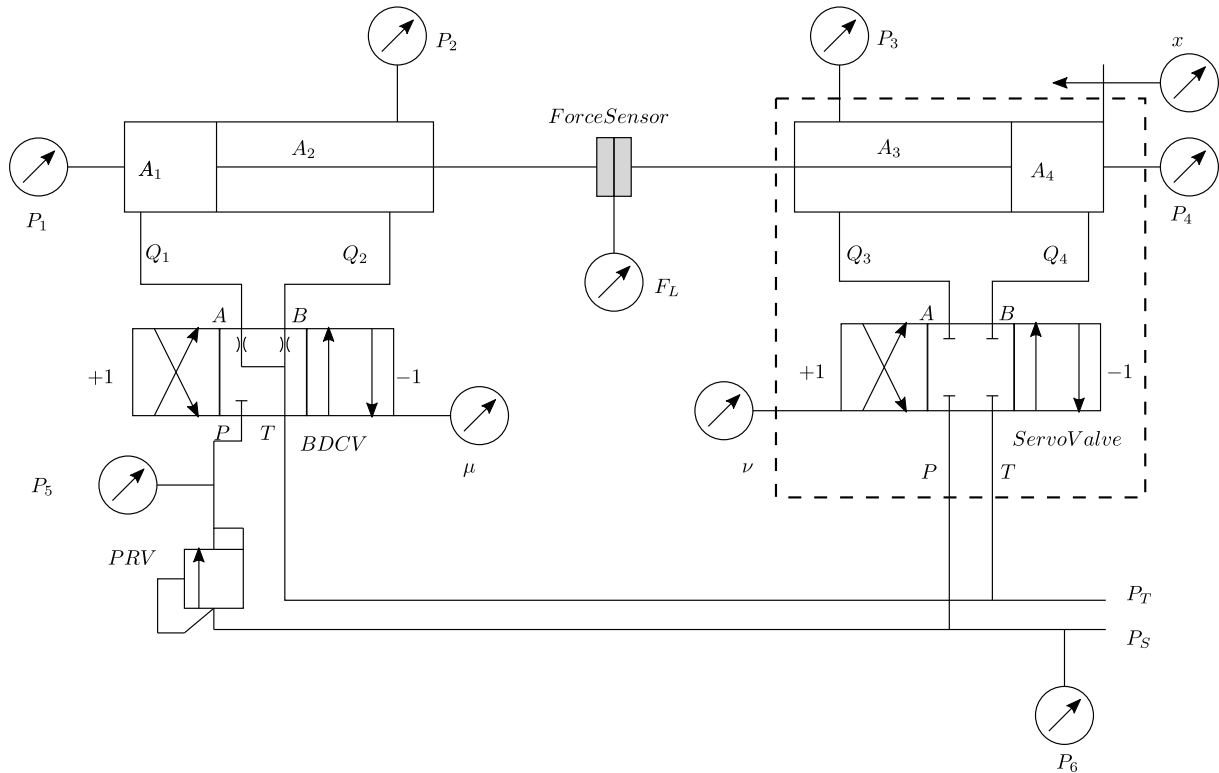


Figure 1.10: Schematic of hydraulic test setup

the linearization process used for obtaining a PWA based model are introduced. Chapter 3 is devoted to control-related topics. First, the control structure itself is elaborated on, followed by a control signal filter, a static compensator, the switching event triggering the respective control modes and the obtainment of controller gains. Chapter 4 is involved with the local stability analysis using pole-zero plots and a multiple Lyapunov function-based approach. Finally, in Chapter 5 the thesis is concluded with further information given with regard to future work.



# Chapter 2

## Modeling of Dynamical Systems

The framework used throughout this thesis to model and describe systems is the state-space representation, which allows the formulation of dynamics by means of several first order differential equations. This method of representation allows for a compact notation that includes multiple inputs and outputs. If the system is also LTI, its dynamics may be expressed as a static matrix having its states, inputs and outputs expressed in static vectors or matrices. These cases also allow for a convenient transformation – from time domain to frequency domain – for further analysis.

In this chapter the concept of a dynamic system's state-space representation is introduced, after which the methodology used to derive models for both test setups is elaborated on and thoughts about the process pointed out. The methods used for identifying the models unknown parameters and characteristics is explained with the presentation of the linearization approach taken to linearize the respective models non-linear characteristics concluding this chapter.

### 2.1 State-Space Modeling - Linear Time Invariant Systems

A system's dynamics are defined by its differential equations. A system is considered LTI if its output may be described via a linear map that is dependent on the system's inputs. If an input is applied at two different times, the system's output will be identical at both times (except for the time passed in-between). Since these systems do not include non-linear characteristics, they may be expressed using the standard state-space representation. A single input, single output (SISO) system's model may be expressed by the following formulation

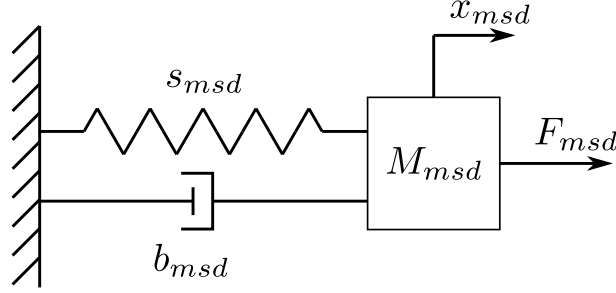


Figure 2.1: Linear time invariant mass spring damper system

$$\begin{aligned}\dot{\mathbf{x}} &= \mathbf{A}\mathbf{x} + \mathbf{b}u, \\ y &= \mathbf{c}\mathbf{x}.\end{aligned}\tag{2.1}$$

The above equation omits the feed-through term that is present in the standard state-space representation since it is not relevant for this work. The variables are defined as  $\mathbf{x} \in \mathbb{R}^{n \times 1}$  being the state vector,  $\mathbf{A} \in \mathbb{R}^{n \times n}$  system matrix,  $\mathbf{b} \in \mathbb{R}^{n \times 1}$  input vector,  $u$  system input,  $y$  system output and  $\mathbf{c} \in \mathbb{R}^{1 \times n}$  output vector.

Let us exemplify these system's modeling processes based on the mass spring damper system shown in Fig. 2.1. Based on Newton's Second Law, stating that the sum of all forces acting on a body is equal to the body's mass times acceleration, the following differential equation may be derived describing the mass' dynamics

$$\ddot{x}_{msd} = \frac{1}{M_{msd}} (F_{msd} - b_{msd}\dot{x}_{msd} - s_{msd}x_{msd}).\tag{2.2}$$

The system's states are the velocity  $\dot{x}_{msd}$  and position  $x_{msd}$ . As can be seen from the equation, there is a linear dependency between the states and the system's acceleration, with the mass  $M_{msd}$ , damping  $b_{msd}$  and the spring constant  $s_{msd}$  being time-invariant. In order to transform the differential equation into the state-space format, a state vector  $\mathbf{x} = [x_1, x_2]^T$  is created with  $x_2 = \dot{x}_{msd}$  and  $x_1 = x_{msd}$ . The system's input  $u$  in this case is the external force  $F_{msd}$  and the output of interest to us is the mass' position as in  $y = x_1$ .

The system's dynamics written in a state-space format may then be expressed as

$$\begin{aligned}\dot{\mathbf{x}} &= \begin{bmatrix} \dot{x}_1 \\ \dot{x}_2 \end{bmatrix} = \begin{bmatrix} 0 & 1 \\ -\frac{s_{msd}}{M_{msd}} & -\frac{b_{msd}}{M_{msd}} \end{bmatrix} \begin{bmatrix} x_1 \\ x_2 \end{bmatrix} + \begin{bmatrix} 0 \\ 1 \\ M_{msd} \end{bmatrix} F_{msd} = \mathbf{A}\mathbf{x} + \mathbf{b}F_{msd}, \\ y &= \begin{bmatrix} 1 & 0 \end{bmatrix} \begin{bmatrix} x_1 \\ x_2 \end{bmatrix} = \mathbf{c}\mathbf{x}.\end{aligned}\tag{2.3}$$



## 2.2 Non-linear Systems

Similarly, a non-linear system to be modeled is investigated and differential equations derived which describe the system's dynamics, the difference being that some or all resulting equations are of a non-linear nature. This point may be illustrated by assuming that the damper in the above described mass spring damper system has a non-linear characteristic that is given by

$$b_{msd}(\dot{x}_{msd}) = a_1 \dot{x}_{msd}^3 + a_2 \dot{x}_{msd}. \quad (2.4)$$

resulting in the differential equation being written as

$$\ddot{x}_{msd} = \frac{1}{M_{msd}} (F_{msd} - b_{msd}(\dot{x}_{msd}) - s_{msd}x_{msd}). \quad (2.5)$$

Since the differential equation now exhibits non-linear terms due to the damper's characteristic, the system's model cannot be expressed using the standard state-space representation since the system matrix  $\mathbf{A}$  is to be static and therefore will not contain system states.

While the above textbook example is fully modeled by only one differential equation, the models for the test setups vary in their levels of complexity. In such more complex systems, it is beneficial to divide the overall system into several subsystems which, while linked together, can be modeled and analyzed individually, basically breaking the system down through a top-down approach and then building up an overall model through a bottom-up approach where the individual submodels are combined.

### 2.2.1 Electric Setup

The electric circuit first presented in Paper A, cf. Fig. 1.9, is based on [80] and consists of a couple of standard electric components and a non-linear tunnel diode. The circuit model may be created by applying Kirchoff's First and Second Laws in combination with the differential equations for the inductance and capacitance, resulting in the system's dynamics being defined as

$$\begin{aligned} \dot{x}_1 &= \frac{1}{C}(-f_D(x_1) + x_2), \\ \dot{x}_2 &= \frac{1}{L}(u - Rx_2 - x_1), \end{aligned} \quad (2.6)$$

where  $x_1 = u_D$  is the voltage across the diode,  $x_2 = i_L$  is the inductance current and the state vector is defined as  $\mathbf{x} = [x_1, x_2]^T$ . The non-linearity  $f_D(x_1)$  represents the diode's characteristics and may be approximated, according to [80], with a polynomial of the fifth order as

$$f_D(x_1) \approx \kappa_1 x_1 + \kappa_2 x_1^2 + \kappa_3 x_1^3 + \kappa_4 x_1^4 + \kappa_5 x_1^5, \quad (2.7)$$

with the coefficients  $\kappa_{1,\dots,5}$  shaping the polynomial. The differential equations in (2.6) with the polynomial in (2.7) represent the system's full-order model and the model's accuracy when compared to the physical system being only affected by the choice of the function representing the non-linearity and its coefficients, assuming the inductance, capacitance and resistor are LTI.

## 2.2.2 Hydraulic Setup

The hydraulic setup first investigated in Paper C is complex and consists of multiple individual components combined in series with one another. To make the modeling process more comprehensible, the system is split up into several subsystems, cf. Fig. 2.2, which may be investigated individually, simplifying the process of creating a suitable model as previously described. In the following the thought process and approach for modeling the different subsystems are presented.

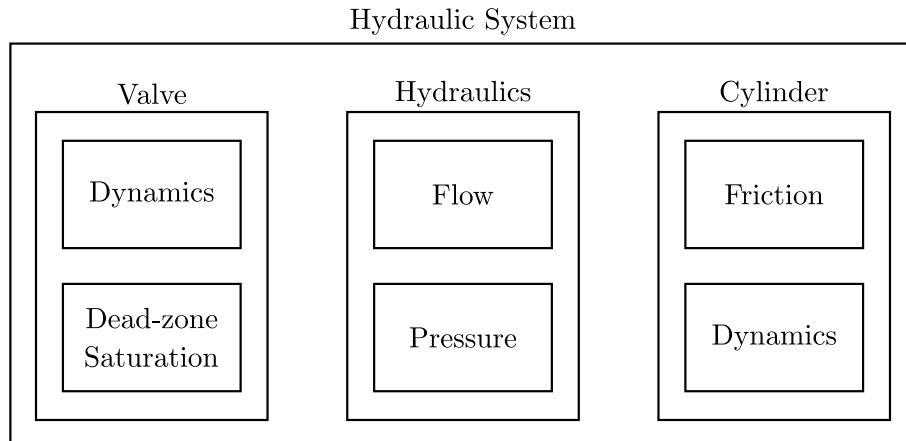


Figure 2.2: Subsystems of hydraulic setup

### Valve

The valve's subsystem consists of the dynamics of the moving parts (spool) along with the dead-zone and saturation combination due to its mechanical construction. The valve used in the test setup comes with an integrated control loop. Since there is no insight given into the control structure or parameters used, it is tedious to create a detailed model of the valve that includes the spool's dynamics, electronics used for control and the control structure deployed. From data sheet inspection, in particular the frequency response function (FRF), it is known that the overall valve has a rather high cutoff frequency in comparison to the rather slow overall hydraulic setup. The assumption can be made that the electronics and control circuit are even faster and therefore have only a negligible impact on the overall hydraulic model's response, which led to omitting the modeling of

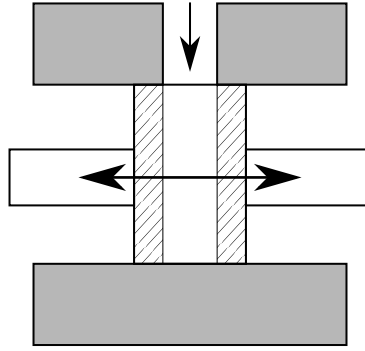


Figure 2.3: Schematic cross-section of overlapped valve

these components.

It is known that an actuator, in this case a solenoid, creates a magnetic field which in return generates a force displacing the spool, its position being proportional to the input signal. Simultaneously, a centering spring is present which ensures that the spool will return to its equilibrium position in case of a power loss. Additionally, any friction forces present add damping to the system. Therefore the spool's dynamics may be approximated, similar to the mass spring damper system, as a 1-DOF (degree of freedom) second-order system

$$\ddot{\nu} + 2\zeta\omega_0\dot{\nu} + \omega_0^2\nu = \omega_0^2u, \quad (2.8)$$

with  $\nu$  being the spool position,  $\zeta$  and  $\omega_0$  the damping and natural frequency and  $u$  the control input.

The saturation limits the spool's movement in either direction from its equilibrium point due to the mechanical construction where the spool reaches an end stop. This is a phenomenon affecting a vast variety of actuators. A dead-zone refers to a behavior in which a varying input signal lying within the dead-zone does not affect the system's output. The dead-zone for hydraulic valves is associated with a construction type where the valve exhibits an overlap, cf. Fig. 2.3. Under ideal conditions this results in no flow through the valve while the spool is moving within the range of the overlap, thereby introducing a dead-zone. In the case of servo valves, as used here, the overlap and subsequent dead-zone is usually rather small, which, when paired with a fast actuation of the spool, makes them suitable for closed loop control.

The dead-zone and saturation in their most generalized form are seen as piecewise linear with the characteristic shown in Fig. 2.4, where sections 1 and 5 represent the actuator's saturation; sections 2 and 4 the proportional characteristics and section 3 depicting the dead-zone. The dead-zone saturation model may simply be written as

$$v = f_{DS}(\nu), \quad (2.9)$$

with  $\nu$  being the spool position,  $f_{DS}(\nu)$  the non-linear characteristic of dead-zone and

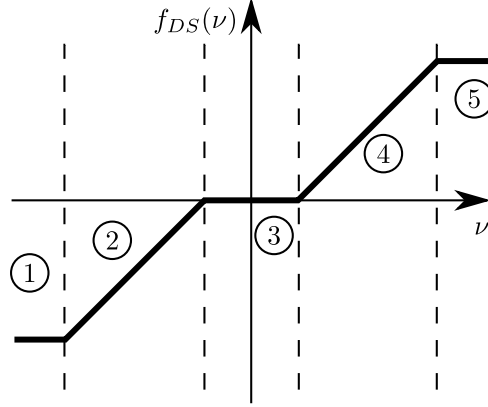


Figure 2.4: Generalized dead-zone, saturation characteristic of a hydraulic valve

saturation and  $v$  the valve's orifice opening, determining the volumetric hydraulic flow.

## Hydraulics

The hydraulics' subsystem consists of the hydraulic flow and pressure; thus, it may be modeled by using standard hydraulic equations, cf. [81, 82]. The flow is expressed by using orifice equations that are dependent on the relative pressure drop over the valve, its orifice opening and shape. The former is defined by the difference in pressure in the lines connected to the valve depending on its current configuration, the latter being defined by the valve's mechanical construction. This determines the maximum flow possible, which is expressed by the valve's flow and pressure rating. The orifice opening is related to the spool's position in combination with the dead-zone. Since the differential cylinder used has two chambers, two flow equations for each valve port, correspondent with the hydraulic line, are needed which have the general form of

$$Q = vK\sqrt{\Delta P}, \quad (2.10)$$

with  $Q$  being the volumetric flow of the hydraulic fluid,  $K$  the valve flow coefficient taking into account the orifice's shape in fully open configuration,  $\Delta P$  the pressure difference over the valve and  $v$  the orifice opening.

The pressure gradient in each hydraulic line is expressed by using continuity equations that take into account the bulk modulus of the hydraulic fluid, describing its compressibility, respectively stiffness and the hydraulic fluid's volume present in the respective line. Besides the hydraulic flow, the cylinder piston's movement also affects the change in pressure, increasing or decreasing it according to its velocity and direction of movement. A final influential factor is the leakage coefficient. The pressure difference between cylinder chambers may be significant. Seals are installed to avoid oil creep between chambers; however, due to the piston's movement in combination with the high pressure difference,

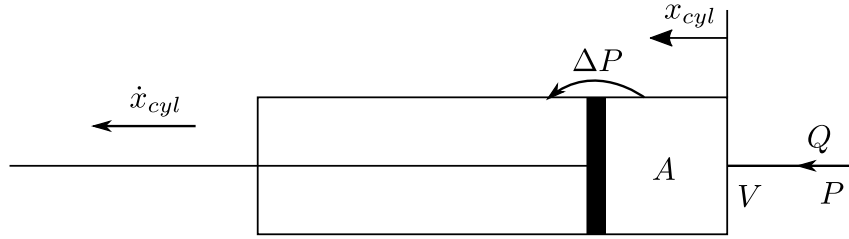


Figure 2.5: Hydraulic differential cylinder schematic

leakage cannot be completely avoided. This issue increases over time due to wear on the seal. The general continuity equation according to Fig. 2.5 is described by

$$\dot{P} = \frac{E}{V} (Q - A\dot{x}_{cyl} - C_L\Delta P). \quad (2.11)$$

$E$  describes the bulk modulus,  $V$  the volume in the hydraulic line and cylinder chamber,  $Q$  the volumetric flow,  $A$  the cross-section of the cylinder's chamber,  $C_L$  the leakage between the two chambers and  $\dot{x}_{cyl}$  the piston's velocity.

## Cylinder

The dynamic piston motion may be derived by applying Newton's Second Law as in section 2.1. The cylinder's driving force is defined by the difference between the chamber pressure's times the respective cross-sections of chambers A and B. Since the cylinder is differential, meaning unequal cross-sections, the maximum driving force for either direction differs. Friction generated due to the seals' installation reduces the driving force. While this amount is not substantial compared to the high forces generated, it needs to be included for proper modeling since it acts as a non-linear damper. Finally, the piston's movement is also affected by applied external forces. Since the piston is only able to move along one axis, its dynamics may be expressed as a second-order system with 1-DOF

$$m\ddot{x} = P_A A_A - P_B A_B - f_r(\dot{x}_{cyl}) - F_L, \quad (2.12)$$

where  $m$  is the lumped moving mass, including the piston itself, plus any other attached masses,  $f_r(\dot{x}_{cyl})$  the friction between cylinder housing and piston and  $F_L$  the external load force.  $P_{A,B}$  describes the respective chamber pressures and  $A_{A,B}$  the respective cross-sections.

The modeling of a friction characteristic for a component has to be evaluated on a case-by-case basis. The most simplistic modeling approach is related to a purely Coulomb-based model using a simple signum function containing an amplification factor. In cases where it is known that the velocity impacts the created friction, a combination of viscous and Coulomb friction may be used which rapidly yields better results than a purely

Coulomb-based approach. However, based on obtained experimental data, an adapted Stribeck-based friction model was used [83].

$$f_r(\dot{x}_{cyl}) = \tanh(\gamma\dot{x}_{cyl}) \left( F_c + (F_s - F_c) \exp\left(-\left|\frac{\dot{x}_{cyl}}{\chi}\right|^\delta\right) \right) + \sigma\dot{x}_{cyl}, \quad (2.13)$$

with  $F_c$  being the Coulomb friction coefficient,  $F_s$  the stiction coefficient,  $\sigma$  representing the viscous friction component,  $\delta$  and  $\chi$  being Stribeck shape parameters.  $\gamma$  scales the smoothness at zero crossing until the hyperbolic tangent function reaches its saturation value of  $\pm 1$  dependent on the sign of the velocity.

As can be seen, the derived complete hydraulic model contains three distinct nonlinearities as given by the dead-zone saturation combination, flow equation and friction affecting the cylinder's dynamics. By no means has every possible dynamic of the hydraulic setup been modeled. Yet the model created describes the test setup's main components and their interaction with each other.

## Model Reduction

The combination of the equations above describe the full-order model of the hydraulic test setup, which consists of several non-linear and differential equations that are linked together. In order to simplify the overall model, a model reduction was performed. Equation (2.10) introduces the valve's flow equation. Since there are two cylinder chambers connected to the valve, two flow equations and thus two continuity equations, cf. (2.11), have to be formulated. These sets may be combined into one by expressing the cylinder's driving force not as a difference between pressures but as a combined load pressure defined as  $P_L = P_A - P_B$ . The cross-section on which this newly defined load pressure acts, thereby constituting the cylinder's driving force, is defined as the average of the cross-sections of the two cylinder chambers as in  $\bar{A} = 0.5(A_A + A_B)$ . This results in one flow and one continuity equation, slightly simplifying the cylinder dynamics in (2.12).

This model reduction quite naturally impacts the model's accuracy compared to the full-order model and physical setup. Assuming a constant difference between chamber pressures  $P_A$  and  $P_B$  the piston's velocity in the full-order model will differ between an extending and retracting motion due to the different cross-sections of the respective chambers. In case of the reduced order model, the load pressure  $P_L$ , representing the difference between chamber pressures, remaining unchanged for both extending and retracting motion as in the full-order model, is multiplied with the average cross-section, resulting in equal velocity for either direction of movement. The reduced order model is further used as the basis for linearization and creating a PWA-based model.

## 2.3 Parameter Identification

A properly developed model is the foundation for a detailed system description. An equally meticulous process has to be used to determine the respective equations' parameters. The more the chosen values conform with the physical system, the more accurate the model is able to represent the system's response. This is a crucial factor when a control structure is to be integrated and simulations are used to verify the system's performance before deploying it on the actual setup, especially as the system has to fulfill high performance requirements.

It is especially a non-linear characteristic that is usually only roughly described in data sheets through having a general shape given alongside certain individual characteristics. While one could try to create a function fitting the given shape and characteristics, the match with the actual component's characteristics is probably mediocre at best and as such does not suit our purpose. Therefore several experiments were conducted to identify the unknown factors.

The performed experiments may be divided into two categories where in the first one, a component and their associated characteristic could be analyzed separately since the signals necessary for analysis could be monitored directly. The second is related to characteristics where the values necessary for analysis could not be obtained directly through measurements but had to be calculated through other monitored values, e.g. friction, dead-zone. These cases add another level of uncertainty to the identification process since the calculated values might depend on other identified parameters through the chain of equations used.

During post-processing of the obtained data, a combination of several different methods was used. For several measurements, it was necessary to average the data in order to obtain a static value from a noise-afflicted signal or obtain the mean value from several measurements performed with identical inputs. As regarded measurements exhibiting an initial transient behavior, only one set of samples associated with steady state behavior was used and averaged, cf. Fig. 2.6, according to

$$x_{avg} = \frac{1}{o_{sam} - n_{sam}} \sum_{i=n_{sam}}^{o_{sam}} x_i^{DATA} \quad (2.14)$$

where  $n_{sam}$  represents the first and  $o_{sam}$  the last sample included in the averaging process with  $x_i^{DATA}$  being the data points and  $x_{avg}$  the calculated average value.

In other instances where the function to which the measured data is supposed to correspond was known, a linear least-squares estimation was used [84]. Examples of this include fitting of the measured cylinder's position with a linear function from which the piston's velocity can be derived at constant valve openings, or the frequency response analysis of

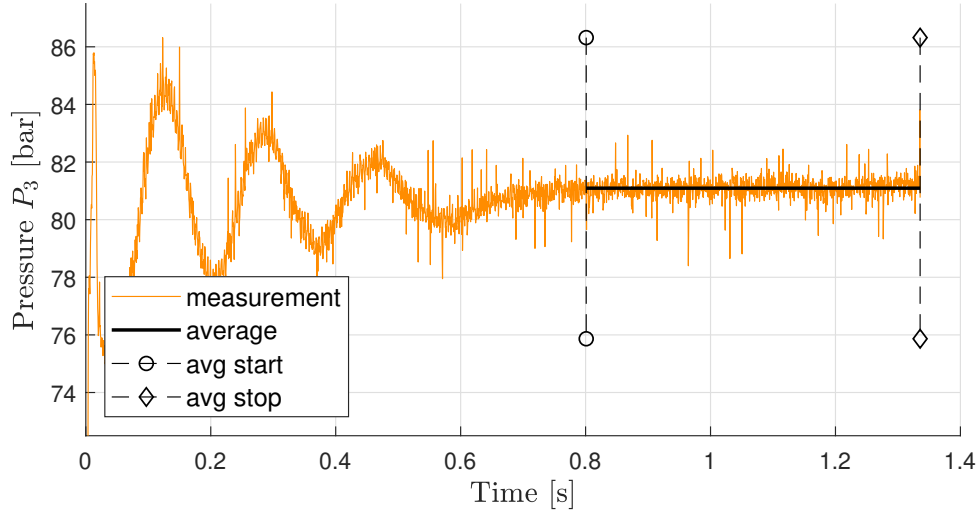


Figure 2.6: Averaging of signals experiencing initial transient behavior between two chosen start/end points

the servo valve where a sinusoidal function was to be fitted to the measured spool position. With respect to the generalized form of the linear least-squares approach, vectors of independent variables  $\mathbf{w}_i = [w_1, w_2, \dots, w_m]^T$  and model parameters  $\boldsymbol{\beta} = [\beta_1, \beta_2, \dots, \beta_m]$  as well as a prediction model defined by  $y_i \approx \boldsymbol{\beta} \mathbf{w}_i$  are needed. The optimum parameters in the least-squares sense are then defined as

$$\hat{\boldsymbol{\beta}} = \arg \min_{\boldsymbol{\beta}} \sum_{i=1}^n (\boldsymbol{\beta} \mathbf{w}_i - y_i)^2. \quad (2.15)$$

The optimum values are obtained if the gradient of the above equation is zero. By expressing the model's input variables and its output in matrix form  $\mathbf{W}$ ,  $\mathbf{Y}$ , the derivative may be taken. Rearranging the derived equation results in the optimized model parameters given by

$$\hat{\boldsymbol{\beta}} = (\mathbf{W}^T \mathbf{W})^{-1} \mathbf{W}^T \mathbf{Y}. \quad (2.16)$$

When the measured signals directly correlated to a characteristic that was greatly distorted due to noise, e.g. Fig. 2.7, the signal was analyzed by using the Fast Fourier Transform (FFT) to identify frequencies of interest. Since the measured data is already discretized due to the sampling time of the real-time target, a Butterworth low-pass filter design was used to generate filter coefficients based on the cutoff frequency determined from the investigation of the signal's frequency spectrum. The digital filter that was used has a general rational transfer function defined as

$$H(z) = \frac{Y(z)}{X(z)} = \frac{\alpha_1 + \alpha_2 z^{-1} + \alpha_3 z^{-2} + \dots + \alpha_{n+1} z^{-n}}{1 + \epsilon_1 z^{-1} + \epsilon_2 z^{-2} + \dots + \epsilon_o z^{-o}}, \quad (2.17)$$

with  $X(z)$  being the measured signal,  $Y(z)$  the filtered signal,  $o$  the feedback and  $n$  the



feedforward filter order,  $\alpha = [\alpha_1, \alpha_2, \dots, \alpha_{n+1}]$  the feedforward and  $\epsilon = [\epsilon_1, \epsilon_2, \dots, \epsilon_o]$  the feedback filter coefficients. [85].

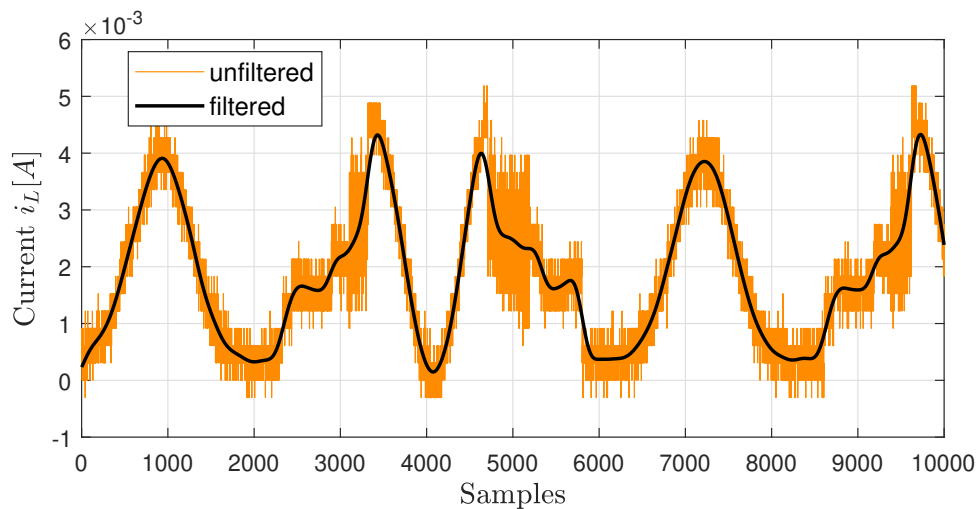


Figure 2.7: Highly distorted signal due to low signal to noise ratio and filtered signal

In order to identify the valve's dynamic model, a frequency response analysis was performed using sinusoidal inputs with varying frequencies. With the measured response being analyzed using the methods described above, the phaseshift was calculated between input signal and the measurement's fitted sinusoidal. The magnitude is described by the difference in amplitude between input and fitted signal and converted into dB with  $y_{db} = 20 \log_{10}(y_{mag})$ . The valve's model parameters were then fitted to the phaseshift and magnitude response obtained, by manually adjusting the parameters.

## 2.4 Linearisation of Dynamic Systems

In order to linearize a defined and identified non-linear function  $f_n(x)$ , verification must be made that the resulting function is differentiable, followed by choosing a point  $x^*$  around which the function is intended to be linearized. The linearization may then be expressed as

$$y = f_n(x^*) + \frac{\partial f_n(x^*)}{\partial x}(x - x^*). \quad (2.18)$$

By rearranging and substituting variables, the above equation may be expressed as

$$y = kx + d, \quad (2.19)$$

where  $k$  represents the linear function's slope and  $d$  the offset. For a non-linearity dependent on more than one input variable e.g.  $f_N(x, y)$ , a point  $p(x^*, y^*)$  at which the linearization is to be performed has to be chosen, which results in the following equation

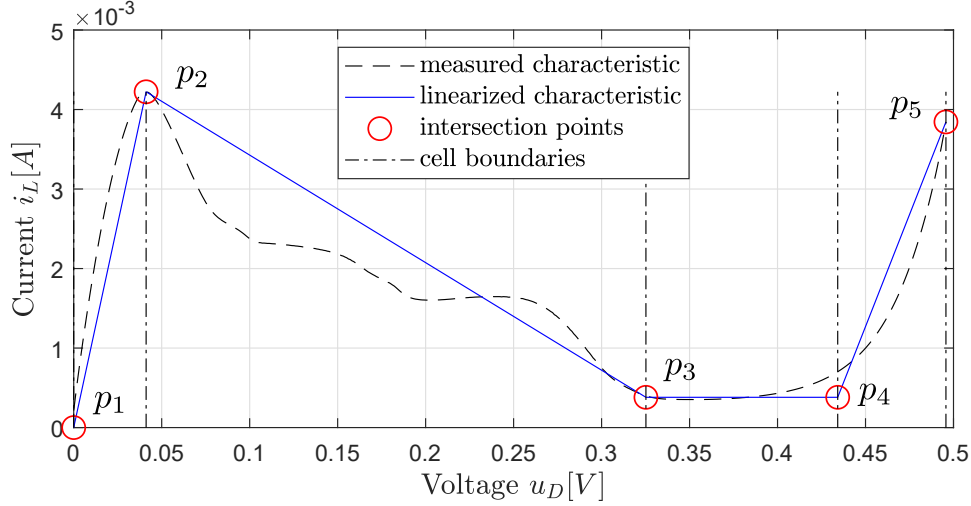


Figure 2.8: Diode characteristic with its linearization. The vertical dash-dotted lines represent the cell boundaries with the circles depicting the points based on which the linear functions were calculated

for linearization:

$$f_N(x, y) \approx f_N(x^*, y^*) + \left. \frac{\partial f_N(x, y)}{\partial x} \right|_{x^*, y^*} (x - x^*) + \left. \frac{\partial f_N(x, y)}{\partial y} \right|_{x^*, y^*} (y - y^*). \quad (2.20)$$

By rearranging and substituting values in the above fashion, the linearization may be expressed as

$$f_N(x, y) \approx k_1 x + k_2 y + d. \quad (2.21)$$

This approach results in a linear function tangential to the non-linear one; they converge at the chosen linearization point.

When acquired data cannot be properly fitted with a function, or the congruence with the function is weak,  $o$  points may be selected and  $n$  linear functions defined connecting these points with  $n = o - 1$ , cf. Fig. 2.8. Each point contains the coordinates describing its location, in the instance of a two-dimensional characteristic defined as  $p_i(x_i^*, y_i^*)$ . The linear function's parameters may then be calculated as

$$\begin{aligned} k_i &= \frac{y_{i+1}^* - y_i^*}{x_{i+1}^* - x_i^*} \quad (i = 1, \dots, n) \\ d_i &= y_i^* - k_i x_i^* \end{aligned} \quad (2.22)$$

Let us consider the mass spring damper example from section 2.2 again. The state vector was defined as  $\mathbf{x} = [x_1, x_2]^T$  with the states  $x_1 = x_{msd}$  being the position and  $x_2 = \dot{x}_{msd}$  being the velocity. The non-linear damper was of the form

$$b_{msd}(\dot{x}_{msd}) = a_1 \dot{x}_{msd}^3 + a_2 \dot{x}_{msd}. \quad (2.23)$$

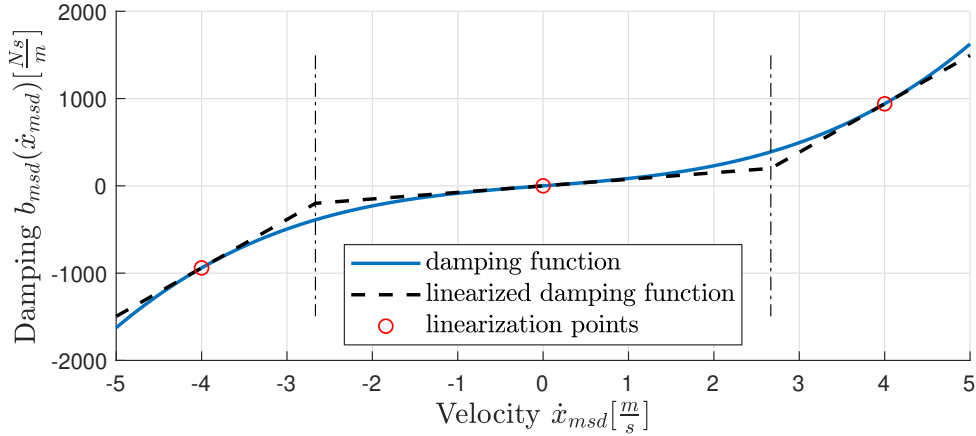


Figure 2.9: Non-linear damping function and its linearization. The circles indicate the points based on which the linear function was calculated with the dash-dotted lines representing the cell boundaries.

Three points are chosen around which the function should be linearized with two of them equidistant from, and one at, zero. In Fig. 2.9 the non-linear damping characteristic and the linearization points, along with the corresponding linearizations, are shown. This results in the characteristic being split into three different cells, where each cell is linked to one of the three linear functions of the linearized damping characteristic. The transition between cells is indicated by the vertical dash-dotted lines. The linearized model is then expressed as

$$\ddot{x}_{msd} = \frac{1}{M_{msd}}(F_{msd} - k_q \dot{x}_{msd} - d_q - s_{msd} x_{msd}) \quad (2.24)$$

where  $k_q$  and  $d_q$  represent the gradient and offset of the linear function for one cell with the index  $q = \{1, 2, 3\}$  referring to the cell.

With the linearizations performed, the mass spring damper model can now be expressed in a PWA manner

$$\begin{aligned} \dot{\mathbf{x}} &= \mathbf{A}_q \mathbf{x} + \mathbf{b} F_{msd} + \mathbf{f}_q, \\ y &= \mathbf{c} \mathbf{x}, \end{aligned} \quad (2.25)$$

with

$$\mathbf{A}_q = \begin{bmatrix} 0 & 1 \\ -\frac{s_{msd}}{M_{msd}} & -\frac{k_q}{M_{msd}} \end{bmatrix}, \quad \mathbf{b} = \begin{bmatrix} 0 \\ \frac{1}{M_{msd}} \end{bmatrix}, \quad \mathbf{f}_q = \begin{bmatrix} 0 \\ -\frac{d_q}{M_{msd}} \end{bmatrix}, \quad \mathbf{c} = \begin{bmatrix} 1 & 0 \end{bmatrix}. \quad (2.26)$$

To incorporate the offset term  $d_q$  of the linearization, which is neither linked to any state nor to the system's input, the standard state-space representation is extended with the affine vector  $\mathbf{f}_q$ . The characteristic being split into three cells also results in the system matrix  $\mathbf{A}_q$ , including the linear function's gradient, being different for each cell, as is the

affine vector  $\mathbf{f}_q$ . Depending on the mass' velocity  $x_2 = \dot{x}_{msd}$  it may be determined which cell is currently active.

Referring back to the general description of hybrid systems, cf. section 1.2.1 the mass spring damper model as described above has the property of autonomously switching its dynamics based on the state  $x_2$ . The continuous state-space  $\mathcal{X}$  is divided into three polytopic regions with adjoining borders; therefore, the set of discrete states includes three entries for each affine region  $\mathcal{Q} = \{q_1, q_2, q_3\}$ , with each region having its respective vector field assigned. The invariants  $inv$  and the guard condition  $\mathcal{G}$  are the same and are described by the border between the affine regions, in this case solely dependent on the mass' velocity. Transitions between regions can only occur in sequential order and are described by  $\mathcal{E}$  with no resets being present and therefore no existence of a reset map  $\mathcal{R}$ .

# Chapter 3

## Hybrid Control System Design

This chapter focuses on the control approach and begins with the control structure's introduction. Subsequently, the approach to signal noise filtering is described, and dead-zone compensation is detailed. The selection of a proper switching event for the hybrid position/force control approach is explained, and the generation of controller gains is discussed.

### 3.1 Integral, Feed-Forward, State-Feedback Control

In section 1.2.2.2 an overview of different kinds of controllers was given, with the literature pointing toward MPC as a promising control approach for PWA systems. This control approach is rather complex and has a somewhat high level of demand in computational power due to its optimization routine. While this is of no concern during simulations, if deployed on a system, the embedded PLC (programmable logic controller) has to perform all necessary calculations within one sampling period, which might not be feasible on low-end hardware.

In comparison, the integral, feed-forward, state-feedback control structure is rather easy to comprehend. While it has a low computational demand, it yields vastly improved performance as compared to PID control, which is still the standard in many industrial applications. While a PID controller only uses the error between reference and a to be controlled system state to generate a control signal, the control method used here allows for additional reference signal shaping through the feed-forward term. Further, the inclusion of available system states into the control signal through state-feedback allows for more freedom with respect to system response adjustment.

In this control structure, the controlled state of the system is compared to a reference that causes an error  $\dot{e}$  which is then integrated, resulting in  $\dot{e} = 0$  for  $t \rightarrow \infty$  which is necessary to eliminate steady-state errors. To accommodate the additional integrated

error  $\dot{e}$ , the models' state vector has to be extended to  $\mathbf{x}_e = [\mathbf{x}^T, e]^T$ . In the feed-forward pathway, the reference signal is prefiltered with a gain factor, while the state-feedback path first multiplies the measured states with the respectively chosen gains and then summarizes them. This introduces additional options for control signal shaping, e.g. on a hydraulic testbench, cf. Paper D where the cylinders' pressure is fed back while controlling the pistons' force for enhanced damping. The integrated error along with the feed-forward and state-feedback signal form the control signal  $u_c$ , cf. Fig. 3.1 which is defined as

$$u_c = FF r - \mathbf{k} \mathbf{x}_e, \quad (3.1)$$

with  $\mathbf{k} = [K_1, K_2, \dots, K_n, K_i]$  being the gain vector containing the state-feedback gains  $K_1, \dots, K_n$  and the integrator gain  $K_i$ , FF the feed-forward term and  $r$  the reference signal.

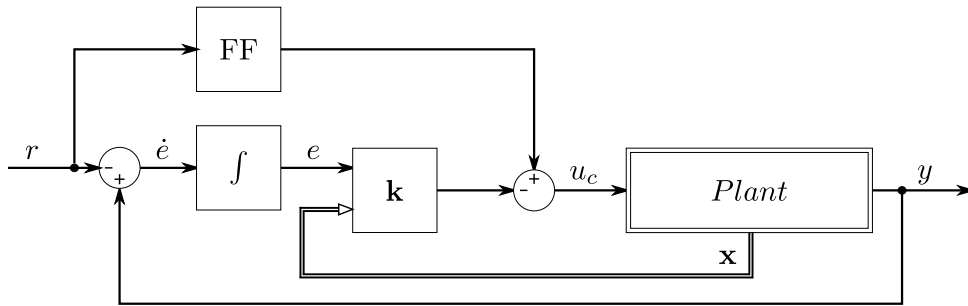


Figure 3.1: Integral error, feed-forward, state-feedback control structure

It should be noted that while the integrator takes into account the error, being a relative value between reference and controlled state, the feed-forward and state-feedback are associated with absolute values for the reference and states.

This may have a major impact on the system's response as identified in Paper E where a hydraulic cylinder was driven in a position-force-position control sequence. While the previous control approach from Paper D omitted the feed-forward term for the position-force control sequence, its inclusion was vital for the switch from force to position control mode in Paper E. The high pressure resulting from force control, cylinder displacement from its zero position, reset of the integrated error to zero due to the mode switch, cf. section 3.4 and change of controller gains influenced the control signal via the state-feedback loop at the time of switching between control modes, resulting in unstable system behavior (limit cycle switching between modes) that was counteracted by the inclusion of said feed-forward term into the control structure.

## 3.2 Control Signal Filtering

While noise is not present in a simulation environment unless explicitly modeled, every physically measured signal is exposed to noise in one way or another. While controlling a system without a proper filtering solution might be possible under certain circumstances, the control signal will be contaminated with noise as well, forcing the system's actuator or actuators to adjust their state in a high frequency manner. While the system's controlled state might still follow the trajectory, the high frequent actuation command merely causes unnecessary wear, which is undesirable.

A common approach is to filter all measured signals before they are used in a control structure, allowing filters to be fitted according to the noise present in the respective signal. However, this may result in issues since a filtering process also adds a phase delay to the signal. This is especially the case when the measured signals are filtered individually, as the phase delays might differ between signals, making it even harder to properly control a system.

Therefore, in this work the control signal  $u_c$  has been calculated based on the unfiltered measurements and then filtered using a digital filter, as introduced in section 2.3. Since the system is to be operated in a low-frequency range, a low-pass filter is used, removing the noise's higher frequency components, cf. Papers D and E. To avoid negatively impacting the system's performance, the actuators' frequency response function (FRF) may be analyzed and the respective cutoff frequency  $\omega_c$  determined, with the cutoff frequency of the filter then being chosen accordingly so as  $\omega_f > \omega_c$  to avoid slowing down the overall system's performance.

## 3.3 Static Compensator

As identified in Paper C, due to its mechanical construction, the servo valve of the hydraulic test setup has an inherent dead-zone saturation combination effect. While this saturation effect limits the maximum actuation possible, the dead-zone prevents changes in the actuators' output for actuations located within the dead-zone's range. This significantly influences the closed loop performance and might even lead to limit-cycles or unstable systemic behavior.

In order to circumvent these issues, a compensator may be designed. Previous work, cf. [86, 87, 88] proposed a dynamic compensator based on fuzzy logic; however, the dead-zone in this work is mechanically defined and may be seen as LTI for which a static compensator is sufficient, cf. Paper D.

A dead-zone saturation combination has an inherent non-linear characteristic which

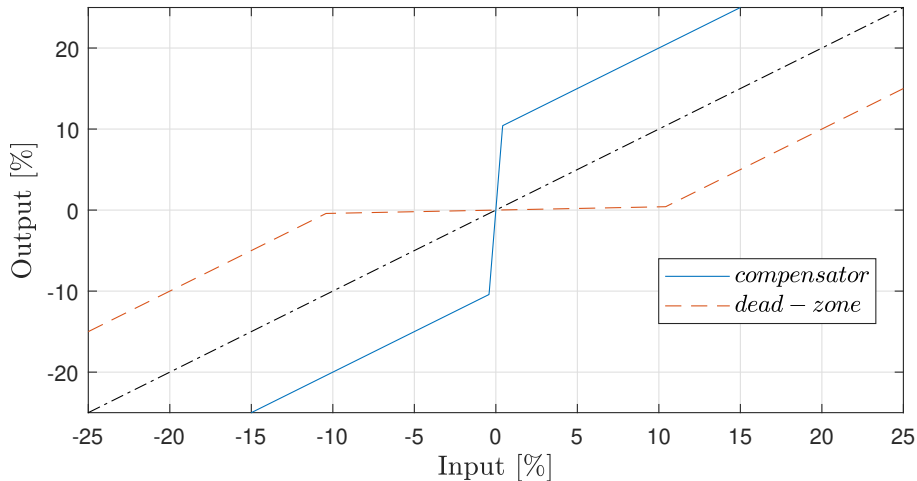


Figure 3.2: Linearized dead-zone and compensator

has been linearized during the process of creating a PWA model. While the saturation effect cannot be compensated for due to physical constraints, the dead-zone, being formed around the actuators' idle position, can. The compensator is designed in an inverting feed-forward manner by mirroring the linearized dead-zone characteristic over a unity gradient, resulting in a compensator characteristic with three cells, cf. Fig. 3.2. This process results in a perfect compensation of the dead-zone characteristic according to the PWA model. The compensator within the control structure is placed directly in front of the model/plant.

A perfect dead-zone would correspond to an absolute zero actuation, introducing a discontinuity at the compensator's zero crossing. In such cases a compensator may be defined as

$$y_{out} = \tanh(\gamma x_{inp}) \quad (3.2)$$

around zero crossing to avoid discontinuities, with  $\gamma$  defining the steepness of the slope when linearizing the function. In the case of the hydraulic valve, due to tolerances in manufacturing, there is still a creeping flow present while the spool is within the dead-zone, resulting in a linearization of the dead-zone with  $k > 0$  at zero crossing. This is advantageous in light of the compensator since the discontinuity is replaced with a linear function exhibiting a steep slope at zero crossing.

### 3.4 Switching Event

In Paper D the hybrid position/force control approach for the hydraulic test setup is introduced. The benefit of this approach is that the control gains for each control mode may be tuned independently from one another, in this case without changing the overall control structure. It is worth mentioning however, that each time the mode is switched,



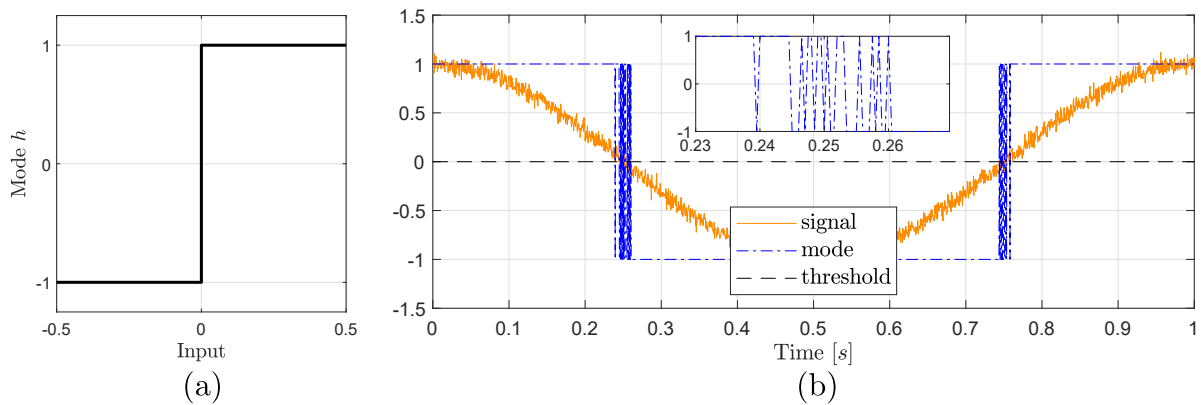


Figure 3.3: Relay function. (a) shows the noise-afflicted input signal to the relay and mode switch over time, with the relay function being illustrated in (b)

the integrated error is also reset to zero. The result is a superior performance compared to traditionally cascaded control loops. In order for the overall system to switch between control modes autonomously, a trigger or switching event has to be defined.

An example where a hybrid position/force control approach might be used that is related to the test setup is an automated excavator that progresses along a defined trajectory in position control mode. Since the ground conditions are unknown and possibly include rather large rocks, a purely position control approach could lead to equipment destruction. In such cases detection of exceedingly high forces that cause a switch to force control would counteract this possible destruction.

A very simple switching event is a relay/signum function defined as

$$h(t) = \text{sign}(x_{sig}(t)), \quad (3.3)$$

which triggers a switch in modes if the measured signal passes a threshold. While this type of switching event may yield the desired results in a simulation environment, it is rarely used in real-life applications related to the topic at hand. This is mostly due to measured signals being afflicted with some form of noise which, by using such a function, could leave the system in a non-conclusive state and possibly lead to dead-locks. The relay function's mode-switching behavior is shown in Fig. 3.3 where it may be seen that fast switching between modes occurs around the zero crossing due to the noise on the signal, making it unsuitable for applications where deterministic behavior is required.

An alternative is an adapted version of the time-delayed relay function. The function may be expressed using an automaton as shown in Fig. 3.4. While this may counteract the noise-induced, non-conclusive switching of the relay function, based on the excavator example, it may still lead to destruction of equipment. This is because the excavator would still continue in position control mode during the specified time-delay, constantly

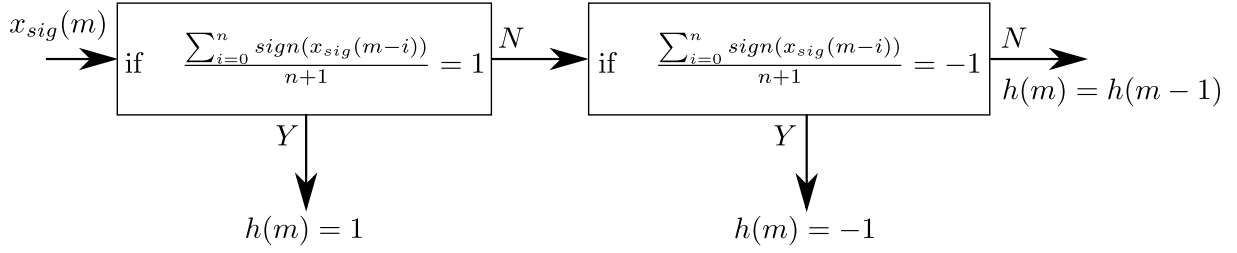


Figure 3.4: Finite-time-automaton for adapted time-delayed relay function.  $x_{sig}(m)$  is the input signal at time step  $m$  with  $n$  being the number of samples related to the time delay  $\Delta t$  and  $h(m)$  the output

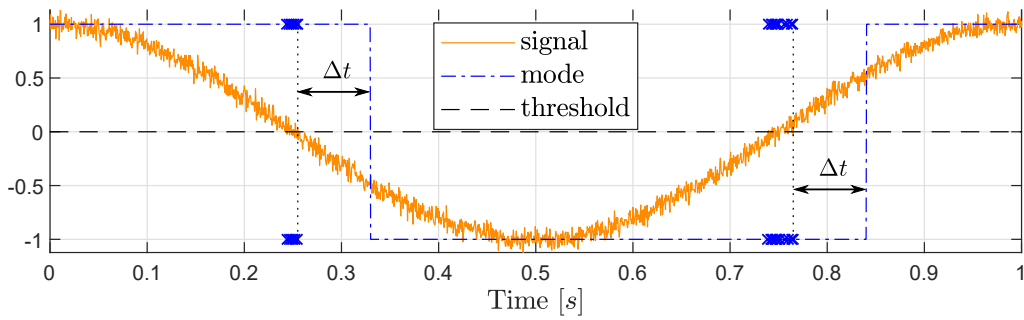


Figure 3.5: Simulation of adapted version of the time-delayed relay function. The input signal is shown alongside the mode propagation. The crosses indicate the relay's switching behavior. A mode switch is only triggered after the time delay  $\Delta t$  has passed based on the relay's last switch.

increasing cylinder pressure and force due to the generated control error. The function's response is shown in Fig. 3.5.

The hysteresis relay is a function ensuring that a switch in control modes is triggered as soon as a defined threshold is surpassed and results in a deterministic mode switching behavior despite the signal's noise [89].

$$h(t) = \begin{cases} -1, & \text{if } x_{sig}(t) \leq \beta_{hys} \\ +1, & \text{if } x_{sig}(t) \geq \alpha_{hys} \\ h(t_0), & \text{if } \beta_{hys} < x_{sig}(\tau) < \alpha_{hys} \quad \forall \tau \in [t_0, t] \end{cases} \quad (3.4)$$

Here, an upper and lower threshold  $\alpha_{hys}$  and  $\beta_{hys}$  is to be defined which causes a switch in modes with the delta between thresholds being chosen according to the peak-to-peak amplitude of the noise to avoid non-deterministic mode switches. The behavior of the hysteresis relay function is shown in Fig. 3.6.

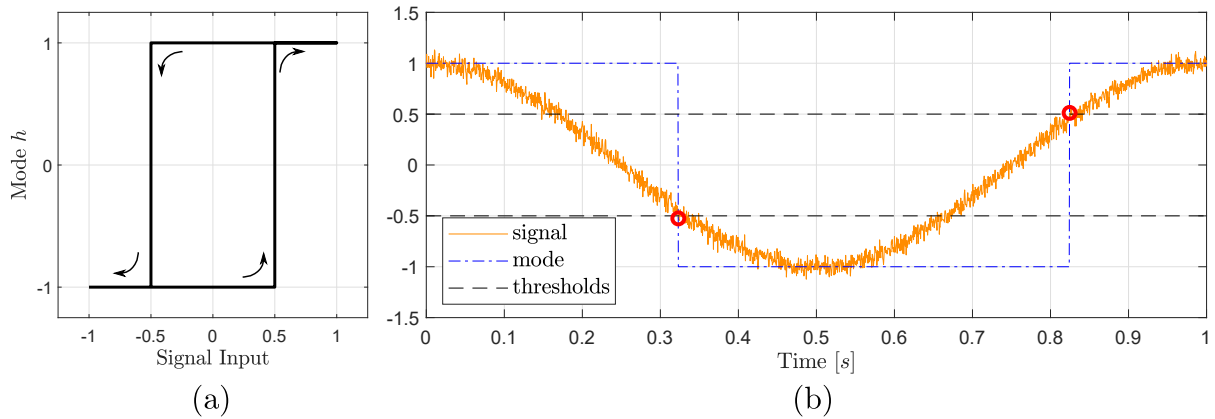


Figure 3.6: Hysteresis relay. The switching function is shown in (a) and the input signal with the upper and lower thresholds and the mode propagation in (b). The mode switches after surpassing the function’s lower and higher thresholds with no non-deterministic switching behavior present.

## 3.5 Control Parameter Adjustment

During the course of this thesis, three sets of control parameters were defined. The first set is related to the electric circuit, cf. Paper B with the other two being related to the hydraulic test setup, the first for the position-force control sequence, cf. Paper D and the second for position-force-position control, cf. Paper E.

Concerning the electric circuit, the control parameters were dialed in manually based on the necessary anticipated control value and overall systemic knowledge. Since this setup/model was mainly used to analyze the overall system behavior, no specific performance criteria were imposed. Therefore a trial and error-based method was deemed sufficient. For the more complex hydraulic setup, a non-linear, least squares-based optimization routine as well as the traditional pole placement method were used.

### 3.5.1 Optimal State Feedback

As input to a non-linear, least squares-based optimization procedure [84], as used in this work, cf. Paper D, a simulation model has to be provided alongside a cost function, which is to be minimized along with an initial guess regarding the values to be optimized. The simulation model  $\mathbf{Y} = \mathbf{F}_{sim}(\boldsymbol{\lambda})$  is dependent on an input vector  $\boldsymbol{\lambda} = [\lambda_1, \lambda_2, \dots, \lambda_o]$ , containing the parameters to be optimized, generating a matrix  $\mathbf{Y} = [\mathbf{y}_1, \mathbf{y}_2, \dots, \mathbf{y}_n]$  where each vector  $\mathbf{y}_{(.)}$  describes a state’s evolution over time, with  $o < n$ , which is used in a cost

function

$$\mathbf{c} = \mathbf{f}_{cost}(\mathbf{Y}) = \begin{bmatrix} f_1(\mathbf{Y}) \\ f_2(\mathbf{Y}) \\ \dots \\ f_i(\mathbf{Y}) \end{bmatrix}. \quad (3.5)$$

The sum of squares, according to the least-squares algorithm, is formed by

$$S = \sum_{j=1}^i f_j^2(\mathbf{Y}) \quad (3.6)$$

which is then potentially minimized by iteratively adjusting the input vector  $\boldsymbol{\lambda}$

$$\min_{\boldsymbol{\lambda}} S, \quad (3.7)$$

The minimum of  $S$  is dependent on  $o$  input parameters and is found if

$$\frac{\partial S}{\partial \lambda_j} = 0 \quad (j = 1, \dots, o) \quad (3.8)$$

The sum of squares  $S$  may be seen as a multidimensional surface with the number of dimensions being equal to the number of input parameters. This type of surface may contain multiple local minima, which are higher in value than the global minimum, which is the lowest value possible. To avoid ending up in a local minima, which will result in the optimization being stopped, the initially given values of  $\boldsymbol{\lambda}$  have to be chosen carefully. A proper initial guess may be obtained through preliminary simulations and in-depth systemic knowledge. In order to ensure that the optimization has not converged into a local minima, the routine may be run multiple times with widely varying initial guesses. If the parameters converge into the same values independent of the initial guesses provided, it is likely that the resulting parameters will be related to the global minimum.

The cost functions may be defined to meet the performance criteria imposed. These functions might be as simple as not only minimizing the error between the reference and controlled state, but also taking into account e.g. the maximum allowed overshoot or restriction of the control signal's range. The more functions a cost function contains, the more complex its evaluation becomes. This is especially true if multiple different performance indicators are combined; the resulting numerical values between indicators may be of different ranges, resulting in a prioritization of minimizing a certain indicator having the highest numerical value. To circumvent this issue, the values may be normalized and different weights applied in order to choose which indicator should have the highest impact on the cost function.

To verify the resulting optimized parameters, simulations may first be performed, after which performance indicators may be computed and compared to the requirements.

Additionally, the convergence of the normalized parameters and  $S$  may be evaluated in accordance with the iterations performed in order to verify either that the values in fact converged to a certain point at the end of the optimization or if additional iterations are necessary.

### 3.5.2 Pole Placement

In order to generate the control parameters in Paper E, the method of pole placement was used. This method is based on the pole-zero plot derived from a transfer function. The plot graphically illustrates a system's stability and response. This method may be directly applied to LTI systems. PWA systems may be seen as a compilation of multiple LTI systems where each system is associated with a region in state-space confined by its respective cell boundaries. This region has its dynamics defined by the corresponding matrices and vectors of the state-space model. Since the transformation to the frequency domain to derive the poles' and zeros' locations is only possible for systems described in the standard state-space representation, the state vector  $\mathbf{x}$  may be extended and the system matrix  $\mathbf{A}$  and affine vector  $\mathbf{f}$  combined into a newly defined extended system matrix  $\bar{\mathbf{A}}$  as shown in section 1.2.2.3. The resulting equations then follow the standard state-space format and are defined as

$$\begin{aligned}\dot{\bar{\mathbf{x}}}(t) &= \bar{\mathbf{A}}\bar{\mathbf{x}}(t) + \bar{\mathbf{b}}u(t), \\ y(t) &= \bar{\mathbf{c}}\bar{\mathbf{x}}(t),\end{aligned}\tag{3.9}$$

with the conversion to frequency domain done by taking the Laplace transformation of the state-space model

$$s\bar{\mathbf{x}}(s) = \bar{\mathbf{A}}\bar{\mathbf{x}}(s) + \bar{\mathbf{b}}u(s),\tag{3.10}$$

$$y(s) = \bar{\mathbf{c}}\bar{\mathbf{x}}(s).\tag{3.11}$$

A transfer function is defined by the ratio of output to input. For example, (3.10) may be solved for  $\bar{\mathbf{x}}(s)$  and then substituted into (3.11). By rearranging the resulting equation, the transfer function may be found as

$$H(s) = \frac{y(s)}{u(s)} = \bar{\mathbf{c}}(s\mathbf{I} - \bar{\mathbf{A}})^{-1}\bar{\mathbf{b}},\tag{3.12}$$

where  $\mathbf{I}$  is the identity matrix. The zeros are then defined by the terms in the numerator and the poles by the denominator of the resulting fraction.

The number of poles and zeros for a controlled system is the sum of poles and zeros related to the plant's dynamics plus the control structure's dynamics. The poles closest to the imaginary axis are dominant and have the highest impact on the system's response,

which in this case are associated with the controller gains and can therefore be placed accordingly to shape the system's response.

While in simulations the controller-related poles may be altered to one's liking, in a physical system there are limitations. The adjustment of the poles and thereby the controller gains directly affect the control signal. By placing poles further from the imaginary axis, the controller gains increase, resulting in an amplified control signal which the actuator might not be able to follow due to saturation effects. These factors have to be taken into consideration while placing poles for a physical setup, limiting the region in which they can be placed.

Further, due to the PWA-based model, the systemic dynamics change dependent on the cell combination. Therefore the right region has to be chosen for placing the controller's poles since gains in the used control structure remain the same throughout the regions. In this work a cell combination was chosen based on the region in state-space associated with steady-state behavior following a reference trajectory, therefore defining the state-space matrix and vectors.

# Chapter 4

## Stability Analysis

The goal of stability analysis is to determine if a system is stable, meaning that from a set of initial conditions, the system's states converge to an equilibrium point and remain there, assuming there are no disturbances. A general distinction may be made between local and global stability. Local stability describes a system's ability to return to an equilibrium point after experiencing a minor disruption, while global stability states that no matter the size of the disruption, the system will converge back to its equilibrium point. It may be seen that the proof of a system's global stability is something for which to strive. However, physical systems have imposed restrictions with regard to the values the respective system states can reach due to physical limitations. While a global stability analysis may still be conducted, for created models based on a physical system, a local stability analysis that is limited to the system's operational range is sufficient. A subset of local stability covering the reachable state-space focuses on the stability analysis covering the state-space region around an operational point. This was performed for the hybrid-controlled hydraulic system for position and force control, respectively, alongside an analysis for the switch between control modes, cf. Paper E.

### 4.1 Stability Analysis of Linear Systems

The stability analysis of LTI systems may be conducted by investigating its pole-zero configuration, whereas if all poles are located in the left half plane, the system is considered stable. Poles in said half plane being on the axis indicate an exponentially decaying response with its values representing the rate of decay and complex pole pairs resulting in an oscillatory decay with the rate of decay being defined by the real and the oscillatory frequency given by the imaginary value. If any of the poles are located within the right half plane, the system is considered unstable. The poles located closer to the origin are considered dominant poles having the highest impact on the system's response.

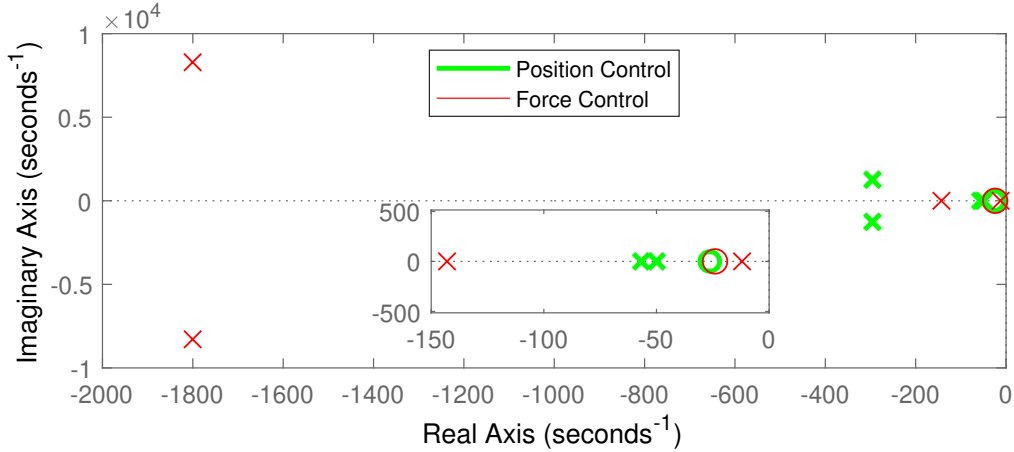


Figure 4.1: Pole-zero plot of controlled hydraulic model for both control modes

The poles and zeros of the controlled hydraulic setup for both control modes are shown in Fig. 4.1 as defined in the previous section of pole placement. The plot reveals one conjugate complex pole pair and one pole pair on the axis in the left half plane for each control mode, respectively, with the latter pair being the dominant one. This indicates a prevalent exponential decay with an overlaid oscillatory behavior.

While this proves the local stability for a region in state-space associated with the cell combination chosen, it gives no indication of the local stability covering the system's reachable state-space, nor the global stability.

In order to broaden the proof of stability covering the entire or reachable state-space, not only an individual investigation of the remaining combination of cells is necessary but the transitions between cells has to be taken into account as well. At this point the model under investigation is no longer linear, but rather hybrid and the other methods introduced in section 1.2.2.3, have to be applied.

## 4.2 Stability Analysis of Non-linear Systems

In the following the issue of verifying stability of a switched system containing two discrete modes is addressed, as it is the case for the autonomously switched hybrid position/force-controlled hydraulic test setup. As previously noted, while the respective mode's local stability around the switching point may be verified by analyzing the pole-zero plot the autonomous switching between these modes can still lead to an overall unstable behavior, cf. section 1.2.1.4. Regarding these hybrid systems, the investigation via the pole-zero configuration is not sufficient; thus, more elaborate methods have to be used. As introduced in section 1.2.2.3 for non-linear and PWA systems a Lyapunov-based approach may be pursued. The stability of these switched systems may be verified by finding a common



Lyapunov function. While conditions for finding such functions have previously been investigated by researchers [10, 12], it is a non-trivial and case-specific process. Therefore, pertaining to the analysis of the switched system at hand, the approach of multiple Lyapunov functions is used [8]. In this approach a switched system is considered to be asymptotically stable if the Lyapunov function's value at the end of one mode is higher than the function's value at the end of the same mode's next period.

For this a quadratic Lyapunov function  $L(h)$  which is dependent on the mode  $h$  may be defined, taking into account the system's potential and kinetic energy, with each of the energy-related terms being multiplied with a positive coefficient  $W_{(\cdot)}^{(\cdot)}(h) > 0$

$$L(h) = \sum_{i=1}^o W_i^{pot}(h)\psi_i^2(\cdot) + \sum_{j=1}^n W_j^{kin}(h)\phi_j^2(\cdot). \quad (4.1)$$

In the equation above  $\psi$  is a function related to potential energy, with  $\phi$  being related to kinetic energy and each of the functions may also be mode dependent.

A simulation of the Lyapunov function for a periodically alternating mode can then reveal a non-increase of the Lyapunov function value for two consecutive operational periods of the same mode, proving that the switched system is asymptotically stable.

Using the multiple Lyapunov functions' approach also restricts the class of admissible switching signals. While by finding a common Lyapunov function, the stability of a switched system may be proven for the occurrence of fast switching between modes, multiple Lyapunov functions are only admissible for systems with a rather slow switching behavior, as is the case in this work.



# Chapter 5

## Concluding Remarks

### 5.1 Conclusions

The focus of this work was to model and control piecewise affine (PWA) systems. This was exemplified in two test setups, one electrical and the other hydraulic, which were constructed and implemented during the course of this project. Full-order models were created, and several non-linearities were derived describing the respective systems' dynamics. Regarding the hydraulic setup in particular, a model reduction was performed in order to slightly lower the created model's complexity; however, in doing so, the implications of reducing this model were clear.

An extensive parameter identification was performed to evaluate the respective parameters and characteristics of each model by consulting data-sheets and performing experimental measurements. The experimentally obtained data was post-processed and analyzed; the respective parameters and characteristics were adjusted accordingly. The identified non-linearities were then linearized at several points, resulting in each non-linear characteristic being expressed by a set of linear functions. The resulting affine linear system dynamics were then combined and formulated in a PWA state-space representation for each system, respectively. Open loop experiments and simulations were performed and compared to one another in order to verify their conformity.

A control structure featuring integral error, feed-forward and state-feedback control was deployed for both systems, the feed-forward term being omitted if unnecessary. For the hydraulic system, including a dead-zone within the actuator, a compensator was designed, canceling out the dead-zone effect. A low-pass filter was then implemented to reduce noise components of the control signal. Controller gains were generated using in-depth system knowledge, an optimization routine and the standard pole-placement method, which was realized by linearizing the model around certain operational points. As for the closed loop hydraulic system, a switching event based on a hysteresis relay

was introduced to allow for autonomous switching between the position and force control mode.

Finally, a stability analysis was conducted proving local stability. Stability around operational points was confirmed via a pole-zero analysis. A multiple Lyapunov function-based approach was used to prove the hybrid controlled system's stability in the vicinity of the switching points.

## 5.2 Potential for Future Works

The hydraulic system in this work represents a single valve-cylinder combination. The PWA-based modeling approach can be used and scaled to model more complex systems, e.g. hydraulic cranes. The described methodology can also be transferred to systems in other domains e.g. robotic manipulators, complex electric circuits, etc. A PWA-based system's conformity in comparison to a full-order model is always less accurate compared to a physical system. This is especially true with regard to an increase in the number of linearized characteristics; thus, when considering their interactions with one another, it remains to be investigated up to which point this type of PWA-based modeling approach is sufficiently congruent with a physical system.

Since the PWA model consists of only linear equations, and the switch between cells can be determined by simple *if*-statements, it may be assumed that the computational time for PWA models is less than for a full-order model – or even a reduced-order model. Using the PWA-based modeling approach for highly complex systems could potentially decrease computational time. This is especially relevant if the models grow in complexity, e.g. scaling the valve-cylinder combination investigated in this work up to an industrial loader crane with multiple actuators and links.

# References

- [1] G. Franklin, J. D. Powell, and A. Emami-Naeini. *Feedback Control Of Dynamic Systems*. Prentice Hall Press Upper Saddle River, NJ, USA, 2015.
- [2] J. Lunze and F. F. Lamnabhi-Lagarrigue. *Handbook of hybrid systems control : theory, tools, applications*. Cambridge University Press, 2009.
- [3] H. Lin and P. Antsaklis. Hybrid dynamical systems: An introduction to control and verification. *Foundations and Trends in Systems and Control*, 1(1):1–172, 2014. doi:10.1561/26000000001.
- [4] S. Paoletti, A. Juloski, G. Ferrari-Trecate, and R. Vidal. Identification of hybrid systems a tutorial. *European Journal of Control*, 13(2-3):242–260, 2007. doi:10.3166/ejc.13.242-260.
- [5] A. Bemporad, G. Ferrari-Trecate, and M. Morari. Observability and controllability of piecewise affine and hybrid systems. *IEEE Transactions on Automatic Control*, 45(10):1864–1876, 2000. doi:10.1109/TAC.2000.880987.
- [6] G. Frehse, C. Le Guernic, A. Donzé, S. Cotton, R. Ray, O. Lebeltel, R. Ripado, A. Girard, T. Dang, and O. Maler. *SpaceEx: Scalable verification of hybrid systems*, volume 6806 LNCS. Springer, Berlin, Heidelberg, 2011. doi:10.1007/978-3-642-22110-1\_30.
- [7] D. Mignone, G. Ferrari-Trecate, and M. Morari. Stability and stabilization of piecewise affine and hybrid systems: An LMI approach. In *Proceedings of the IEEE Conference on Decision and Control*, volume 1, pages 504–509, 2000.
- [8] D. Liberzon and A. Morse. Basic Problems in Stability and Design of Switched Systems. *IEEE Control Systems*, 19(5):59–70, 1999. doi:10.1109/37.793443.
- [9] M. Branicky. Multiple Lyapunov functions and other analysis tools for switched and hybrid systems. *IEEE Transactions on Automatic Control*, 43(4):475–482, 1998. doi:10.1109/9.664150.

- [10] R. Decarlo, M. Branicky, S. Pettersson, and B. Lennartson. Perspectives and results on the stability and stabilizability of hybrid systems. *Proceedings of the IEEE*, 88(7):1069–1082, 2000. doi:10.1109/5.871309.
- [11] J. Daafouz, P. Riedinger, and C. Iung. Stability analysis and control synthesis for switched systems: A switched Lyapunov function approach. *IEEE Transactions on Automatic Control*, 47(11):1883–1887, 2002. doi:10.1109/TAC.2002.804474.
- [12] R. Shorten, F. Wirth, O. Mason, K. Wulff, and C. King. Stability criteria for switched and hybrid systems. *SIAM Review*, 49(4):545–592, dec 2007. doi:10.1137/05063516X.
- [13] J. Hespanha. Uniform stability of switched linear systems: Extensions of LaSalle’s invariance principle. *IEEE Transactions on Automatic Control*, 49(4):470–482, 2004. doi:10.1109/TAC.2004.825641.
- [14] J. Lygeros, K. Johansson, S. Simić, J. Zhang, and S. Sastry. Dynamical properties of hybrid automata. *IEEE Transactions on Automatic Control*, 48(1):2–17, 2003. doi:10.1109/TAC.2002.806650.
- [15] S. Pettersson and B. Lennartson. Stability and robustness for hybrid systems, 1996. doi:10.1109/cdc.1996.572653.
- [16] R. Alur, C. Courcoubetis, N. Halbwachs, T. Henzinger, P.-H. Ho, X. Nicollin, A. Olivero, J. Sifakis, and S. Yovine. The algorithmic analysis of hybrid systems. *Theoretical Computer Science*, 138(1):3–34, 1995. doi:10.1016/0304-3975(94)00202-T.
- [17] M. S. Branicky. Introduction to Hybrid Systems. In *Handbook of Networked and Embedded Control Systems*, pages 91–116. Birkhäuser Boston, Boston, MA, 2005. doi:10.1007/0-8176-4404-0\_5.
- [18] N. Lynch, R. Segala, F. Vaandrager, and H. Weinberg. *Hybrid I/O automata*, volume 1066. Elsevier BV, 1996. doi:10.1007/BFb0020971.
- [19] R. David and H. Alla. Petri nets for modeling of dynamic systems. A survey. *Automatica*, 30(2):175–202, 1994. doi:10.1016/0005-1098(94)90024-8.
- [20] C. Cassandras and S. Lafortune. *Introduction to discrete event systems*. Springer US, 2008. doi:10.1007/978-0-387-68612-7.
- [21] T. A. Henzinger. Theory of hybrid automata. In *Proceedings - Symposium on Logic in Computer Science*, pages 278–292, 1996.

## References

- [22] A. Bemporad and M. Morari. Control of systems integrating logic, dynamics, and constraints. *Automatica*, 35(3):407–427, 1999. doi:10.1016/S0005-1098(98)00178-2.
- [23] G. Ferrari-Trecate, E. Gallestey, P. Letizia, M. Spedicato, M. Morari, and M. Antoine. Modeling and Control of Co-Generation Power Plants: A Hybrid System Approach. *IEEE Transactions on Control Systems Technology*, 12(5):694–705, 2004. doi:10.1109/TCST.2004.826958.
- [24] G. Ferrari-Trecate, D. Mignone, and M. Morari. Moving horizon estimation for hybrid systems. *IEEE Transactions on Automatic Control*, 47(10):1663–1676, 2002. doi:10.1109/TAC.2002.802772.
- [25] S. Karaman, R. Sanfelice, and E. Frazzoli. Optimal control of mixed logical dynamical systems with Linear Temporal Logic specifications. In *Proceedings of the IEEE Conference on Decision and Control*, pages 2117–2122, 2008. doi:10.1109/CDC.2008.4739370.
- [26] A. Van Der Schaft and J. Schumacher. Complementarity modeling of hybrid systems. *IEEE Transactions on Automatic Control*, 43(4):483–490, 1998. doi:10.1109/9.664151.
- [27] W. Heemels, B. De Schutter, and A. Bemporad. Equivalence of hybrid dynamical models. *Automatica*, 37(7):1085–1091, 2001. doi:10.1016/S0005-1098(01)00059-0.
- [28] W. Heemels, J. Schumacher, and S. Weiland. Linear complementarity systems. *SIAM Journal on Applied Mathematics*, 60(4):1234–1269, 2000. doi:10.1137/S0036139997325199.
- [29] O. Stursberg, S. Kowalewski, J. Preußig, and H. Treseler. Block-diagram based modelling and analysis of hybrid processes under discrete control. *Journal Europeen des Systemes Automatises*, 32(9-10):1097–1118, 1998.
- [30] J. Lunze. Fault diagnosis of discretely controlled continuous systems by means of discrete-event models. *Discrete Event Dynamic Systems: Theory and Applications*, 18(2):181–210, 2008. doi:10.1007/s10626-007-0022-3.
- [31] H. Toubakh and M. Sayed-Mouchaweh. Hybrid dynamic classifier for drift-like fault diagnosis in a class of hybrid dynamic systems: Application to wind turbine converters. *Neurocomputing*, 171:1496–1516, 2016. doi:10.1016/j.neucom.2015.07.073.
- [32] A. Schild and J. Lunze. *Stabilization of limit cycles of discretely controlled continuous systems by controlling switching surfaces*, volume 4416 LNCS. Springer, Berlin, Heidelberg, 2007.

- [33] G. Lafferriere, G. Pappas, and S. Yovine. *A new class of decidable hybrid systems*, volume 1569. Springer, Berlin, Heidelberg, 1999.
- [34] G. Behrmann, A. Fehnker, T. Hune, K. Larsen, P. Pettersson, J. Romijn, and F. Vaandrager. *Minimum-cost reachability for priced timed automata*, volume 2034. Springer, Berlin, Heidelberg, 2001.
- [35] R. Alur, S. La Torre, and G. Pappas. *Optimal paths in weighted timed automata*, volume 2034. Springer, Berlin, Heidelberg, 2001.
- [36] A. David, K. Larsen, A. Legay, U. Nyman, and A. Wasowski. Timed I/O automata: A complete specification theory for real-time systems. In *HSCC'10 - Proceedings of the 13th ACM International Conference on Hybrid Systems: Computation and Control*, pages 91–100, 2010. doi:10.1145/1755952.1755967.
- [37] T. Henzinger, P. Kopke, A. Puri, and P. Varaiya. What's Decidable about Hybrid Automata? *Journal of Computer and System Sciences*, 57(1):94–124, 1998. doi:10.1006/jcss.1998.1581.
- [38] T. Henzinger, P.-H. Ho, and H. Wong-Toi. Algorithmic analysis of nonlinear hybrid systems. *IEEE Transactions on Automatic Control*, 43(4):540–554, 1998. doi:10.1109/9.664156.
- [39] J.-P. Aubin, J. Lygeros, M. Quincampoix, S. Sastry, and N. Seube. Impulse differential inclusions: A viability approach to hybrid systems. *IEEE Transactions on Automatic Control*, 47(1):2–20, 2002. doi:10.1109/9.981719.
- [40] R. Goebel and A. Teel. Solutions to hybrid inclusions via set and graphical convergence with stability theory applications. *Automatica*, 42(4):573–587, 2006. doi:10.1016/j.automatica.2005.12.019.
- [41] A. Teel, A. Subbaraman, and A. Sferlazza. Stability analysis for stochastic hybrid systems: A survey. *Automatica*, 50(10):2435–2456, 2014. doi:10.1016/j.automatica.2014.08.006.
- [42] A. D. Ames and S. Sastry. Characterization of zeno behavior in hybrid systems using homological methods. In *Proceedings of the American Control Conference*, volume 2, pages 1160–1165, 2005. doi:10.1109/acc.2005.1470118.
- [43] L. Fridman, J. A. Moreno, B. Bandyopadhyay, S. Kamal, and A. Chalanga. Continuous Nested Algorithms : The Fifth Generation of Sliding Mode Controllers. In X. Yu and M. Önder Efe, editors, *Recent Advances in Sliding Modes: From Control to*



## References

- Intelligent Mechatronics*, pages 5–35. Springer International Publishing, Cham, 2015. doi:10.1007/978-3-319-18290-2\_2.
- [44] P. Collins. A trajectory-space approach to hybrid systems. *Mathematical Theory of Networks and Systems Conference, Leuven, BG*, 2004.
- [45] E. D. Sontag. *Mathematical Control Theory*, volume 6 of *Texts in Applied Mathematics*. Springer New York, New York, NY, 1998. doi:10.1007/978-1-4612-0577-7.
- [46] M. Camlibel, W. Heemels, and J. Schumacher. Algebraic necessary and sufficient conditions for the controllability of conewise linear systems. *IEEE Transactions on Automatic Control*, 53(3):762–774, 2008. doi:10.1109/TAC.2008.916660.
- [47] V. Blondel and J. Tsitsiklis. Complexity of stability and controllability of elementary hybrid systems. *Automatica*, 35(3):479–489, 1999. doi:10.1016/S0005-1098(98)00175-7.
- [48] P. Collins and J. Van Schuppen. *Observability of piecewise-affine hybrid systems*, volume 2993. Springer, Berlin, Heidelberg, 2004.
- [49] F. Küsters and S. Trenn. Switch observability for switched linear systems. *Automatica*, 87:121–127, 2018. doi:10.1016/j.automatica.2017.09.024.
- [50] O. Mayr. The Origins of Feedback Control. *Scientific American*, 223(4):110–119, 1970.
- [51] Z.-P. Jiang and D. Hill. 6 - Adaptive nonlinear control: Passivation and small gain techniques. In G. Feng and R. B. T. A. C. S. Lozano, editors, *Adaptive control systems*, pages 119–158. Newnes, Oxford, 1999. doi:10.1016/B978-075063996-5/50007-5.
- [52] M. G. Singh and A. Titli. Closed loop hierarchical control for non-linear systems using quasilinearisation. *Automatica*, 11(5):541–546, sep 1975. doi:10.1016/0005-1098(75)90032-1.
- [53] P. Melin and O. Castillo. Intelligent control of non-linear dynamic plants using type-2 fuzzy logic and neural networks. In *Annual Conference of the North American Fuzzy Information Processing Society - NAFIPS*, volume 2002-Janua, pages 22–27, 2002. doi:10.1109/NAFIPS.2002.1018024.
- [54] E. Engel, I. Kovalev, and V. Kobezhikov. Intelligent control of non-linear dynamical system based on the adaptive neurocontroller. In *IOP Conference Series: Materials Science and Engineering*, volume 94. IOP Publishing Ltd, 2015. doi:10.1088/1757-899X/94/1/012009.

- [55] S. P. Sethi. What Is Optimal Control Theory? In S. P. Sethi, editor, *Optimal Control Theory*, chapter 1, pages 1–26. Springer International Publishing, Cham, 2019. doi:10.1007/978-3-319-98237-3\_1.
- [56] C. E. García, D. M. Prett, and M. Morari. Model predictive control: Theory and practice—A survey. *Automatica*, 25(3):335–348, may 1989. doi:10.1016/0005-1098(89)90002-2.
- [57] E. C. Özelkan, Á. Galambosi, E. Fernández-Gaucherand, and L. Duckstein. Linear quadratic dynamic programming for water reservoir management. *Applied Mathematical Modelling*, 21(9):591–598, sep 1997. doi:10.1016/S0307-904X(97)00078-4.
- [58] Z. Qu. *Robust Control of Nonlinear Uncertain Systems*. John Wiley & Sons, Inc., New York, NY, USA, 1st edition, 1998.
- [59] E. Gershon, U. Shaked, and I. Yaesh. H-Infinity Control and Estimation of State-Multiplicative Linear Systems. *H-infinity Control and Estimation of State-multiplicative Linear Systems*, by E. Gershon, U. Shaked, and I. Yaesh. Berlin: Springer, 2005., 318, sep 2005.
- [60] M. Lazar, W. Heemels, S. Weiland, and A. Bemporad. Stabilizing model predictive control of hybrid systems. *IEEE Transactions on Automatic Control*, 51(11):1813–1818, 2006. doi:10.1109/TAC.2006.883059.
- [61] K. Alexis, G. Nikolakopoulos, and A. Tzes. Model predictive quadrotor control: Attitude, altitude and position experimental studies. *IET Control Theory and Applications*, 6(12):1812–1827, 2012. doi:10.1049/iet-cta.2011.0348.
- [62] C. Lim, N. Rahim, W. Hew, and E. Levi. Model predictive control of a two-motor drive with five-leg-inverter supply. *IEEE Transactions on Industrial Electronics*, 60(1):54–65, 2013. doi:10.1109/TIE.2012.2186770.
- [63] C. Seatzu, D. Corona, A. Giua, and A. Bemporad. Optimal control of continuous-time switched affine systems. *IEEE Transactions on Automatic Control*, 51(5):726–741, 2006. doi:10.1109/TAC.2006.875053.
- [64] E. Kerrigan and D. Mayne. Optimal control of constrained, piecewise affine systems with bounded disturbances. In *Proceedings of the IEEE Conference on Decision and Control*, volume 2, pages 1552–1557, 2002.
- [65] L. Habets, P. Collins, and J. van Schuppen. Reachability and control synthesis for piecewise-affine hybrid systems on simplices. *IEEE Transactions on Automatic Control*, 51(6):938–948, 2006. doi:10.1109/TAC.2006.876952.

## References

- [66] L. Rodrigues and S. Boyd. Piecewise-affine state feedback for piecewise-affine slab systems using convex optimization. 54(9):835–853, 2005. doi:10.1016/j.sysconle.2005.01.002.
- [67] Y.-H. Gao, Z.-Y. Liu, and H. Chen. Observer-based controller design of discrete-time piecewise affine systems. *Asian Journal of Control*, 12(4):558–567, 2010. doi:10.1002/asjc.207.
- [68] W. Heemels, M. Lazar, N. Van De Wouw, and A. Pavlov. Observer-based control of discrete-time piecewise affine systems: Exploiting continuity twice. In *Proceedings of the IEEE Conference on Decision and Control*, pages 4675–4680, 2008. doi:10.1109/CDC.2008.4739094.
- [69] A. Juloski, W. Heemels, and S. Weiland. Observer design for a class of piece-wise affine systems. In *Proceedings of the IEEE Conference on Decision and Control*, volume 3, pages 2606–2611, 2002.
- [70] A. Pavlov, N. Van De Wouw, and H. Nijmeijer. Convergent piecewise affine systems: Analysis and design Part I: continuous case. In *Proceedings of the 44th IEEE Conference on Decision and Control, and the European Control Conference, CDC-ECC '05*, volume 2005, pages 5391–5396, 2005. doi:10.1109/CDC.2005.1583019.
- [71] L. Rodrigues and J. How. Observer-based control of piecewise-affine systems. *International Journal of Control*, 76(5):459–477, 2003. doi:10.1080/0020717031000091432.
- [72] L. Rodrigues and J. How. Observer-based control of piecewise-affine systems. *Proceedings of the IEEE Conference on Decision and Control*, 2:1366–1371, 2001. doi:10.1109/CDC.2001.981080.
- [73] L. Zhang, Z. Ning, and W. Zheng. Observer-Based Control for Piecewise-Affine Systems with Both Input and Output Quantization. *IEEE Transactions on Automatic Control*, 62(11):5858–5865, 2017. doi:10.1109/TAC.2016.2641585.
- [74] W. R. Perkins. Feedback Control Systems. In *Reference Data for Engineers*, pages 15–1–15–33. Elsevier, 2002. doi:10.1016/B978-075067291-7/50017-0.
- [75] S. Wiggins. Poincaré Maps. In *Introduction to Applied Nonlinear Dynamical Systems and Chaos*, chapter 10, pages 122–150. Springer New York, New York, NY, 2003. doi:10.1007/0-387-21749-5\_11.
- [76] A. M. Lyapunov. The general problem of the stability of motion. *International Journal of Control*, 55(3):531–534, 1992. doi:10.1080/00207179208934253.

- [77] O. Föllinger. *Nichtlineare Regelungen I, Grundbegriffe, Anwendungen der Zustandsebene, Direkte Methode*. De Gruyter Oldenbourg, Berlin, Boston, 2014. doi:10.1524/9783110406153.
- [78] M. Johansson. *Piecewise Linear Control Systems*. Lund Institute of Technology, 1999. doi:10.1007/3-540-36801-9.
- [79] A. Hassibi and S. Boyd. Quadratic stabilization and control of piecewise-linear systems. In *Proceedings of the American Control Conference*, volume 6, pages 3659–3664, 1998. doi:10.1109/ACC.1998.703296.
- [80] H. K. Khalil. *Nonlinear Systems - Third Edition*. *Journal of Climate J Clim Vol 18*, 18(16):750, 2002. doi:10.1016/j.physa.2006.08.011.
- [81] H. E. Merritt. *Hydraulic control systems*. John Wiley and Sons, 1967.
- [82] M. Jelali and A. Kroll. *Hydraulic servo-systems : modelling, identification, and control*. Springer, 2003.
- [83] M. Ruderman. On break-away forces in actuated motion systems with nonlinear friction. *Mechatronics*, 44:1–5, 2017.
- [84] T. Strutz. *Data Fitting and Uncertainty: A practical introduction to weighted least squares and beyond*. 2011. doi:10.1007/978-3-8348-9813-5.
- [85] S. K. Mitra and J. F. Kaiser. *Handbook for digital signal processing*. Wiley, 1993.
- [86] J. O. Jang. A deadzone compensator of a dc motor system using fuzzy logic control. *IEEE Transactions on Systems, Man and Cybernetics Part C: Applications and Reviews*, 31(1):42–48, feb 2001. doi:10.1109/5326.923267.
- [87] F. L. Lewis, W. K. Tim, L. Z. Wang, and Z. X. Li. Deadzone compensation in motion control systems using adaptive fuzzy logic control. *IEEE Transactions on Control Systems Technology*, 7(6):731–742, 1999. doi:10.1109/87.799674.
- [88] Y. Wakasa, S. Kanagawa, K. Tanaka, and Y. Nishimura. FRIT for Systems with Dead-Zone and Its Application to Ultrasonic Motors. *IEEE Transactions on Electronics, Information and Systems*, 131(6):1209–1216, 2011. doi:10.1541/ieejeiss.131.1209.
- [89] M. Ruderman. Computationally Efficient Formulation of Relay Operator for Preisach Hysteresis Modeling. *IEEE Transactions on Magnetics*, 51(12):1–4, 2015.

# Appendices



# Paper A

## Design and Analysis of non-linear Circuit with Tunnel Diode for Hybrid Control Systems

Philipp Pasoli, Michael Ruderman

This paper has been published as:

P. Pasoli, M. Ruderman. Design and Analysis of non-linear Circuit with Tunnel Diode for Hybrid Control Systems. *Proceeding of IEEE 15th International Workshop on Advanced Motion Control (AMC2018)*, 181-186, 2018.

doi: 10.1109/AMC.2019.8371084.



# Design and Analysis of non-linear Circuit with Tunnel Diode for Hybrid Control Systems

Philipp Pasolli, Michael Ruderman

University of Agder

Department of Engineering Sciences

Jon Lilletunsvet 9, 4879 Grimstad, Norway

*Abstract* – Electric circuits with tunnel diode’s represent a classical example of dynamic systems with nonlinearities, which feature piecewise negative damping and multiple equilibria and, as consequence, nontrivial trajectories in the state-space. In this paper, we describe the experimental design and analysis of an electrical circuit, including a tunnel diode, allowing for a storage behavior with bistable output voltage states – *low* and *high*. The system is modeled for simulation and an experimental setup is designed and implemented in order to run a formal verification on different tools, applying a variety of hybrid control methods. The nonlinear diode’s characteristic curve is experimentally determined and evaluated. The transient response of circuit is also analyzed. Furthermore the circuit is controlled in an open loop manner, by a biased sequence of pulse signals, showing a bistable switching behavior of the output voltage state.

## A.1 Introduction

Since invented and introduced, the tunnel diodes belong to standard electronic elements, which can be used for a wide variety of functions such as amplifying, switching, frequency conversion, etc [1]. Formerly used in microwave oscillators [2], tunnel diodes have entered diversity of semiconductor technologies and micro-electronics applications, like for example in computer memory, but also in various other logic circuits, see e.g. [3]. Even though representing a well-understood and widely established semiconductor technology, the tunneling diodes remain further in focus of investigation in conjunction with unique current-voltage characteristics and associated properties of nonlinear electric circuits. For instance, the resonant tunneling diodes in oscillating circuits can be used for strain detection and therefore as sensing elements [4].

In the recent work, we fall back on the strongly pronounced nonlinear current-voltage characteristics of a tunnel diode, and therewith associated multiple equilibria, correspond-

ingly, nontrivial trajectories in the state-space. Due to its negative differential resistance, the diode's non-linear characteristic has two stable operating points with the same current response, cf. Fig. A.1. This characteristic combined, with standard diode behavior as ultra-fast heterostructure device, allows it to be used in circuits as a storage element with bistable output voltage, *low* and *high*, and fast switching transients between both. Switching between the two states can be accomplished by the pulse signal added to a necessary voltage offset (bias). Such a nonlinear circuit with tunnel diode and output voltage to be controlled is used in our study, while representing a reach-on-dynamics nonlinear control system with hybrid, i.e. mixed time-continuous and discrete, behavior. Recall that the hybrid systems are ubiquitous and we see and interact with them on a daily basis [5, 6, 7]. Therefore, the objective of this paper is an experimental design and analysis of the nonlinear circuit, based on the tunnel diode, which can later on serve for investigation and verification/validation of various hybrid control strategies, with particular focus on stability, reachability, and computational efficiency.

The paper is organized as follows: In Section II, we summarize the modeling of the nonlinear circuit with the tunnel diode. Following, the designed and assembled circuit with measuring and controlling devices are described in Section III. The experimental identification of diode characteristics is shown in Section IV. The analysis of transient response circuits behavior is provided in Section V. A simple open loop switching control of bistable output voltage is demonstrated with experiments in Section VI. Finally, Section VII summarizes the paper and gives brief outlook on the future works.

## A.2 Modeling of Non-linear Circuit

The system under consideration is based on an electric circuit using a tunnel diode as a non-linear component. The idea for this nonlinear system is inspired by a classical example from Khalil [8]. Besides the tunnel diode, the energy storage elements, i.e. capacitor and inductance, are also involved, equally as a resistive element and a voltage source.

In order to analyze and allow for numerical simulation of the circuit, the following differential equations are assumed first. Seeing the capacitance and the inductance to be time-invariant and linear we can write

$$i_C = C \frac{dv_C}{dt}, \quad v_L = L \frac{di_L}{dt}, \quad (\text{A.1})$$

where  $i$  and  $v$  represent the current and, respectively, the voltage across the components. The subscript describes which component is referred to, while  $C$  and  $L$  represent the components. For the state model we define state  $x_1$  as the voltage across the diode  $v_R$ , and state  $x_2$  as the current through the inductance  $i_L$ . Furthermore the controllable input

voltage is given by  $u$ . In order to get a state equation for  $x_1$ ,  $i_C$  has to be expressed as a function of the state variables  $x_1$ ,  $x_2$ , and input  $u$ .

Applying the first of Kirchoff's law at the intersection point, meaning that the sum of all currents must be equal to zero, we obtain the following equation

$$i_R + i_C = i_L. \quad (\text{A.2})$$

Further, knowing that the characteristic of the tunnel diode is a function of  $x_1$ , we can rewrite (A.2) to

$$i_C = -h(x_1) + x_2. \quad (\text{A.3})$$

Also  $v_L$  should be described as a function of state variables  $x_1, x_2$  and input  $u$ . Applying Kirchoff's second law, meaning that all voltages in a closed pathway must be equal to zero, we can write

$$E = Ri_L + v_L + v_c, \quad (\text{A.4})$$

while the total potential difference is set to be the input control value, i.e.  $E = u$ . Therefore, we obtain

$$v_L = -x_1 - Rx_2 + u. \quad (\text{A.5})$$

Now  $v_L$  and  $i_C$  from (A.1) can be substituted by (A.3) and (A.5) which results in the two state equations

$$\dot{x}_1 = \frac{1}{C}[-h(x_1) + x_2], \quad (\text{A.6})$$

$$\dot{x}_2 = \frac{1}{L}[-x_1 - Rx_2 + u]. \quad (\text{A.7})$$

For further reference, the state  $x_2$  will be referred to as  $u_D$  instead of  $u_R$ , since the voltage across the diode is an output value of interest. Using both state equations, a nonlinear state model can be directly implemented for numerical simulations.

### A.3 Test Setup and Experiment

The experimental test setup corresponds to the circuit provided in [8]. For hardware assembly, the components with values different from those assumed in [8] where used, due to the parts in stock, cf. Table A.1.

For the diode element, a vintage tunnel diode from General Electric, Type 1N3716 has been used [9]. A typical static curve with most relevant characteristic points for a chosen diode can be seen in Fig. A.1 and Table A.2.

The circuit is set up on a universal interface bread board. As a measurement and control interface for the electric circuit, a dSpace MicroLabBox has been used [10]. To

Table A.1: Initial components configuration

Components	Reference values [8]	Experimental values
R	1.5k $\Omega$	1.5k $\Omega$
C	2pF	12pF
L	5 $\mu$ H	4.7 $\mu$ H

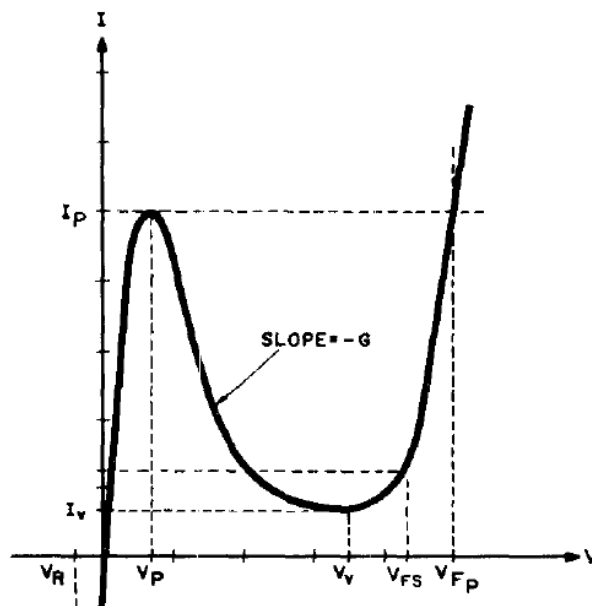


Figure A.1: Typical characteristic curve of tunnel diode [9]

Table A.2: Diode characteristic points [9]

Static Characteristics	Symbol	Value
Peak Point Current	$I_P$	4.7mA
Valley Point Current	$I_V$	0.6mA
Peak Point Voltage	$V_P$	65mV
Valley Point Voltage	$V_V$	350mV
Forward Voltage	$V_{FP}$	500mV

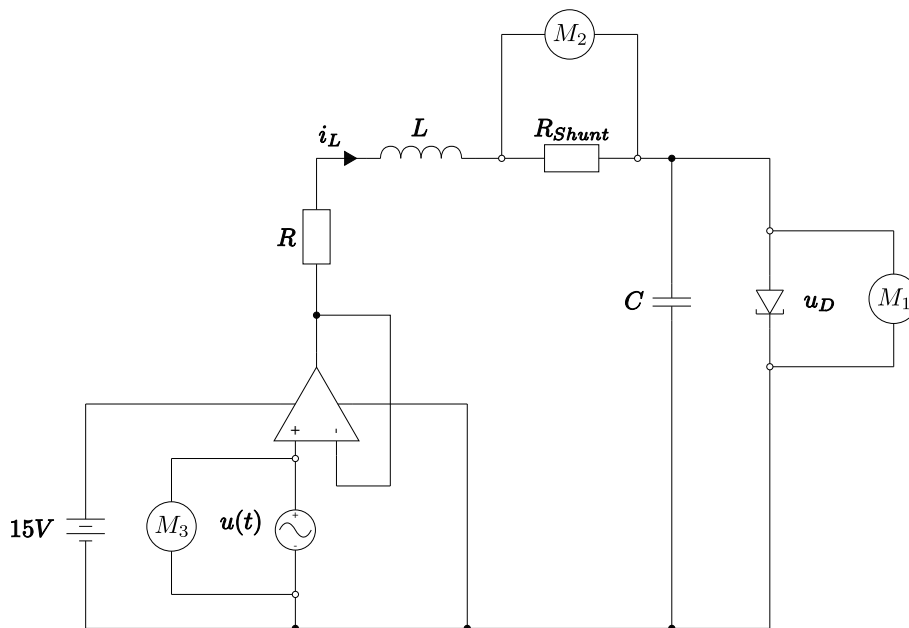


Figure A.2: Electrical diagram for experimental setup of complete circuit

connect the MicroLabBox to the circuit, standard BNC connectors are used. The output ports of the MicroLabBox provide  $\pm 10V$  with a current range of  $\pm 8mA$  and an offset error of  $\pm 4mV$ . The settling time is given with  $1\mu s$  and the resolution of A/D conversion is 16bit. The board channels have also a circuit protecting them from over-voltage or -current.

The analogue out-port is the input voltage to the circuit representing  $u$  in (A.7). The voltage to drive the circuit is directly supplied by the analogue output channel. Although the current provided from the MicroLabBox would be enough for the diode only, the rest of the circuit should be additionally energized. Therefore an operational amplifiers (OP) of type LM324AN [11] has been used to boost the maximum available current up to  $30mA$ . The OP is in voltage follower configuration without any gain, having the same output voltage as the input.

On the input side of the MicroLabBox, the measuring input channels have the voltage range of  $\pm 11V$ , with a resolution of 16bit and a sampling rate of  $10^6 Hz$ , i.e.  $1\mu s$  sampling time. For measurements, three BNC cables where connected to the circuit. One to measure  $u$ , another one – across a shunt resistor of  $1\Omega$  – to measure the state  $x_2$ , which is the inductor current  $i_L$ . The last one is directly connected across the diode, for measuring the state  $x_1$ , corresponding to  $u_D$  output. Thus, the electric diagram of the implemented setup is shown in Fig. A.2, where the points of measuring are indicated with the symbols  $M_x$ . Respectively, the experimental setup in the room temperature environment is shown on the picture in Fig. A.3.

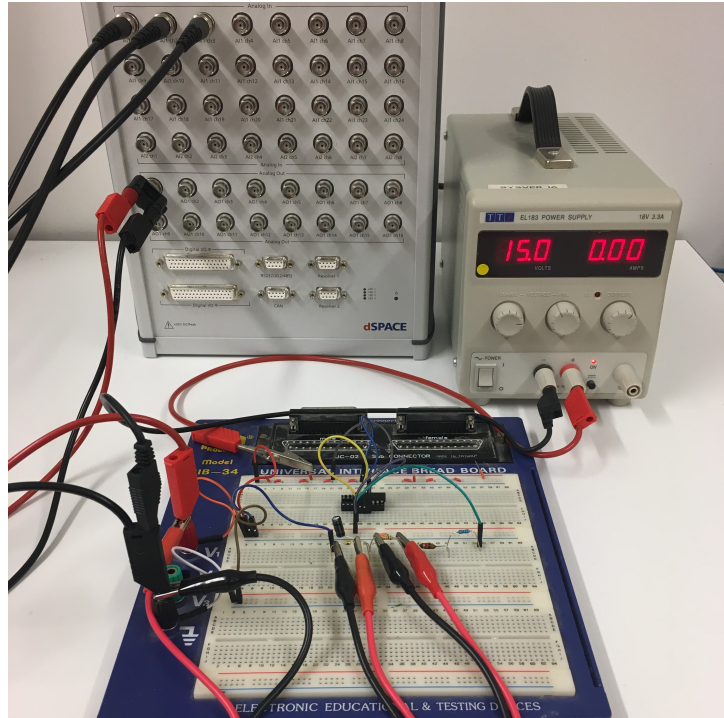


Figure A.3: Experimental setup

## A.4 Measuring of Diode Characteristic

For reliable modeling and numerical simulation of the circuit, the actual characteristic of the diode had to be determined from measurements. For that,  $R$ ,  $L$ , and  $C$  shown in Fig. A.2 have been first taken out, and a sinusoidal voltage was supplied to  $u$  in a closed-loop configuration, with a feedback integrator only. The current, via a shunt resistor added in front of the diode, and the voltage across the diode have been measured. The feedback integrator has been used in order to ensure that the diode's voltage follows the input voltage closely. Multiple measurements were taken, with the configuration values shown in Table A.3.

For each of the listed configurations, 10 measurements were performed at different times, with 10 periods each. Trigger conditions for measurement recording was set to 0.4V rising flank for the voltage across the diode. The following diagrams show one exemplary measurement, corresponding to  $M.2$  configuration as in Table A.3. The raw measurement data couldn't be used for identification, as it turns out the signal of the diode's voltage seems to be rather smooth while the current measurement included non-neglectable noise and quantization effects, see Fig. A.4. Trying to boost the signal of the current measurement, using an instrumentation amplifier, appears less useful due to a low signal to noise ratio of the signal. Therefore, a Fast Fourier Transformation (FFT) has been first performed on both the current and voltage measurements, see Fig. A.5. It can be seen that while, the power spectrum of the measured voltage disclose the

Table A.3: Configuration of diode characteristic measurement values

<b>Configuration</b>	<b>M.1</b>	<b>M.2</b>	<b>M.3</b>
Sine amplitude	0.25V	0.25V	0.25V
Sine offset	0.25V	0.25V	0.25V
Sine frequency	5Hz	10Hz	100Hz
Integrator	100	100	5000

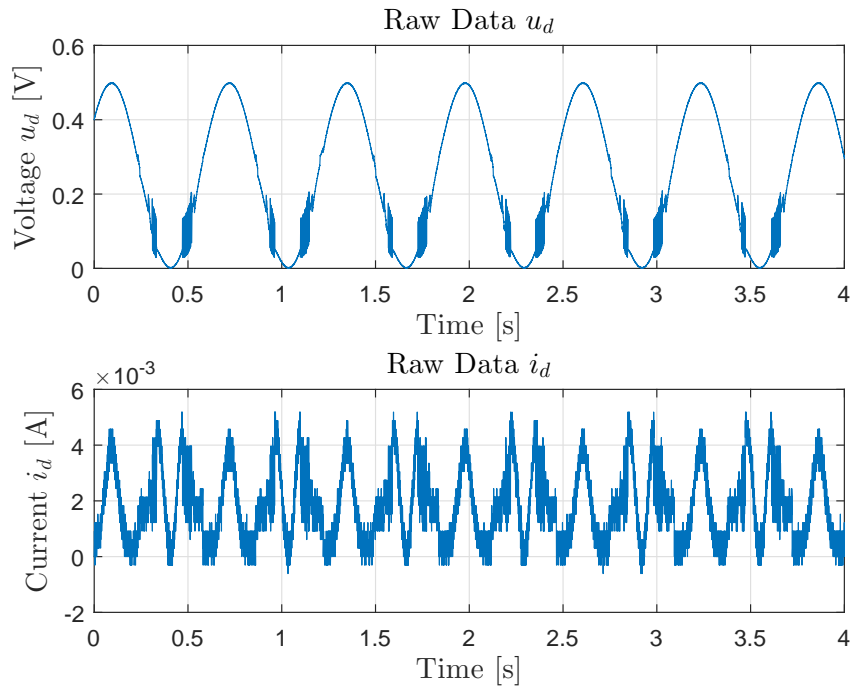


Figure A.4: Diode characteristic - raw voltage and current measurement

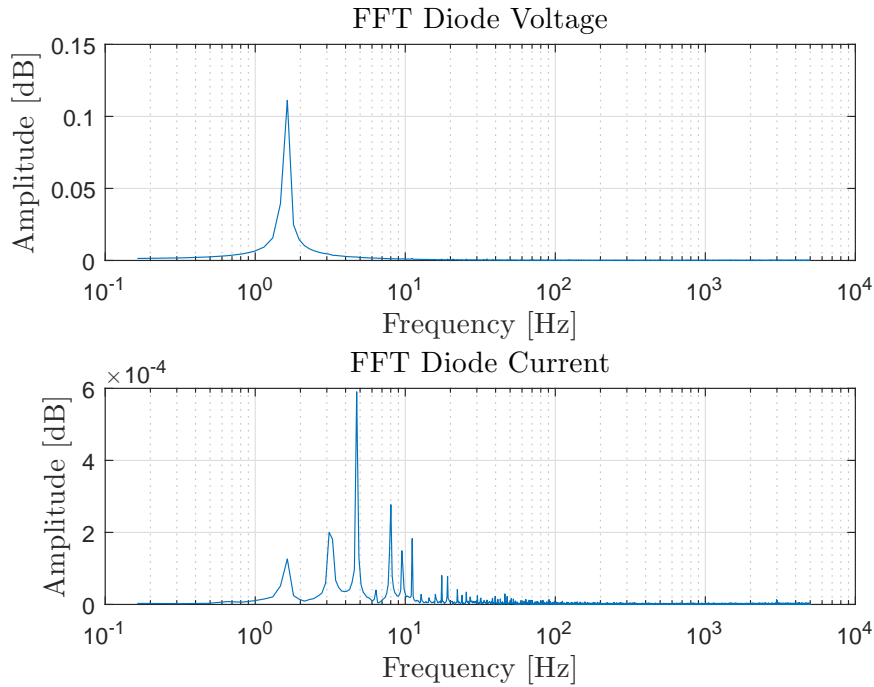


Figure A.5: Diode characteristic - Fast Fourier Transform

one principal harmonic, the spectrum distrusting of the measured diode current clearly demonstrate multiple frequency components right-hand side to the principal harmonic. This is supposedly due to inherently nonlinear nature of the tunnel diode, though will not be further analyzed, correspondingly discussed, due to a different focus of the recent work. Afterwards, a low pass filter has been applied, resulting in a more smooth measured characteristic. Also, the filtered data was cropped to full periods so as to avoid the initial "bending" of signals due to the filtering.

Next, all data points within a moving frame of  $1mV$ , were averaged for the voltage and current signal, thus giving a data point every  $1mV$  within the range of 0 to  $0.5V$ . Finally, the obtained characteristic points have been shifted to start at  $0V$  and, if necessary, smoothed out using a moving average. Note hat the shift of zero voltage is reasonably required since the shunt, connected in series, provided an additional low voltage drop which is not belonging to diode's characteristic. The settings applied for filtering and smoothing the data from the chosen configuration M.2 are as follows: filter order  $2^9$  and cutoff frequency  $30Hz$ .

After evaluating all measurements in the same manner, we came to the conclusion, that the determined (final) characteristic from the measurements with M.2 configuration are closest to the generalized characteristic curve and nominal (manufacturer provided) data points. The final characteristic curve, as well as the characteristic points from the data sheet A.2, are shown in Fig. A.6. Further it can be noted that the data spread of



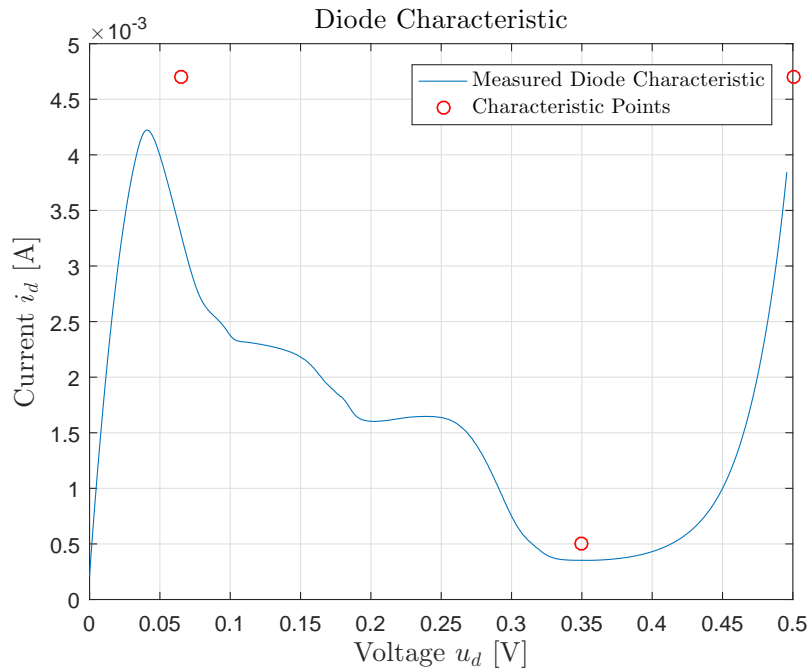


Figure A.6: Diode characteristic curve with characteristic points from data sheet

the 10 repeated measurements has been equally evaluated and yielded negligible.

## A.5 Transient Response and Circuit Analysis

Performing a numerical simulation when applying a pulse signal at the system  $u$ , we see the state response as shown in Fig. A.7. Here, the parameter reference values as in Table A.1, have been used in order to analyze the circuits behavior. From the open loop response it can be recognized, that the time constants are relatively short and are in the region of a few nano-seconds. Therefore, initial circuits configuration is significantly faster than available sampling time of the MicroLabBox controller. Therefore, the circuits time response is required to be slower than about  $100\mu s$ , so as to allow for sufficient sampling during the transient phases. Different values for the components  $C$  and  $L$  have been tried to alter the response time. The chosen values, based on components available, are shown in Table A.4. The results of numerical simulation and experimental measurements are compared with each other in Fig. A.8 for all three components' configurations. One can see, that for all three configurations, the measured response of the circuit is well in accord with the modeled one, in both steady-state and transient (rise time) phases. This argues in favor of the designed and identified system, and allows for using numerical simulation for future analysis in control strategies. For further experiments, the components' configuration  $V.3$  has been chosen as a sufficiently slow and, therefore, suitable for capturing the transient response.

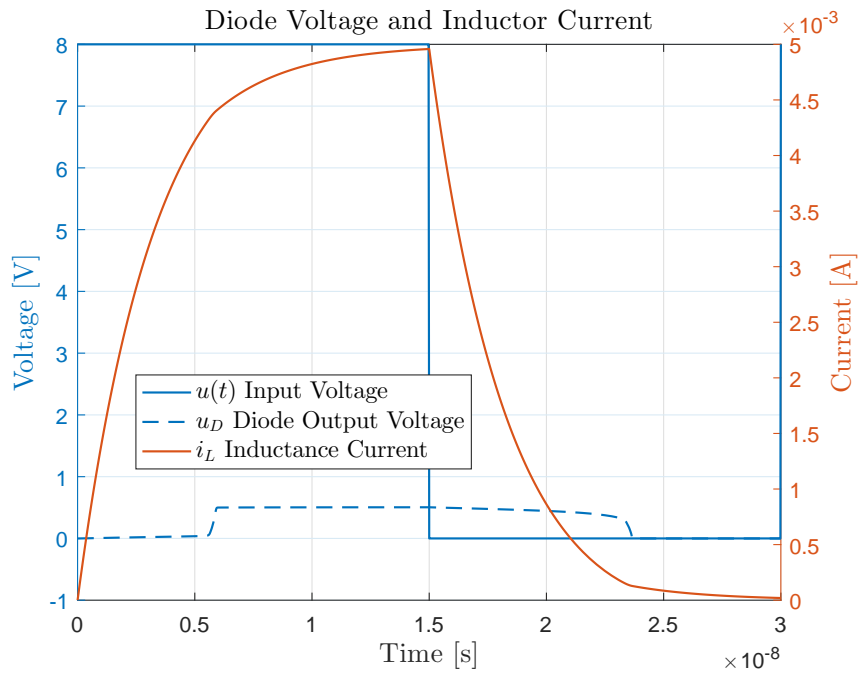


Figure A.7: Transient response of diode, numeric simulation as in Table A.1

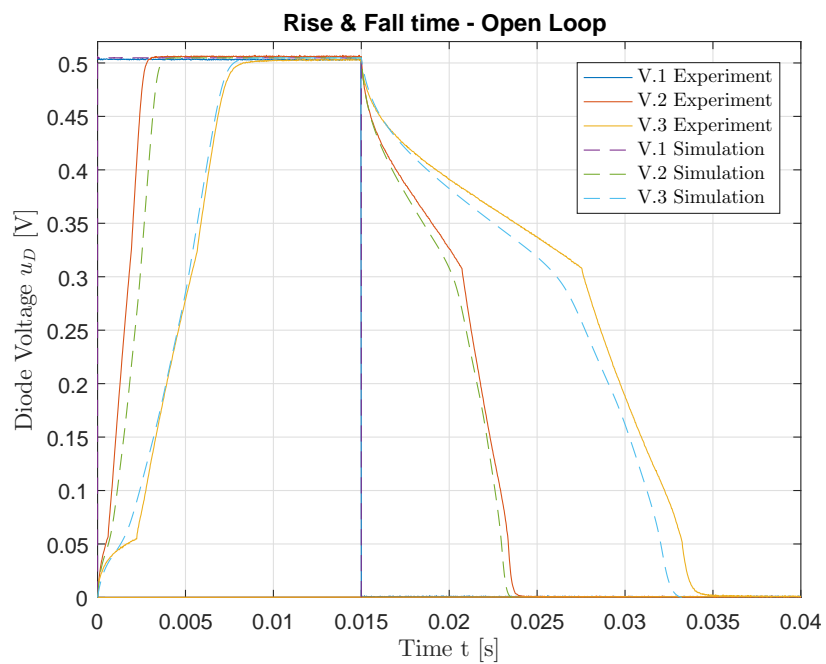


Figure A.8: Simulation and experiment response according to Table A.4

Table A.4: Components' configurations

Component	V.1	V.2	V.3
R	1.5k $\Omega$	1.5k $\Omega$	1.5k $\Omega$
C	12pF	22 $\mu$ F	47 $\mu$ F
L	4.7 $\mu$ H	1mH	1mH

Also, a frequency sweep has been simulated in order to check at which signal frequencies the corresponding response of the circuit is going to be affected. For the simulation, the values of configuration *V.3* from Table A.4 have been assumed as well. From Fig. A.9 one can see, that starting from about 100Hz, a magnitude decrease is already observable. Also the phase starts decaying already at relatively low frequencies. Furthermore, it has to be mentioned that the numerical simulation has performed for a system model based on Fig. A.2, therefore including the OP, supply voltage and measuring elements. The model for simulation was created using the National Instrument Multisim 14.0 which has the OP LM324AN in library. However, the exact diode used in our test setup was not available, and the next best match was taken in order to perform the simulation, i.e. a diode of type 1N3715 instead of 1N3716. Despite the dynamic system with only two integrators is expected to have the phase response converging to  $-180^\circ$ , from Fig. A.9 one can see that the phase goes far beyond  $-180^\circ$ . This is mainly caused by high frequency behavior of LM324AN amplifier and possible impact of nonlinearities on the estimation of frequency response function.

Next, in order to analyze the fast (transient) switching between two bistable states, a sine signal with the frequency of 10Hz, amplitude of 5V, and offset of 5V was applied to the input of the circuit. The measured results are shown in Fig. A.10, from which one can clearly see a two-level output state behavior, as hysteresis in the input-output voltage coordinates. Diode output voltages of less than 0.1V can be considered as *low* level, while the voltages above 0.4V can be considered as *high* level. Obviously, the designed circuit provides the expected memory effect due to the energy storage in combination with nonlinear voltage-current characteristics of the tunnel diode.

## A.6 Open Loop Control

The open loop control setup, which the following measurements were taken from, is shown in Fig. A.11. Varying configurations of pulse signals have been used. The goal is to switch

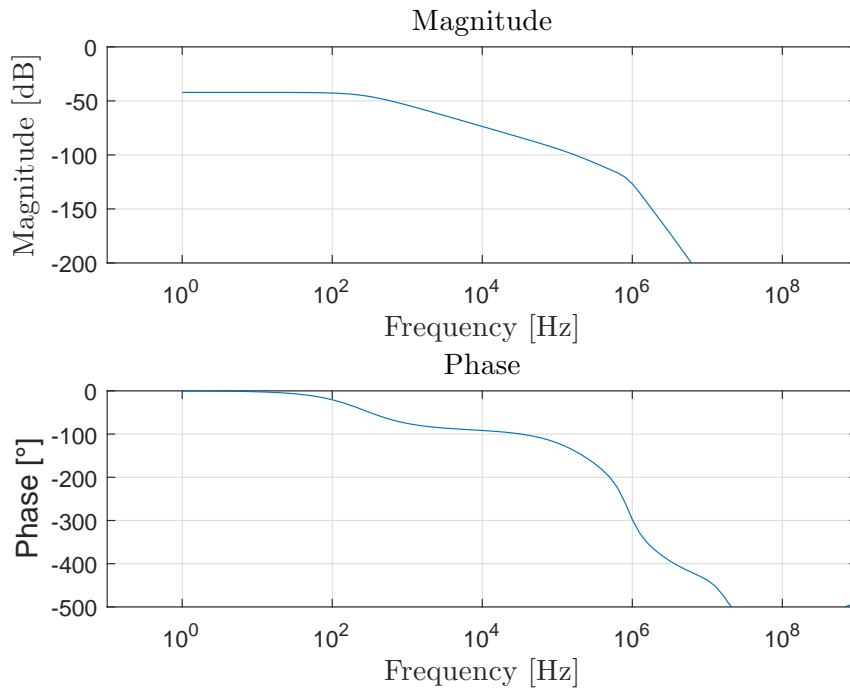


Figure A.9: Bode plot of the circuit

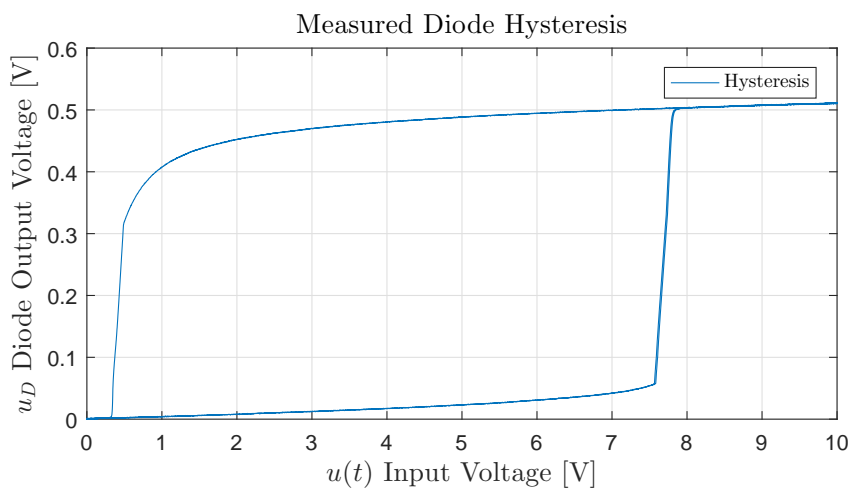


Figure A.10: Measured input-output hysteresis curve of diode

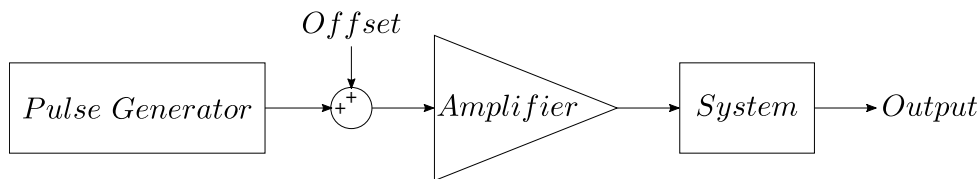


Figure A.11: Open loop control structure

Table A.5: Amplitude, offset and pulse-width settings for experiments and corresponding figure references

	<b>Amplitude 3.4V</b>	<b>Amplitude 5V</b>
	<b>Offset 4.1V</b>	<b>Offset 5V</b>
<b>Pulsewidth 32%</b>	Fig. A.14	Fig. A.12
<b>Pulsewidth 18%</b>	Fig. A.15	Fig. A.13

between two bistable states, with a short pulse around the offset voltage, which value is  $4.1V$ . The configurations applied to the system are shown in Table A.5.

Taking a look at Fig. A.12 one can see that both states are easily reached, when a pulse in positive or negative direction is applied over the offset. However, once we reduce the pulse-width to less than 19% (using 1% increments), the signal is not able to reach both states anymore which can be seen from Fig. A.13. Interesting to mention is that although the output voltage reached almost its lower state, it bounces back up to the state *high* only due to the voltage of the offset.

Furthermore, coming back to a pulse-width of 32% but lowering the voltage gradually (using  $0.1V$  increments), one can see that at the input voltage level of  $3.4V$  the system is not able to switch between the two states anymore either, as can be seen in Fig A.14. The same behavior, not being able to switch between states, can be observed in the *worst case scenario*, combining low voltage and and short pulse width, see Fig. A.15.

Therefore it can be concluded, that the minimum pulse-width at which the system is still able to switch between states *high* and *low* is depending on the systems input voltage provided and the pulsewidth, assuming that the offset voltage is in the middle of the hysteresis. On our test setup, one is limited to the maximal  $10V$ , therefore the maximum possible pulse amplitude to induce is  $5V$ .

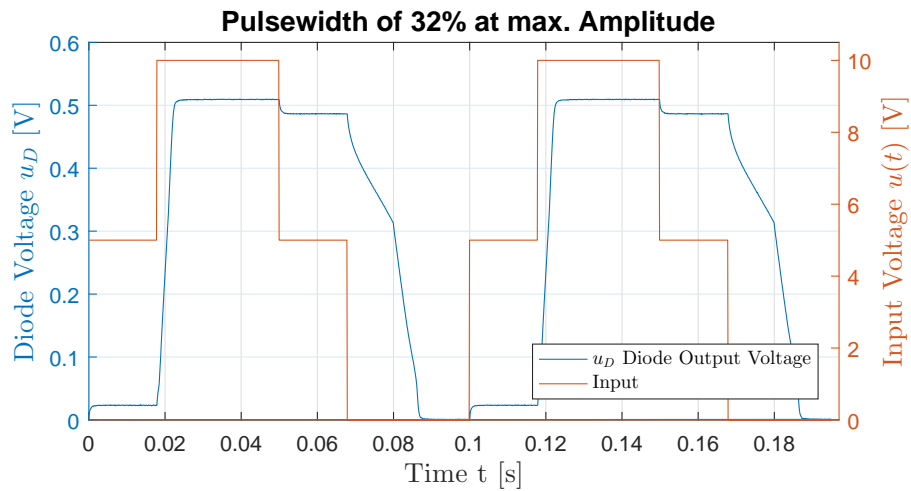


Figure A.12: Measured input voltage and system response at amplitude of 5V, offset 5V with pulse-width of 32%

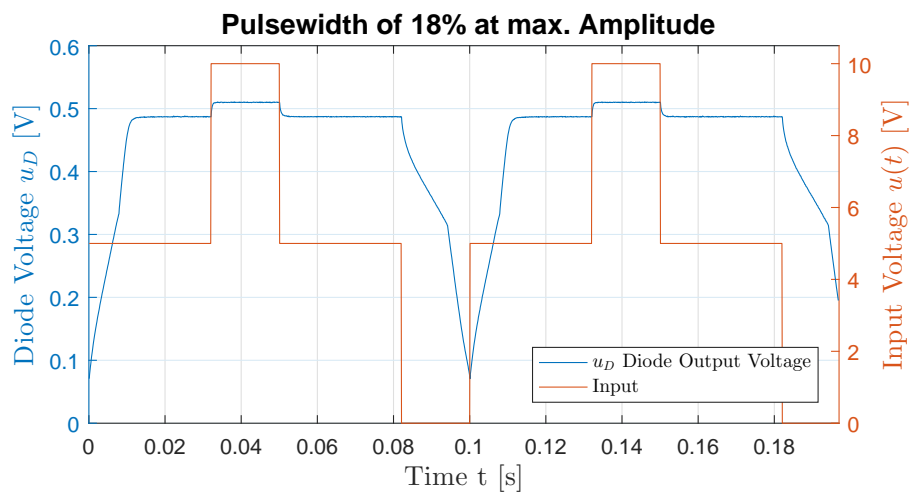


Figure A.13: Measured input voltage and system response at amplitude of 5V, offset 5V with pulse-width of 18%

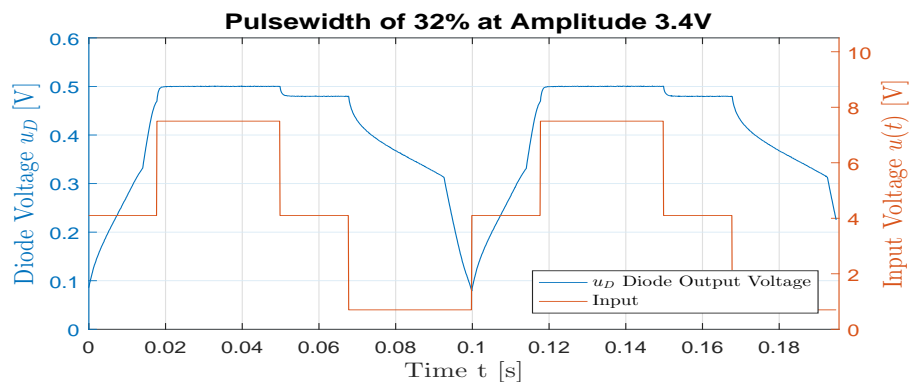


Figure A.14: Measured input voltage and system response at amplitude of 3.4V, offset 4.2V with pulse-width of 32%

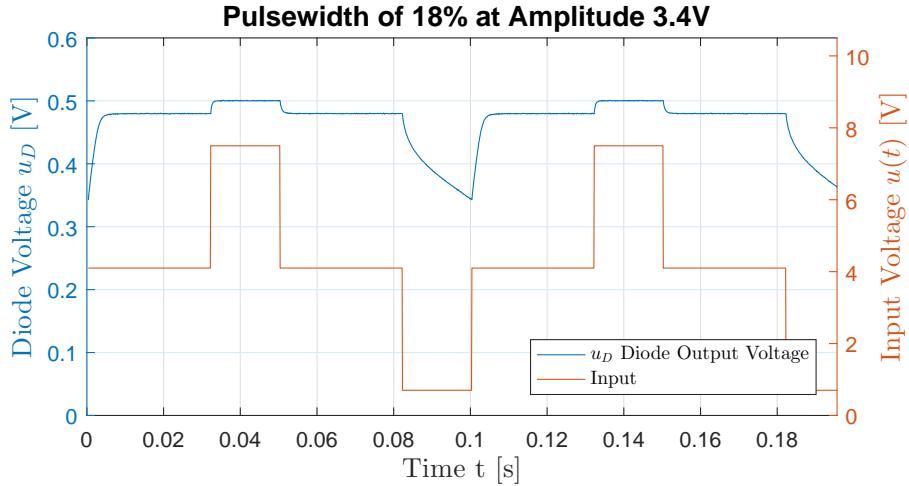


Figure A.15: Measured input voltage and system response at amplitude of  $3.4V$ , offset  $4.2V$  with pulse-width of 18%

## A.7 Summary and Outlook

In this work, the non-linear electric circuit with tunnel diode has been designed and implemented on an experimental setup. The classical model, known from literature [8], has been assumed, while the system parameters have been assumed from the data sheets of standard linear components and identified by series of dedicated experiments. The nonlinear characteristics of the tunnel diode have been determined from the measurements and compared with typical characteristic curves and the few characteristic points available from the components' documentation. Both, the steady-state and transient responses of the overall system have been analyzed based on experiments. Also, an open loop control with biased impulses have been realized and evaluated, allowing for a bistable output voltage behavior. The knowledge gained by conducting the simulations and experiments for this setup, now enables us to apply various hybrid control methods [7], [12] and perform a formal analysis [13], [14] for different tools designed for hybrid control verification. Having validated analysis tools to verify the proper function of the control scheme is therefore of utmost importance.





# REFERENCES

- [1] R. Hall. Tunnel diodes. *IRE Transactions on Electron Devices*, 7(1):1–9, 1960.
- [2] H. Sommers. Tunnel Diodes as High-Frequency Devices. *Proceedings of the IRE*, 47(7):1201–1206, 1959.
- [3] R. H. Bergman. Tunnel diode logic circuits. *IRE Transactions on Electronic Computers*, (4):430–438, 1960.
- [4] T. Tajika, Y. Kakutani, M. Mori, and K. Maezawa. Experimental demonstration of strain detection using resonant tunneling delta-sigma modulation sensors. *Physica status solidi (a)*, 214(3):1600548, 2017.
- [5] J. Lunze and F. Lamnabhi-Lagarrigue. *Handbook of hybrid systems control: theory, tools, applications*. Cambridge University Press, 2009.
- [6] R. Goebel, R. G. Sanfelice, and A. R. Teel. Hybrid dynamical systems. *IEEE Control Systems*, 29(2):28–93, 2009.
- [7] H. Lin and P. Antsaklis. *Hybrid Dynamical Systems: An Introduction to Control and Verification*. Now Publishers, 2014.
- [8] H. Khalil. *Nonlinear Systems*. Prentice Hall, 3rd edition, 2002.
- [9] ElfaDistrelec. Tunnel Diodes, 2017. URL: <https://www.elfadistrelec.no>.
- [10] dSpace. MicroLabBox - dSPACE, 2017. URL: <https://www.dspace.com/de/gmb/home/products/hw/microlabbox.cfm>.
- [11] T. Instruments. LM324AN Texas Instruments — Mouser Germany, 2017. URL: <https://www.mouser.de/ProductDetail/Texas-Instruments/LM324AN/?qs=KaAww0lwapuGsi7hHRx1kw==>.
- [12] K. H. Johansson. Hybrid control systems. 2004. URL: <http://www.diva-portal.org/smash/record.jsf?pid=diva2%7B3A505356%7D&dswid=-8266>.

- [13] R. Alur. Formal verification of hybrid systems. *Emsoft*, pages 273—278, 2011. URL: <http://dl.acm.org/citation.cfm?doid=2038642.2038685>[http://ieeexplore.ieee.org/xpls/abs/\\_all.jsp?arnumber=6064535](http://ieeexplore.ieee.org/xpls/abs/_all.jsp?arnumber=6064535), doi:10.1145/2038642.2038685.
- [14] A. Fehnker, A. Fehnker, F. Ivancic, and F. Ivancic. Benchmarks for Hybrid Systems Verification. *Hybrid Systems: Computation and Control*, 15213:326 – 341, 2004. URL: <http://www.springerlink.com/content/bf2mw0g2m4mvwudu>, doi:10.1007/978-3-540-24743-2\_22.

## Paper B

# Design, Control, and Analysis of Nonlinear Circuits with Tunnel Diode with Piecewise Affine Dynamics

Philipp Pasolli, Michael Ruderman

This paper has been published as:

P. Pasoli, M. Ruderman. Design, Control, and Analysis of Nonlinear Circuits with Tunnel Diode with Piecewise Affine Dynamics. *IEEJ Journal of Industry Applications*, Vol.8 No.2 pp.280-249, 2018. doi: 10.1541/ieejia.8.240.

# Design, Control, and Analysis of Nonlinear Circuits with Tunnel Diode with Piecewise Affine Dynamics

Philipp Pasolli, Michael Ruderman

University of Agder

Department of Engineering Sciences

Jon Lilletunsvet 9, 4879 Grimstad, Norway

*Abstract* – A classic example of dynamic systems with nonlinearities is considered, using an electrical circuit including the tunnel diode, that features several equilibria points due to a piecewise positive and negative damping. These system-properties allow us to investigate the possible limit cycles, and the formal analysis of the closed-loop dynamics of such. In this paper, an experimental setup of nonlinear circuits is designed, followed by the system modeling and identification of the diodes' characteristics. An integral-state-feedback control is designed and evaluated for demonstrating the appearance of the limit cycles depending on the reference level. A piecewise affine (PWA) system formulation is also provided for allowing the use of formal verification tools for hybrid dynamic systems. An available tool, *PWLTool*, is applied in line with trajectory prediction from the numerical simulation of the identified closed-loop system.

## B.1 Introduction

Complex systems often include nonlinearities creating extensive challenges in the analysis, identification, and design of controllers. Often, such systems have to be linearized, for different purposes, around operation points that drastically restrict their extent of validity to a certain range, i.e. in the state and parameter spaces. By linearizing more complex systems, such as introducing additional nonlinearities to possibly already existing ones, the chance that a system becomes unstable is increased. Using standard approaches (e.g. simulation with different initial conditions) for simulating a system leads only to a partial verification and does not necessarily cover the whole possible operating range of a system. By introducing Formal Analysis Tools, one is given the opportunity to possibly fully evaluate a system in regards of stability and other important criteria. The *PWLTool* used in this scenario is able to handle our so called piecewise affine (PWA) System. However, these systems [1] allow for interconnecting several linearized parts, where each

linearization region becomes one polyhedral cell within the entire state-space. This enables greater extension of the linear state-space notation by the affine terms and, therefore, considering more complex dynamic systems, such as including saturations and dead-zones, [2, 3], equally as various, and also including switching, control strategies [4, 5, 6, 7]. PWA systems require definition of, in addition to the vector field, the set of polyhedral cells which assemble the whole state-space and transitions between them. The PWA modeling is accomplished by extending the standard state-space representation by an additional affine part, acting as an offset in the vector field, coupled with the descriptive matrices of the cells boundaries and transitions, cf. [8]. Various systems with nonlinearities can be modeled as having piecewise dynamics, among them mechanical, hydraulic, and electrical – all mostly containing some static nonlinearities in the single elements with corresponding transfer characteristics. The recent work focuses on an electrical circuit, including the tunnel diode with the well-pronounced nonlinear characteristics [9].

Since introduction, tunnel diodes belong to the standard electronic elements, which can be used for a wide variety of functions such as amplifying, switching, frequency converting, etc. Formerly used in the microwave oscillators [10], tunnel diodes have entered a diversity of semiconductor technologies and micro-electronics applications, for example in computer memory, but also in other logic circuits, see e.g. [11] for a formal overview. Even though representing well-understood and widely established semiconductor technology, the tunnel diodes remain further in focus of investigations in conjunction with unique current-voltage characteristics and associated properties. For instance, the resonant tunneling diodes in oscillating circuits are used for the strain detection and, therefore, as sensing elements [12].

In the recent work, we fall back on the strongly pronounced nonlinear current-voltage characteristics of a tunnel diode, and with associated multiple equilibria, correspondingly, nontrivial trajectories in the state-space. Due to its negative differential resistance, the diode's nonlinear behavior has two stable operating points for the same current response, cf. Fig. B.6 further in Section B.4. These characteristics, combined with standard diode behavior as an ultra-fast heterostructure device, allows it to be used in circuits as a storage element with bistable output voltage, *low* and *high*, and fast switching transients between both. Switching between the two states can be accomplished by a pulse signal added to the required voltage offset (bias). Such a nonlinear circuit with tunnel diode and output voltage to be controlled has been shown in our previous work [13], while representing a reach-on-dynamics nonlinear system with hybrid behavior. While this type of circuits is well-known and described in the literature on nonlinear systems, see e.g. [14], our focus is also on the experimental design, identification, and analysis under real measurements, accessibility and controllability of the system states, and hybrid, i.e. mixed continuous

and discrete, system consideration.

It is important to state that hybrid systems are ubiquitous and one sees and interacts with them on a daily basis [15, 16, 17]. Dealing with hybrid systems means adding complexity to the system description, which makes it harder to be analyzed and formally verified [18, 19, 20] in terms of the specified properties and desired features. While proofing concepts with prototypes provide the most reliable results, they are also the most costly, safety critical, and time consuming. Therefore, a verification via formal numerical tools is highly desirable in system and within control engineering. Different tools are available, see e.g. references in [21, 22, 23, 24, 25, 15], and that for different classes of hybrid systems, depending on their modeling paradigm, computational requirements, and case-specific applications. The PWA formalism, mentioned above, provides one of the apparently prosperous ways for hybrid (control) system modeling and analysis.

In the recent work, the nonlinear diode characteristics are piecewise linearized so that the entire circuit dynamics are brought into the PWA form. Previously, a standard numerical simulation of the identified analytic model would be compared with measurements carried out on the developed experimental setup. After evaluating and analyzing the controlled closed-loop behavior of a nonlinear circuit, a formal analysis of the designed PWA system is also shown. In this work we use the PWLTool [26], as suitable for dealing with the PWA system dynamics. The rest of the paper is organized as follows. In Section 2, we summarize the modeling of the nonlinear circuit with a tunnel diode. The designed and assembled experimental setup with measuring and controlling devices are described in Section 3. The experimental identification of the diode characteristics is shown in Section 4. Section 5 deals with the transient response analysis of the system. Section 6 introduces the state feedback control with reference-dependent limit cycles, and shows the corresponding simulation and experimental results. Piecewise affine formulation of our system is introduced in Section 7, while Section 8 deals with formal verification case. Finally, Section 9 summarizes the paper.

## B.2 Modeling of Nonlinear Circuit

The system to be modeled, identified correspondingly, is based on a nonlinear electric circuit known from the literature, cf. Chapters 1-2 of [14]. Besides the tunnel diode, the energy storage elements, i.e. capacitor and inductor, are involved equally as a resistive element and a voltage source. Assuming the capacitor and inductor to be LTI (linear time-invariant) elements, their behavior is given by eqs. (B.1) and (B.2). Here  $i$  and  $v$  are representing the current and voltage across the capacitor and inductance respectively, while  $C$  and  $L$  represent the capacitance and inductance constants. We define the voltage

across the diode  $v_D$  (correspondingly capacitor  $v_C$ ) as the state variable  $x_1$ , while  $x_2$  is the state variable representing the current  $i_L$  flowing through the inductance, correspondingly resistor. The voltage source will be referred to as  $u$ , thus constituting the controllable input of the whole system.

In order to derive the dynamics equations, the Kirchoff's law is applied to the junction point between the tunnel diode, capacitance and inductance, eq. (B.3). Knowing the nonlinear characteristics of the tunnel diode as a function of the voltage state  $h(x_1)$ , we obtain the expression (B.4). Substituting (B.1) into (B.4) we obtain the first dynamic state equation (B.6). By applying the Kirchoff's first law to the circuit and keeping in mind the assignments made above, we obtain eq. (B.5). Now we substitute (B.2) into (B.5), resulting in the second dynamic state equation (B.7). It is evident that the obtained state-space model (B.6), (B.7) contains the tunnel diode nonlinearity in feedback, that cannot be directly decoupled since being unmatched with the control value  $u$ .

$$i_C = C \frac{dv_C}{dt} \quad (\text{B.1})$$

$$v_L = L \frac{di_L}{dt} \quad (\text{B.2})$$

$$i_D = i_L - i_C \quad (\text{B.3})$$

$$i_C = -h(x_1) + x_2 \quad (\text{B.4})$$

$$v_L = -x_1 - Rx_2 + u \quad (\text{B.5})$$

$$\dot{x}_1 = \frac{1}{C}[-h(x_1) + x_2] \quad (\text{B.6})$$

$$\dot{x}_2 = \frac{1}{L}[-x_1 - Rx_2 + u] \quad (\text{B.7})$$

### B.3 Experimental Setup

An experimental setup, described by the model (B.6)-(B.7) and therefore approaching the circuits analyzed in [14], has been designed and instrumented. However, the values for  $R$ ,  $C$  and  $L$  have been chosen slightly different from [14], due to availability of the laboratory components, see Table B.1.

For the tunnel diode, a vintage diode from General Electric of the type 1N3716 [27] was chosen, with the characteristic values provided in Table B.2, as available from the manufacturer data sheet; the corresponding points are also depicted further in Fig. B.6. All electrical components have been set up on a standard bread board. As interface between the development computer and experimental setup, a dSpace MicroLabBox [28] has been used as a real-time board, with standard BNC-connectors for analog signals. The control output voltage is limited by  $\pm 10V$ , and the maximal output current by  $8mA$  correspondingly. The 16bit D/A and A/D converters, with the settling time of  $1\mu s$ ,



Table B.1: Circuit components' values

component	reference values [14]	designed setup values
R	1.5k $\Omega$	1.5k $\Omega$
C	2pF	12pF
L	5 $\mu$ H	4.7 $\mu$ H

onboard. An output channel of the MicroLabBox serves as the input  $u$  to the system, and

Table B.2: Diode characteristic points [27]

Static characteristics	symbol	value
Peak Point Current	$I_P$	4.7mA
Valley Point Current	$I_V$	0.6mA
Peak Point Voltage	$V_P$	65mV
Valley Point Voltage	$V_V$	350mV
Forward Voltage	$V_{FP}$	500mV
Forward Current	$I_{FP}$	4.7mA

is provided via the analog port. However, due to the limited output current, the circuit is energized through an auxiliary operational amplifier (OP), of type LM324AN [29], and that in a voltage follower configuration with ability to supply up to 30mA. In the voltage follower configuration the OP has a unity input-output gain. Three different signals have been measured, namely the voltage across the diode  $x_1$ , the input voltage to the circuit  $u$ , and the current through the inductor  $i_L$ . In order to measure the current, a shunt resistor of 1 $\Omega$  has been added in series to the inductance. The image of the above described setup is shown in Fig. B.1.

While initially using the dSpace MicroLabBox, in the later control experiments, the real-time platform has been switched to the Speedgoat board, baseline model S [30] with the IO183 interface card [31]. This hardware allows to operate the system with a sampling rate of 2kHz. Furthermore, it supports 8 single-ended or 4 differential analog channels with a 16bit A/D and D/A converter. Input voltages of  $\pm 10V$  and outputs of 0 – 5V are supported with a maximum output current of 5mA. The designed OP has been configured

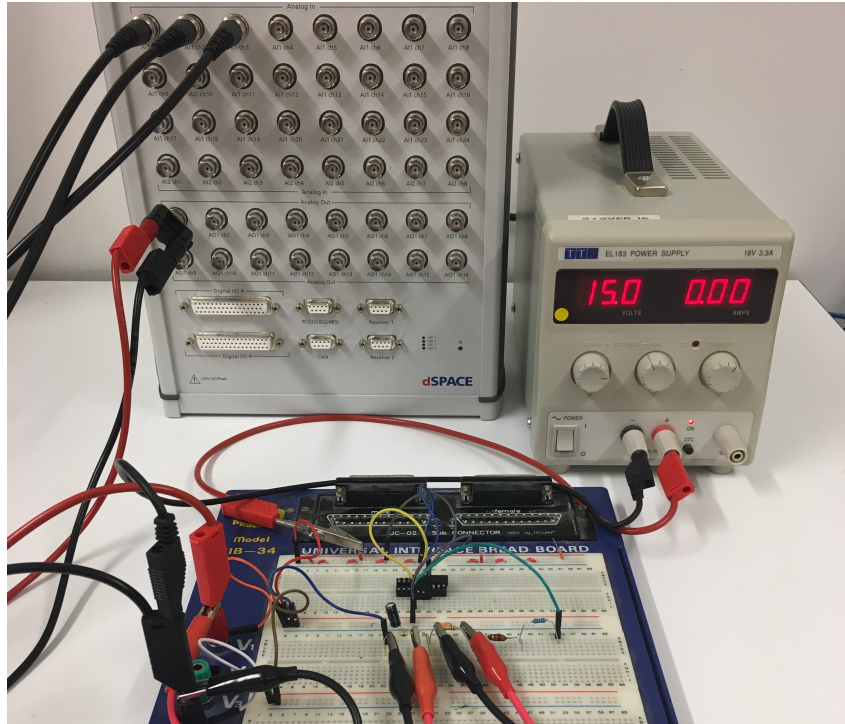


Figure B.1: Laboratory experimental setup of circuits with amplifier unit and real-time control board

as a differential amplifier (see Fig. B.2) which output voltage is given by

$$V_{out} = -\frac{R_2}{R_1}(V_1 - V_2). \quad (\text{B.8})$$

By connecting  $V_1$  and the open end of  $R_2$  to the ground, one obtains positive output voltage for positive  $V_2$  values, with the  $R_2/R_1$  gain. The gain has chosen to be 3.03, with  $R_1 = 330k\Omega$  and  $R_2 = 1M\Omega$ , that ensures to reach maximum output voltage, while the supply voltage is  $\pm 15V$ . By introducing a physical gain of 3.03, it is possible to

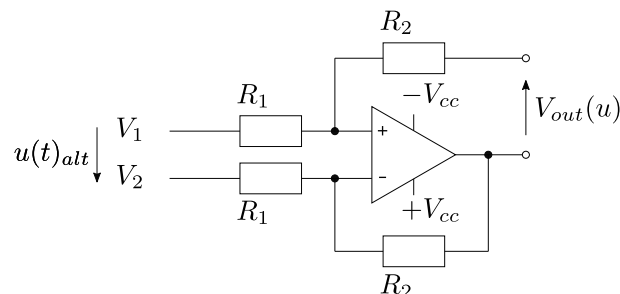


Figure B.2: Differential operational amplifier

stay within  $0 - 5V$  output voltage range of the real-time interface. Though, whenever referring to  $u$  we will always refer to the unaltered control signal, while the modified one (divided by OP gain) is referred to as  $u_{alt}$ . Applying all these hardware modifications to

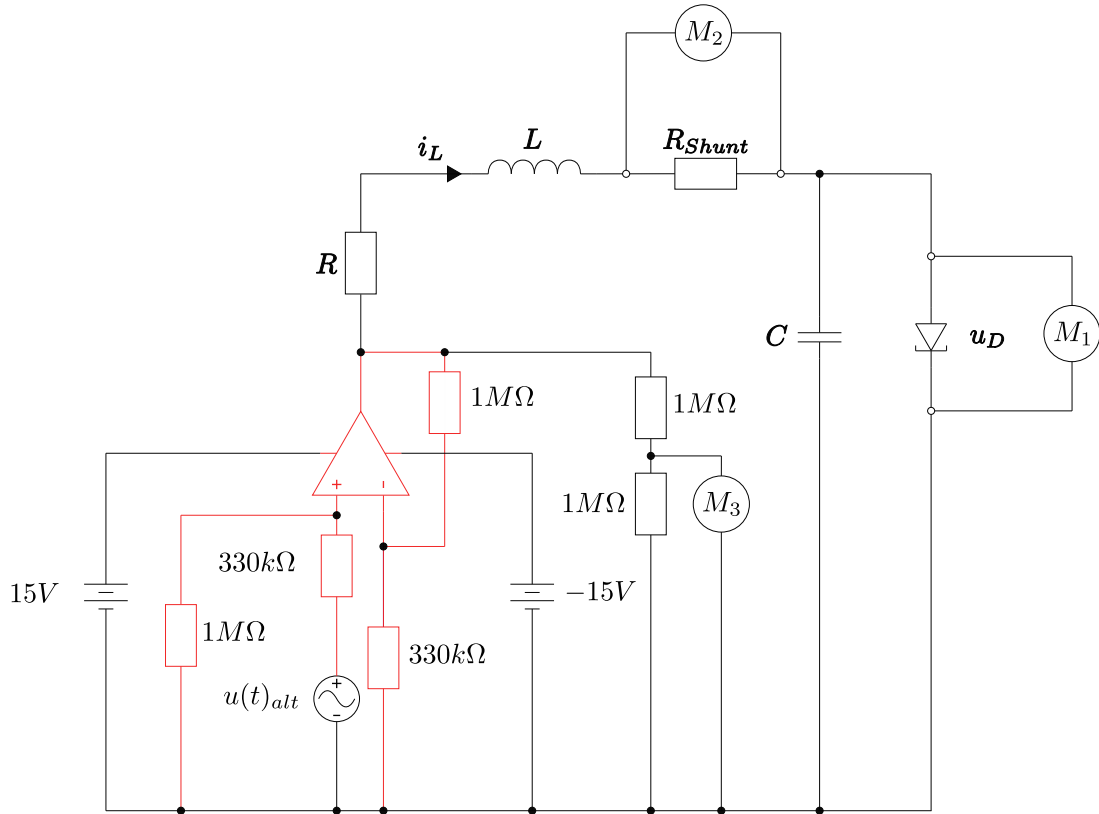


Figure B.3: Circuit diagram of experimental setup including differential operational amplifier (red) and measurement points

our physical setup, the layout of the experimental system results in the circuit diagram as shown in Fig. B.3. Here the points of measurement are indicated by  $M_x$ .

## B.4 Identification of Diode Characteristics

For  $h(x_1)$  mapping, cf. eq. (B.6), the diode characteristics have been identified from the measurements. Recall that the diodes' data-sheet has been limited to three characteristic points. Therefore, the setup from Fig. B.3, has been temporary disconnected in such a way that  $L$ ,  $C$ , and  $R$  elements are disabled. This configuration allows measuring the voltage across the diode, and the total flowing current through the shunt resistor in series with the diode. This circuit, dedicated for  $u_D$ - $i_D$  characteristics measurement, has been set in a closed-loop control configuration with an integrator, making sure that the diodes' voltage follows the desired reference closely. As a reference, a sinusoidal wave has been used. The diodes' voltage and current have been measured for three different configurations of the integrator gain and sinusoidal parameters, as listed in Table B.3. For each configuration, a total of 10 trials have been recorded, each one containing at least 10 periods of the sinusoidal wave. In Fig. B.4, one measurement from the  $EM.2$

Table B.3: Diode characteristic measurement configurations

Configuration	EM.1	EM.2	EM.3
Sine amplitude	0.25V	0.25V	0.25V
Sine offset	0.25V	0.25V	0.25V
Sine frequency	5Hz	10Hz	100Hz
Integrator	100	100	5000

configuration is shown as an example, with the voltage above and corresponding current below.

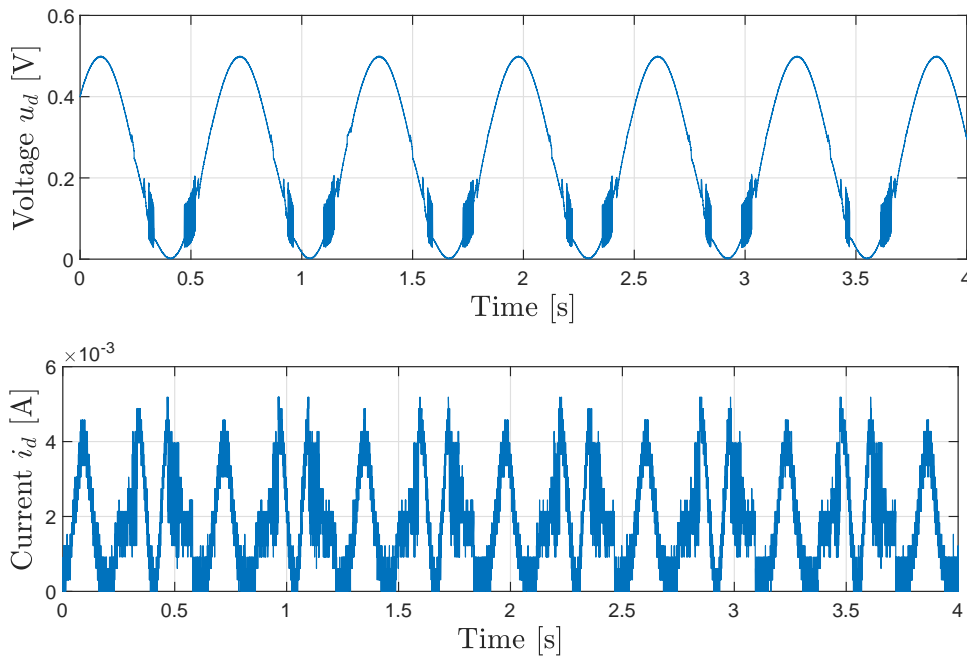


Figure B.4: Measured diode data: raw voltage measurement above and raw current measurement below

The raw data showed that the measurements have to be processed first before being suitable for extracting the stationary characteristics. While the voltage across the diode contains only some minor noise, the current measurement contains noise to a larger extent, which is mainly due to a low signal to noise ratio. Therefore the signals have to be cleaned up during the signal processing. For preliminary signal analysis, a fast Fourier transformation (FFT) has been performed, see Fig. B.5, so as to highlight the frequency components of both signals. While the first reference peak is dominant in the measured voltage, the spectrum of the diode current has multiple non-negligible distortions, clearly pointing on the nonlinear transfer characteristics of the diode circuit. An FIR (Finite

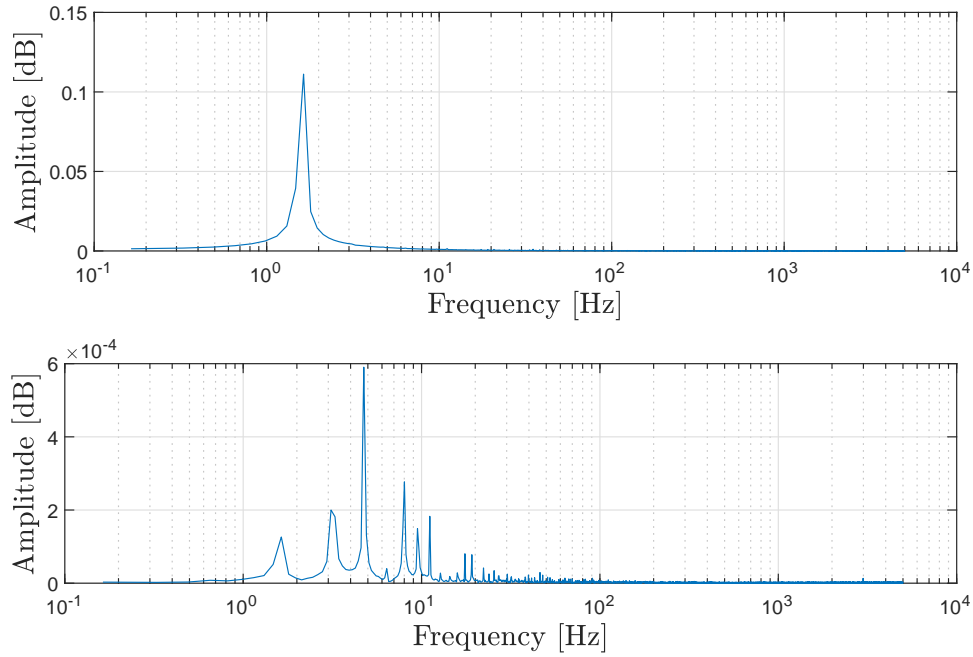


Figure B.5: FFT transformed diode measurements: voltage spectrum above and current spectrum below

Impulse Response) low-pass filter has been applied to both signals. The signals have been also cut to the full periods, so as to avoid the initial deviation from the reference signal due to the filtering. All periods from all measurements have been averaged, within an equidistant sampling with  $1mV$  step. As a result, a sufficient number of points between  $0V$  and  $0.5V$  have been obtained to describe the diodes' characteristic curve. Finally, the characteristic curve has been shifted to start at  $0V$  since an additional voltage drop, due to shunt, provides a certain minor bias deteriorating the diodes' characteristics.

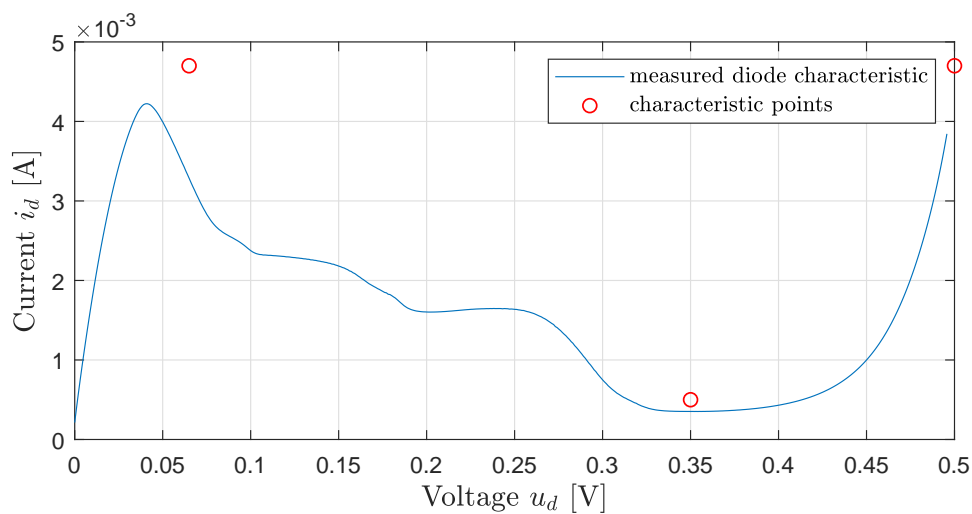


Figure B.6: Diode characteristic measurement including characteristic points from datasheet

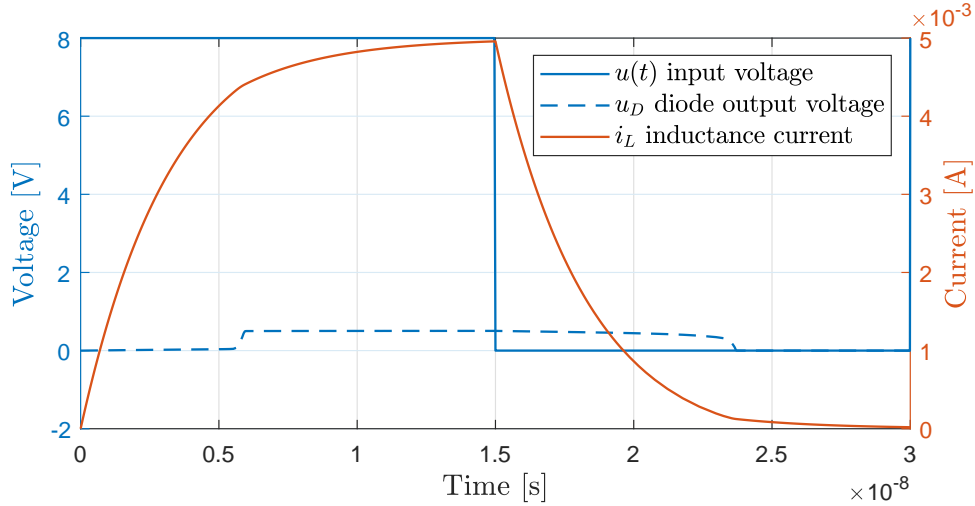


Figure B.7: Numerically simulated transient response of the circuit with parameter values from Table B.1

After processing all measurements in the same way, the resulting characteristic curves for *EM.1-EM.3* configurations have been compared opposite to each other and to characteristic points from the data sheet. The data distribution within each configuration has been analyzed and it has been found that the data variance is negligible. The identification results from *EM.2*, shown in Fig. B.6, have been selected as closest to the generalized characteristics, known from the literature, and to the characteristic points provided by the manufacturer.

## B.5 Analysis of Transient and Steady-State Response

The transient response and, in particular, time constants of the modeled circuit were qualitatively analyzed by applying square pulse signals as input to the numerical simulation. The (output) diode voltage and the total current, i.e.  $x_1$  and  $x_2$ , are shown in Fig. B.7, together with the input voltage  $u$ , and for parameter values from Table B.1. From the simulation, the response times were in the range of several nanoseconds. Neither of the real-time boards at our disposal operate at this time scale and, hence, capture the transient phases of the circuit. Therefore, other inductor and capacitor elements with different  $C$ ,  $L$  values, as those who mainly determine the time constant, have been tested as listed in Table B.4. Both, simulations and measurements have been performed for all three configurations from Table B.4. The results are shown opposite to each other in Fig. B.8. Based on that, the *V.3* configuration of  $R$ ,  $C$ ,  $L$  elements has been selected for further use, as the one with a slowest transient response and, correspondingly, largest number of the samplings captured at the stepwise excitation.

Table B.4: Component values for rise time simulation

Component	V.1	V.2	V.3
R	1.5k $\Omega$	1.5k $\Omega$	1.5k $\Omega$
C	12pF	22 $\mu$ F	47 $\mu$ F
L	4.7 $\mu$ H	1mH	1mH

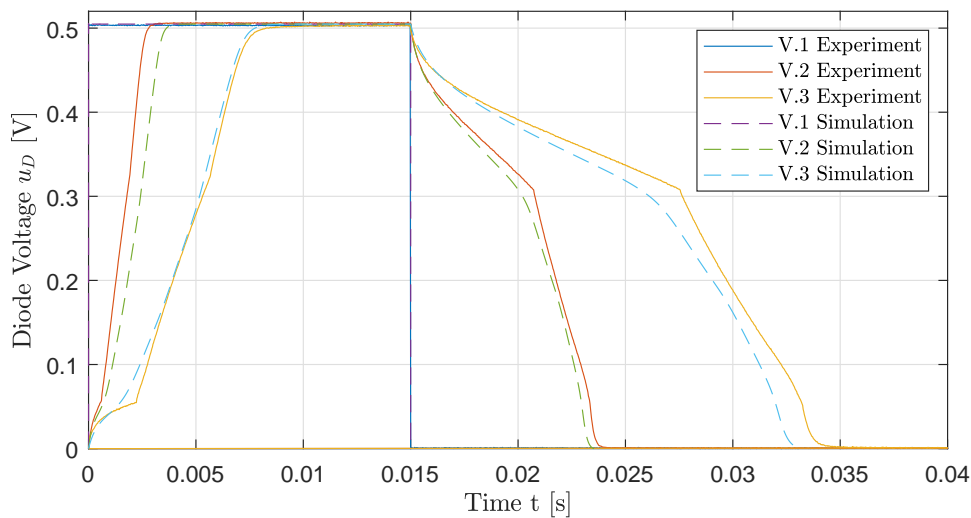


Figure B.8: Simulation and experiment of the circuit pulse response for different  $R$ ,  $C$ ,  $L$  values, as in Table B.4

A frequency sweep has been simulated in order to obtain the frequency response function (FRF) of the system as whole, shown in Fig. B.9. A noticeable decrease in both, magnitude and phase starts first around  $100\text{Hz}$ . The simulation is based on the entire circuit as shown in Fig. B.3, i.e. with OP in a voltage follower configuration, by using National Instrument Multisim 14.0. However, a slightly different type of the tunnel diode 1N3716 has been taken here, as available in the simulation libraries, instead of the actual one of the type 1N3715. From our system modeling containing two integrators, a maximum phase shift by  $-180^\circ$  is expected. Yet from the shown FRF, the phase goes far beyond  $-180^\circ$  at higher frequencies. This can be attributed to the high-frequency behavior of the OP incorporated into the Multisim simulation. Note that all further tests and simulations are limited to the input signal frequencies below  $10\text{Hz}$ , thus without additional phase lag produced by the residual circuit elements, like OP, which are not implicitly incorporated into our modeling.

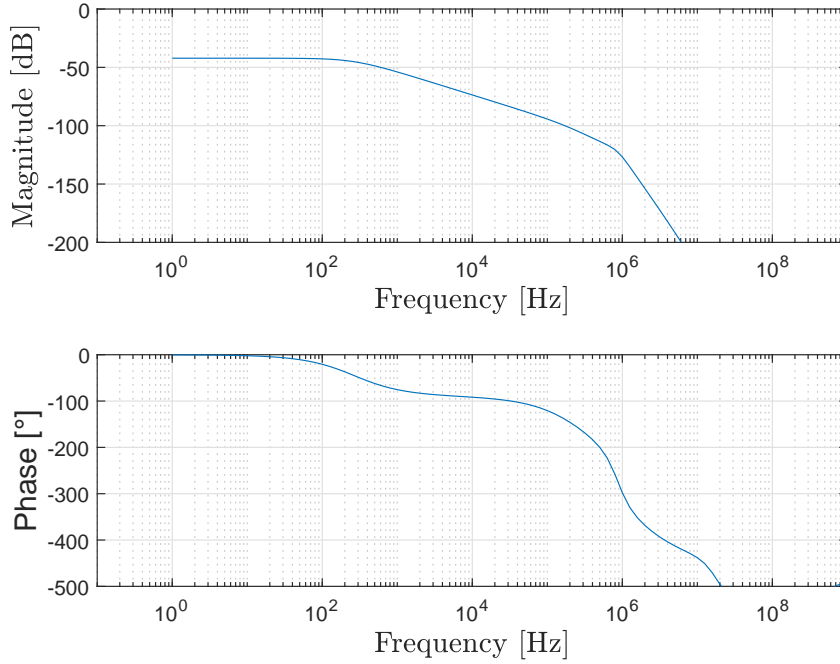


Figure B.9: Simulated FRF of the entire circuit

## B.6 Controlled Closed-loop Behavior of Circuit with Reference-dependent Limit Cycles

In this Section we are investigating the controlled behavior of the circuit at different reference levels and different regions of the state-space when applying an integral-state-feedback control. Our purpose is to demonstrate a qualitatively different closed-loop response of the nonlinear system, depending on the operational subspace, with one and the same state-feedback controller which also uses entirely available system state information.

### B.6.1 Integral-State-Feedback Controller

In order to ensure that the system follows the reference we designed an integral-state-feedback controller of the form

$$u = -\mathbf{k}^T \mathbf{x} = - \begin{pmatrix} k_1 & k_2 & k_i \end{pmatrix} \begin{pmatrix} x_1 \\ x_2 \\ x_3 \end{pmatrix}, \quad (\text{B.9})$$

Note that an auxiliary state  $x_3$  is introduced as output of the integrator of the tracking control error. The  $k_1, k_2, k_i > 0$  are the state feedback gains and the control design parameters. Substituting (B.9) into (B.7) and adding one more differential equation for



the new state results in the extended state space model of closed control loop

$$\dot{x}_1 = \frac{1}{C}[-h(x_1) + x_2], \quad (\text{B.10})$$

$$\dot{x}_2 = \frac{1}{L}[-x_1 - Rx_2 - k_1x_1 - k_2x_2 - k_ix_3], \quad (\text{B.11})$$

$$\dot{x}_3 = x_1 - r, \quad (\text{B.12})$$

that describes the controlled dynamics of the system. Here  $r$  is the reference value for the output voltage under control.

In the following, a square pulse signal of different amplitudes is applied as a reference. The amplitudes correspond to the three different levels, respectively regions in the state-space, which are of interest to distinguish. All parameters, for simulation and subsequent experiments, are listed in Table B.5. The control gains have been tuned within the simulation and experiment, also taking into account the control signal constrains, i.e. actuator saturations.

Table B.5: Closed-loop system parameters

Parameter	Value
Pulse Amplitude	0.025V
	0.2V
	0.5V
Pulse width	50%
R	1.5kΩ

Parameter	Value
C	47μF
L	1mH
$k_i$	30000
$k_1$	10
$k_2$	5

## B.6.2 Simulation Results

Figure B.10 shows the simulated controlled system response to the reference pulse of the 0.025V amplitude. The state  $x_1$  follows exactly the reference signal at steady-state and discloses transients without overshoot, oscillations, or additional time delays.

Figure B.11 above shows the output (diode) voltage for the 0.2V reference. One can see that the controlled system does not converge to the reference value and ends up in a sustained oscillatory behavior, i.e. limit cycle. It becomes further traceable when inspecting the corresponding phase portrait in Fig. B.11 below, plotted in the state coordinates. Starting from the initial state (0, 0) (blue arrow on the left) one can follow the repeatable, i.e. steady-state, cycle along the blue arrows as long as the reference remains constant,  $r = 0.2V$ . Afterwards, the trajectory follows one transient cycle, indicated by the red arrows, until reaching zero equilibrium at  $r = 0V$ .

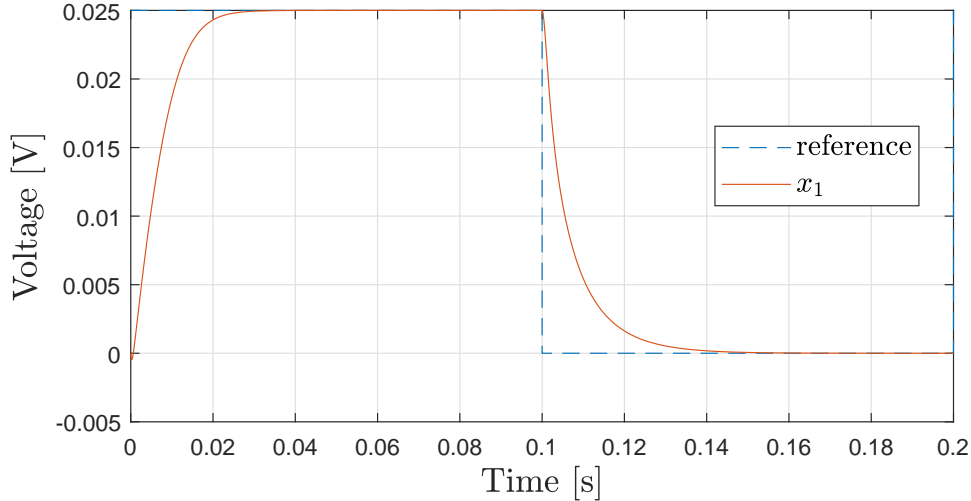


Figure B.10: Simulated closed-loop response of the output voltage  $x_1$  to the  $0.025V$  reference

When increasing the reference level to  $0.5V$ , it is possible to observe the closed-loop behavior as shown in Fig. B.12. There are no limit cycles present, and the controlled output voltage again reaches the steady-state reference after a certain transient overshoot. This closed-loop system behavior can be seen as largely acceptable, in terms of the control design, comparing to that shown for  $r = 0.025V$  in Fig. B.10 in particular since both reference amplitudes differ by the factor 20.

The above results clearly indicate that the same controller performs satisfactory at the low and high reference levels, but can lead to rather unexpected, in this case parasitic, limit cycles in between. This scenario, due to the nonlinear characteristics of the plant under control, highlights the problem of piecewise affine system dynamics and challenges posed on the tools for analysis.

### B.6.3 Experimental Results

The experimental evaluation of the control scenarios, shown and analyzed above, has been performed with the same parameters, cf. Table B.5, and double runtime for the sake of testing reproducibility of the results. Real-time measurements were taken with  $2kHz$  sampling rate. All signals displayed below are raw, i.e. unprocessed, except for the phase portrait, for which the signals have been FIR filtered. This is done for the sake of a better visualization for the measured current, which is otherwise subject to relatively high noise components.

In Fig. B.13, the measured system response to the  $0.025V$  reference is shown. The results are very close to the simulated one in both transient and steady-state, cf. with Fig. B.10.

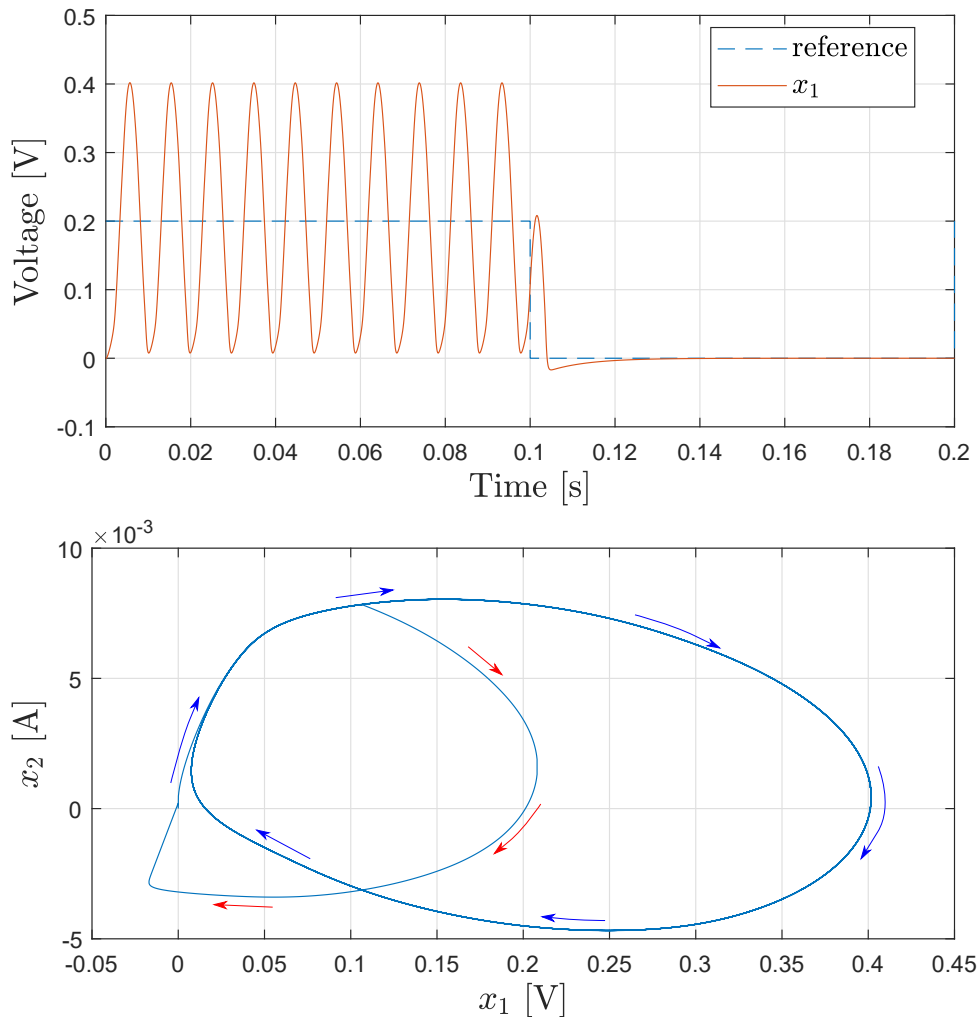


Figure B.11: Simulated closed-loop response to the 0.2V reference: output voltage above and phase portrait below

Reviewing the experimental system response to the 0.2V reference, shown in Fig. B.14, one can see certain differences to the simulation, cf. Fig. B.11, especially in the shape and period of the limit cycles. One should note that in the simulation, the control signal  $u$  varies between around 12V and  $-6$ V, while our experiment allows for positive control voltages only. Nevertheless, the appearance and principle shape of the stable limit cycles are experimentally confirmable, as can be seen in the lower part of Fig. B.14.

Finally, the response to the 0.5V reference has been measured, as shown in Fig. B.15. The principle closed-loop behavior coincides with the simulation, cf. with Fig. B.12, while the transients slightly differ – mainly due to the control unipolarity and saturations in the real system, and the related wind-up of the integral control action.

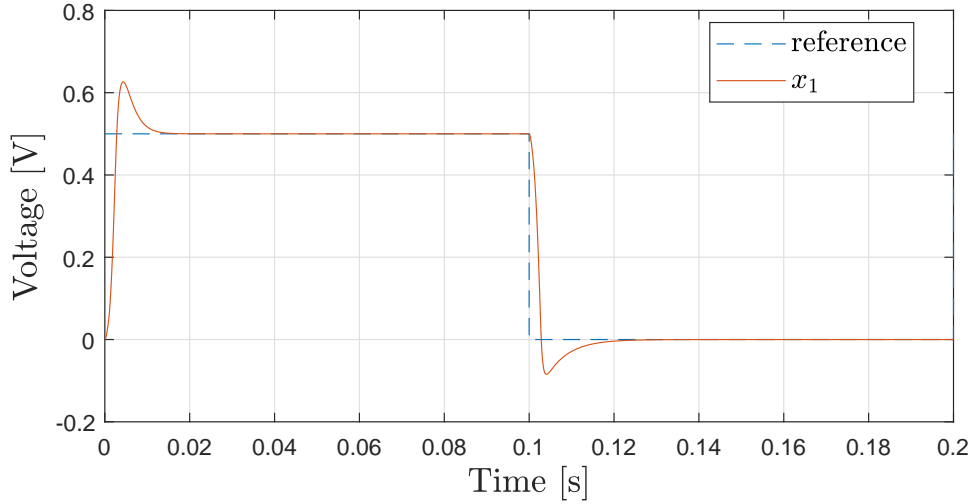


Figure B.12: Simulated closed-loop response of the output voltage  $x_1$  to the  $0.5V$  reference

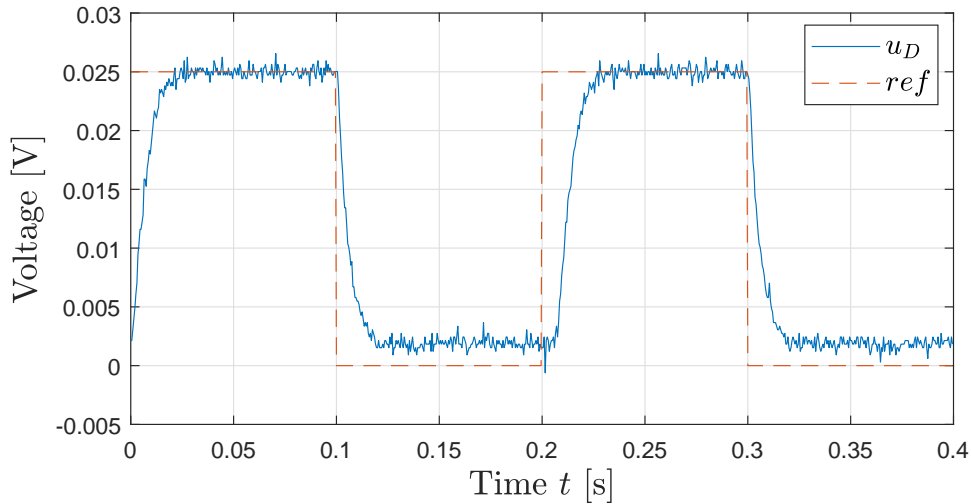


Figure B.13: Measured closed-loop response of the output voltage  $x_1$  to the  $0.025V$  reference

## B.7 Piecewise Affine (PWA) Model Formulation

For the purpose of further analysis and compatibility to formal verification methods and tools, our system model is further transformed into a PWA form, cf. Section B.1. In order to do so, the diodes' characteristics are first linearized as shown in Fig. B.16. This results in the total of four cells within the state-space with the corresponding boundaries denoted by  $W_1$  to  $W_3$ , cf. Fig. B.16 and Table B.6.

In order to transfer the nonlinear state dynamics into the PWA form, the diode characteristics  $h(x_1)$  can be approximated by  $k_n x_1 + d_n$ , where  $n$  is the cells' index. Furthermore, eqs. (B.10), (B.11) and (B.12) have to be converted into the PWA state-space notation

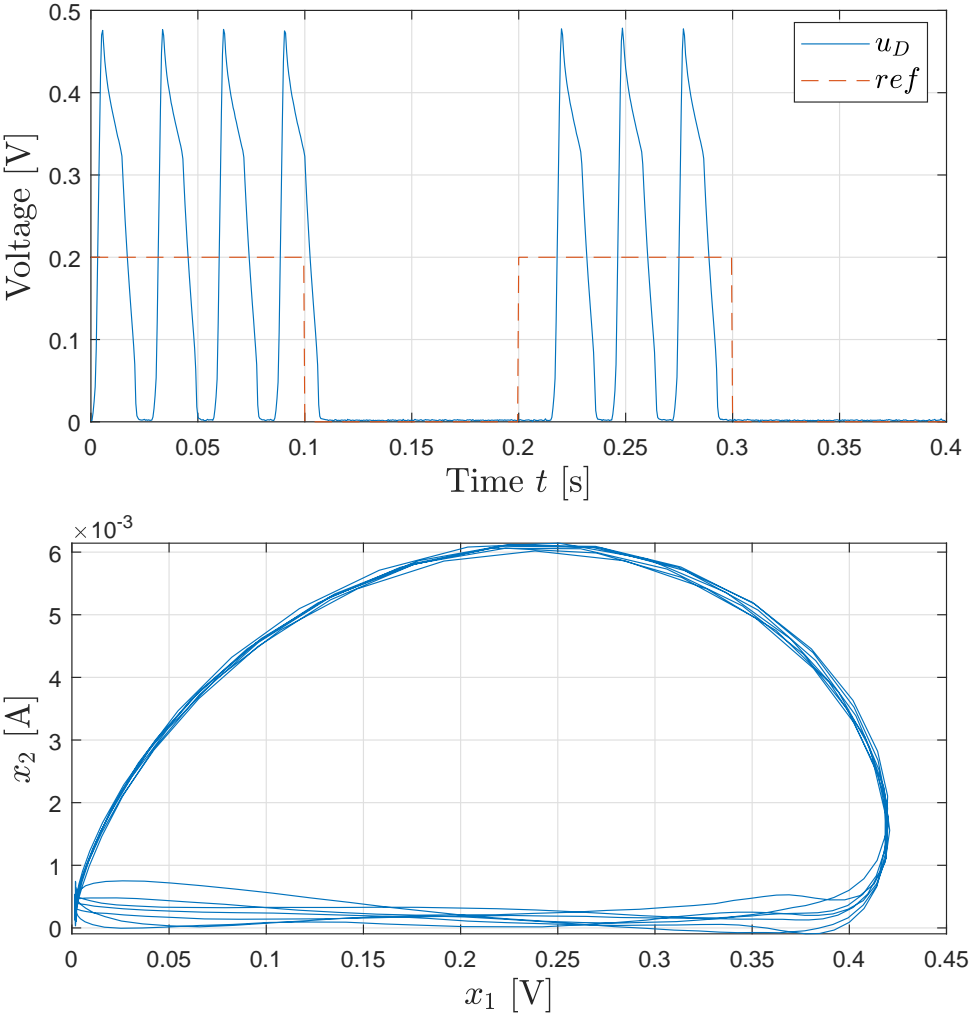


Figure B.14: Measured closed-loop response to the 0.2V reference: output voltage above and phase portrait below

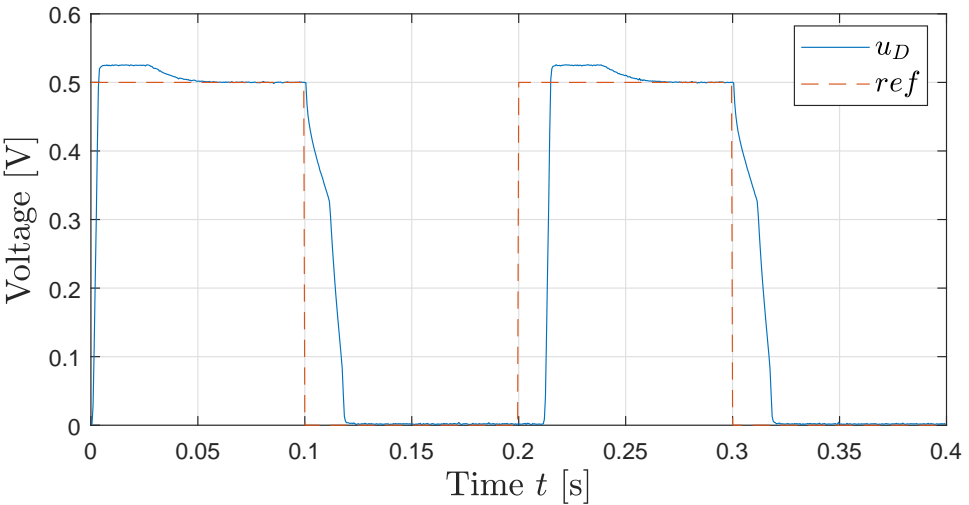


Figure B.15: Measured closed-loop response of the output voltage  $x_1$  to the 0.5V reference

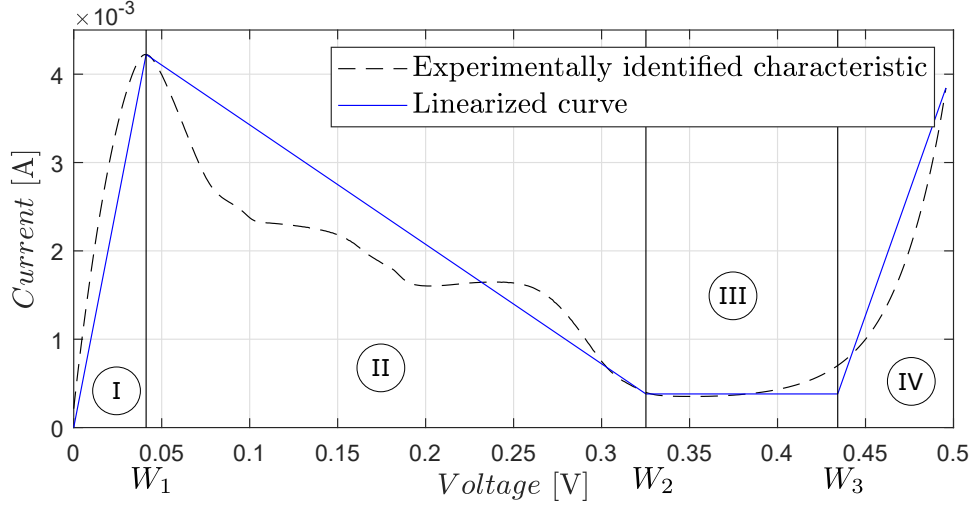


Figure B.16: Linearization of the diode characteristics

Table B.6: Cells and boundary constants of piecewise affine model

Cell	$k_n$	$d_n$
I	0.1026	0
II	-0.0135	0.048
III	0	0.0004
IV	0.0563	-0.0241

Variable	Value
$W_1$	0.0411
$W_2$	0.3252
$W_3$	0.4342

of the form

$$\dot{\mathbf{x}} = \mathbf{A}\mathbf{x} + \mathbf{b}r + \mathbf{f}, \quad (\text{B.13})$$

$$y = \mathbf{c}\mathbf{x}, \quad (\text{B.14})$$

with the system matrix

$$\mathbf{A} = \begin{pmatrix} -\frac{k_n}{C} & \frac{1}{C} & 0 \\ -\frac{1+k_1}{L} & -\frac{R+k_2}{L} & -\frac{k_i}{L} \\ 1 & 0 & 0 \end{pmatrix}, \quad (\text{B.15})$$

and input and output distribution vectors

$$\mathbf{b} = \begin{pmatrix} 0 \\ 0 \\ -1 \end{pmatrix}, \quad (\text{B.16})$$

$$\mathbf{c} = \begin{pmatrix} 1 & 0 & 0 \end{pmatrix}, \quad (\text{B.17})$$

correspondingly. The affine term is captured by

$$\mathbf{f} = \begin{pmatrix} -\frac{d_n}{C} \\ 0 \\ 0 \end{pmatrix}, \quad (\text{B.18})$$

and the full-state vector  $\mathbf{x} = (x_1, x_2, x_3)^T$  is the same as defined in Section B.6. The determined cells and boundary constants  $k_n$ ,  $d_n$ , and  $W_j$  are given in Table B.6.

For completely defining the PWA model, the identified cells should be equally described in a matrix form. We first extend the state vector so as to allow for the bias terms as

$$\mathbf{x}_A = \begin{pmatrix} \mathbf{x} \\ 1 \end{pmatrix} \quad (\text{B.19})$$

and, then, introduce the cells matrix  $\mathbf{G}_n$  which satisfies

$$\mathbf{G}_n \mathbf{x}_A \succeq 0 \quad (\text{B.20})$$

if and only if  $\mathbf{x} \in \mathbf{X}_n$ . Note that  $\{\mathbf{X}_n\}_{n=I, \dots, IV} \subseteq \mathbb{R}^3$  represents the set of polyhedral cells, with pairwise disjoint interior, which divide the entire state-space in the so-called modes of the system dynamics, correspondingly trajectories. Further we note that  $z \succeq 0$  has meaning that all entries of  $z$ -vector are non-negative. Therefore, the inequality condition (B.20) governs which part of the state-space is described by each matrix, also defining the outer boundaries of the cells. For exemplification, consider the II-nd cell, i.e.  $n = II$ . The cell matrix is defined by

$$\mathbf{G}_{II} = \begin{pmatrix} 1 & 0 & 0 & -W_1 \\ -1 & 0 & 0 & W_2 \end{pmatrix}. \quad (\text{B.21})$$

Evaluating (B.20) one obtains the set of inequalities

$$x_1 \geq W_1, \quad (\text{B.22})$$

$$x_1 \leq W_2, \quad (\text{B.23})$$

which define the boundaries of the cell within the state-space. The residual cells are defined as follows:

$$\mathbf{G}_I = \begin{pmatrix} -1 & 0 & 0 & W_1 \end{pmatrix}, \quad (\text{B.24})$$

$$\mathbf{G}_{III} = \begin{pmatrix} 1 & 0 & 0 & -W_2 \\ -1 & 0 & 0 & W_3 \end{pmatrix}, \quad (\text{B.25})$$

$$\mathbf{G}_{IV} = \begin{pmatrix} 1 & 0 & 0 & -W_3 \end{pmatrix}. \quad (\text{B.26})$$

In addition, the auxiliary matrices  $\mathbf{E}_n$  have to be specified such that satisfying

$$\mathbf{E}_n \mathbf{x}_A = \mathbf{E}_m \mathbf{x}_A \quad (\text{B.27})$$

for  $\mathbf{x} \in \mathbf{X}_n \cap \mathbf{X}_m$ . This matrix equality defines pairwise the state values on the intersection between the cells. Note that the  $\mathbf{E}$ -matrices are not a part of a standard PWA system description itself and are merely used to parameterize Lyapunov functions and to provide computational aid in the system analysis such as stability, input output gain, etc, see [26] for more details. Consequently, the simulation with the PWLTool system does not require these matrices. For the sake of completeness, the auxiliary matrices are still defined as follows

$$\mathbf{E}_I = \begin{pmatrix} 0 & 0 & 0 & 0 \\ 1 & 0 & 0 & 0 \\ 0 & 1 & 0 & 0 \\ 0 & 0 & 1 & 0 \end{pmatrix} \quad (\text{B.28})$$

$$\mathbf{E}_{II} = \begin{pmatrix} 1 & 0 & 0 & -W_1 \\ 1 & 0 & 0 & 0 \\ 0 & 1 & 0 & 0 \\ 0 & 0 & 1 & 0 \end{pmatrix} \quad (\text{B.29})$$

$$\mathbf{E}_{III} = \begin{pmatrix} -1 & 0 & 0 & -W_1 + 2W_2 \\ 1 & 0 & 0 & 0 \\ 0 & 1 & 0 & 0 \\ 0 & 0 & 1 & 0 \end{pmatrix} \quad (\text{B.30})$$



$$\mathbf{E}_{IV} = \begin{pmatrix} 0 & 0 & 0 & -W_1 + 2W_2 - W_3 \\ 1 & 0 & 0 & 0 \\ 0 & 1 & 0 & 0 \\ 0 & 0 & 1 & 0 \end{pmatrix}. \quad (\text{B.31})$$

## B.8 Formal verification

The verification tool we use in this work is the PWLTool [26]. The recent purpose is to detect the limit cycles, observed in the simulation and experiments above, and an unstable system response as well, when e.g. changing the control parameters. The PWLTool-based simulation does not allow to input reference, correspondingly control, values. Therefore, the dynamic simulation scenarios should be captured by the initial state values. For the stepwise references, i.e.  $r = \text{const}$ , we incorporate it into the affine part of the PWA formulation, thus solely modifying the  $\mathbf{f}$  vector. While our numerical simulation (using the Simulink software) incorporates the identified characteristics of the tunnel diode, the PWLTool inherently uses the linearized characteristics only. Therefore, one can expect differences in the predicted state trajectories resulting from both simulations.

Figures B.17 to B.19 show the computed state trajectories, resulting from the Simulink- and PWLTool-based simulations. A qualitative accordance, especially in case of the stable limit cycles, can be observed for all three reference values, i.e.  $r = 0.025V$ ,  $r = 0.2V$ , and  $r = 0.5V$ .

Since a more detailed analysis i.e. concerning the Lyapunov stability, correspondingly finding and evaluating the Lyapunov function candidates, is out of scope in the recent work, the single (artificially forced) unstable response has been tested in terms of its prediction. For that purpose, a positive integral state feedback, i.e.  $k_i < 0$  has been assumed. All residual parameters have been kept with the same values as before. The simulation results are shown in Fig. B.20 where the trajectories, starting from zero initial state, continue towards infinity in direction indicated by the arrows.

## B.9 Conclusions

The model for a nonlinear electric circuit including the tunnel diode, based on [14], has been considered and identified in an experimental setup. System parameters for the

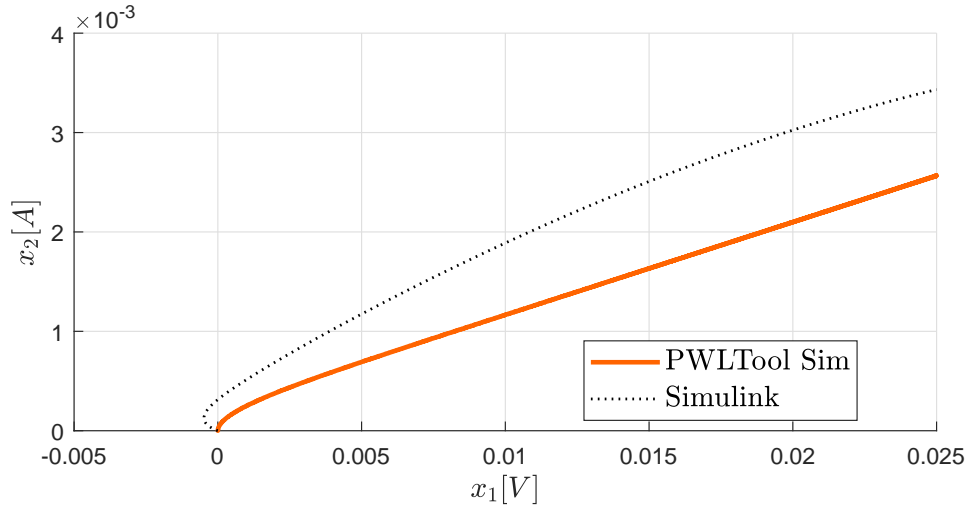


Figure B.17: Simulink and PWLTool trajectories for  $r = 0.025V$

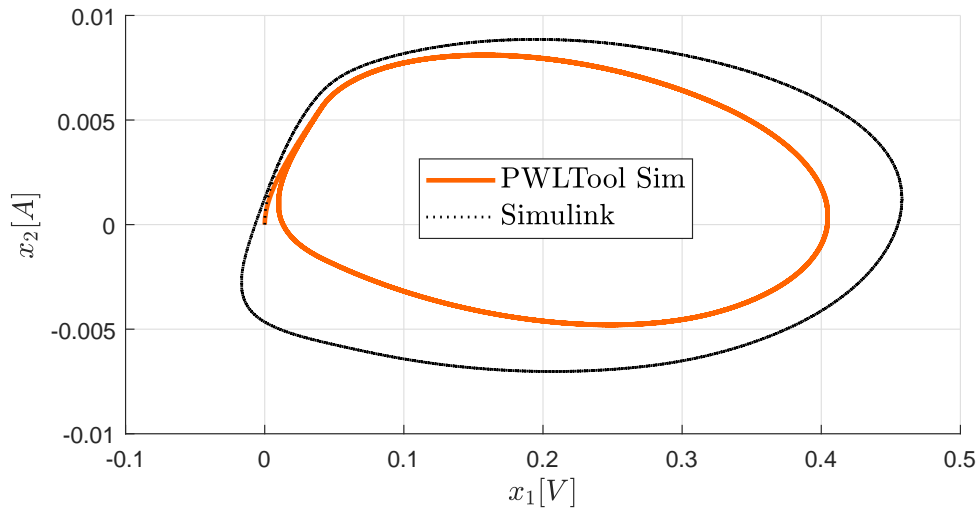


Figure B.18: Simulink and PWLTool trajectories for  $r = 0.2V$

linear components have been assumed from the data sheets and validated by experiments. The nonlinear characteristics of the tunnel diode have been determined from a series of dedicated measurements and compared to the principal shape given by the data sheet, including the available characteristic points. Furthermore, the steady-state and transient response of the system have been analyzed and showed a good accord between the model and experiment. A closed-loop system has been designed with a integral-state-feedback controller to which the pulsed signals with varying amplitudes have been applied leading to different steady-state and limit cycle behaviors. Simulations have been compared to measurements, showing a good accord in all scenarios. Residual differences between the simulation and experiments have been also discussed.

Beyond, the identified nonlinear model has been converted into the piecewise affine (PWA) notation, with a corresponding cells division and boundaries within the state-

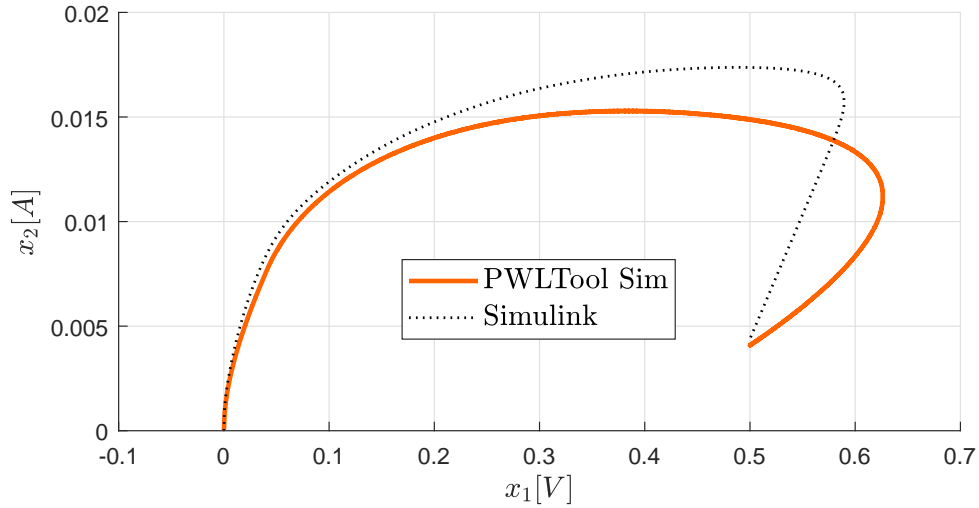


Figure B.19: Simulink and PWLTool trajectories for  $r = 0.5V$

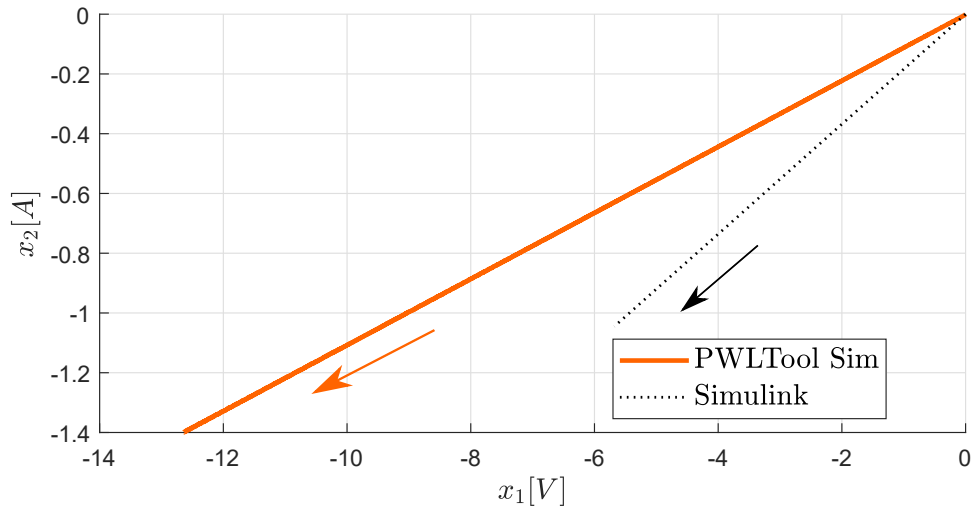


Figure B.20: Simulink and PWLTool simulated trajectories for an instable system with  $r = 0.2V$  and  $k_i = -30000$

space. A formal verification has been exemplary tested by using the PWLTool [26] and the predicted trajectories have been compared with those from the numerical simulation of the analytic model. Future works will be concerned with more detailed analysis of the designed PWA system in terms of stability and reachability analysis and hybrid system properties. Other available tools to be tested and deployed for formal analysis and verification are also under consideration.



# REFERENCES

- [1] E. Sontag. Nonlinear regulation: The piecewise linear approach. *IEEE Transactions on automatic control*, 26(2):346–358, 1981.
- [2] M. Johansson and A. Rantzer. Computation of piecewise quadratic Lyapunov functions for hybrid systems. *IEEE Transactions on Automatic Control*, 43(4):555–559, apr 1998.
- [3] M. Johansson. Piecewise Linear Control Systems. *PhD Diss., Lund Institute of Technology*, 1999.
- [4] A. Rantzer and M. Johansson. Piecewise linear quadratic optimal control. *IEEE transactions on automatic control*, 45(4):629–637, 2000.
- [5] L. Rodrigues and J. P. How. Observer-based control of piecewise-affine systems. *International Journal of Control*, 76(5):459–477, 2003.
- [6] P. Rostalski, T. Besselmann, M. Barić, F. V. Belzen, and M. Morari. A hybrid approach to modelling, control and state estimation of mechanical systems with backlash. *International Journal of Control*, 80(11):1729–1740, 2007.
- [7] Y. S, R. M, and F. H. Piecewise affine (PWA) modeling and switched damping control of two-inertia systems with backlash. In *IEEE 15th International Workshop on Advanced Motion Control (AMC2018)*, pages 479–484, 2018.
- [8] F. J. Christophersen. Piecewise Affine Systems. In *Optimal Control of Constrained Piecewise Affine Systems*, pages 39–42. Springer, 2007.
- [9] R. N. Hall. Tunnel diodes. *IRE Transactions on Electron Devices*, 7(1):1–9, jan 1960.
- [10] H. Sommers. Tunnel Diodes as High-Frequency Devices. *Proceedings of the IRE*, 47(7):1201–1206, jul 1959. doi:10.1109/JRPROC.1959.287351.
- [11] R. H. Bergman. Tunnel Diode Logic Circuits. *IRE Transactions on Electronic Computers*, EC-9(4):430–438, dec 1960.

- [12] T. Tajika, Y. Kakutani, M. Mori, and K. Maezawa. Experimental demonstration of strain detection using resonant tunneling delta-sigma modulation sensors. *Physica status solidi (A)*, 214(3):1600548, mar 2017.
- [13] P. Pasolli and M. Ruderman. Design and analysis of non-linear circuit with tunnel diode for hybrid control systems. In *IEEE 15th International Workshop on Advanced Motion Control (AMC2018)*, pages 181–186, 2018.
- [14] H. K. Khalil. Nonlinear Systems - Third Edition. *Journal of Climate J Clim Vol 18*, 18(16):750, 2002. doi:10.1016/j.physa.2006.08.011.
- [15] J. Lunze and F. Lamnabhi-Lagarrigue. *Handbook of hybrid systems control : theory, tools, applications*. Cambridge University Press, 2009.
- [16] R. Goebel, R. G. Sanfelice, and A. R. Teel. *Hybrid Dynamical Systems : Modeling, Stability, and Robustness*. Princeton University Press, 2012.
- [17] L. Hai and P. J. Antsaklis. *Hybrid Dynamical Systems: An Introduction to Control and Verification*. Now Publishers Inc, 2014.
- [18] R. Alur, T. A. Henzinger, and E. D. Sontag, editors. *Hybrid Systems III*, volume 1066 of *Lecture Notes in Computer Science*. Springer, 1996.
- [19] C. J. Tomlin, I. Mitchell, A. M. Bayen, and M. Oishi. Computational techniques for the verification of hybrid systems. *Proceedings of the IEEE*, 91(7):986–1001, 2003.
- [20] P. Tabuada. *Verification and control of hybrid systems: a symbolic approach*. Springer, 2009.
- [21] J. Bengtsson, K. G. Larsen, F. Larsson, P. Pettersson, and W. Yi. Uppaal – a tool suite for automatic verification of real-time systems. *Workshop on Verification and Control of Hybrid Systems III*, (1066):232–243, 1995.
- [22] T. A. Henzinger, P. H. Ho, and H. Wong-Toi. HyTech: A model checker for hybrid systems. *International Journal on Software Tools for Technology Transfer*, 1(1-2):110–122, 1997.
- [23] M. Bozga, C. Daws, O. Maler, A. Olivero, S. Tripakis, and S. Yovine. Kronos: A model-checking tool for real-time systems. In *International Symposium on Formal Techniques in Real-Time and Fault-Tolerant Systems*, pages 298–302. Springer, 1998.
- [24] E. Asarin, T. Dang, and O. Maler. The d/dt Tool for Verification of Hybrid Systems. *Computer Aided Verification*, 2404:746–770, 2002.

## REFERENCES

- [25] G. Frehse. PHAVer: algorithmic verification of hybrid systems past HyTech. *International Journal on Software Tools for Technology Transfer*, 10(3):263–279, 2008.
- [26] M. Johansson and S. Hedlund. PWLTool, a Matlab Toolbox for Piecewise Linear System. *Report TFRT*, 7582, 1999.
- [27] Elfa Distrelec. Tunnel Diodes, 2017.
- [28] dSpace. MicroLabBox - dSPACE, <https://www.dspace.com>, nov 2017.
- [29] T. Instruments. LM324AN Texas Instruments — Mouser Germany, <https://www.mouser.de/ProductDetail/Texas-Instruments/LM324AN>, nov 2017.
- [30] Speedgoat. Speedgoat - Rugged Baseline embedded controller for Simulink real-time, <https://www.speedgoat.com/products-services/real-time-target-machines/baseline>, apr 2018.
- [31] Speedgoat. Speedgoat - IO183: 16-bit analog input/output module with digital I/O, <https://www.speedgoat.com/products/io-connectivity-analog-io183>, apr 2018.





# Paper C

## Linearized Piecewise Affine in Control and States Hydraulic System: Modeling and Identification

Philipp Pasoli, Michael Ruderman

This paper has been published as:

P. Pasolli, M. Ruderman. Linearized Piecewise Affine in Control and States Hydraulic System: Modeling and Identification. *IECON 2018-44th Annual Conference of the IEEE Industrial Electronics Society*, pp. 4537-4544, 2018. doi: 10.1109/IECON.2018.8591572.

# Linearized Piecewise Affine in Control and States Hydraulic System: Modeling and Identification

Philipp Pasolli, Michael Ruderman

University of Agder

Department of Engineering Sciences

Jon Lilletunsvet 9, 4879 Grimstad, Norway

*Abstract* – In this paper, the modeling and identification of a nonlinear actuated hydraulic system is addressed. The full-order model is first reduced in relation to the load pressure and flow dynamics and, based thereupon, linearized over the entire operational state-space. The dynamics of the proportional control valve is identified, analyzed, and intentionally excluded from the reduced model, due to a unity gain behavior in the frequency range of interest. The input saturation and dead-zone nonlinearities are considered while the latter is identified to be close to 10% of the valve opening. The mechanical part includes the Stribeck friction detected and estimated from the experiments. The linearization is performed in multiple steps, for the most pronounced terms of nonlinear system dynamics. Out of this follows a linearized piecewise affine in the control and state model in a state-dependent matrix form. A series of measurements were performed on the designed and implemented experimental setup, while identifying uncertain parameters of the system, in addition to those obtained from the technical data and characteristics of components. The models behavior are compared with experimental measurements and discussed.

## C.1 Introduction

When it comes to applications demanding high power in relatively small form factor, hydraulic systems and actuators [1, 2] still remain the first choice. However, hydraulic systems are also known for their nonlinear behavior making it challenging for operation in the force control [3] and motion control [4] modes, and a hybrid combination of both e.g. [5]. Correspondingly, the control design, tuning, and evaluation require an advanced system knowledge and associated modeling and identification. One goal can be to create simplified models, mostly linearized around some operation points, e.g. [3, 6, 7, 8, 9]. On the other hand, more detailed modeling of the single hydraulic components, like a unified

one proposed for proportional valves in [10], requires yet an explicit knowledge of the mechanical assemblies and, mostly, an accurate identification of the internal states and characteristics, that is generally not feasible under regular operation conditions. Nevertheless, multiple system- and control-oriented studies considered

extended, to say full-order, system dynamics while incorporating the most pronounced nonlinearities nested within electrical, hydraulic, and mechanical subsystems of a hydraulic drive as a whole, see e.g. [11, 4, 5, 12]. A comparison between a full-order model and its reduced counterpart, including local linearization, has been recently shown in [13]. At the same time, a hybrid system consideration, and piecewise affine as one of the particularly handy subclasses of that, appears promising also for hydraulic systems over a large operation range. For more advanced studies on identification techniques for the hybrid systems we refer to [14, 15, 16].

In this paper, we assume the main sources of nonlinearities during the system modeling and introduce, based thereupon, a linearized piecewise affine in the control and states model of an actuated hydraulic cylinder supplied via a controlled servo valve. Recall that a general class of nonlinear systems affine in the control assumes a vector field state-space notation

$$\dot{\mathbf{x}} = f(\mathbf{x}) + g(\mathbf{x})u,$$

cf. [17], while the affine (linear with offset) state dynamics [18] requires from us inclusion of an additional constant vector term. We rely on a linearized piecewise affine formulation of a state-space model, while believing it can yield further advantages for the analysis and control design, also in spirit of the hybrid control systems [19, 20] and their computational, to say formal, verification [21]. It is worth noting that even without affine state dynamics, the affine (only in control) linear parameter-varying models are challenging as for structural identifiability and parameterizations [22]. For particular dynamic systems, i.e. valve-controlled hydraulic drives, we propose an approach for linearized piecewise affine modeling.

The rest of the paper is organized as follows. The paper starts with the full-order model in Section II, while taking the necessary steps of the model reduction in Section III. The state-space model, affine in both control and states, is formulated in Section IV, including the piecewise affine linearization at various points. In Section V the experimental setup is described. The parameter identification is shown in Section VI, and an evaluating comparison between the different models and data from the motion experiments is provided in Section VII. Lastly a brief summary is given in Section VIII.

## C.2 Full-Order Model

Below, the full-order model of the system is first described. We distinguish between modeling the valves characteristics, orifice equations, continuity equations, and mechanical sub-model of the hydraulic cylinder. Note that the full-order model can be directly derived from the basics on hydraulic systems to be found in the standard literature e.g. [1, 2].

### C.2.1 Servo Valve Approximation

The controlled servo valve can be approximated by a second-order dynamic system, with the spools' position  $\nu$  as output, so that the input-output transfer function is

$$G(s) = \frac{\nu(s)}{u(s)} = \frac{\omega_0^2}{s^2 + 2\zeta\omega_0s + \omega_0^2}. \quad (\text{C.1})$$

Here,  $\zeta$  is the damping coefficient and  $\omega_0$  is the natural frequency of the closed-loop dynamics. The external control signal is denoted by  $u$ . Values for  $\omega_0$  and  $\zeta$  are subject to variations, depending on the input amplitude  $|u|$ , as pointed out in the FRF (frequency response function) of the data sheets provided by the valves' manufacturer. According to the technical data sheet, the servo valve we consider has a 10% overlap in the spool-orifice area, thus, introducing a dead-zone. Furthermore, the valve is inherently limited in how far it can open, therefore being subject to an additional saturation. The combination of dead-zone and saturation nonlinearities can be described as in [13] by

$$h(\nu) = \begin{cases} \alpha \cdot \text{sign}(\nu), & \text{if } |\nu| \geq \alpha + \beta, \\ 0, & \text{if } |\nu| < \beta, \\ \nu - \beta \cdot \text{sign}(\nu), & \text{otherwise,} \end{cases} \quad (\text{C.2})$$

where the parameters  $\alpha$  and  $\beta$  are the valve saturation and dead-zone width, respectively. As the dead-zone is of a constructive, i.e. mechanical, nature, its transfer characteristic has to be placed in series with the servo valve model. Several previous works [11, 3, 4, 5, 23] neglected or only partially accounted for the mentioned combination of the saturation and dead-zone. Both can, however, have a non-negligible impact on the overall system dynamics. At the end, the entire sub-model of the controlled servo valve is described by

$$\ddot{\nu} + 2\zeta\omega_0\dot{\nu} + \omega_0^2\nu = \omega_0^2u, \quad (\text{C.3})$$

$$z = h(\nu), \quad (\text{C.4})$$

while  $z$  is an internal state representing the orifice opening.

## C.2.2 Orifice and Continuity Equations

The orifice equations describe the hydraulic flow  $Q$  through the valve, respectively in regards of the pressure drop, as

$$Q_A = \begin{cases} zK\sqrt{P_S - P_A} & \text{for } z > 0 \\ zK\sqrt{P_A - P_T} & \text{for } z < 0 \\ 0 & \text{otherwise,} \end{cases} \quad (\text{C.5})$$

$$Q_B = \begin{cases} zK\sqrt{P_B - P_T} & \text{for } z > 0 \\ zK\sqrt{P_S - P_B} & \text{for } z < 0 \\ 0 & \text{otherwise,} \end{cases} \quad (\text{C.6})$$

and that for both ports, correspondingly load connections of the hydraulic circuit. The pressure indices  $A, B, T, S$  refer to the servo valves' inlets and outlets, i.e. to the  $A$  and  $B$  connection ports, tank, and pressure supply respectively. Well-known,  $K$  represents the valves' flow coefficient

$$K = c_d \omega \sqrt{\frac{2}{\rho}}, \quad (\text{C.7})$$

with the constructive valves' parameters, in addition to the oil density  $\rho$ . At the same time, from the technical data sheet, one can assume a characteristic relationship

$$Q = Q_n \sqrt{\frac{\Delta p}{p_n}}, \quad (\text{C.8})$$

where  $\Delta p$  is the pressure drop across the valve, and  $Q_n, p_n$  are the nominal flow and pressure drop, describing the valves behavior in a fully open state. By rearranging (C.8), it can be seen that  $Q_n(\sqrt{p_n})^{-1}$  is equivalent to the flow coefficient  $K$ , that allows omitting the identification of  $\omega, c_d$  and  $\rho$  parameters. This way, the valves' flow coefficient is determined from the nominal pressure drop and flow characteristics given by the technical data sheet.

Knowing the flow through the valve, the pressure drop can be calculated directly, via the continuity equations

$$\begin{aligned} \dot{P}_B &= \frac{E}{V_B + A_B(l - x)} \cdot (Q_B + A_B \dot{x} + C_L(P_A - P_B)) \\ \dot{P}_A &= \frac{E}{V_A + A_A x} \cdot (Q_A - A_A \dot{x} + C_L(P_B - P_A)), \end{aligned} \quad (\text{C.9})$$

where  $V_{A/B}$  is the volume of the hydraulic oil in the tubing between the valve and both  $A/B$ -chambers of the cylinder, while  $A_A x$  and  $A_B(l - x)$  are the operational volumes of cylinder. Note that the total (maximal) stroke  $l$  provides mechanical constraints for the piston motion, so that  $0 \leq x \leq l$ , while  $x$  is the relative cylinders' rod position.  $E$  is the bulk modulus and  $C_L$  is an internal leakage coefficient. The latter characterizes the pressure drop across the membrane which is separating both cylinder chambers.

### C.2.3 Mechanical Sub-Model of Cylinder

The cylinder dynamics is modeled as a second-order system with one DOF (degree of freedom) described by

$$m\ddot{x} = P_A A_A - P_B A_B - f(\dot{x}) - F_L. \quad (\text{C.10})$$

The total mass under actuation is  $m$ , and  $f(\dot{x})$  constitutes the entire friction force acting against the rods' motion.  $F_L$  is the load force applied externally, which can be measured by a force sensor, cf. further Fig. C.4. The lumped mass is calculated from the data sheets of all moving components in the assembly, while the cross sections of both chambers  $A_A \neq A_B$  are taken from the available technical drawings. The nonlinear velocity-dependent Stribeck friction model, see e.g. [24], is taken for  $f(\dot{x})$ . To avoid a sign-related discontinuity, a hyperbolic tangent has been assumed, cf. [13], therefore resulting in a Stribeck type friction model

$$f(\dot{x}) = \tanh(\gamma\dot{x}) \left( F_c + (F_s - F_c) \exp\left(-\left|\frac{\dot{x}}{\chi}\right|^\delta\right) \right) + \sigma\dot{x}. \quad (\text{C.11})$$

The Coulomb friction coefficient is stated as  $F_c > 0$ , stiction coefficient as  $F_s > F_c$ , the linear viscous friction coefficient as  $\sigma > 0$ . Two Stribeck shape parameters are  $\delta \neq 0$  and  $\chi > 0$ . The parameter  $\gamma$  scales the smoothness of zero crossing transition, until its saturated value  $\rightarrow \pm 1$  approaches the velocity-dependent sign. Note that more complex dynamic friction behavior [25] is purposefully not considered, since for the largely damped and relatively slow hydraulic systems the modeling (C.11) can yield as fairly sufficient, cf. [3, 23].

## C.3 Model Reduction

From the available FRFs of the servo valve, shown further in Section VI, as identified for 10%, 25% and 90% opening, one can neglect the closed-loop dynamics in the lower frequency range of interest. Therefore, a unity gain and an acceptably low phase lag can be considered, leading to the replacement of (C.3) by  $u = v$ . Note that a hydraulic cylinder is to be operated clearly below 10Hz frequency, cf. Figs. C.5a, C.5b, so that the above assumption is valid for modeling reduction. Note that (C.2) remains an input nonlinearity to be accounted for.

For the further model reduction, cf. [13] for details, a load-dependent pressure  $P_L = P_A - P_B$  is introduced and  $|Q_A| = |Q_B|$  is assumed for a closed hydraulic circuit. Therefore, the orifice equations (C.5), (C.6) are combined into

$$Q_L = zK \sqrt{\frac{1}{2} (P_S - \text{sign}(z)P_L)}, \quad (\text{C.12})$$

while

$$P_A = \frac{P_S + P_L}{2}, \quad P_B = \frac{P_S - P_L}{2}. \quad (\text{C.13})$$

Following the above aggregation, the continuity eqs. (C.9) can be also combined into one:

$$\dot{P}_L = \frac{4E}{V_t} (Q_L - \bar{A}\dot{x} - C_L P_L). \quad (\text{C.14})$$

In (C.14),  $V_t = V_A + V_B$  represents the total actuator volume, and  $\bar{A} = 0.5(A_B + A_A)$  is the averaged piston area. The latter will inherently lead to a certain model-reduction error once the piston has a single rod, thus yielding an asymmetric cylinder. Incorporating both above reduced equations into the cylinder dynamics (C.10) results in

$$m\ddot{x} = P_L \bar{A} - f(\dot{x}) - F_L. \quad (\text{C.15})$$

## C.4 Non-linear System Affine in Control and States

In order to model the system dynamics in a piecewise affine state-space formulation, several linearization steps are required.

Obviously, the combined dead-zone and saturation nonlinearity (C.2) can be described by

$$z = k_g \cdot u + d_g, \quad (\text{C.16})$$

that partitions the total input range into the adjoining cells, indexed by  $g$  while  $g = 1, \dots, 5$ .

For linearizing the orifice equation, the partial derivatives are first taken with respect to both variables  $z$  and  $P_L$ , thus resulting in two linearized parameters  $\hat{C}_q$  and  $\hat{C}_{qp}$ . These, multiplied with the orifice opening and load pressure states respectively, yield the total load flow rate as

$$\hat{Q}_L = \hat{C}_q z + \hat{C}_{qp} P_L, \quad (\text{C.17})$$

and that for a chosen working point  $(\hat{z}, \hat{P}_L)$ . Both terms of linearization can be computed as

$$\hat{C}_q = \left. \frac{\partial Q_L}{\partial z} \right|_{\hat{P}_L} = K \sqrt{0.5 (P_S - \text{sign}(z) \hat{P}_L)}, \quad (\text{C.18})$$

$$\hat{C}_{qp} = \left. \frac{\partial Q_L}{\partial P_L} \right|_{\hat{z}} = \frac{\hat{z} K \text{sign}(\hat{z})}{4 \sqrt{0.5 (P_S - \text{sign}(\hat{z}) \hat{P}_L)}}. \quad (\text{C.19})$$

One can recognize that, in order to capture the whole operation space, a piecewise affine mapping is required. That results in the state-dependent coefficients

$$C_q(P_L) = k_o P_L + d_o, \quad (\text{C.20})$$



$$C_{qp}(P_L, z) = (k_n P_L + d_n) z. \quad (\text{C.21})$$

Here again, the subscripts  $o$  and  $n$  represent the indices of the cells within state-space;  $k$  and  $d$  are the corresponding constants that parameterize the total piecewise affine model. Figure C.1 shows  $\hat{C}_q$  as well as its linearization  $C_q$ .

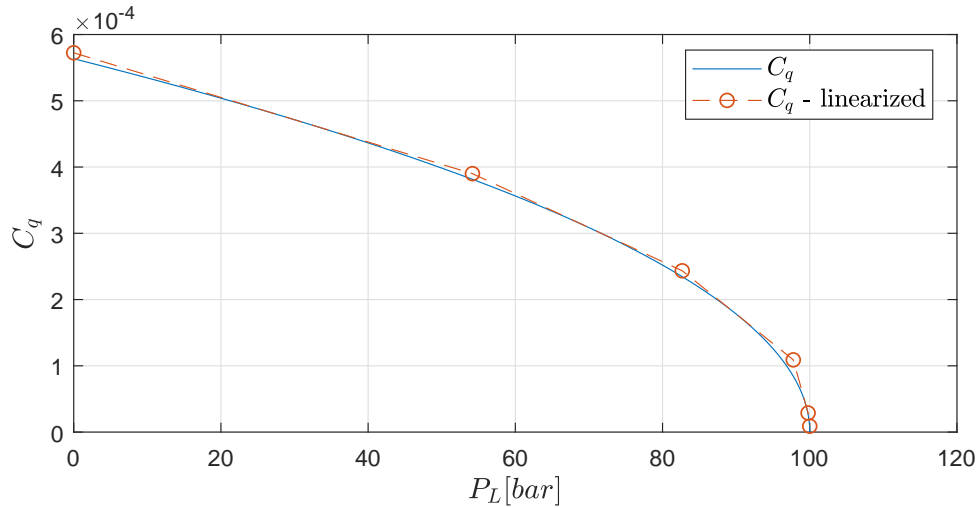


Figure C.1:  $\hat{C}_q$  coefficient and its linearization

For  $\hat{C}_{qp}$ , the characteristic curves are shown in Fig. C.2, together with linearization, for several representative values of  $z$ . Note that here the linearization was performed for a fully opened valve state, i.e.  $z = 1$ . The characteristic curves for  $z < 1$  are then scaled down by multiplication with  $\hat{z}$ , according to (C.19). Note, that the linearized model does not take the supply pressure into account. Therefore the linearization process has to be performed for the intended supply pressure and, consequently, the  $k$  and  $d$  values have to be recalculated once the supply pressure changes. By substituting (C.20) and (C.21) into (C.17), one can easily obtain the total orifice equation with the piecewise affine, yet state-dependent, coefficients.

In a similar way, the Stribeck friction model (C.11) is piecewise linearized as well, that results in

$$f(\dot{x}) = k_w \cdot \dot{x} + d_w, \quad (\text{C.22})$$

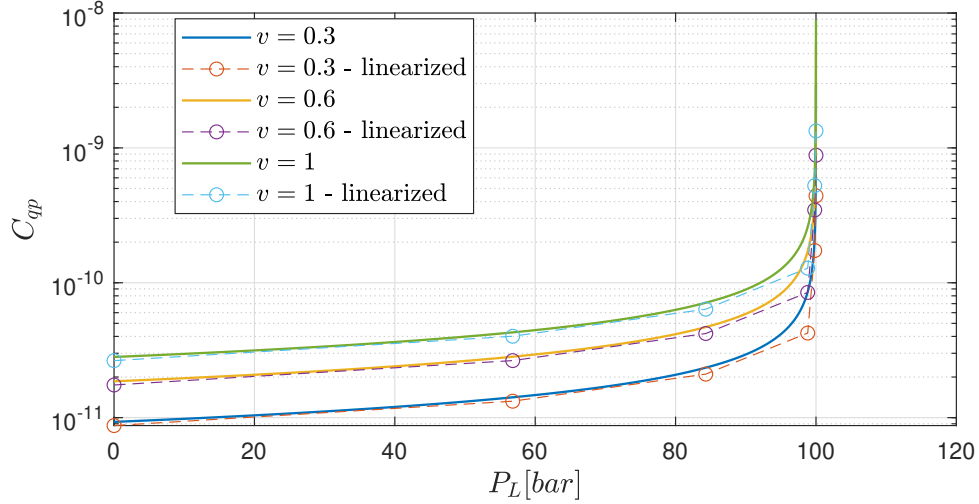
while  $w$  in the cells index in the  $\dot{x}$ -space, and  $k$  and  $d$  are the corresponding constants.

When merging the above equations into the state dynamics (C.14), (C.15) one obtains the overall model in the following form

$$\dot{\mathbf{x}} = \mathbf{A}(\mathbf{x})\mathbf{x} + \mathbf{b}(\mathbf{x})u + \mathbf{f}, \quad (\text{C.23})$$

$$y = \mathbf{c}^T \mathbf{x}, \quad (\text{C.24})$$

with the state vector  $\mathbf{x} = [P_L, \dot{x}]^T$ . That one incorporates the state-dependent system matrix  $\mathbf{A}$ , input coupling vector  $\mathbf{b}$ , and affine vector term  $\mathbf{f}$ . Note that since the cylinder


 Figure C.2:  $\hat{C}_{qp}$  coefficient and its linearization

stroke is not directly affecting the system dynamics, the total order is reduced by one. Obviously, one free integrator can be always connected in series with the system output (C.24), as it is done further for the model evaluation in Section VII, as there is no velocity measurement is provided. The modeling matrices, correspondingly vectors, are given by

$$\mathbf{A} = \begin{pmatrix} \frac{4Ed_g}{V_t} \left( k_o + k_n P_L + d_n - \frac{C_L}{d_g} \right) & -\frac{4E\bar{A}}{V_t} \\ & \frac{\bar{A}}{m} \\ & -\frac{k_w}{m} \end{pmatrix} \quad (\text{C.25})$$

$$\mathbf{b} = \begin{pmatrix} \frac{4Ek_g P_L}{V_t} \left( k_o + \frac{d_o}{P_L} + k_n P_L + d_n \right) \\ 0 \end{pmatrix} \quad (\text{C.26})$$

$$\mathbf{f} = \begin{pmatrix} \frac{4Ed_o d_g}{V_t} \\ -\frac{d_w + F_L}{m} \end{pmatrix} \quad (\text{C.27})$$

$$\mathbf{c}^T = \begin{pmatrix} 0 & 1 \end{pmatrix} \quad (\text{C.28})$$

## C.5 Experimental Setup

The hydraulic system under investigation is shown in Fig. C.3 (laboratory view). The schematic representation of the decoupled right-hand side cylinder is drawn in Fig. C.4, where the sensing interfaces are indicated by  $\odot$ . The system consists of a single rod, double-acting cylinders of type [26], with a linear force sensor [27] attached, that is measuring the respective load from the perspective of each cylinder. The cylinder under consideration is actuated via a 4/3 servo valve [28], attached to a hydraulic pump, with a

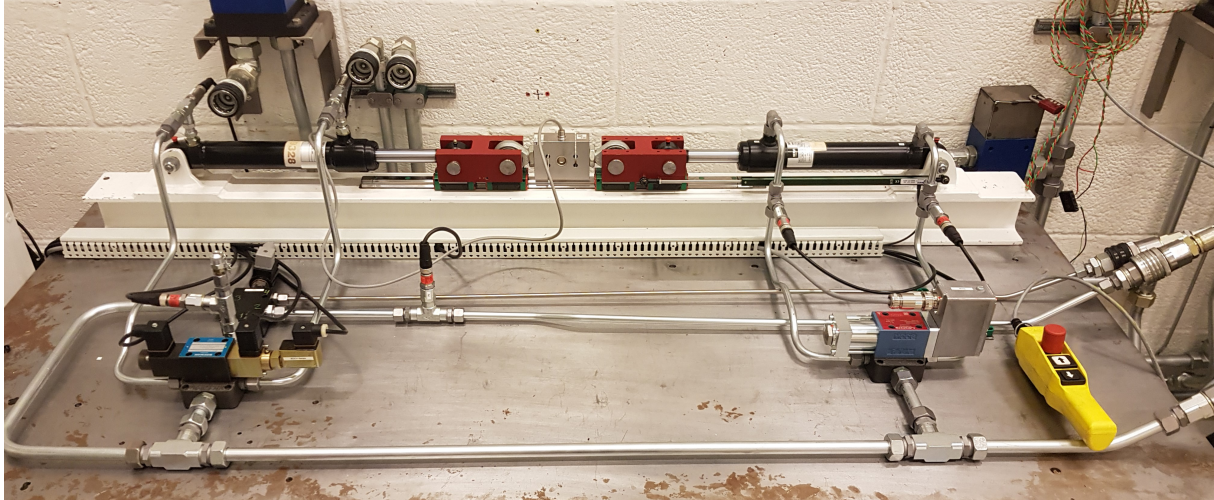


Figure C.3: Experimental hydraulic setup (laboratory view)

maximum supply pressure of 350bar<sup>1</sup> and maximum flow rate of 120l/min. The pressures in both chambers of the cylinder are measured by the sensors [29]. Further, a linear potentiometer [30] is installed to track the cylinders' rod position. The servo valve also includes a sensor for the spool position monitoring. As the real-time control interface between the development computer and experimental setup, the Speedgoat platform, baseline model S [31], with the IO183 and IO397 interface cards is used. This hardware allows for a sampling rate of 2kHz. Furthermore, it supports 8 single-ended or 4 differential analogue input and 4 single ended output channels with a 16bit A/D and D/A converter each, as well as analog input voltages of  $\pm 10V$  and output voltages of  $0 - 5V$ , with a maximum output current of 5mA on IO183. On IO387, 4 single-ended or 4 differential analogue input and 4 single ended output channels with a 16bit A/D and D/A converter each, as well as a analog input voltages of  $\pm 10.24V$  and output voltages of  $\pm 10V$  with a maximum output current of 5mA are available. An emergency break circuit was designed and implemented, switching all valves into a system pressure relieving, that means a 'no-motion' correspondingly 'no-force', configuration. The instrumented components are listed in Table C.1.

## C.6 Parameter Identification

In this section, the single identification steps for determining the unknown, correspondingly uncertain, system parameters are described. All experimental measurements, described below, were performed with a sampling frequency of 2kHz.

---

<sup>1</sup>Note that the pressure is denoted in bar, as conventionally for hydraulics, while standard SI units, i.e. Pa, are used for all calculations made

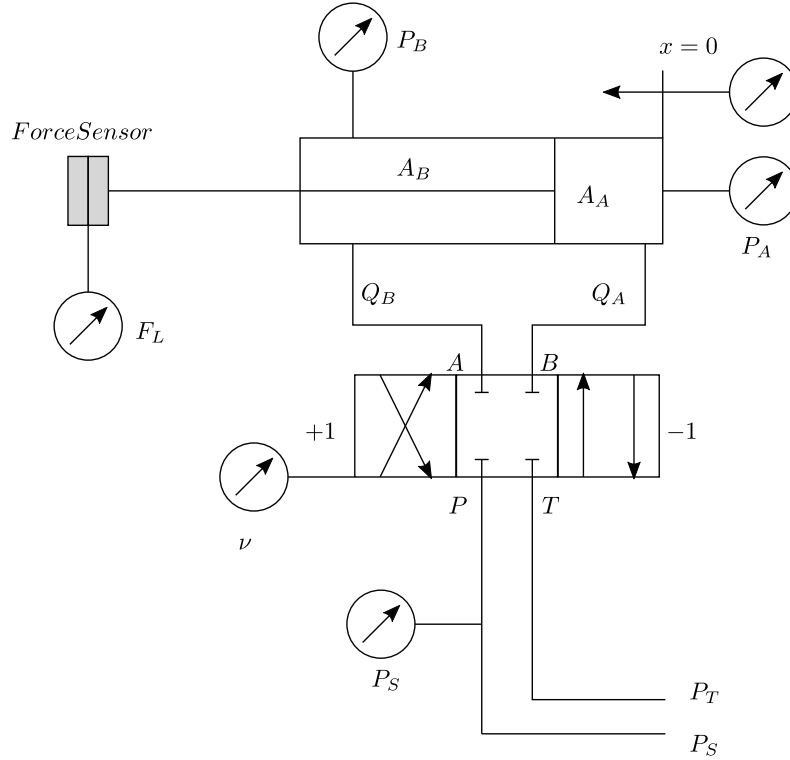


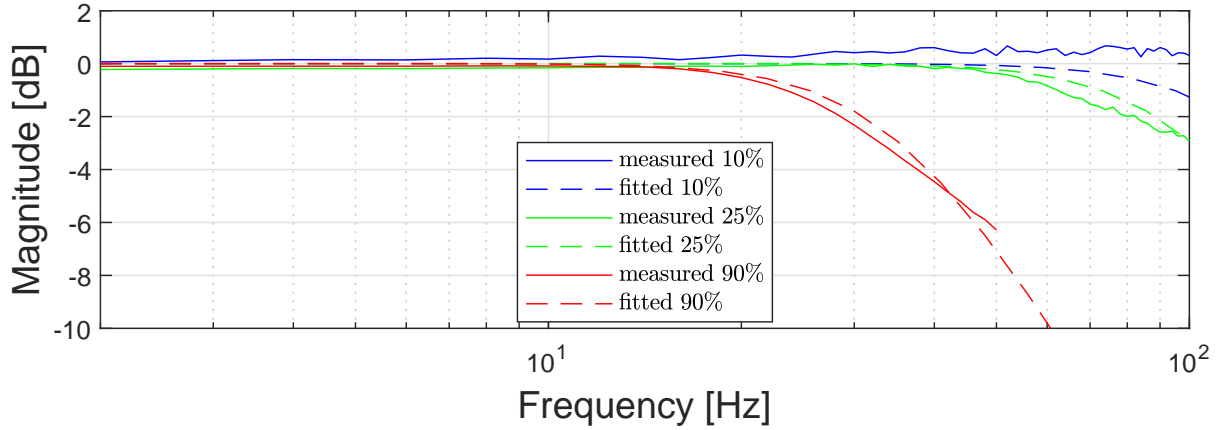
Figure C.4: Schematic representation of experimental setup

Table C.1: Installed components of experimental system

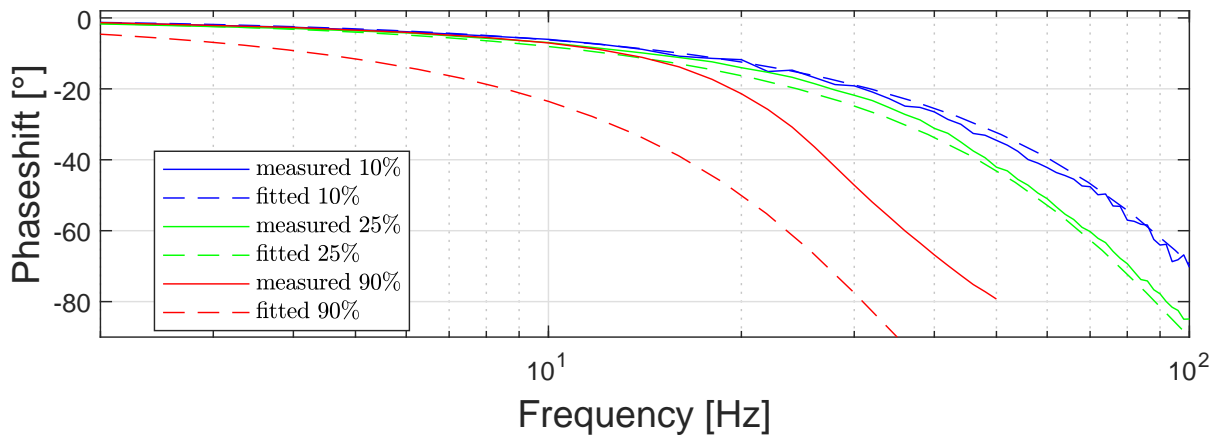
Description	Model number
Moog servo valve	D633 R16KD1M0NSM2
Cylinder	CD25-40 25x200-SS-HC-SSN-NNN
Danfoss P-sensor	MBS 1250 063G1229
Celesco linear-pot.	CLP-250
HBM Force sensor	1-S9M/50kN-1

### C.6.1 Servo Valve

In order to evaluate FRFs of the controlled servo valve, mentioned before, measurements were made to identify closed-loop frequency characteristics. Referring to (C.1), identification of the  $\omega_0$  and  $\zeta$  parameters is required. To approach the nominal FRF characteristics, available from the data sheets, three different levels of the valve opening, 10%, 25% and 90%, are assumed, i.e. corresponding to the input magnitude  $|u|$ . For FRF measurements, sinusoidal signals were used, with frequencies starting from 2Hz and going up to 50Hz for 90% opening, and up to 100Hz for the rest. The equidistant frequency interval is taken to be 2Hz. During the signal analysis the measured spool position was fitted over 4 peri-



(a) Magnitude of the servo valve with different opening references



(b) Phase of the servo valve with different opening references

Figure C.5: Measured FRFs versus linear model fit

ods with a sinusoidal curve for calculating, based thereupon, the magnitude and phase for each frequency measurement. The measurements and the fitted models are shown in Figs. C.5a and C.5b, while the determined model parameters are listed in Table C.2. The plots

Table C.2: Servo valve second-order model parameters

Valve opening [%]	$\omega_0$ [ $rad\ s^{-1}$ ]	$\zeta$
10	816.8	0.7
25	628.3	0.7
90	220	0.7

show that for 10% and 25% valve opening, the model and the measurements are close to each other, while at 90% the parameters are adjusted to better fit the magnitude, to be inline with approximation from Section C.4, while the phase response shows a stronger divergence.

### C.6.2 Dead-zone

Measurements were performed to test the extend of the dead-zone in either direction from the middle (zero) position. For  $u > 0$  the cylinders' initial position was fully retracted, while for  $u < 0$  fully extended. The constant input signals were applied starting from 1% to 20% valve opening, and that in 0.5% steps. During the signal processing the cylinders' position signal was fitted with a linear function using the least squares method, revealing the slope and, therefore, constant velocity estimate of the rod  $\hat{x}$ , shown in Fig. C.6. Note

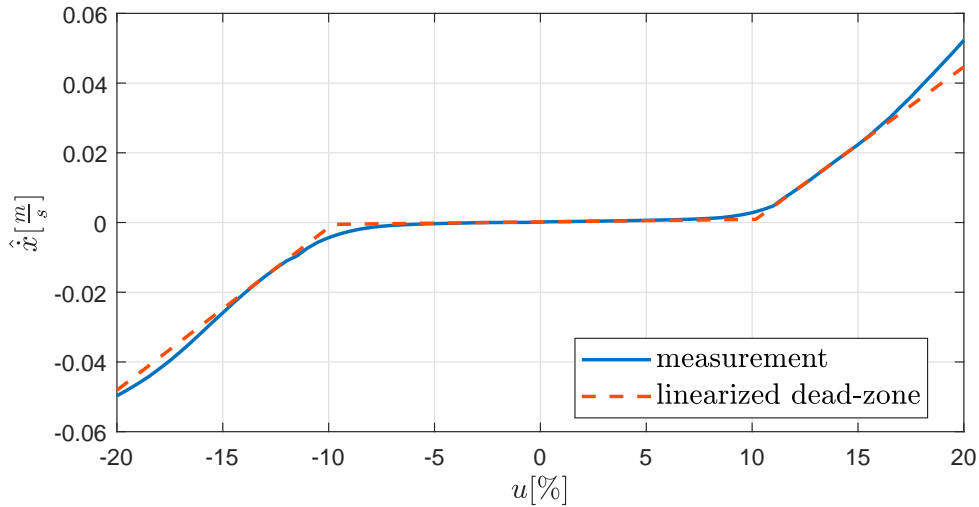


Figure C.6: Experimental test of the dead-zone and linearization

that under these experimental conditions, a quasi-static behavior can be assumed, so that the appearance of non-zero velocity is directly associated with boundaries of the dead-zone. The plot shows a dead-band of around 10%, yet we still observe a very slow (rather creeping) cylinder motion also within the dead-band. Therefore, an ideal assumption of a fully locking dead-zone (C.2), is here not fully justified and a flat slope should be assumed for  $|\nu| < \beta$ , corresponding  $k_g > 0$  in (C.16).

### C.6.3 Stribeck Friction

For positive  $u$  values, the rods' initial position is fully retracted, and fully extended for negative  $u$  values. Constant input signals, starting from 5% in 1% intervals up to 50% valve opening, were sent to the valve, while a constant counteracting force, produced by the second cylinder, was applied. Since the constant valve opening is expected to generate a constant relative velocity at steady-state, and the full cylinder stroke was driven for all input values, the normed drive time is taken for the sake of comparison. The driven cylinder position over the normed time is shown in Fig. C.7 for all measurements, and that for both directions. On the contrary to the full-order model, all measurements do

not reveal an expected linear slope that corresponds to constant relative velocities. At the same time, a fairly good match of all curves and their mirroring symmetry for both directions point on some rather systematic behavior, which is obviously not captured even by the full-order model. A detailed analysis of this by-effect is, however, out of the focus of this paper and builds an outlook for future works. For obtaining a reasonable estimate of relative velocities from the recorded experiments a least-squares fit of linear function (i.e. slope) has been made for all curves shown in Fig. C.7. This yields a corresponding

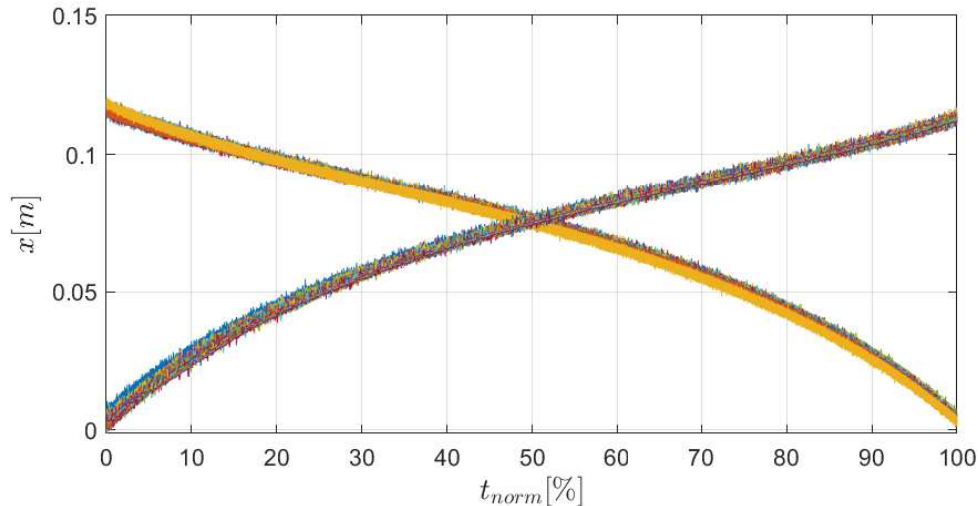


Figure C.7: Cylinder position measurements over normed time for all Stribeck curve measurements, 46 measurements for retracting and 45 measurements for extending motion

set of bidirectional relative velocities, and that with the same extend of residual errors for the assumed linear slope. When calculating the friction force, the initial samples of each measurement show a transient, and that on both pressure sensors and force sensor. However, it has no apparent affect on the velocity of cylinder, as can be seen from Fig. C.7. Therefore, only the steady-state part of each measurement was used for averaging  $P_B$ ,  $P_A$  and  $F_L$ , thus allowing for calculating the cylinder forces according to (C.10). The obtained velocity-force data was used to fit the Stribeck parameters, according to (C.11), by using the standard nonlinear least-squares method. During the following linearization, the curve was split into seven segments, four from which are representing the purely viscous and Coulomb friction contributions for both directions. The fitted Stribeck model and its piecewise linearization are shown together with the measured data in Fig. C.8.

## C.7 Model Evaluation

Simulations were performed for all three models and compared with the corresponding measurements. As input a sinusoidal signal with frequencies of  $f = [1, 2, 3]$ Hz and am-



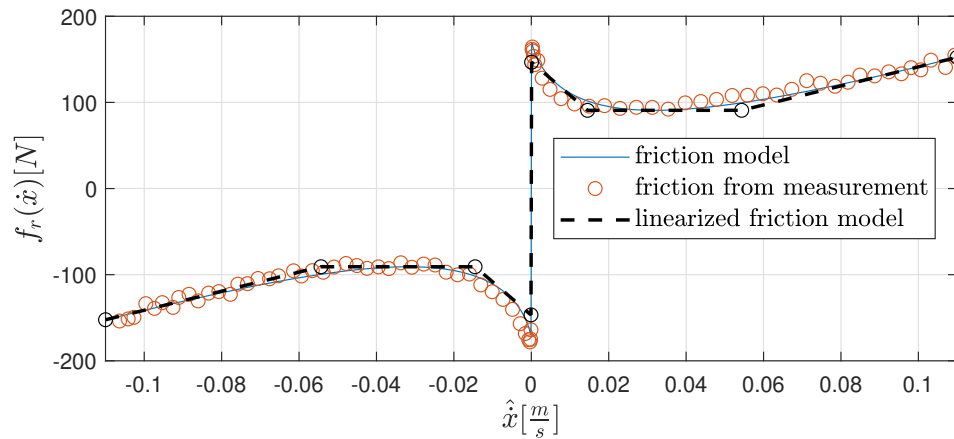
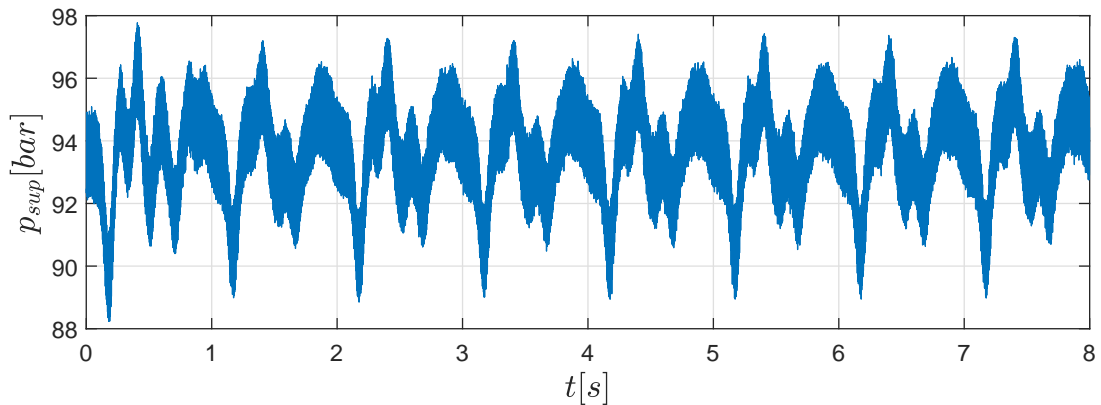
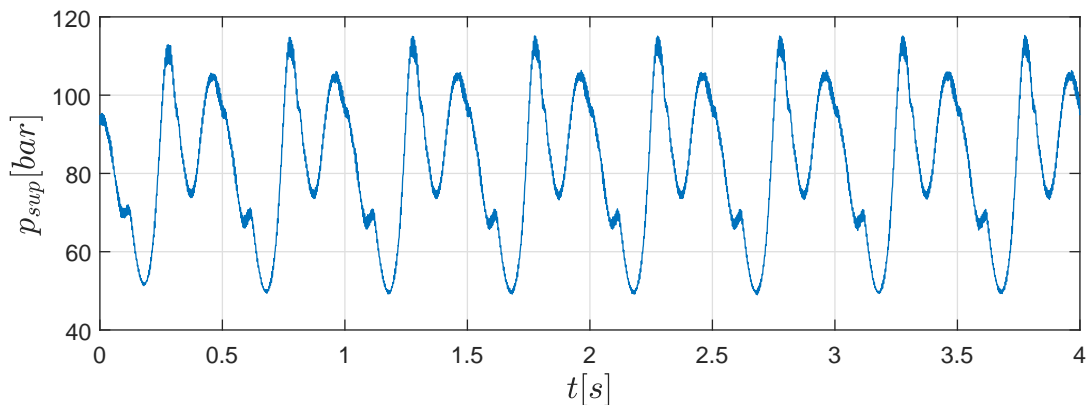


Figure C.8: Measured data points and fitted Stribeck model

plitudes corresponding to the valve opening of  $u = [20, 40, 60]\%$  were used. From the signals monitoring it was obvious that the supply pressure was varying from the 100bar set value during the drive, despite being connected to an oversized hydraulic power unit, cf. Fig. C.9. Therefore, the measured pressure was used as the supply pressure input signal for the simulation. Plots of the ‘corner’ configurations, relating to amplitude and



(a) 20% valve opening amplitude and frequency of 1Hz



(b) 60% valve opening amplitude and frequency of 2Hz

Figure C.9: Measured supply pressure at sinusoidal input



frequency, are shown in Figs. C.10, C.11, C.12 and C.13. Initial conditions for pressures and cylinder position for the simulation were taken from the measurements at the start of the next full period once the steady-state condition can be observed. Also, starting from that point all initial values of the simulation were taken over from the available measurements. All identified, correspondingly computed, system parameters are given in Table C.3, while the corresponding linearization parameters are listed in Tables C.4, C.5, C.6, C.7, C.8, C.9. The linearization parameters for  $C_q$  and  $C_{qp}$ , listed in the tables, are each with four values, shown as an ordered set, with the order corresponding to four simulations presented. The experimental signals were processed using a moving average function, smoothing them for a better visual comparison.

From the results we can see a qualitatively similar behavior for all three models. The full-order model, equally as the measurements, shows an overall positive slope due to different cross sections of the piston, i.e. asymmetric cylinder. Furthermore, it can be seen that the qualitative response of the simulation and the measurement are fairly close. From Figs. C.10, C.12 one can recognize that at lower valve opening, i.e. at lower relative velocities, the measured displacement amplitude differs stronger compared to the models. One of the possible reasons lies in a not fully linear displacement map at constant valve opening, correspondingly flow, cf. Fig. C.7, and related identification of model parameters.

For the linearized model we observe a slightly drifting behavior. As mentioned in section C.4, the linearization parameters for this model have to be recalculated if the supply pressure changes. For the shown simulation, an average supply pressure was calculated and used for calculation of the linearization parameters. An attempt of on-line recalculating the linearization parameters at the time-varying supply pressure fails due to an exponential increase in simulation time. The reduced model shows no drift in the graphs, in accord with the assumption that both sides piston areas are equal. Here the average supply pressure, the same as for the linearized model, was used to have a better comparison between the reduced and linearized model.

From comparison of the plots it can be said, that the cylinder motion predicted by the full-order model is best in accord with the measurements, especially in view of the relative displacement which has a free integrator behavior. Furthermore it can be noted, that there are almost no differences between the linearized and reduced order model besides a slight drifting motion of the linearized model due to the afore mentioned cell segmentation.

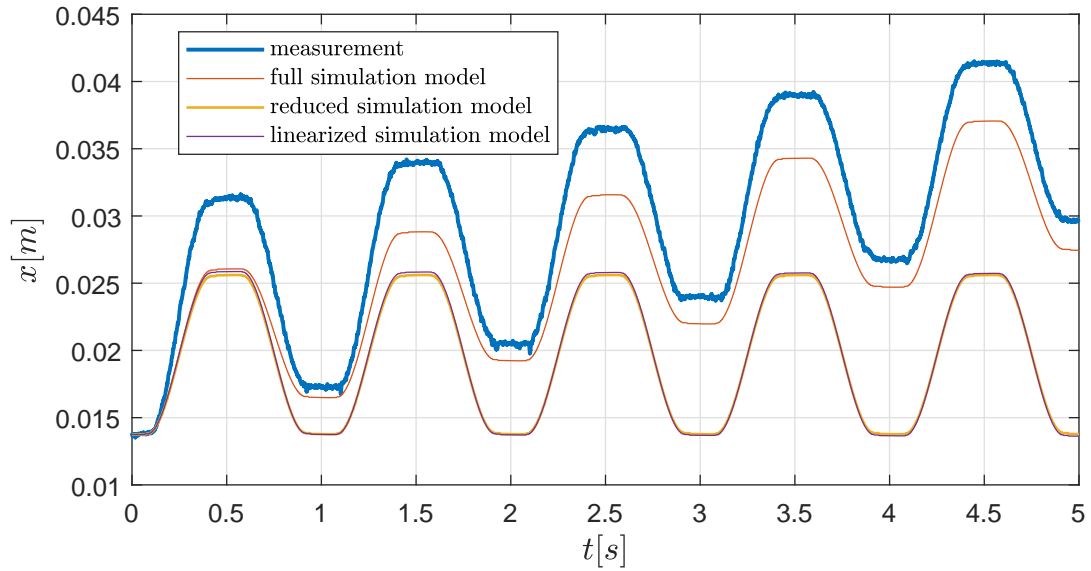


Figure C.10: Measurement and simulation for sinusoidal input with 20% valve opening and 1Hz frequency

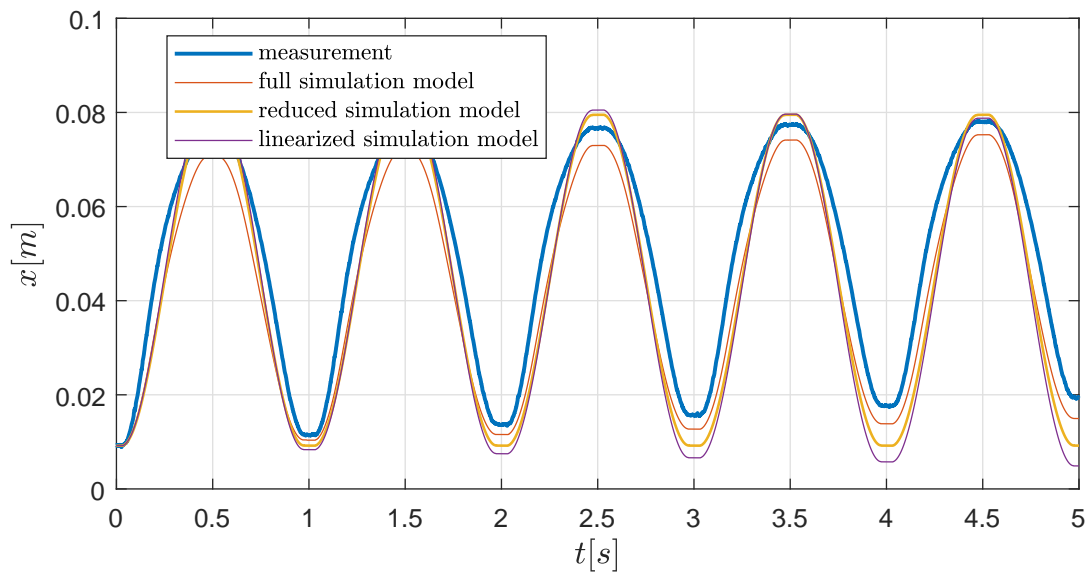


Figure C.11: Measurement and simulation for sinusoidal input with 60% valve opening and 1Hz frequency

## C.8 Summary

Modeling of a hydraulic drive system was performed, including the full-order, reduced, and linearized models. Furthermore, the nonlinearities in the reduced model were located and linearized over the whole operational state-space, therefore resulting in a state-dependent matrix form affine in the control and states. The experimental hydraulic system was designed, constructed and instrumented, while incorporating a standard single-rod hydraulic cylinder operated via the controlled servo valve. Measurements were performed for ana-

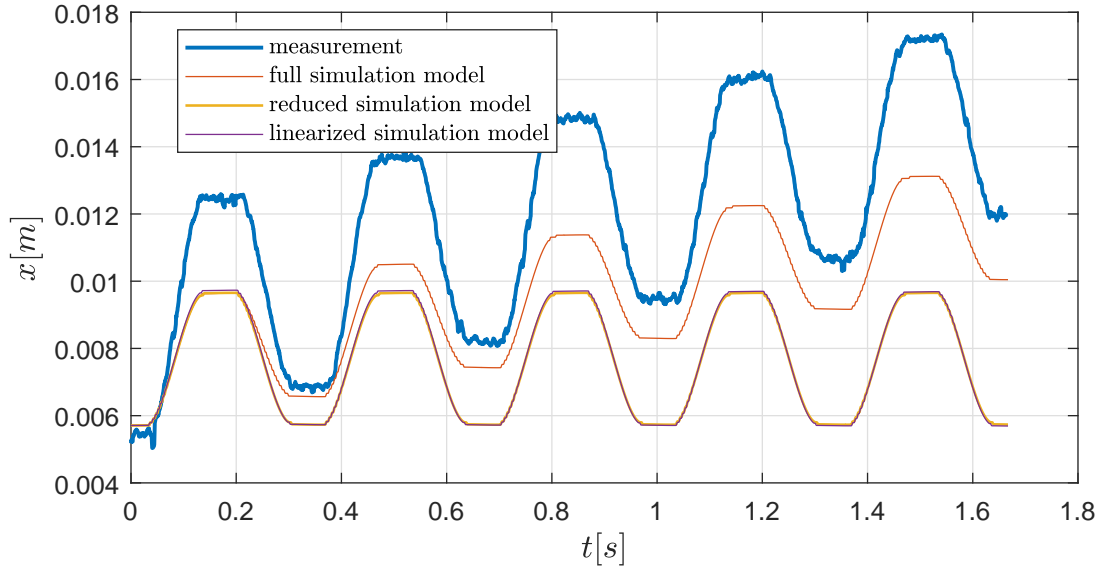


Figure C.12: Measurement and simulation for sinusoidal input with 20% valve opening and 3Hz frequency

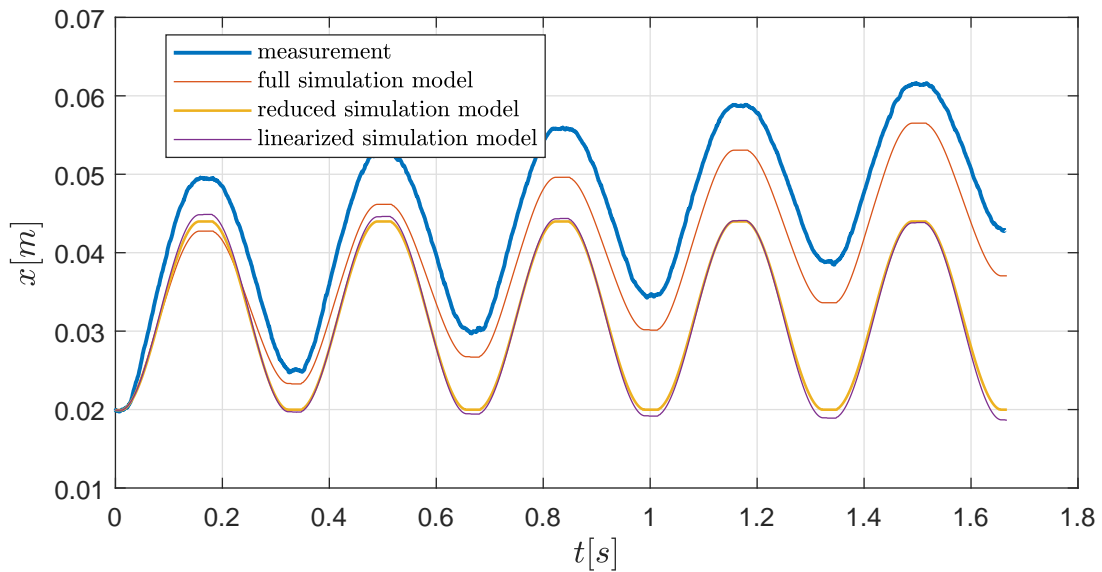


Figure C.13: Measurement and simulation for sinusoidal input with 60% valve opening and 3Hz frequency

lyzing the system dynamics and identifying the free parameters, otherwise weakly known from the technical data. These included FRFs of the valve closed-loop, the dead-zone and the nonlinear Stribeck-type friction. Simulations of all three models were exposed opposite to each other and compared with a set of measurements at different amplitudes and frequencies. Observed deviations were analyzed and discussed concerning the inherent sources and implications for modeling.

Table C.3: Simulation Parameters

Param.	Value	Unit
$m$	1.394	$kg$
$A_A$	$1.3E^{-3}$	$m^2$
$A_B$	$0.76E^{-3}$	$m^2$
$K$	$0.252E^{-6}$	$\frac{m^3}{s\sqrt{Pa}}$
$E$	$10^9$	$Pa$

Param.	Value	Unit
$P_T$	0	$Pa$
$V_A$	$0.7E^{-3}$	$m^3$
$V_B$	$0.7E^{-3}$	$m^3$
$F_L$	0	$N$
$C_L$	0	$1/s$
$l$	0.2	$m$

Table C.4: Values for linearized dead-zone and saturation

Cell	$k_g$	$d_g$
I	0	-1
II	1	0.1
III	0.04	0
IV	1	-0.1
V	0	1

Table C.5: Values for linearized Stribeck friction

Cell	$k_w$	$d_w$
I	1105	-30.7
II	-0.254	-90.8
III	-3867	-147
IV	$1.833E^3$	0
V	-3867	147
VI	-0.819	90.7
VII	1105	30.7

Table C.6: Values for  $k_o$  for linearized  $C_q$

Cell	$k_o$
I	$[-0.034E^{-9}, -0.038E^{-9}, -0.035E^{-9}, -0.037E^{-9}]$
II	$[-0.053E^{-9}, -0.058E^{-9}, -0.053E^{-9}, -0.056E^{-9}]$
III	$[-0.092E^{-9}, -0.100E^{-9}, -0.092E^{-9}, -0.097E^{-9}]$
IV	$[-0.412E^{-9}, -0.447E^{-9}, -0.411EE^{-9}, -0.435E^{-9}]$
V	$[-0.920E^{-9}, -0.998E^{-9}, -0.919E^{-9}, -0.972E^{-9}]$

Table C.7: Values for  $d_o$  for linearized  $C_q$

Cell	$d_o$
I	$[0.554E^{-3}, 0.510E^{-3}, 0.554E^{-3}, 0.525E^{-3}]$
II	$[0.647E^{-3}, 0.597E^{-3}, 0.648E^{-3}, 0.613E^{-3}]$
III	$[0.949E^{-3}, 0.874E^{-3}, 0.950E^{-3}, 0.899E^{-3}]$
IV	$[0.388E^{-3}, 3.573E^{-3}, 3.882E^{-3}, 3.671E^{-3}]$
V	$[8.632E^{-3}, 7.957E^{-3}, 8.646E^{-3}, 8.177E^{-3}]$

Table C.8: Values for  $k_n$  for linearized  $C_{qp}$

Cell	$k_o$
I	$[0.027E^{-15}, 0.034E^{-15}, 0.026E^{-15}, 0.031E^{-15}]$
II	$[0.095E^{-15}, 0.121E^{-15}, 0.094E^{-15}, 0.111E^{-15}]$
III	$[0.491E^{-15}, 0.627E^{-15}, 0.489E^{-15}, 0.578E^{-15}]$
IV	$[43.93E^{-15}, 56.09E^{-15}, 43.71E^{-15}, 51.68E^{-15}]$
V	$[491.1E^{-15}, 627.1E^{-15}, 488.8E^{-15}, 577.8E^{-15}]$

Table C.9: Values for  $d_n$  for linearized  $C_{qp}$

Cell	$d_o$
I	$[0.027E^{-9}, 0.030E^{-9}, 0.027E^{-9}, 0.029E^{-9}]$
II	$[-0.009E^{-9}, -0.009E^{-9}, -0.009E^{-9}, -0.009E^{-9}]$
III	$[-0.322E^{-9}, -0.349E^{-9}, -0.321E^{-9}, -0.340E^{-9}]$
IV	$[-40.54E^{-9}, -43.98E^{-9}, -40.48E^{-9}, -42.80E^{-9}]$
V	$[-458.8E^{-9}, -497.7E^{-9}, -458.1E^{-9}, -484.3E^{-9}]$

## Acknowledgment

This work has received funding from the European Union Horizon 2020 research and innovation programme H2020-MSCA-RISE-2016 under the grant agreement No 734832. The authors are also thankful to Jan Andreas Holm for technical support in designing and assembling the hydraulic setup.



# REFERENCES

- [1] H. E. Merritt. *Hydraulic control systems*. John Wiley and Sons, 1967.
- [2] M. Jelali and A. Kroll. *Hydraulic Servo-systems: Modelling, Identification and Control*. Springer London, 2003.
- [3] A. Alleyne and R. Liu. A simplified approach to force control for electro-hydraulic systems. *Control Engineering Practice*, 8(12):1347–1356, 2000. doi:10.1016/S0967-0661(00)00081-2.
- [4] Bin Yao, Fanping Bu, J. Reedy, and G.-C. Chiu. Adaptive robust motion control of single-rod hydraulic actuators: theory and experiments. *IEEE/ASME Transactions on Mechatronics*, 5(1):79–91, 2000. doi:10.1109/3516.828592.
- [5] J. Komsta, N. van Oijen, and P. Antoszkiewicz. Integral sliding mode compensator for load pressure control of die-cushion cylinder drive. *Control Engineering Practice*, 21(5):708–718, 2013. doi:10.1016/J.CONENGPRAC.2011.12.006.
- [6] G. Liu and S. Daley. Optimal-tuning nonlinear PID control of hydraulic systems. *Control Engineering Practice*, 8(9):1045–1053, 2000. doi:10.1016/S0967-0661(00)00042-3.
- [7] S. S. Tørdal, A. Klausen, and M. K. Bak. Experimental System Identification and Black Box Modeling of Hydraulic Directional Control Valve. *Modeling, Identification and Control: A Norwegian Research Bulletin*, 36(4):225–235, 2015. doi:10.4173/mic.2015.4.3.
- [8] M. B. Kjelland and M. R. Hansen. Offshore Wind Payload Transfer Using Flexible Mobile Crane. *Modeling, Identification and Control: A Norwegian Research Bulletin*, 36(1):1–9, 2015. doi:10.4173/mic.2015.1.1.
- [9] M. H. Rudolfson, T. N. Aune, O. Auklend, L. T. Aarland, and M. Ruderman. Identification and control design for path tracking of hydraulic loader crane. In *2017 IEEE International Conference on Advanced Intelligent Mechatronics (AIM)*, pages 565–570, 2017. doi:10.1109/AIM.2017.8014077.

- [10] B. Eryilmaz and B. H. Wilson. Unified modeling and analysis of a proportional valve. *Journal of the Franklin Institute*, 343(1):48–68, 2006. doi:10.1016/J.JFRANKLIN.2005.07.001.
- [11] G. Sohl and J. Bobrow. Experiments and simulations on the nonlinear control of a hydraulic servosystem. *IEEE Transactions on Control Systems Technology*, 7(2):238–247, 1999. doi:10.1109/87.748150.
- [12] H. C. Pedersen and T. O. Andersen. Pressure Feedback in Fluid Power Systems—Active Damping Explained and Exemplified. *IEEE Transactions on Control Systems Technology*, 26(1):102–113, 2018. doi:10.1109/TCST.2017.2650680.
- [13] M. Ruderman. Full- and reduced-order model of hydraulic cylinder for motion control. In *IECON 2017 - 43rd Annual Conference of the IEEE Industrial Electronics Society*, pages 7275–7280, 2017. doi:10.1109/IECON.2017.8217274.
- [14] G. Ferrari-Trecate, M. Muselli, D. Liberati, and M. Morari. A clustering technique for the identification of piecewise affine systems. *Automatica*, 39(2):205–217, 2003. doi:10.1016/S0005-1098(02)00224-8.
- [15] A. L. Juloski, W. P. M. H. Heemels, G. Ferrari-Trecate, R. Vidal, S. Paoletti, and J. H. G. Niessen. Comparison of Four Procedures for the Identification of Hybrid Systems. pages 354–369. Springer, Berlin, 2005. doi:10.1007/978-3-540-31954-2\_23.
- [16] S. Paoletti, A. L. Juloski, G. Ferrari-Trecate, and R. Vidal. Identification of Hybrid Systems A Tutorial. *European Journal of Control*, 13(2-3):242–260, 2007. doi:10.3166/EJC.13.242-260.
- [17] J.-J. E. Slotine and W. Li. *Applied Nonlinear Control*. Prentice Hall, Massachusetts, 1991.
- [18] L. Rodrigues and S. Boyd. Piecewise-affine state feedback for piecewise-affine slab systems using convex optimization. *Systems & Control Letters*, 54(9):835–853, 2005. doi:10.1016/J.SYSCONLE.2005.01.002.
- [19] N. McClamroch and I. Kolmanovsky. Performance benefits of hybrid control design for linear and nonlinear systems. *Proceedings of the IEEE*, 88(7):1083–1096, 2000. doi:10.1109/5.871310.
- [20] Rafal Goebel, Ricardo G. Sanfelice and A. R. Teel. Hybrid Dynamical Systems. *IEEE Control Systems*, 29(2):28–93, 2009.



## REFERENCES

- [21] C. Tomlin, I. Mitchell, A. Bayen, and M. Oishi. Computational techniques for the verification of hybrid systems. *Proceedings of the IEEE*, 91(7):986–1001, 2003. doi:10.1109/JPROC.2003.814621.
- [22] Z. Alkhoury, M. Petreczky, and G. Mercère. Identifiability of affine linear parameter-varying models. *Automatica*, 80:62–74, 2017. doi:https://doi.org/10.1016/j.automatica.2017.01.029.
- [23] L. Márton, S. Fodor, and N. Sepeshri. A practical method for friction identification in hydraulic actuators. *Mechatronics*, 21(1):350–356, 2011. doi:10.1016/J.MECHATRONICS.2010.08.010.
- [24] M. Ruderman. On break-away forces in actuated motion systems with nonlinear friction. *Mechatronics*, 44:1–5, 2017. doi:10.1016/J.MECHATRONICS.2017.03.007.
- [25] M. Ruderman and M. Iwasaki. Observer of Nonlinear Friction Dynamics for Motion Control. *IEEE Transactions on Industrial Electronics*, 62(9):5941–5949, 2015. doi:10.1109/TIE.2015.2435002.
- [26] Kramp. NH 30 cylinder, may 2018.
- [27] HBM. Force Transducers, may 2018.
- [28] Moog. Direct articulated proportional servovalve D633/D634, may 2009.
- [29] Danfoss. MBS 1250, Heavy Duty Pressure sensors, may 2018.
- [30] Celesco. Linear Potentiometer, may 2015.
- [31] Speedgoat. Speedgoat - Rugged Baseline embedded controller for Simulink real-time, apr 2018.



**Paper D**

**Hybrid State Feedback  
Position-Force Control of Hydraulic  
Cylinder**

**Philipp Pasoli, Michael Ruderman**

This paper has been published as:

P. Pasoli, M. Ruderman. Hybrid State Feedback Position-Force Control of Hydraulic Cylinder. *2019 IEEE International Conference on Mechatronics (ICM)*, Vol. 1, pp. 54-59, 2019. doi: 10.1109/ICMECH.2019.8722829.

# Hybrid State Feedback Position-Force Control of Hydraulic Cylinder

Philipp Pasolli, Michael Ruderman

University of Agder

Department of Engineering Sciences

Jon Lilletunsvet 9, 4879 Grimstad, Norway

*Abstract* – A hybrid position-force control is proposed using a unified state feedback controller in combination with feed-forward dead-zone compensation. The dead-zone compensator was constructed as inverse of the identified static map while the state feedback gains were obtained using a numerical optimization routine. An accurate state-space model affine in states and control, derived in previous work, was used for closed-loop simulations and control tuning. A trigger event for automatic switching between position and force control was defined and integrated into the overall control architecture alongside with a feed-forward low-pass filter reducing high frequency components in the control signal. Experimental evaluations were performed for different references with automatic switching between the position trajectory following and force set value regulation.

## D.1 Introduction

Hydraulic systems are widely used in various industries due to their longevity, compactness, modularity and excellent power to mass ratio. Further they have the ability of holding large forces constantly without overheating, as most other actuators would. However, hydraulic systems contain multiple nonlinearities e.g. in the orifice equations, mechanical friction, leakage, and others, which either can not be modeled completely or require some in depth investigation to come up with a proper modeling solution. On top of that, there are uncertain model properties e.g. wear of components, bulk modulus, and others which make hydraulic systems not only more challenging to model but also to control.

In several cases of hydraulic applications a lot of tasks are highly repetitive and tedious e.g. in excavators, while still being controlled manually by operators. While at least semi-automatic control already entered these application fields, it is still the standard to use PID controllers for most of the closed-loop controls. Some optimal control designs for PID, with additional nonlinear extensions, were reported e.g. [1] for improving the control system performance. In other motion control researches, different types of controllers,

like adaptive, extended state-feedback and variable structure, are shown as superior to the standard PID, not just for hydraulic systems, cf. [2, 3, 4, 5].

Keeping in mind an example with excavator, it could be destructive for equipment to run with position control only, so that a force control approach might be required. Here it is worth to recall that a high-performant position control is inherently stiff, so that an impact with environment might lead to destructive or at least wearing by-effects. Control approaches are, however, especially challenging if an environment has uncertainties in resistive force and either an alternative control strategy or a kind of universal controller with relatively wide operational range is needed. For several force control strategies, including those designed for hydraulic systems, we refer to [6, 7, 8, 9]. Yet if a fully automated system is desired, a combination of position and force control should be sought, capable of utilizing both types of controllers depending on the environmental factors. Such hybrid control approaches are quite common and continue to be a field of intense research especially in robotics, cf. [10, 11, 12].

In this paper a hybrid position and force control approach is pursued based on an integral state feedback controller, see e.g. [13] for overview. While for position control the system can basically be regulated using a PID, for a force control it is a pressure feedback which becomes vital for actively damping the system, cf. [14]. Other research showed that a pressure feedback control can also be implemented directly using additional hardware, cf. [15].

For laying out a proper control architecture, a detailed model of the system is required. In [16] a reduced hydraulic model in approach to our test setup is described which was expanded upon in [17] by linearizing it and creating a state-space model affine in both control and states. The proposed hybrid position-force control is based on the latter. The rest of the paper is structured as follows. In section II the modeling from previous work [17] is revised and summed up while introducing the integral state feedback controller in section III. Section IV evaluates the measurements performed and in V an outlook for future work is shown. Finally in VI a summary of the work done is given.

## D.2 System Modeling

The hydraulic system modeled is a single rod, double acting cylinder attached to a servo valve connected to a HPU (Hydraulic Power Unit). Characteristics of both the valve and the cylinder were previously identified in [17]. Simulations and measurements were compared verifying the model and its identified parameters, including a dead-zone-saturation combination, the valves dynamics as a second-order system, orifice and continuity equations and the Stribeck friction model for cylinder. For the model reduction the assumption

of equal cross sectional areas of the cylinder was made, therefore introducing a load dependent pressure, and simplifying both the orifice and continuity equations. Also, the valves' dynamics was neglected due to an observed unity gain and negligible phase lag in the frequency range of interest. Linearizations of type  $y = kx + d$ , i.e. with slope  $k$  and offset  $d$ , were performed for the identified nonlinearities, therefore resulting in a state-space model affine in control and states, representing the plant itself only, of the form

$$\dot{\mathbf{x}} = \mathbf{A}(\mathbf{x})\mathbf{x} + \mathbf{b}(\mathbf{x})u + \mathbf{f}, \quad (\text{D.1})$$

$$y = \mathbf{c}^T \mathbf{x}, \quad (\text{D.2})$$

with  $u$  being the input to the plant.

For this work, the state-space model was expanded by an event switching between the position and force control, denoted by  $h$ . Expanding the state vector for state feedback control with integral term results in the following formulation

$$\dot{\mathbf{x}} = \mathbf{A}(\mathbf{x}, h)\mathbf{x} + \mathbf{b}(\mathbf{x})r(h) + \mathbf{f}, \quad (\text{D.3})$$

$$y = \mathbf{c}(h)^T \mathbf{x}, \quad (\text{D.4})$$

which is represented in Fig. D.2.

The state vector is given by  $\mathbf{x}^T = (x, \dot{x}, P_L, F_L, e)$  where  $e$  is the error between reference and measured output (position or force),  $x$  is the cylinder's position,  $\dot{x}$  the relative velocity,  $P_L$  the load-dependent pressure and  $F_L$  is the load force. The introduction of  $h$  and switching between control schemes leads inherently to a change of the system dynamics and, therefore, to two different system matrices  $\mathbf{A}$  and output vectors  $\mathbf{c}$ , depending on the instantaneous control mode.  $r$  is the corresponding reference signal, again dependent on  $h$ .  $\mathbf{b}$  is the input coupling vector and  $\mathbf{f}$  is correspondingly the affine term, cf. [17].

## D.3 Control Design

This section describes the single steps of designing the closed-loop control system, its parameter optimization, definition of the switching event, static dead-zone compensator, and feed-forward filter for the control signal.

### D.3.1 Static Dead-zone Compensation

The valve to be controlled contains a dead-zone-saturation combination. While the saturation only limits the maximum output values, the dead-zone affects the valve's behavior around its origin in the range of  $\pm 10\%$  of the valves command, thus directly influencing

the closed-loop behavior. To overcome this issue a static dead-zone compensation is introduced. This is done by flipping the identified dead-zone of the system over a slope with unity gradient, so as to achieve best possible compensation results, cf. Fig. D.1. The

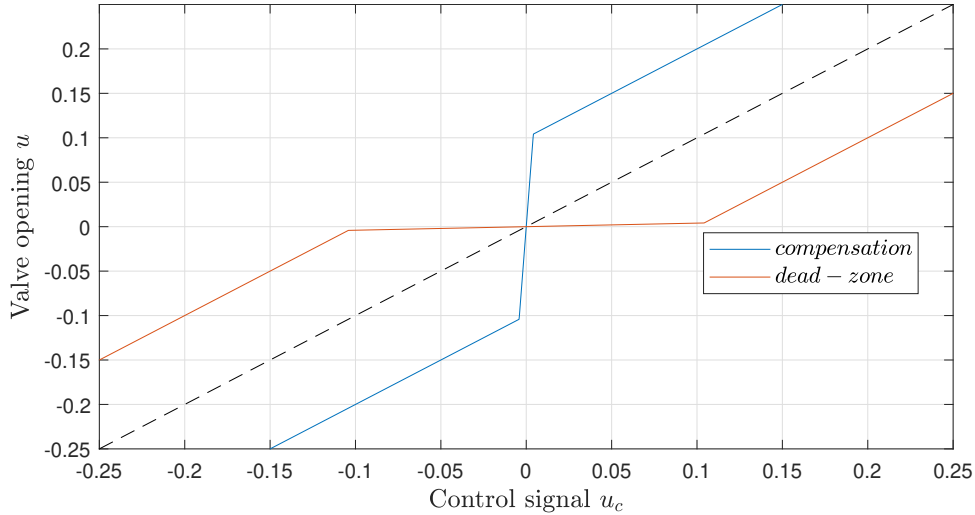


Figure D.1: Static dead-zone compensation

static compensator function is then linearized resulting in 3 linearisation regions described by

$$u = k_a u_c + d_a, \quad (\text{D.5})$$

where  $u_c$  is the control signal and  $u$  the input to the valve. The corresponding linearization regions (further denoted as cells) are indexed by  $a$ . As seen in the dead-zone analysis in [17], the dead-zone does not correspond to zero movement of the cylinder, therefore a slight slope in the range of  $\pm 10\%$  was used instead of  $k = 0$ , and the slope is not infinite for the respective part of the linearized dead-zone compensation.

### D.3.2 Integral Error State-Feedback Control

After feed forward compensating the dead-zone of the valve, a state-feedback controller was designed to follow the desired reference for each control strategy.

One should note that a rather classical cascaded control loop, consisting of an inner force controller with saturated control signal and an outer position control loop, always constitutes a trade-off between both. Well-known, the stiffness of an ideal force controller goes towards zero, while that of an ideal position controller towards infinity. Therefore, designing a combined position/force control mostly cannot comply with high performance specification of both arranged in a cascade manner. On the contrary, a hybrid, i.e. switching, position and force controller allows for meeting enhanced performance requirements by each one separately, while the design challenges shift to a reliable switching strategy



and corresponding transient behavior. Because of the mentioned above, a switched state feedback controller was implemented of the form

$$u_c = -\mathbf{k}(h)\mathbf{x} \quad (\text{D.6})$$

with  $\mathbf{k} = (K_1, K_2, K_3, K_4, K_i)$  to be the vector of control gains, determined separately for position ( $h = -1$ ) and force ( $h = 1$ ) control modes. Implementing the proposed controller results in the overall structure shown in Fig. D.2, where  $\gamma$  is the static dead-zone compensator.

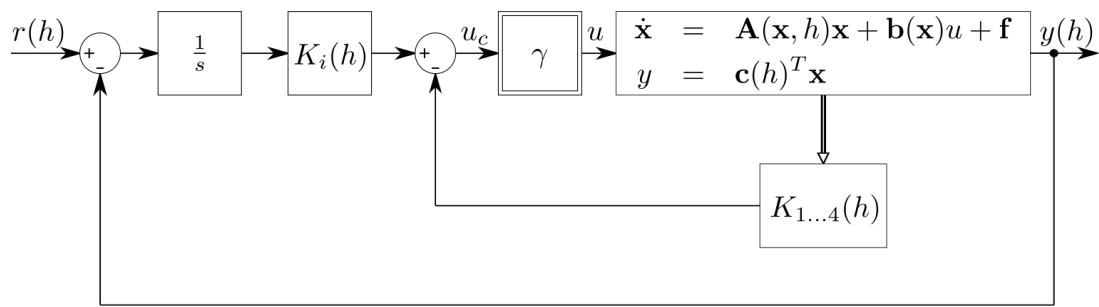


Figure D.2: Control Structure

The matrix and vectors of (D.3) and (D.4) are given by

$$\mathbf{A}(\mathbf{x}, h) = \begin{pmatrix} 0 & 1 & 0 & 0 & 0 \\ 0 & -\frac{k_w}{m} & \frac{\bar{A}}{m} & -\frac{1}{m} & 0 \\ a_{31} & a_{32} & a_{33} & a_{34} & a_{35} \\ 0 & 0 & 0 & 0 & 0 \\ -1 & 0 & 0 & 0 & 0 \end{pmatrix}, \quad h = -1$$

$$\mathbf{A}(\mathbf{x}, h) = \begin{pmatrix} 0 & 1 & 0 & 0 & 0 \\ 0 & -\frac{k_w}{m} & \frac{\bar{A}}{m} & -\frac{1}{m} & 0 \\ a_{31} & a_{32} & a_{33} & a_{34} & a_{35} \\ 0 & c & 0 & 0 & 0 \\ 0 & 0 & 0 & -1 & 0 \end{pmatrix}, \quad h = 1$$
(D.7)

with the coefficients given by

$$\begin{aligned}
 a_{31} &= -\frac{4Ek_gk_aK_1}{V_t}(k_nP_L^2 + d_nP_L + k_oP_L + d_o) \\
 a_{32} &= -\frac{4E}{V_t}(k_gk_aK_2(k_nP_L^2 + d_nP_L + k_oP_L + d_o) + \bar{A}) \\
 &\quad -\frac{4E}{V_t}(-k_gk_aK_3(k_nP_L^2 + d_nP_L + k_oP_L + d_o) \\
 a_{33} &= \quad \quad \quad +k_o(k_gd_a + d_g) + d_g(k_nP_L + d_n) \\
 &\quad \quad \quad +k_gd_a(k_nP_L + d_n) - C_L \\
 a_{34} &= -\frac{4Ek_gk_aK_4}{V_t}(k_nP_L^2 + d_nP_L + k_oP_L + d_o) \\
 a_{35} &= \frac{4Ek_gk_aK_i}{V_t}(k_oP_L + d_o + k_nP_L^2 + d_nP_L)
 \end{aligned} \tag{D.8}$$

with the rest of the vectors described by:

$$\mathbf{b} = \begin{pmatrix} 0 \\ 0 \\ 0 \\ 0 \\ 1 \end{pmatrix} \tag{D.9}$$

$$\mathbf{f} = \begin{pmatrix} 0 \\ -\frac{d_w}{m} \\ \frac{4E(k_gd_o d_a + d_o d_g)}{V_t} \\ 0 \\ 0 \end{pmatrix} \tag{D.10}$$

$$\begin{aligned}
 \mathbf{c}(h)^T &= (1 \ 0 \ 0 \ 0 \ 0), \quad h = -1; \\
 \mathbf{c}(h)^T &= (0 \ 0 \ 0 \ 1 \ 0), \quad h = 1;
 \end{aligned} \tag{D.11}$$

In the above equations,  $E$  describes the bulk modulus of the hydraulic fluid with  $V_t$  being the sum of volumes in the lines from the valve to the cylinder.  $\bar{A}$  is the averaged cross section of cylinder,  $m$  is the lumped mass moved in the system, and  $c$  is the spring constant of a *hard stop* against environment when the system is operated with force control.  $k$  and  $d$  with the corresponding indices refer to the different cells of linearization of the state space, cf. with (D.5).  $C_L$  is the leakage coefficient between both cylinder chambers.

### D.3.3 Filtering of Control Signal

High frequency components were observed in the valve response. This is directly related to the amplification of the noisy sensor signals. While the integrator smoothes the noise out, the state feedback control terms amplify the noise afflicted signals, thus resulting in a high frequency control signal fed to the valve. While the fast servo-valve is able to follow the reference, such high frequencies on the command signal are not desired, introducing unnecessary wear for the component. An analysis of the control signal showed, that the valve mainly operates at around 25% of its maximum opening which corresponds, according to the measured FRF (Frequency Response Function), to a cutoff frequency of about  $100Hz$ . Therefore, a second-order low-pass filter with a cut-off frequency of  $100Hz$  was inserted after the dead-zone compensation. This aims filtering out the higher frequencies of the control signal, while not slowing down the overall system dynamics.

### D.3.4 Event-based Switching

For the system to automatically switch between the position and force control a switching event  $h$  had to be defined. The system starts at  $t = 0s$  with  $x = 0$  and  $\dot{x} = 0$  with position control of following a given reference, in this case a ramp function, until it reaches a mechanical hard stop that should trigger switching from position to the force control and, correspondingly, reset the integral error. The event trigger is then the load force surpassing a predefined threshold. Analysis of sensor's signal showed that due to the noise, force peaks of up to  $1500N$  in either direction can be observed on top of the current value. Unsuitable threshold definition, therefore, could lead to a limit cycle behavior of periodically switching from force to position control and vice versa. To overcome this issue a delayed relay was introduced, defined by [18]

$$h(t) = \min[\text{sign}(F_H - \beta), \max[h(t_-), \text{sign}(F_H - \alpha)]] \quad (\text{D.12})$$

with the initial state

$$h(t_0) = \begin{cases} \text{sign}(F_H(t_0)) & \text{if } F_H(t_0) \in (-\infty, \beta) \vee (\alpha, \infty) \\ [-1, +1] & \text{otherwise} \end{cases} \quad (\text{D.13})$$

The previous to switching time instance is denoted by  $t_-$ , while the assigned parameters are  $\alpha = 1500N$ ,  $\beta = -1500N$ , and the relay's input value is assigned to be  $F_H = F_L - 2000N$ .

While the test setup has a mechanical hard stop which introduces a rapid increase of the measured force and therefore triggers switching between the controllers, in the simulation an artificial hard stop was created to verify the control functionality. The

hard stop is modeled as a high stiffness spring, without damping, based on the Youngs' modulus equation. Rearranging the equation leads to the spring constant

$$\frac{E_s A_s}{L_0} = \frac{F_L}{\Delta L} = c, \quad (\text{D.14})$$

where  $E_s = 210\text{GPa}$  is the Youngs' modulus of steel,  $A_s$  is the cross section of the "spring",  $L_0$  its non deformed length,  $\Delta L$  the deformation, and  $F_L$  the load force. As can be seen,  $F_L/\Delta L$  is equal to  $c$  and therefore only  $E_s$ ,  $A_s$  and  $L_0$  are needed for calculating the spring constant.

In the experimental setup, see further in section IV, the hard stop is reached once the left cylinder is fully retracted. The I-beam the cylinders are mounted to, cf. Fig. D.5, is assumed to be much stiffer than the combination of cylinder rods plus force sensor and therefore  $L_0 = 0.88\text{m}$ , being the summed length of both cylinder rods and force sensor, is assumed. While there are various components in that chain,  $A_s = 5\text{E}^{-4}\text{m}^2$  was assumed to be uniform and given by the cylinders cross section, leading to a spring constant of  $c = 1.2\text{E}^8\text{N/m}$ .

### D.3.5 Optimal State Feedback

For the designed control structure, the state feedback gains are determined as follows. A set of initial gain values was empirically determined first as a starting point for optimization. Different cost functions were assumed for each controller to achieve the desired outcome.

For position control, the cost function is given by

$$\min \int ((r - x)t + u_d t)^2 dt \quad (\text{D.15})$$

with  $r$  being a ramp reference with a slope of  $0.05\text{m/s}$ ,  $x$  the cylinder's position and  $u_d$  the difference between the control signal after dead-zone compensation and the signal after saturation of the valve. This is included to minimize not only the control error, but also the amount of control signals exceeding the maximum command input admissible by the valve. Multiplications with the time  $t$  were performed to punish deviations from the reference harder with increasing time. The initial set of gain values was  $[50, 0.001, 1\text{E}^{-8}, 1\text{E}^{-6}, 5000]$ . The convergence of the normalized gain values and the cost function are shown in Fig. D.3.

The cost function for the force control is given by

$$\min \int ((r - F_L)t)^2 dt. \quad (\text{D.16})$$

where  $r$  is the reference force defined to be  $3500\text{N}$  and  $F_L$  is the measured load force. Again the difference is multiplied by time to punish deviations from the reference harder

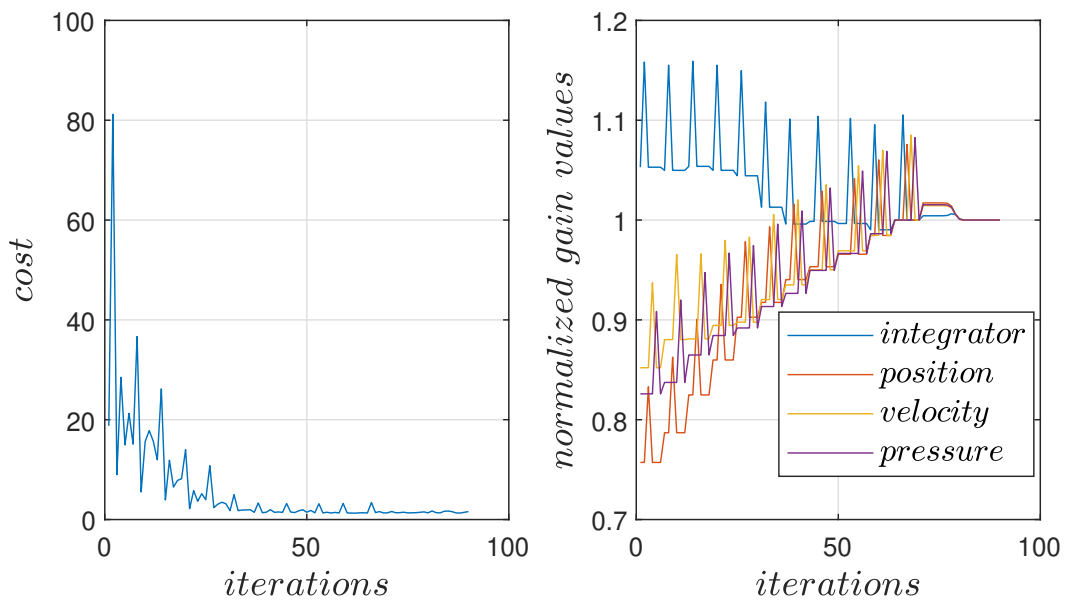


Figure D.3: Cost and gain value convergence for position control from (D.15)

with increasing time. Initial values for parameters were taken from previous measurements to be as close as possible to the real conditions. The initial set of gain values was  $\mathbf{K} = [6E^{-7}, 3E^{-4}, 5E^{-8}, 2E^{-5}, 1.4E^{-3}]$ ; this was determined empirically. The convergence of the gain values and minimization function are shown in Fig. D.4.

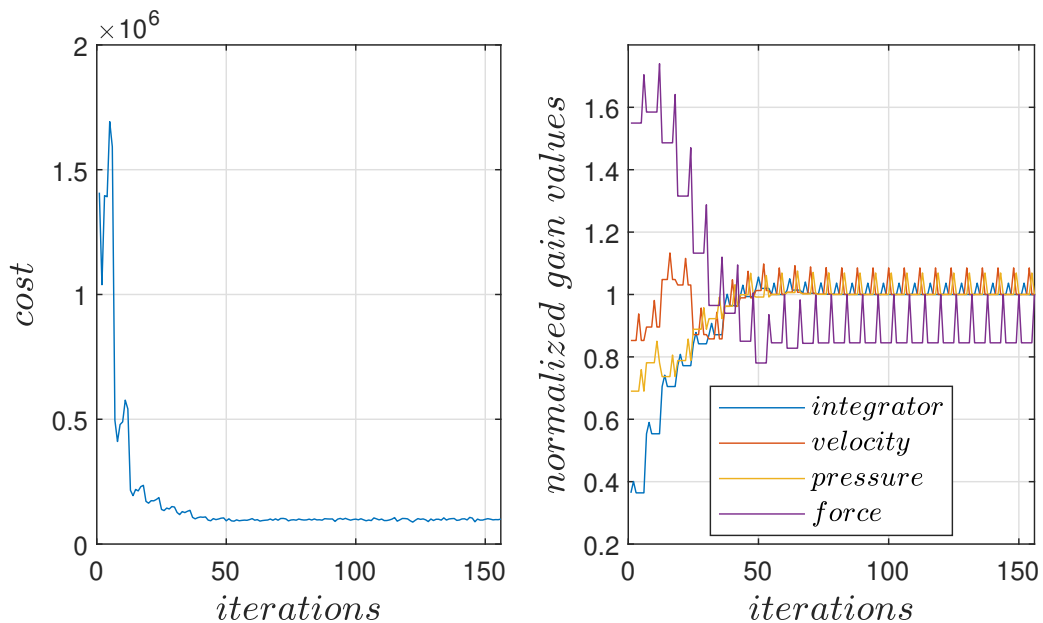


Figure D.4: Cost and gain value convergence for force control from (D.16)

Note that  $K_4$  was set to zero for position control because there is no external force acting against the cylinders movement. For the force control,  $K_1$  was set to zero because there is only negligible micro-movement once the hard stop is reached. The optimized

values for the control gains are shown in Table D.1.

Table D.1: Optimized gain values for position and force control

Gain parameter	Position control	Force control
$K_i$	$5E^3$	0.0014
$K_1$	73.3	0
$K_2$	$9E^{-4}$	$3.1E^{-4}$
$K_3$	$1.65E^{-8}$	$5E^{-8}$
$K_4$	0	$2.5E^{-9}$

## D.4 Experimental Evaluation

The experimental setup used in this work is shown in Fig. D.5, where the right cylinder-valve combination is to be controlled, while the force sensor is connecting both cylinders. A hard stop is reached by extending the right cylinder until the left cylinder is fully retracted. All state variables are measured and more details on the developed setup can be found in [17].

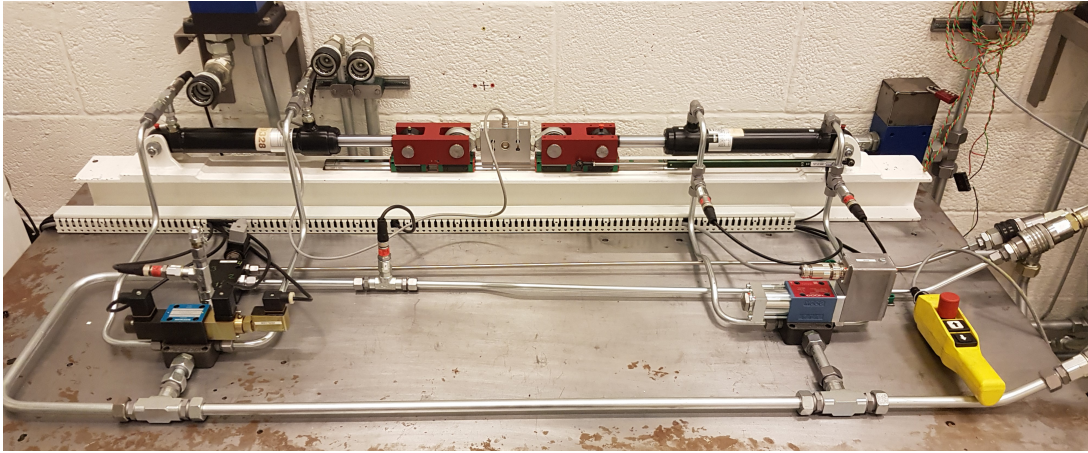


Figure D.5: Experimental setup of hydraulic cylinders

After confirming with simulations that the obtained control parameters lead to the desired system behavior, experiments on the laboratory setup were performed. For position control, the system was supposed to follow two different slopes of  $0.03m/s$  and  $0.07m/s$  starting from a fully retracted position, i.e.  $x_0 = 0$ ,  $\dot{x}_0 = 0$ , while the reference values for force control are  $3500N$  and  $7000N$  correspondingly. The measured values for the ramp with slope of  $0.03m/s$  and reference force of  $3500N$  are shown in Figs. D.6 and D.7, while

the measured position and force for the slope of  $0.07m/s$  and reference force of  $7000N$  are shown in Figs. D.8 and D.10.

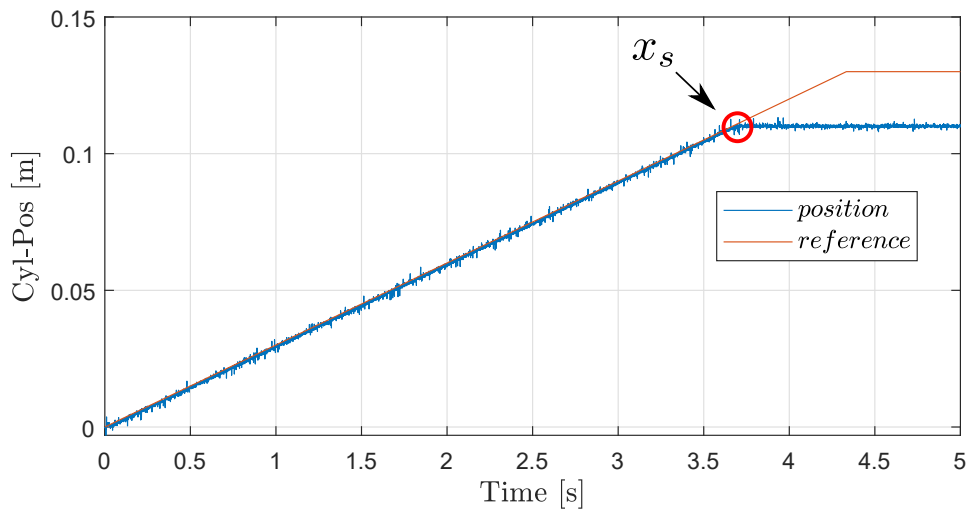


Figure D.6: Measured cylinder position and reference for ramp with  $0.03m/s$  slope

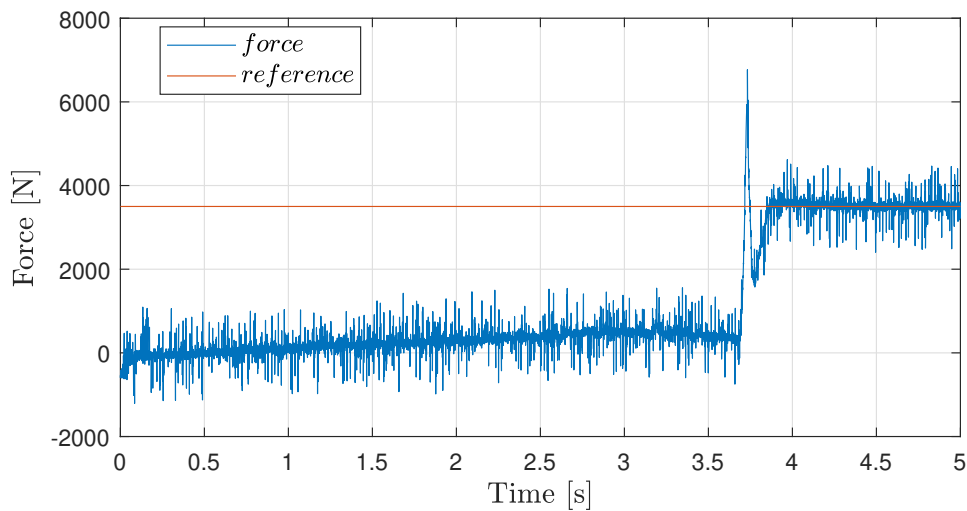


Figure D.7: Measured load force and reference for  $3500N$

As can be seen from the figures, the cylinder follows the reference position closely for both ramps until reaching the hard stop at a position of about  $x_s = 0.11m$  when a rapid increase of the measured force can be observed for both cases. Surpassing the threshold of  $3500N$  triggers the event switching from position to force control.

After a short transient the system reaches steady-state, holding a constant force against the hard stop for both cases according to their references. This also confirms, that the optimized gains are equally valid for varying reference signals. The validity of the simulation model and optimization routine is confirmed by determined gain factors equally suitable set for both simulated and real (measurement) control response. Taking a closer

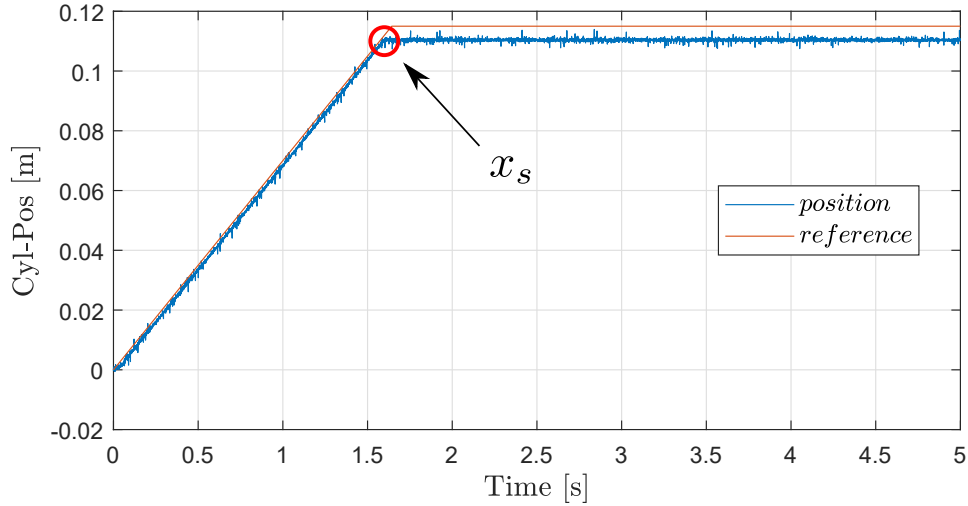


Figure D.8: Measured cylinder position and reference for ramp with 0.07m/s slope

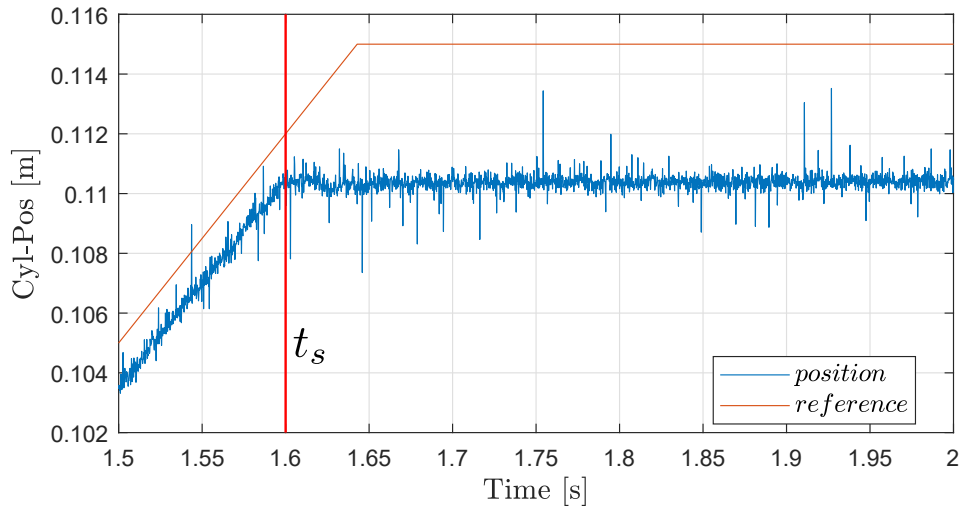


Figure D.9: Outtake of measured position and reference of ramp with slope of 0.07m/s

look at the position, exemplary for the ramp with a slope of  $0.07\text{m/s}$  as shown in Fig. D.9, it can be also observed that the cylinder is marginally penetrating into the hard stop around  $t_s = 1.6\text{s}$ , where the initial peak of the force is generated. This minimal penetration and well-matched transient to the force control response argues in favor of the designed event-based switching strategy.

Table D.2 shows numerical indicators for both measurements taken. ISE (Integral Square Error, (D.17)) and MSE (Mean squared error, (D.17)) show both relatively small errors for both cases for position control and rather high values for force control. Bare in mind, that due to the switch of the controller and the reset of the integral error at the point of switching and the initial force peaks due to the impact, the initial values of the force controller weigh into both criteria heavily. For the SSE (Steady State Error, (D.17)) an average, to compensate for the noise of the signal, of the values for position and force



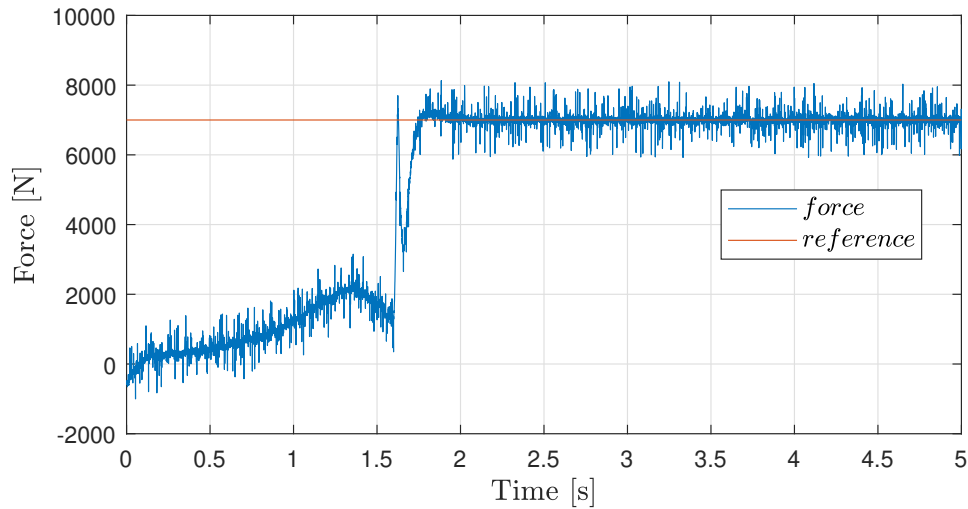


Figure D.10: Measured load force and reference for 7000N

Table D.2: Numerical Indicators

	0.03m/s, 3500N		0.07m/s, 7000N	
	<b>Position</b>	<b>Force</b>	<b>Position</b>	<b>Force</b>
<b>SSE</b>	$0.7E^{-3}\text{m}$	10.7N	$1.6E^{-3}\text{m}$	1.72N
<b>ISE</b>	0.012m	$1.25E^9\text{N}$	0.0237m	$3.72E^9\text{N}$
<b>MSE</b>	$5.65E^{-7}\text{m}$	$178E^3\text{N}$	$2.65E^{-6}\text{m}$	$197E^3\text{N}$

control were compared to the references once a steady state behavior was observed. As can be seen the state error in both cases for position and force control is very small.

$$\begin{aligned}
 ISE &= \int e^2 dt \\
 MSE &= \frac{1}{\delta} \sum_{i=1}^{\delta} e_i^2 \\
 SSE &= \frac{1}{\epsilon_{sse} - \epsilon_{ss}} \sum_{i=\epsilon_{ss}}^{\epsilon_{sse}} e_i
 \end{aligned} \tag{D.17}$$

whereas  $\delta$  is the number of samples for MSE analyzed for the respective control phase and  $\epsilon_{ss}$  the first and  $\epsilon_{sse}$  the last sample observed being in steady state condition for each control phase for SSE.

## D.5 Summary

The state-space model of a hydraulic cylinder affine in control and states was expanded. Based on the identified dead-zone, a pre-compensator was designed and an integral-error-state-feedback controller implemented. The proposed approach realizes a closed-loop sys-

tem capable of switching automatically between the position and force regulation depending on a measured mechanical resistance of environment. The trigger event initializing the switching from position to force control was introduced and the control gains for both integrator and state-feedback were found using optimization routines of position and force controls. A low-pass filter was added to the control signal while maintaining the comparably fast response of the overall system. Most important that a unified state feedback control structure has been developed equally suitable for both position and force control and well-matched switch between them. Practically close hydraulic experiments were performed and evaluated confirming efficiency of the proposed control approach and accuracy of the simulation model. As seen from simulations and measurements, the proposed hybrid system manages to follow the references, both before and after the switch from position to force control and reaches a steady state after a short transition period in both cases. Future works are to include stability analysis, starting from the local one and developing towards an extended over the whole operational state-space. Further analysis and experimental investigations towards switching back from the force to motion control are also of interest.

## Acknowledgment

This work has received funding from the European Union Horizon 2020 research and innovation programme H2020-MSCA-RISE-2016 under the grant agreement No 734832.

# REFERENCES

- [1] G. Liu and S. Daley. Optimal-tuning nonlinear PID control of hydraulic systems. *Control Engineering Practice*, 8(9):1045–1053, 2000. doi:10.1016/S0967-0661(00)00042-3.
- [2] Bin Yao, Fanping Bu, J. Reedy, and G.-C. Chiu. Adaptive robust motion control of single-rod hydraulic actuators: theory and experiments. *IEEE/ASME Transactions on Mechatronics*, 5(1):79–91, 2000. doi:10.1109/3516.828592.
- [3] M. Ruderman, D. Weigel, F. Hoffmann, and T. Bertram. Extended SDRE control of 1-DOF robotic manipulator with nonlinearities. Proc. 18th IFAC World Congress, 2011.
- [4] S. Koch and M. Reichhartinger. Observer-based sliding mode control of hydraulic cylinders in the presence of unknown load forces. *Elektrotechnik und Informationstechnik*, 133(6):253–260, 2016. doi:10.1007/s00502-016-0418-6.
- [5] C. Vazquez, S. Aranovskiy, L. Freidovich, and L. Fridman. Second order sliding mode control of a mobile hydraulic crane. In *53rd IEEE Conference on Decision and Control*, pages 5530–5535, 2014. doi:10.1109/CDC.2014.7040254.
- [6] A. Alleyne and R. Liu. A simplified approach to force control for electro-hydraulic systems. *Control Engineering Practice*, 8(12):1347–1356, 2000. doi:10.1016/S0967-0661(00)00081-2.
- [7] N. Niksefat and N. Sepehri. Design and experimental evaluation of a robust force controller for an electro-hydraulic actuator via quantitative feedback theory. *Control Engineering Practice*, 8(12):1335–1345, 2000. doi:10.1016/S0967-0661(00)00075-7.
- [8] J. Komsta, N. van Oijen, and P. Antoszkiewicz. Integral sliding mode compensator for load pressure control of die-cushion cylinder drive. *Control Engineering Practice*, 21(5):708–718, 2013. doi:10.1016/J.CONENGPAC.2011.12.006.

- [9] S. Katsura, Y. Matsumoto, and K. Ohnishi. Analysis and experimental validation of force bandwidth for force control. *IEEE Transactions on Industrial Electronics*, 53(3):922–928, 2006. doi:10.1109/TIE.2006.874262.
- [10] O. Khatib. A unified approach for motion and force control of robot manipulators: The operational space formulation. *IEEE Journal on Robotics and Automation*, 3(1):43–53, 1987. doi:10.1109/JRA.1987.1087068.
- [11] M. H. Raibert and J. J. Craig. Hybrid Position/Force Control of Manipulators. *Journal of Dynamic Systems, Measurement, and Control*, 103(2):126, 1981. doi:10.1115/1.3139652.
- [12] W.-H. Zhu, S. Salcudean, S. Bachmann, and P. Abolmaesumi. Motion/force/image control of a diagnostic ultrasound robot. In *Proceedings ICRA. Millennium Conference. IEEE International Conference on Robotics and Automation. Symposia Proceedings*, volume 2, pages 1580–1585, 2000. doi:10.1109/ROBOT.2000.844822.
- [13] G. Roppenecker. State Feedback Control of Linear Systems — a Renewed Approach. *at - Automatisierungstechnik*, 57(10), 2009. doi:10.1524/auto.2009.0796.
- [14] H. C. Pedersen and T. O. Andersen. Pressure Feedback in Fluid Power Systems—Active Damping Explained and Exemplified. *IEEE Transactions on Control Systems Technology*, 26(1):102–113, 2018. doi:10.1109/TCST.2017.2650680.
- [15] J. K. Sørensen, M. R. Hansen, and M. K. Ebbesen. Novel concept for stabilising a hydraulic circuit containing counterbalance valve and pressure compensated flow supply. *International Journal of Fluid Power*, 17(3):153–162, 2016. doi:10.1080/14399776.2016.1172446.
- [16] M. Ruderman. Full- and reduced-order model of hydraulic cylinder for motion control. In *43rd Annual Conference of the IEEE Industrial Electronics Society*, pages 7275–7280, 2017. doi:10.1109/IECON.2017.8217274.
- [17] P. Pasolli and M. Ruderman. Linearized Piecewise Affine in Control and States Hydraulic System: Modeling and Identification. IECON2018 - 44th Annual Conference of the IEEE Industrial Electronics Society, 2018.
- [18] M. Ruderman. Computationally Efficient Formulation of Relay Operator for Preisach Hysteresis Modeling. *IEEE Transactions on Magnetics*, 51(12):1–4, 2015. doi:10.1109/TMAG.2015.2455517.

# Paper E

## Hybrid Position/Force Control for Hydraulic Actuators

Philipp Pasoli, Michael Ruderman

This paper has been submitted as:

P. Pasoli, M. Ruderman. Hybrid Position/Force Control for Hydraulic Actuators.  
Under review at *IEEE Transactions on Industrial Electronics*.

# Hybrid Position/Force Control for Hydraulic Actuators

Philipp Pasolli, Michael Ruderman

University of Agder

Department of Engineering Sciences

Jon Lilletunsvai 9, 4879 Grimstad, Norway

*Abstract* – In this paper a novel hybrid position/force control with autonomous switching between both control modes is introduced for hydraulic actuators. A full-order model which describes the system dynamics is first derived for simulation and analysis, including servo-valve, orifice equations, hydraulic continuity equations and mechanical subsystem. A reduced model, in its linearizable form, is used to simplify the control design and stability analysis. A hybrid position/force control structure with feed-forwarding, full-state feedback, including integral control error, and pre-compensator of the dead-zone nonlinearity followed by the low-pass filtering of control value, is designed. Controller gains are obtained via local linearization and pole placement accomplished for the position and force control separately. A hysteresis-based autonomous switching is integrated into the closed control loop, while multiple Lyapunov function based approach is applied for stability analysis of the hybrid control system. Experimental evaluation is shown on the developed test rig, with standard industrial hydraulic cylinders, for different motion and load profiles.

## E.1 Introduction

Different actuators are used in most mechatronic applications. While electric motors, linear drives, or pneumatic actuators are well suitable for a fast system response, hydraulic actuators are still the first choice if compact form factor combined with high power density and reliability are demanded, see [1, 2] for backgrounds. At the same time, hydraulic actuators are also well known for their nonlinearities and the challenges which come alongside if used with the closed-loop force or motion control. To implement a suitable control strategy and tune the control parameters accordingly, an in-depth system knowledge is required for a detailed modeling and identification of unknown parameters. While often simplified system models, linearized around a certain operational point, are used [3, 4, 5, 6], a more complex modeling yields inherently more accurate analysis and

simulation of hydraulic (sub)systems, as shown e.g. in [7] for a decomposed proportional valve. This level of modeling demands explicit knowledge of not only the overall setup but also the subsystems, down to the e.g. mechanical design of subcomponents. Although a such in-depth analysis of the system parameters is less feasible under regular operation conditions, many studies aim to consider extended and often full-order system dynamics, also incorporating nonlinearities nested within electric, mechanical and hydraulic subsystems [8, 9, 10, 11]. In this paper, only major sources of nonlinearities are attempted to be taken into account, while deriving a full-order model of the system under investigation, including the parameters identification in the principal subsystems. One can note that among various control-oriented strategies for modeling and identification of hydraulic systems, following approaches can be distinguished as the state-dependent (partially) linearized [12], piecewise affine [13, 14], and local linear, like Fourier transforms [15] based of the quantitative feedback theory, which are particularly suitable for a robust linear design.

Several applications using the hydraulic actuators are repetitive and tedious for human operators, e.g. excavators, but remain yet to be controlled manually. During an, at least, semi-automatic control emerges in these fields, the widespread PID-controllers keep yet standard also in those applications. While improvements like optimal design of PID-control with non-linear extensions were reported [5], other research promotes different control strategies like for example adaptive control or variable structure control, showing often a superior performance to the classic PID-controllers, see e.g. [16, 17, 11]. When a hydraulically actuated equipment or machine interacts with environment, like given example of an excavator, the use of position control only can be destructive due to inherently stiff control properties. In that case a force-based control approach is necessary. Several force control strategies for hydraulic systems were proposed [3, 8, 18], while the force control issues are equally well-known in robotics and mechatronics, see e.g. [19]. However, for a fully automatic operation of such equipment, a combination of force and position control should be taken into consideration, where the individual controllers can be switched, correspondingly reconfigured upon the motion constraints and interaction with the environment. Such hybrid control approaches remain topical, even though addressed former in robotics e.g. [20, 21].

In this paper, a hybrid position and force control approach is pursued based on a feed-forwarding and full-state feedback, including the integral control error. An appropriate hysteresis-based switching strategy is integrated into the closed feedback loop, while changing between the parameter settings of both control modes. Remarkable is that the derived control structure itself does not change and, therefore, represents an uniform architecture for the position and force control simultaneously. Some preliminary results of



this work have been partially reported in [14, 22]. In the recent work, we present the fully developed hybrid position/force control with extended design, analysis, and evaluation. The rest of the paper is structured as following. In Section II, the detailed system description, including experimental setup and modeling, are provided. Section III describes the proposed control architecture, control gains tuning, linearized system behavior, and local stability analysis based on [23]. An exhaustive experimental control evaluation is reported in Section IV. Finally, the paper’s summary in Section V.

## E.2 System Description

In this section an overview of the experimental setup (depicted in Fig. E.1) is first given. The right-hand side, which is the combination of servo valve and linear cylinder, will then be described together with the derived full-order model. For the standard modeling equations in use we refer to the basic hydraulics literature e.g. [1, 2] for further details.

### E.2.1 Hydraulic Actuator Setup

The recent system is a hydraulic setup with two cylinders arranged in an antagonistic way. The right-hand cylinder is attached to the 4/3 servo valve, with an internal closed-loop control, connected to the HPU (hydraulic power unit) which is supporting up to 350 bar and 120 l/min. The left-hand cylinder is connected to the valve which is only used at fully open states to change the flow direction, further referred to as BDCV (bi-directional control valve), which is connected to the PRV (pressure relief/reduction valve). The latter has a direct inlet connected to the HPU line. Pressure sensors are attached to the right and left chambers of the cylinders, to the line between PRV and BDCV, and on the interface to HPU. An absolute position sensor is attached to the right-hand cylinder, while the servo valve spool position can also be monitored and read out. A force sensor, with rigid mechanical interface, is installed and connects both cylinder rods with each other. Fig. E.1 shows the laboratory view of the experimental setup.

As control interface, the Speedgoat real-time (RT) target Baseline S was used with interfacing cards IO183 and IO397. The RT board is running the closed-loop control, sending and receiving the analog signals to and from the setup correspondingly. The RT target allows for a sampling frequency of 2 kHz while both cards support 16 bit A/D and D/A converters respectively. The input voltage level supports  $\pm 10V$ , while output voltages are in the range of 0-5V and  $\pm 10V$  respectively, with a maximum current draw of 5mA. In addition, a hard-wired emergency break circuit was installed, setting all valves into zero state and, therefore, stopping all motion and releasing the remaining pressure, correspondingly force, from the system. The setup components are listed in Table E.1.

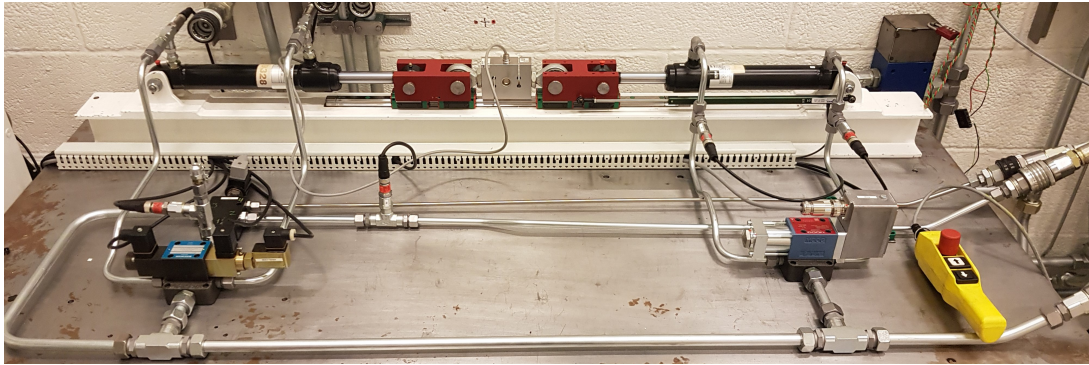


Figure E.1: Experimental setup of hydraulic actuators

Table E.1: Hardware components of experimental setup

Description	Model number
Moog servo valve	D633 R16KD1M0NSM2
Cylinder	CD25-40 25x200-SS-HC-SSN-NNN
Danfoss P-sensor	MBS 1250 063G1229
Parker P-sensor	SCP01-400-44-07
Celeco linear-pot.	CLP-250
HBM Force sensor	S9M/20kN

## E.2.2 System Modeling

While only the right-hand cylinder, correspondingly servo valve, cf. Fig. E.1, are to be controlled, a full-order model is derived below. The developed model is used for the plant and controlled system simulation and validation before integration on the hardware. A series of dedicated experiments was accomplished to identify several free (unavailable) parameters of the following system modeling. Residual standard components parameters were determined based on the available data sheets. Due to the space limits and more control-oriented focus of the recent work, the details of system identification are not included and the interested reader is referred to [14, 22].

### E.2.2.1 Servo valve model

The servo valve to be modeled is internally low-level controlled and can be approximated as a second-order system with the transfer function

$$G(s) = \frac{\nu(s)}{u(s)} = \frac{\omega_0^2}{s^2 + 2\zeta\omega_0s + \omega_0^2}, \quad (\text{E.1})$$

where  $\nu$  describes the spool position and  $u$  the control signal. The characteristics of the closed-loop system are defined by its natural frequency  $\omega_0$  and damping factor  $\zeta$ . As can be seen in the FRF (frequency response function) of the valve data sheet, cf. [14]  $\omega_0$  and  $\zeta$  vary depending on the amplitude of the control signal  $|u|$ . Due to the valve overlap, of 10%, in the spool-orifice area introduced by its mechanical construction, a static input dead-zone is assumed. In addition, the spool experiences mechanical end stops in either direction, thus introducing a saturation effect. The combination of dead-zone and saturation can be expressed as in [24] by

$$g(\nu) = \begin{cases} \alpha \cdot \text{sign}(\nu), & \text{if } |\nu| \geq \alpha + \beta \\ 0, & \text{if } |\nu| < \beta \\ \nu - \beta \cdot \text{sign}(\nu), & \text{otherwise,} \end{cases} \quad (\text{E.2})$$

where  $\alpha$  and  $\beta$  describe the valves' saturation and dead-zone properties respectively. The valve dynamics and dead-zone/saturation nonlinearity are inherently serial connected due to mechanical structure of the valve. Since the dead-zone and saturation can have non-negligible impact on the overall system performance, they have to be incorporated into modeling. That was however only partially accounted for, or neglected, in several previous works [8, 25, 3, 11, 10]. The sub-model of the valve can therefore be described as

$$\ddot{\nu} + 2\zeta\omega_0\dot{\nu} + \omega_0^2\nu = \omega_0^2u, \quad (\text{E.3})$$

$$z = g(\nu), \quad (\text{E.4})$$

with  $z$  representing the output orifice opening of the valve.

### E.2.2.2 Orifice equations

The hydraulic flow  $Q$  through the valve is described by the orifice equations based on the pressure drop over the valve. Since two lines are connecting the valve to cylinder, the two corresponding flow equations are

$$Q_A = \begin{cases} zK\sqrt{P_S - P_A} & \text{for } z > 0 \\ zK\sqrt{P_A - P_T} & \text{for } z < 0 \\ 0 & \text{otherwise,} \end{cases} \quad (\text{E.5})$$

$$Q_B = \begin{cases} zK\sqrt{P_B - P_T} & \text{for } z > 0 \\ zK\sqrt{P_S - P_B} & \text{for } z < 0 \\ 0 & \text{otherwise.} \end{cases} \quad (\text{E.6})$$

The pressure indices  $A, B, P, S$  refer to the respective ports of the valve, where  $A$  and  $B$  correspond to the connecting lines to cylinder (sometimes referred to as A and B chambers),

$S$  to the HPU line (meaning supply), and  $T$  to the tank line.  $K$  is the valve flow coefficient given by

$$K = c_d w \sqrt{\frac{2}{\rho}}, \quad (\text{E.7})$$

where  $c_d$  and  $w$  represent the structural valve parameters and  $\rho$  is the oil density. While several valve parameters are weakly known, the available manufacturer data sheet reveals

$$Q = Q_n \sqrt{\frac{\Delta p}{p_n}}, \quad (\text{E.8})$$

which describes the flow as a function of the pressure drop  $\Delta p$ , the nominal flow  $Q_n$  and the nominal pressure  $p_n$  in a fully open state, while the latter two are known from the data sheet. From the above it can be seen that the flow coefficient  $K$  is equivalent to  $Q_n(p_n)^{-1/2}$ , therefore omitting necessity to identify the  $c_d$  and  $w$  parameters.

### E.2.2.3 Continuity equations

Knowing the valves flow for either line, the pressure drop can be calculated as

$$\begin{aligned} \dot{P}_B &= \frac{E}{V_B + A_B(l - x)} \cdot (Q_B + A_B \dot{x} + C_L (P_A - P_B)), \\ \dot{P}_A &= \frac{E}{V_A + A_A x} \cdot (Q_A - A_A \dot{x} + C_L (P_B - P_A)). \end{aligned} \quad (\text{E.9})$$

In the equations above  $E$  constitutes the bulk modulus reflecting compressibility of the hydraulic fluid,  $V_A$  and  $V_B$  are the hydraulic fluid volumes in the connecting lines,  $A_{A/B}$  are the cross sections of the respective chambers of cylinder,  $l$  is the maximal piston stroke, and  $x$  is the relative piston position, while  $\dot{x}$  is correspondingly the relative velocity.  $C_L$  represents the leakage coefficient between both chambers.

### E.2.2.4 Mechanical subsystem

The relative motion of the piston rod can be described by the second-order dynamics, with one DOF (degree of freedom), as

$$m\ddot{x} = P_A A_A - P_B A_B - f(\dot{x}) - F_L, \quad (\text{E.10})$$

with  $F_L$  being an external load acting axial on the stiff rod interface, and  $m$  being the lumped mass of all moving parts. The latter is an accumulated value from the respective data-sheets of the mechanical components in the drive chain. The non-linear Stribeck friction force, cf. [26], is included by  $f(\dot{x})$ . To avoid discontinuities in the static friction model, see e.g. [25, 27] for details, the signum term is replaced by a tangent hyperbolic function, cf. [24], resulting in

$$f(\dot{x}) = \tanh(\gamma \dot{x}) \left( F_c + (F_s - F_c) \exp\left(-\left|\frac{\dot{x}}{\chi}\right|^\delta\right) \right) + \sigma \dot{x}. \quad (\text{E.11})$$

Here  $F_c > 0$  describes the Coulomb friction constant.  $F_s > F_c$  refers to the stiction friction coefficient, while  $\sigma$  characterizes the viscous friction term. The parameters  $\delta \neq 0$  and  $\chi > 0$  are the Stribeck shaping factors. Finally,  $\gamma$  relates to the hyperbolic tangent and adjusts the transitions smoothness at zero-crossing, until the function saturates at  $\pm 1$  depending on the velocity sign. While more complex dynamic friction behavior can be taken into account, see e.g. [28, 29, 27, 26], the chosen model was deemed to be satisfying due to the cylinder being a slow moving and heavily damped system [25, 3, 24].

### E.3 Control Design

This Section discusses the control architecture, while describing the entire closed-loop control system. That includes the feed-forward dead-zone compensation and control signal filtering, determining the control parameters, defining the switching strategy, and providing the local stability analysis.

In order to simplify the control synthesis, a model reduction, correspondingly linearization, was made. Out of that a piecewise linear model suitable for the control parametrization via pole placement and analysis was obtained. It is worth noting that the closed-loop control system simulations, and therefore numerical evaluation of the nominal design, were further performed using the full-order model provided in Section E.2. In the valve transfer characteristics, see [14], a unity gain can be observed up to the frequency of about 10Hz, even for 90% opening. The reference signals specified for both, simulations and experiments, are not exceeding that frequency. Therefore, the internal valve dynamics are largely neglected, hence, resulting in  $u = \nu$ . For further model reduction a load-dependent pressure is introduced as  $P_L = P_A - P_B$  with  $|Q_A| = |Q_B|$ , cf. [1], resulting in an aggregated equation

$$Q_L = zK\sqrt{\frac{1}{2}(P_S - \text{sign}(z)P_L)}, \quad (\text{E.12})$$

while it is valid

$$P_A = \frac{P_S + P_L}{2}, \quad P_B = \frac{P_S - P_L}{2}. \quad (\text{E.13})$$

Both continuity equations are, same way, reduced to one

$$\dot{P}_L = \frac{4E}{V_t}(Q_L - \bar{A}\dot{x} - C_L P_L), \quad (\text{E.14})$$

where  $V_t = V_A + V_B$  and  $\bar{A} = 0.5(A_A + A_B)$ . Note that inside of an ideal cylinder, the leakage coefficient between both chambers is further assumed to be zero i.e.  $C_L = 0$ . The piston rod dynamics (E.10) can then be expressed as

$$m\ddot{x} = P_L\bar{A} - f(\dot{x}) - F_L. \quad (\text{E.15})$$

Since the above reduced model still contains some nonlinear terms, (E.12) can be linearized around an operational point as

$$\hat{Q}_L = \hat{C}_q z + \hat{C}_{qp} P_L, \quad (\text{E.16})$$

with

$$\hat{C}_q = \left. \frac{\partial \hat{Q}_L}{\partial z} \right|_{\hat{P}_L}, \quad \hat{C}_{qp} = \left. \frac{\partial \hat{Q}_L}{\partial P_L} \right|_{\hat{z}}, \quad (\text{E.17})$$

often referred to as the flow-gain and flow-pressure coefficients, correspondingly. The Stribeck friction term in (E.15) is linearized as well, so as to allow for the state-space representation of the whole system dynamics. For an operation range under consideration the Stribeck function  $f(\dot{x})$ , can also be linearized in a piecewise affine form as

$$\hat{f}(\dot{x}) = k_s \dot{x} + d_s. \quad (\text{E.18})$$

The entire linearized state-space model of the plant is

$$\begin{aligned} \dot{\mathbf{x}} &= \mathbf{A}\mathbf{x} + \mathbf{b}u + \mathbf{f}, \\ y &= \mathbf{c}\mathbf{x}, \end{aligned} \quad (\text{E.19})$$

where  $\mathbf{x} = (x, \dot{x}, P_L, F_L)^T$  is the state vector, inclusive the external load force  $F_L$ . The system matrix, input coupling, affine term, and output coupling vectors are given by

$$\mathbf{A} = \begin{bmatrix} 0 & 1 & 0 & 0 \\ 0 & -\frac{k_s}{m} & \frac{\bar{A}}{m_k} & -\frac{1}{m} \\ 0 & -\frac{4E\bar{A}}{V_t} & \frac{4E\hat{C}_{qp}}{V_t} & 0 \\ 0 & 0 & 0 & 0 \end{bmatrix}, \quad (\text{E.20})$$

$$\mathbf{b} = \begin{bmatrix} 0 \\ 0 \\ \frac{4E\hat{C}_q k_q}{V_t} \\ 0 \end{bmatrix}, \quad \mathbf{f} = \begin{bmatrix} 0 \\ -\frac{d_s}{m} \\ \frac{4E\hat{C}_q d_q}{V_t} \\ 0 \end{bmatrix}, \quad \mathbf{c}^T = \begin{bmatrix} 1 \\ 0 \\ 0 \\ 0 \end{bmatrix}, \quad (\text{E.21})$$

correspondingly. It is worth emphasizing that the modeled load force, as a state, provides zero eigen-dynamics since being an exogenous external quantity. Note that the above state-space model is configured to have the piston position as output value. This will be reconfigured next when switching between the position and force control.

### E.3.1 Hybrid Control Structure

The proposed control architecture includes the feed-forward and integral-error- and full-state-feedback. While a more classical architecture would refer to a cascaded structure,

where the inner-loop represents a force control and the outer-loop the position control, such control approaches have considerable drawbacks. An ideal force control tends to zero control stiffness, while an ideal position control stiffness tends towards infinity. Therefore a cascaded combination would always constitute a tradeoff and offer a suboptimal performance when targeting the position and force control simultaneously.

For enhancing the control performance of both operation modes, a hybrid switched position/force control was developed, see Fig. E.2. Note that an additional vector of external disturbances  $\Psi(t)$  is drawn, for the sake of completeness, although not explicitly modeled or analyzed due to limited process knowledge. For the rest of the paper,  $h$  represents the discrete switching event variable and therefore the corresponding operation mode, with  $h = -1$  for the position and  $h = 1$  for the force control. Note that the hybrid position/force control structure remains the same upon switching and allows for control parameters to be determined separately, so as to meet the performance requirements in both cases.

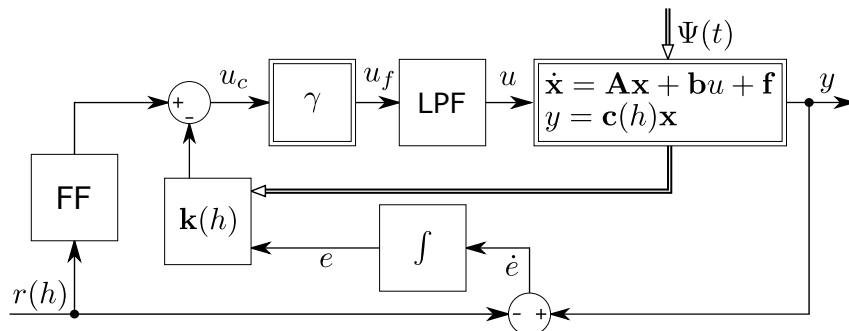


Figure E.2: Block-diagram of the hybrid position/force control

For the closed-loop control system the state vector of (E.19) is extended by an additional integral control error state with  $\dot{e} = y - r(h)$  dynamics, thus resulting in  $\mathbf{x}_e = (\mathbf{x}^T, e)^T$ . Here  $r(h)$  is the control reference value, while the output  $y$  depends on the control mode and is switched through the output coupling vector  $\mathbf{c}(h)$ . Note that in order to accommodate the integral error state, the system matrix (E.20) and vectors (E.21) of the state-space model are directly extendable to  $\mathbf{A}_e \in \mathbb{R}^{5 \times 5}$  and  $\mathbf{b}_e, \mathbf{c}_e^T, \mathbf{f}_e \in \mathbb{R}^{5 \times 1}$ . The resulting control law is then

$$u_c = \text{FF} r(h) - \mathbf{k}(h)\mathbf{x}_e, \quad (\text{E.22})$$

where  $\mathbf{k}(h) = (K_1, K_2, K_3, K_4, K_i)$  is the vector of control gains, which are determined separately for position and force control. FF represents the feed-forward control part, which is a single gain value for the given structure, and that  $\text{FF} = K_1$  for position control and  $\text{FF} = K_4$  for force control. The overall control structure, as in Fig. E.2, includes also a pre-filtering dead-zone compensator  $\gamma$  and low-pass filtering (LPF) of the control signal, both addressed below in more detail.

### E.3.2 Dead-zone Compensation

As shown before in Section E.2.2.1, the servo valve is subject to a dead-zone nonlinearity due to the mechanical assembly. While the saturation only limits the maximum control amplitude, the dead-zone, on the contrary, can significantly affect the closed-loop performance. This is apparent since the control signal within the range of  $-10\% \leq u \leq 10\%$  will result in no flow and therefore no rod movement. To overcome this issue, a dead-zone compensator is designed in an inverting feed-forward manner. The static compensator is obtained by flipping the linearized dead-zone characteristics over a slope with unity gradient. The compensator is also split into three linearisation regions, further denoted as cells, which are described by

$$u_f = \gamma(u_c) = k_a u_c + d_a, \quad (\text{E.23})$$

with  $k$  and  $d$  representing the linearization constants and index  $a \in \{1, 2, 3\}$  referring to the corresponding cells. From experimental analysis of the valve behavior it is given that no absolute zero movement appears close to the  $u = \pm 10\%$  thresholds, and some minor and slow flow drift occurs also at  $|u| < 10\%$ . For that reason and in order to avoid the control discontinuities at zero crossing of the  $\gamma$ -map, a steeply slope for  $a = 2$  was chosen instead of  $k_a = \infty$ , which corresponds to the  $\beta \text{sign}(u_c)$  with some  $\beta > 0$  scaling factor.

### E.3.3 Filtering of Control Signal

Due to a relatively high level of both the process and measurement noise in the system, a low-pass filtering appears indispensable for controller implementation on the hardware. While the servo valve is well-capable of following the control signal up to certain frequencies, cf. [14], high-frequent control components are not desired due to possible wear and damage of the mechanical and hydraulic parts. At the same time, the full-state feedback controller poses inherent limitations on filtering the single measured system states, that due to a possible loss of the phase conditions and individually lagged dynamics of the single states. Therefore, a low-pass filter is applied to the control signal, after the dead-zone pre-compensation, thus resulting in entirely smoothing the mechanical system excitation and avoiding chattering. The numerical analysis of the closed-loop control system behavior confirmed that the valve is operating within 25% opening, that for the given test scenarios. This corresponds to the cutoff frequency of 100Hz, cf. [14]. Following to that, the LPF cutoff frequency was set to the same 100Hz, for not additionally restricting the actuator dynamics.



### E.3.4 Event-based Switching

A discrete switching event  $h$  determines which control mode is active at any instance of time. Using a simple relay function to switch between the control modes is not deemed viable due to the sensor noise, possibly introducing the non-conclusive switching and undesirable dead-lock of the operational state of the hybrid control system. Instead, a hysteresis relay was chosen, resulting in an amplitude-delayed and therefore robust switching between the control operation modes. The hysteresis switching function [27] is given by

$$h(t) = \min[\text{sign}(F_H - \beta), \max[h(t_-), \text{sign}(F_H - \alpha)]], \quad (\text{E.24})$$

with the initial state

$$h(t_0) = \begin{cases} \text{sign}(F_H(t_0)) & \text{if } F_H(t_0) \in (-\infty, \beta) \vee (\alpha, \infty), \\ [-1, +1] & \text{otherwise.} \end{cases} \quad (\text{E.25})$$

The term  $t_-$  represents the time instant prior (immediately before) the switching, while  $\alpha = 1500N$  and  $\beta = -1500N$  represent the set threshold values. The delta between  $\alpha$  and  $\beta$  was chosen according to the observable peak to peak amplitudes of the noisy force sensor signal. The relay input is  $F_H = F_L - \xi$  where  $\xi = 2000N$  was assigned as the load force offset which shifts the switching hysteresis relay along the  $F_L$ -state axis. Note that the integral control error  $e$  is reset to zero every time  $h(t)$  changes its discrete value.

### E.3.5 Determining of Control Gains

The control gain parameters are determined via standard pole placement accomplished for the linearized models, that separately for the position and force control modes. The pole placement is made for the test case scenarios, the same which are lately evaluated with experiments. The controlled rod displacement is driven with a constant speed until it reaches a hard stop (by environment), that triggers an autonomous switching to the force control at which the rod is holding a constant force. Since the steady-state velocity and force are defined by reference, the residual state values required for model linearization are extrapolated from the simulation of the full-order (nonlinear) model, cf. Section E.2.

The state-space model (E.19) does not allow for directly using the pole placement, that due to inclusion of the affine terms. In order to deal with affine vector  $\mathbf{f}_e$ , that when deriving the state-space form applicable for pole placement, the state vector is further extended to  $\bar{\mathbf{x}} = [\mathbf{x}_e^T, 1]^T$ , thus resulting in

$$\dot{\bar{\mathbf{x}}} = \begin{bmatrix} \dot{\mathbf{x}}_e \\ 0 \end{bmatrix} = \bar{\mathbf{A}}\bar{\mathbf{x}} + \bar{\mathbf{b}}r = \begin{bmatrix} \mathbf{A}_e & \mathbf{f}_e \\ \mathbf{0} & 0 \end{bmatrix} \bar{\mathbf{x}} + \begin{bmatrix} \mathbf{b}_e \\ 0 \end{bmatrix} r, \quad (\text{E.26})$$

with the output coupling vector extended to  $\bar{\mathbf{c}} = [\mathbf{c}_e, 0]$ . This allows establishing the set of two state-space forms, where the switching discrete state  $h = [-1, 1]$  refers to the position and force control respectively. The overall hybrid control system, in the linearized form, is then defined by

$$\begin{aligned}\dot{\bar{\mathbf{x}}} &= \bar{\mathbf{A}}(h)\bar{\mathbf{x}} + \bar{\mathbf{b}}(h)r(h), \\ y &= \bar{\mathbf{c}}(h)\bar{\mathbf{x}}.\end{aligned}\tag{E.27}$$

Since the feedback control design relies on the linearized modeling at steady-state operational conditions, following assumptions/simplifications can be made for obtaining the constant system matrices and vectors of (E.27). For the steady-state velocity, equally as reactive force of the environment, a steady-state load pressure of the cylinder can be assumed. This is inherent since the load pressure is equivalent to the hydraulic driving force, correspondingly pressure difference between both chambers. Therefore, the flow equation (E.12) can be simplified to

$$\bar{Q}_L = zK\Omega,\tag{E.28}$$

where  $\Omega = \sqrt{0.5(P_S - P_L)}$  for  $z > 0$ , and it is valid  $0 \leq \Omega \leq \sqrt{0.5P_S}$  for  $|P_L| = \text{const} < P_S$  at the steady-state. Moreover  $z = u_c$  with saturations can be assumed due to the cancelation of the dead-zone by the forward compensator (E.23). Since the numerical simulation does not highlight saturated control values, that for the reference scenarios under evaluation, the nonlinear saturation by-effect can also be neglected when tuning the linear control parameters. Also the dynamic behavior of LPF, cf. Fig. E.2, is neglected since the LPF bandwidth coincides with that of the servo-valve. Both corner frequencies (of LPF and servo-valve) are significantly higher compared to the dynamics of the operated hydraulic actuator. With respect to the above assumptions, the matrices and vectors of (E.27) are given by

$$\bar{\mathbf{A}}(-1) = \begin{bmatrix} 0 & 1 & 0 & 0 & 0 & 0 \\ 0 & -\frac{k_s}{m} & \frac{\bar{A}}{m} & 0 & 0 & -\frac{d_s}{m} \\ a_{31} & a_{32} & a_{33} & a_{34} & a_{35} & 0 \\ 0 & 0 & 0 & 0 & 0 & 0 \\ -1 & 0 & 0 & 0 & 0 & 0 \\ 0 & 0 & 0 & 0 & 0 & 0 \end{bmatrix},\tag{E.29}$$

$$\bar{\mathbf{b}}(-1) = \begin{bmatrix} 0 & 0 & \frac{4E}{V_t}K\Omega K_1 & 0 & 1 & 0 \end{bmatrix}^T,\tag{E.30}$$

$$\bar{\mathbf{c}}(-1) = \begin{bmatrix} 1 & 0 & 0 & 0 & 0 & 0 \end{bmatrix}\tag{E.31}$$

for the position control, i.e.  $h = -1$ , and by

$$\bar{\mathbf{A}}(1) = \begin{bmatrix} 0 & 1 & 0 & 0 & 0 & 0 \\ 0 & -\frac{k_s}{m} & \frac{\bar{A}}{m} & -\frac{1}{m} & 0 & -\frac{d_s}{m} \\ a_{31} & a_{32} & a_{33} & a_{34} & a_{35} & 0 \\ 0 & c & 0 & 0 & 0 & 0 \\ 0 & 0 & 0 & -1 & 0 & 0 \\ 0 & 0 & 0 & 0 & 0 & 0 \end{bmatrix}, \quad (\text{E.32})$$

$$\bar{\mathbf{b}}(1) = \begin{bmatrix} 0 & 0 & \frac{4E}{V_t} K \Omega K_4 & 0 & 1 & 0 \end{bmatrix}^T, \quad (\text{E.33})$$

$$\bar{\mathbf{c}}(1) = \begin{bmatrix} 0 & 0 & 0 & 1 & 0 & 0 \end{bmatrix} \quad (\text{E.34})$$

for the force control, i.e.  $h = 1$ , respectively. The individual summarized matrix elements are

$$\begin{aligned} a_{31} &= -\frac{4E}{V_t} K \Omega K_1, \\ a_{32} &= -\frac{4E}{V_t} (K \Omega K_2 + \bar{A}), \\ a_{33} &= -\frac{4E}{V_t} K \Omega K_3, \\ a_{34} &= -\frac{4E}{V_t} K \Omega K_4, \\ a_{35} &= \frac{4E}{V_t} K \Omega K_i. \end{aligned} \quad (\text{E.35})$$

The available system parameters are  $\bar{A} = 0.001m^2$ ,  $m = 1.7026kg$ ,  $K = 0.25E^{-6} \frac{m^3}{s\sqrt{Pa}}$ ,  $E = 10^9 Pa$ ,  $V_t = 0.0014m^3$  and  $c = 1.2E^8 N/m$ . The latter, which is an equivalent environmental stiffness, is determined as a lumped parameter of the coupled rods, force sensor, and material properties of the cylinder cap. The residual constants are dependent on which operation mode is active. According to the test scenarios,  $\Omega = 2.23E^3$ ,  $k_s = 1.0151E^3$  and  $d_s = 30.755$  for the position control, while  $\Omega = 2.0125E^3$ ,  $k_s = 6.2499E^3$  and  $d_s = 0$  for the force control. Recall that  $k_s$  represents the slope and  $d_s$  the offset of the linearized Stribeck function. The gain parameters, entering eqs. (E.30), (E.33) and (E.35), are determined for each control mode by the corresponding pole placement.

In Fig. E.3, the poles of both closed-loop controls are shown versus those of the system plant (open loop). Note that the most left complex pole pair is associated with hydraulics behavior that is marginally influenced by adjusting the respective gains. The dominant poles, i.e. closer to origin, refer to the controlled actuator system dynamics. The gains were chosen so that no complex pole pairs occur close to the origin, and the most right real pole satisfies the requirements on the control system dynamics. In addition, higher

Table E.2: Control gain parameters

	Position Control	Force Control
$K_1$	190	0
$K_2$	$9.019E^{-4}$	$2.5E^{-4}$
$K_3$	$30.539E^{-9}$	$5.9E^{-8}$
$K_4$	0	$5E^{-5}$
$K_i$	5000	$1.2E^{-3}$

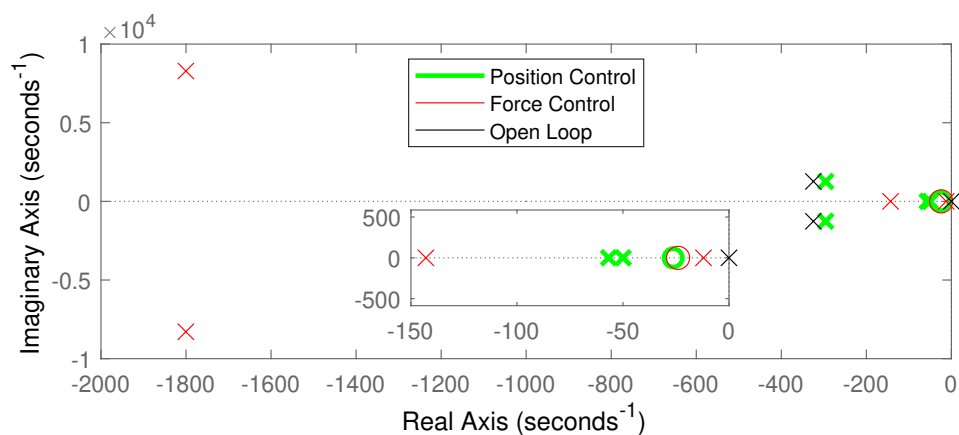


Figure E.3: Pole-zero diagram of closed-loop controls versus plant

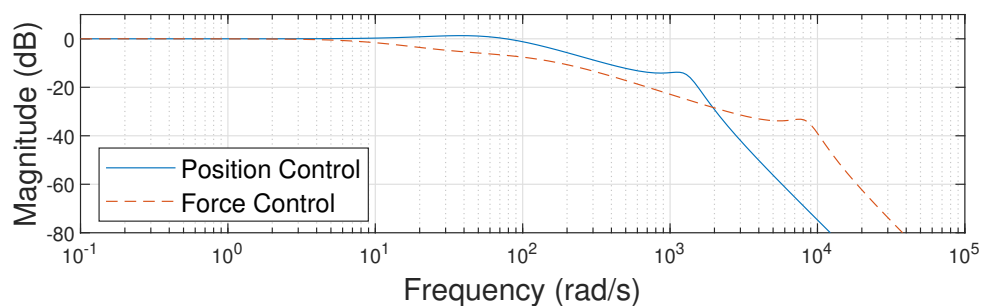


Figure E.4: Bode diagram of designed closed-loop controls

gain values were avoided by taking into account the control saturations and measurement noise included into numerical simulation. From the Bode plot shown in Fig. E.4, it can be seen that the first corner frequency, correspondingly bandwidth, is about 21Hz for the position control and about 2.5Hz for the force control. The determined control gains are listed in Table E.2. Note that  $K_4$  is set to zero for the position control since no force feedback is required. Correspondingly,  $K_1$  is set to zero for the force control, since an absolute position feedback is irrelevant during a forced contact with stiff environment.

### E.3.6 Stability Analysis

The local stability analysis relies on the stability of both linearized closed-loop control systems, see poles configuration in Section E.3.5, and multiple Lyapunov function approach applicable to the switched systems, see [30]. Note that the stability of switching between the motion and force control has been recently discussed in detail in [23], that for the linearized closed-loop behavior and autonomous switching by means of a hysteresis relay. Thus, we give here the main statement and exemplifying result only, while for details on using the multiple Lyapunov function an interested reader is referred to [30, 23]. For both closed-loop control systems, given by (E.27), the quadratic Lyapunov function candidate can be assumed as

$$L(h) = W_1 \dot{x}^2 + W_2 P_L^2 + W_3 (r(h) - y(h))^2. \quad (\text{E.36})$$

Note that this contains all terms related to energy storage in the control system: kinetic energy of relative motion, potential energy of hydraulic pressure and potential energy of the feedback control loop reflected through the quadratic control error. The positive coefficients  $W_{1-3}$  can be found for Lyapunov stability proof and, below, are used as mode-dependent, i.e.  $W_i(h)$ , that for the sake of better visualization/comparison of multiple Lyapunov function. The multiple Lyapunov function of both control modes is shown in

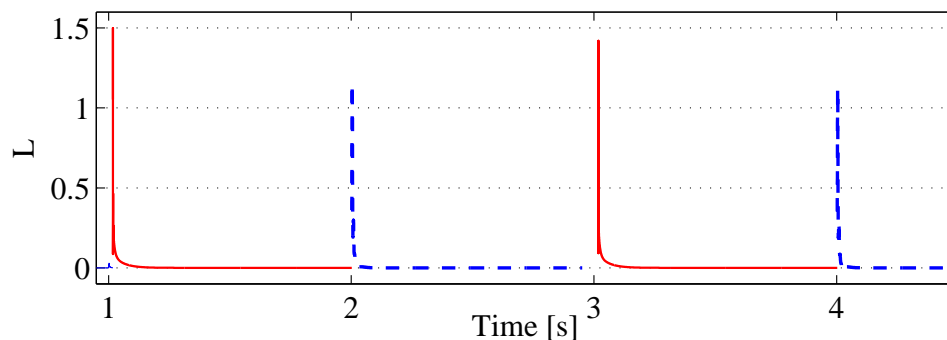


Figure E.5: Multiple Lyapunov function for position (red solid line) and force (blue dashed line) controls at periodic switching

Fig. E.5 for a periodic switching, meaning an alternating position and force control mode. A non-increase in the Lyapunov function level for two consecutive operations of the same mode implies the entire switched system is asymptotically stable, cf. [23]. Since both closed-loop dynamics are linearized in the vicinity to the switching point, the shown local stability appears sufficient for analysis of the designed hybrid control system with the intended test scenarios.

## E.4 Experimental Evaluation

An elaborated experimental evaluation of the proposed hybrid control is given below. Two test scenarios are considered: in the first one the controlled motion of the piston rod is executed until hard-stop at the cylinder boundary, while in the second one a slow dynamic counteracting force, produced by the left-hand cylinder, is introduced during which the piston rod is moving within  $0 \leq x < l$  range. The supply pressure was set to  $P_S = 100E^5\text{Pa}$  with a maximum flow limited to 40 l/min.

### E.4.1 Hard-stop Environment

The controlled motion starts at zero position (right-hand cylinder fully retracted) and follows the ramp reference with a slope corresponding to 0.03m/s velocity, cf. Fig. E.6. The controlled motion reaches hard-stop when the overall drive of both cylinders, connected stiffly, reaches the left-hand cylinder boundary. Note that during the experiment the BDCV is in zero position, thus opening both cylinder chamber lines to the tank and providing no active counteraction force but passive additional load only. When reaching hard-stop by environment, the counteracting force rises, due to the stiff position control, and the hysteresis relay-based switching triggers the force control at the set threshold value, cf. Section E.3.4. The force reference trajectory is initially set to the constant value  $r(1) = 3500N$  and afterwards decreases towards zero in a slow cosine shape. This reference trajectory is assigned in order to evaluate simultaneously the set value and trajectory following of the force control and autonomous switching back to position control once passing the lower threshold value of the load force, that is releasing from the contact with environment. After switching back, the position control tracks the negative ramp, with slope corresponding to -0.03m/s velocity, until reaching the initial zero position.

Fig. E.6 shows the reference and measured position values of the right-hand cylinder rod. The transient phases at the beginning of relative motion and after switching back (from force control) are additionally zoomed-in, around the time of 0.1s and 8.5s correspondingly. Accurate reference following with solely minor transient overshoots can be recognized.

Fig. E.7 shows the sensor measured counteraction force versus the corresponding reference. Note that the triggered force control is active only during the time span where the reference is indicated, while the residual force measurements correspond to both slopes of the controlled motion, i.e. position control, where the load force occurs between the right-hand (driving) cylinder and left-hand (driven) cylinder. An accurate force following can be recognized, while some transient swinging occurs at the hard-stop contact, that is inherent and a well-known issue of the force control in general, compare with e.g. [3, 19].

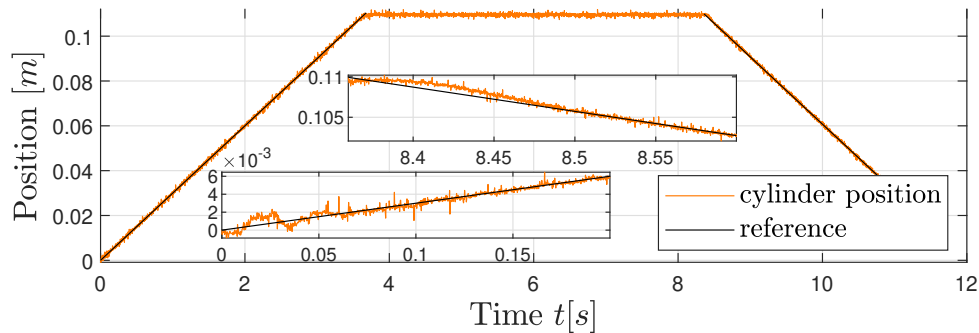


Figure E.6: Reference and measured position control response

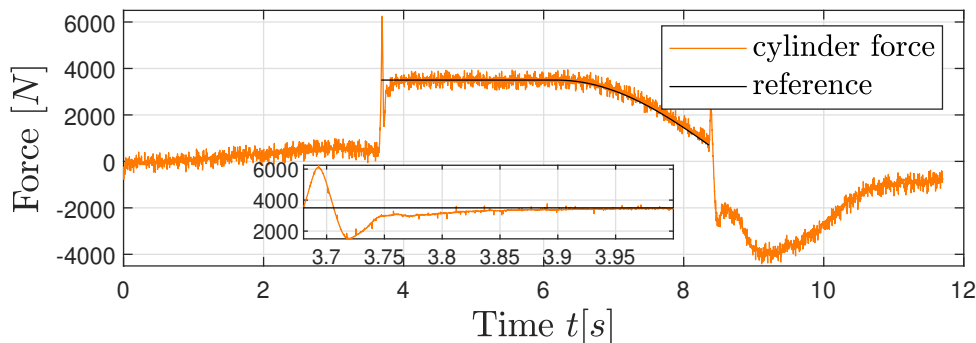


Figure E.7: Reference and measured force control response

In order to assess repeatability of the proposed hybrid control scheme, a total of 20 experiments were conducted. The mean values and standard deviations of the control errors are evaluated from the signals processed by the second-order LPF with 100Hz cutoff frequency. The low-pass filtering is done for the sake of better visualization of all tests against each other. Recall that the inherent level of process and measurement noise in the hydraulic system is relatively high. Figs. E.8a and E.8b show the mean values and standard deviations of the position control error for both ramp segments of the rod displacement. The mean values and standard deviations of the force control errors are shown in Fig. E.9.

#### E.4.2 Dynamic Environment

For the test scenario with dynamic environment, the controlled motion starts at fully retracted zero position, following a ramp reference within 1.5s, after which the reference trajectory has a slow sinusoidal pattern, cf. Fig. E.10. Note that the reference trajectory  $r(-1)$  is shown for the position control mode only; after switching back from the force control, the position reference is recalculated on fly. The left-hand cylinder is feed-forward controlled in an open-loop manner, while being stiffly coupled to the right-hand (controlled) one. This way, a varying counteraction force is generated. The BDCV feed-forward control value is chosen such that it is continuously driving the left-hand cylinder,

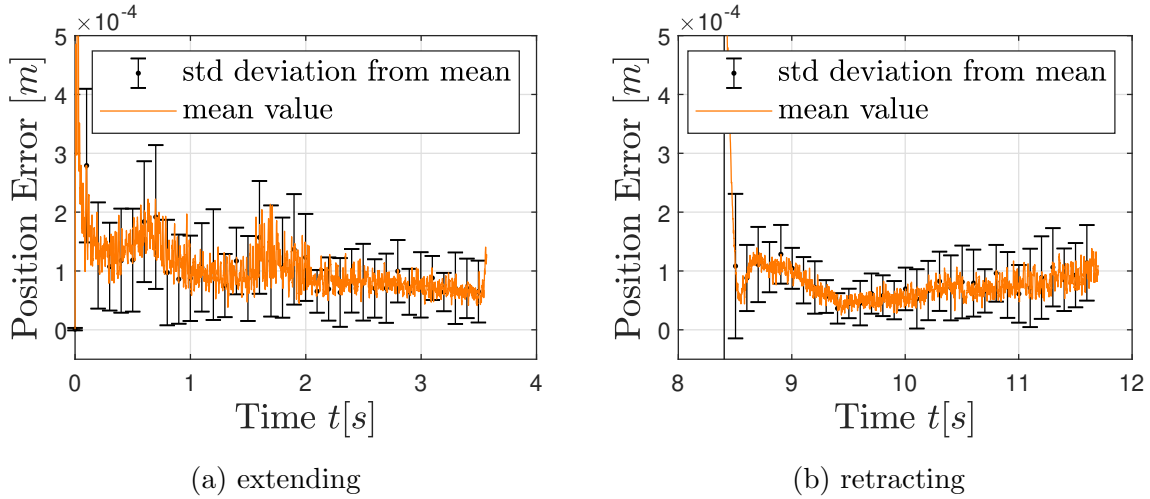


Figure E.8: Mean values and standard deviations of position error

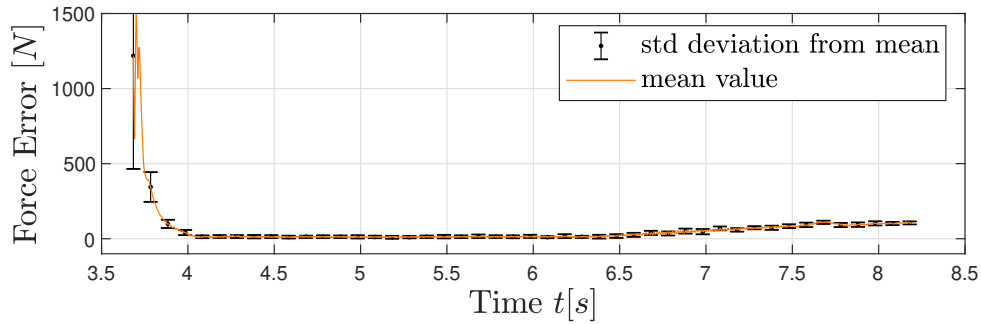


Figure E.9: Mean values and standard deviations of force error

while the PRV is controlled in a pulsed pattern with 10s period and 60% pulse-width. The force reference trajectory  $r(1)$  starts at 3375N and then steps up and down to 4500N and 3150N respectively, see Fig. E.11. These step values are chosen such that the controlled cylinder rod cannot reach fully extended/retracted states while pushing against the left-hand cylinder rod. Fig. E.10 shows the position measurement together with the reference trajectory segments. After 4s, labeled by the dashed bar, the PRV controlling the left-hand load cylinder switches to high, thus resulting in an increased load force and hence triggering switch to the force control mode. The corresponding reference force and (all time) measured load force can be seen in Fig. E.11. After 10s, the PRV control value is again at low-level, the load force drops below the relay switching threshold and the hybrid controller changes back to the position control mode, labeled by the second dashed bar in Fig. E.11. Note that between both dashed bars, a relative motion occurs (see Fig. E.10), while the required controlled force is kept constant, cf. Fig. E.11. Also here the experiments were repeated 20 times, while the same signals filtering, as described above, was applied when evaluating the mean values and standard deviations of the control error. Both are shown in Figs. E.12a and E.12b for the position control mode, and



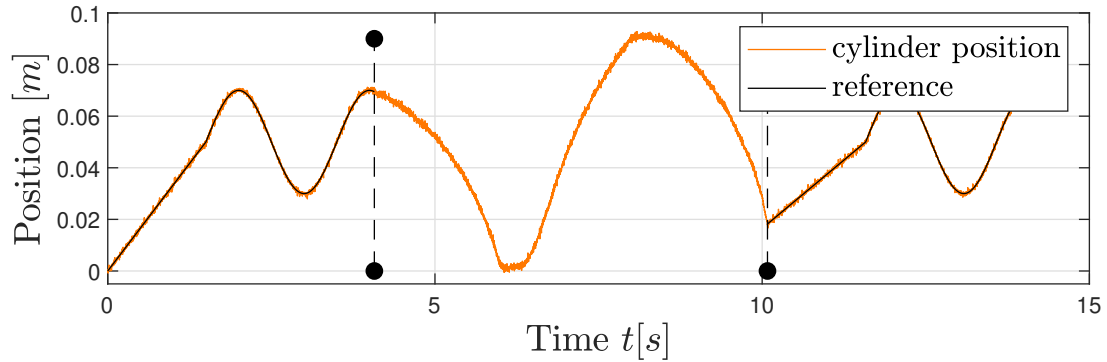


Figure E.10: Reference and measured position control response

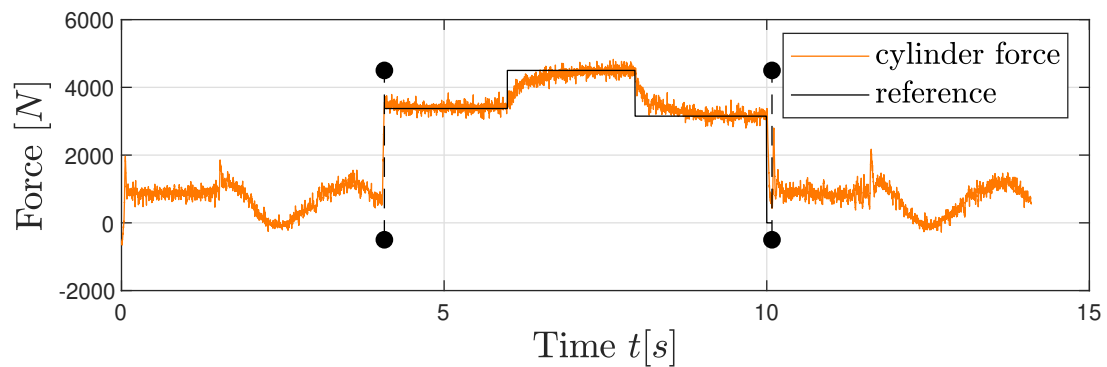


Figure E.11: Reference and measured force control response

in Fig. E.13 for the force control mode respectively.

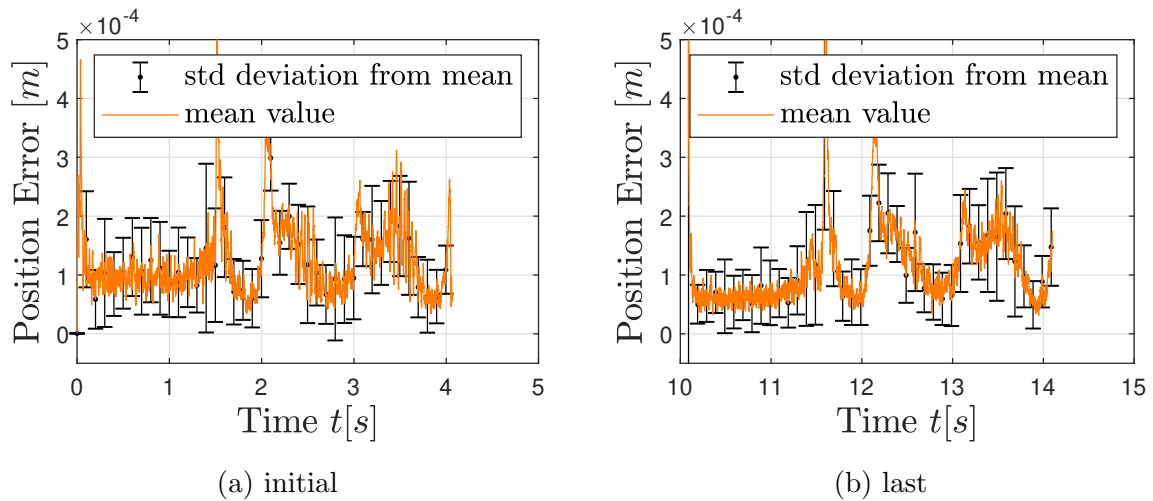


Figure E.12: Mean values and standard deviations of position error

## E.5 Summary

A novel hybrid position/force control for standard linear hydraulic actuators was proposed. For its development an experimental hydraulic test rig with two cylinders in

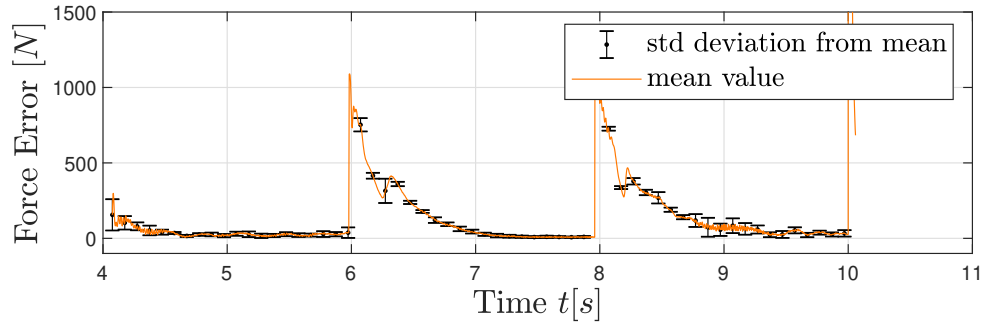


Figure E.13: Mean values and standard deviations of force error

antagonistic setup was assembled, instrumented and the corresponding full-order model was derived. A reduction of the state-space model was introduced, forming the basis for hybrid control loop design, while an autonomous switching between the position and force control relies on the hysteresis relay, that without changing the overall control structure. Control parameters were obtained based on the pole placement and the local stability was proven. Two experimental studies were illustrated for evaluating repeatability and performance of both, position and force controls, and switching between them.

# REFERENCES

- [1] M. Jelali and A. Kroll. *Hydraulic Servo-systems: Modelling, Identification and Control*. Springer London, 2003.
- [2] H. E. Merritt. *Hydraulic control systems*. John Wiley and Sons, 1967.
- [3] A. Alleyne and R. Liu. A simplified approach to force control for electro-hydraulic systems. *Control Engineering Practice*, 8(12):1347–1356, 2000.
- [4] M. B. Kjelland and M. R. Hansen. Offshore Wind Payload Transfer Using Flexible Mobile Crane. *Modeling, Identification and Control: A Norwegian Research Bulletin*, 36(1):1–9, 2015.
- [5] G. Liu and S. Daley. Optimal-tuning nonlinear PID control of hydraulic systems. *Cont. Engin. Practice*, 8(9):1045–1053, 2000.
- [6] M. H. Rudolfson, T. N. Aune, O. Auklend, L. T. Aarland, and M. Ruderman. Identification and control design for path tracking of hydraulic loader crane. In *2017 IEEE International Conference on Advanced Intelligent Mechatronics (AIM)*, pages 565–570, 2017.
- [7] B. Eryilmaz and B. H. Wilson. Unified modeling and analysis of a proportional valve. *Journal of the Franklin Institute*, 343(1):48–68, 2006.
- [8] J. Komsta, N. van Oijen, and P. Antoszkiewicz. Integral sliding mode compensator for load pressure control of die-cushion cylinder drive. *Control Engineering Practice*, 21(5):708–718, 2013.
- [9] H. C. Pedersen and T. O. Andersen. Pressure Feedback in Fluid Power Systems - Active Damping Explained and Exemplified. *IEEE Tran. on Cont. Syst. Technology*, 26(1):102–113, 2018.
- [10] G. Sohl and J. Bobrow. Experiments and simulations on the nonlinear control of a hydraulic servosystem. *IEEE Transactions on Control Systems Technology*, 7(2):238–247, 1999.

- [11] Bin Yao, Fanping Bu, J. Reedy, and G.-C. Chiu. Adaptive robust motion control of single-rod hydraulic actuators: theory and experiments. *IEEE/ASME Trans. on Mechat.*, 5(1):79–91, 2000.
- [12] S. Strano and M. Terzo. A SDRE-based tracking control for a hydraulic actuation system. *Mechanical Systems and Signal Processing*, 60:715–726, 2015.
- [13] M. Vaezi and A. Izadian. Piecewise affine system identification of a hydraulic wind power transfer system. *IEEE Transactions on Control Systems Technology*, 23(6):2077–2086, 2015.
- [14] P. Pasolli and M. Ruderman. Linearized piecewise affine in control and states hydraulic system: Modeling and identification. In *IEEE 44th Annual Conf. of Ind. Electr. Soc.*, pages 4537–4544, 2018.
- [15] M. Esfandiari and N. Sepehri. Controller design and stability analysis of output pressure regulation in electrohydrostatic actuators. *ASME J. of Dyn. Syst., Meas., and Con.*, 141(4):041008, 2019.
- [16] S. Koch and M. Reichhartinger. Observer-based sliding mode control of hydraulic cylinders in the presence of unknown load forces. *Elektrotechnik und Informationstechnik*, 133(6):253–260, 2016.
- [17] C. Vazquez, S. Aranovskiy, L. Freidovich, and L. Fridman. Second order sliding mode control of a mobile hydraulic crane. In *53rd IEEE Conference on Decision and Control*, pages 5530–5535, 2014.
- [18] N. Niksefat and N. Sepehri. Design and experimental evaluation of a robust force controller for an electro-hydraulic actuator via quantitative feedback theory. *Cont. Eng. Prac.*, 8:1335–1345, 2000.
- [19] S. Katsura, Y. Matsumoto, and K. Ohnishi. Analysis and experimental validation of force bandwidth for force control. *IEEE Transactions on Industrial Electronics*, 53(3):922–928, 2006.
- [20] M. H. Raibert and J. J. Craig. Hybrid Position/Force Control of Manipulators. *Journal of Dynamic Systems, Measurement, and Control*, 103(2):126, 1981.
- [21] O. Khatib. A unified approach for motion and force control of robot manipulators: The operational space formulation. *IEEE Journal on Robotics and Automation*, 3(1):43–53, 1987.

## REFERENCES

- [22] P. Pasolli and M. Ruderman. Hybrid State Feedback Position-Force Control of Hydraulic Cylinder. In *2019 IEEE International Conference on Mechatronics (ICM)*, pages 54–59. IEEE, mar 2019.
- [23] M. Ruderman. On switching between motion and force control. In *IEEE 27th Mediterranean Conference on Control and Automation (MED'19)*, pages 445–450, 2019.
- [24] M. Ruderman. Full- and reduced-order model of hydraulic cylinder for motion control. In *43rd Annual Conference of the IEEE Industrial Electronics Society*, pages 7275–7280, 2017.
- [25] L. Márton, S. Fodor, and N. Sepehri. A practical method for friction identification in hydraulic actuators. *Mechatronics*, 21(1):350–356, 2011.
- [26] M. Ruderman. On break-away forces in actuated motion systems with nonlinear friction. *Mechatronics*, 44:1–5, 2017.
- [27] M. Ruderman and M. Iwasaki. Observer of Nonlinear Friction Dynamics for Motion Control. *IEEE Transactions on Industrial Electronics*, 62(9):5941–5949, 2015.
- [28] B. Armstrong-Hélouvry, P. Dupont, and C. De Wit. A survey of models, analysis tools and compensation methods for the control of machines with friction. *Automatica*, 30:1083–1138, 1994.
- [29] F. Al-Bender and J. Swevers. Characterization of friction force dynamics. *IEEE Control Systems Magazine*, 28(6):64–81, 2008.
- [30] D. Liberzon and A. S. Morse. Basic problems in stability and design of switched systems. *IEEE Cont. Syst. Mag.*, 19:59–70, 1999.



# Appendix F

## Hydraulic Test Setup

Philipp Pasolli

# Hydraulic Test Setup

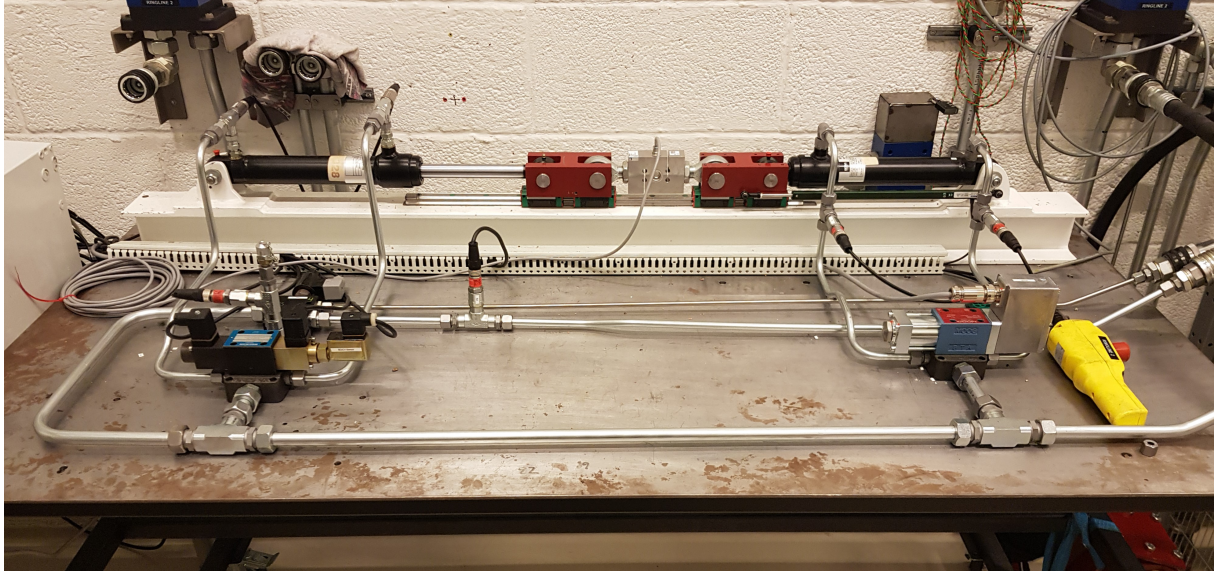


Figure F.1: Experimental hydraulic test setup

## F.1 Hydraulic/Mechanical components

### F.1.1 Overview

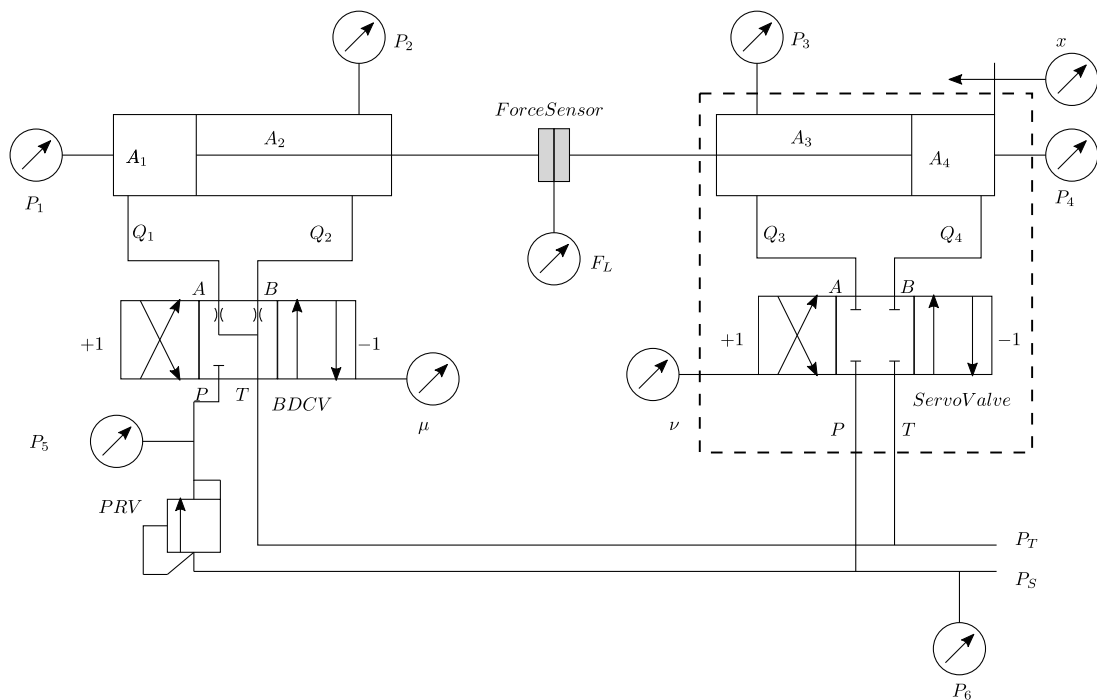


Figure F.2: Testbench schematic




Table F.1: Pressure relief/reduction valve

<b>Component</b>	<b>Manufacturer</b>	<b>Model No.</b>
Main stage	Sun Hydraulics	PVDA8
Electro-proportional relief valve	Sun Hydraulics	RBAP
24VDC Coil	Sun Hydraulics	770-224

A picture of the constructed experimental testbench is shown in Fig. F.1 and a schematic showing the arrangement of the testbench's components is given in Fig. F.2. The testbench features two different cylinders arranged in an antagonistic setup which may be connected to each other with a force gauge. The righthand side differential cylinder of the test setup is connected to a servo valve connected to the HPU (hydraulic power unit). The position of the cylinder rod is monitored by an absolute resistor-based linear potentiometer. The valve has an internal closed loop control circuit to control the spool's position, which is measurable. The spool's position is determined by the command signal.

The lefthand differential cylinder is connected to a directional valve which up to this point has only been used in its fully open state to switch the hydraulic flow's direction. It is therefore called a BDCV (bidirectional control valve). The BDCV spool position is adjusted by two solenoids moving the spool in either direction. These actuator solenoids are named BDCV1 and BDCV2, respectively. The BDCV spool position may be measured via BDCV Sense. In order to adjust the pressure – and thereby force – of the left cylinder, a PRV (pressure relief/reduction valve) is installed prior to the BDCV. The PRV is then connected to the HPU. Overall testbench pressure and flow may be manually adjusted with values during testing set to 100bar and 40l/min.

The relative force between the two cylinders is measured by a force gauge. Pressure sensors are installed in the chambers of both cylinders, between PRV and BDCV as well as on the HPU line. Sensors are indicated by  in Fig. F.2.

The components used in this setup are listed in table F.2 with the components for the PRV assembly listed in table F.1.

### **F.1.2 Component specification overview**

In table F.3 a short list appears of the components installed with their respective input/output voltages/currents. For further detailed properties I refer to the components' data sheets based on their model no. given in table F.2 and F.1.

Table F.2: Hydraulic and Mechanical Components

Decription	Manufacturer	Model No.
Cylinder	Servi Group	CD25 S-E/S-E
Force Sensor	HBM	S9M/20 kN
Servo Valve	Moog	D633 R16KD1M0NSM2
BDCV	Mecman Rexroth	WRL 43 G4B-6-1
Pressure Sensor $P_{1,2}$	Parker	SCP01-400-44-07
Pressure Sensor $P_{3...6}$	Danfoss	MBS 1250 063G1229
Linear Potentiometer	Variohm	VLP-250

Table F.3: Component input/output voltages and currents

Component	Input		Output	
	Voltage	Current	Voltage	Current
Linear Potentiometer	10VDC	n.a.	0...10VDC	n.a.
Pressure Sensore $P_{1,2}$	14...36VDC	n.a.	0...10V	n.a.
Pressure Sensore $P_{3...6}$	8...40VDC	n.a.	n.a.	4...20mA
Servo Valve	24VDC, $-10...10V_c$	n.a.	n.a.	4...20mA
Force Sensor	Handled by signal converter in electric cabinet			
BDCV Actuator	Handled by signal converter in electric cabinet			
BDCV Sensor	24VDC	n.a.	3...12V	n.a.
PRV	24VDC	590mA	n.a.	n.a.

## F.2 Electric Cabinet

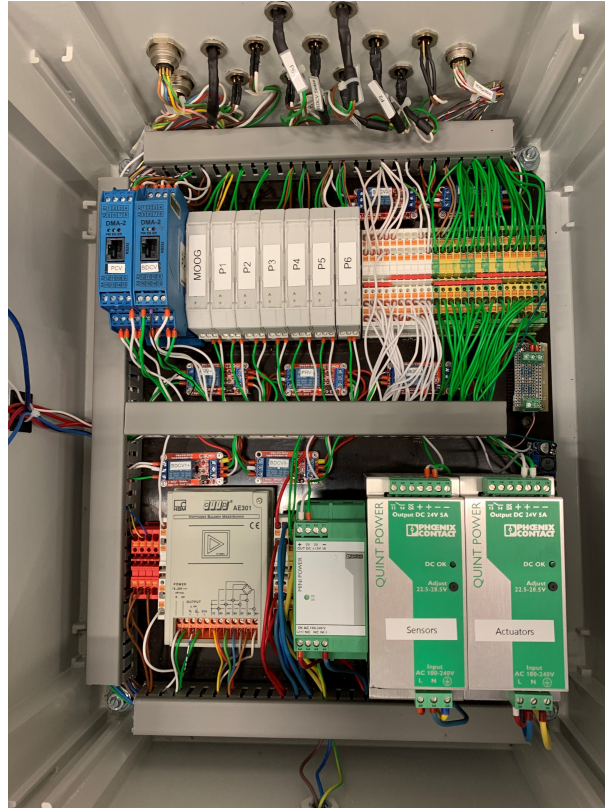


Figure F.3: Electric cabinet

All signals to and from the testbench are routed through the electric cabinet, where signal conversions are performed and power is distributed to the respective components. Three power supplies are installed, two 24VDC and one 15VDC. The 15VDC power supply is connected to a DC/DC converter (15VDC to 10VDC) to power the linear potentiometer while one of the 24VDC power supplies delivers power to the remaining sensors while the other powers the actuators. By associating sensors and actuators with different power supplies, it was possible to reduce the noise affecting the sensor's signals. Regarding the force sensor, a signal converter/power supply was installed to convert the 6-wire configuration into a real-time target compatible voltage signal. Current to voltage converters for the sensors  $P_{3..6}$  and servo valve as well as digital module amplifiers (DMA) for the proportional and servo valves to actuate the PRV and BDCV were installed. The BDCV uses two actuators to displace the spool in either direction (BDCV1 and BDCV2). The DMA of the BDCV automatically adjusts actuation for BDCV1 and BDCV2 in accordance with the command signal. Two additional current to voltage converters for sensors  $P_{1,2}$  are already pre-installed and wired up in case these sensors are replaced with current-based sensors in the future. A custom circuit board with two voltage dividers reduces the voltages of the BDCV sensor by 50% for real-time target compatibility purposes.

Five relays were installed that are triggered by an emergency stop button to set all actuators to their zero positions (connecting actuator inputs to ground (GND)), stopping the movement of the right cylinder and flushing any remaining pressure in the left cylinder into the tank. The relays are configured in such a way that a sudden power loss is equal to pushing the emergency stop button. On the outside of the cabinet are both a switch to turn on/off the mains power and an emergency stop button. All components in the cabinet, including incoming cables, are labeled accordingly.

A list of the components installed in the electric cabinet, including their respective manufacturer and model no., is given in table F.4. Schematics of how the components are connected to one another is presented in section F.5.

Table F.4: List of electric components in cabinet

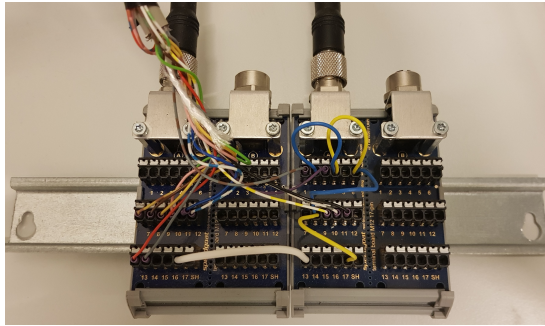
Description	Manufacturer	Model No.
Power Supply 15V	Phoenix Contact	MINI-PS-100-240AC/2x15DC/1
Power Supply 24V	Phoenix contact	QUINT-PS-100-240AC/24DC/5
Force Sensor Converter	HBM	clip AE301
PRV DMA	HCS	DMA-22-02-110-x-S0
BDCV DMA	HCS	DMA-22-01-080-X-SHAWE
A to V Converter	LEG	TV2-3-1-2

### F.3 Real-Time Target

As a computer to testbench interface, the Speedgoat Baseline S real-time target is currently being used, including two extension cards IO183 and IO397. Both cards feature 16bit A/D and D/A converters with IO183 having 8 single ended or 4 differential analogue inputs having a range of  $\pm 10V$  and 4 single ended analogue outputs having a range of  $0 - 5V$  with a maximum current draw of 5mA. IO397 adds an additional 4 single ended or 4 differential analogue inputs having a range of  $\pm 10.24V$  and 4 single ended analogue outputs having a range of  $\pm 10V$  and a maximum current draw of 5mA. The cards are connected to an interface terminal with two modules, one for each card, respectively. IO183 is connected to module 1 and IO397 to module 2. The terminals on each module are numbered accordingly. The RT target is shown in Fig. F.4a and the interface terminal in Fig. F.4b.



(a) Speedgoat RT Target



(b) RT Target Interface

Figure F.4: RT Target and interface terminal

## F.4 Interfaces

The cabinet is designed to be mounted directly to the testbench with interfaces for connecting sensors and actuators on the top and a mains voltage input cable on the bottom. At this stage the cabinet is not yet mounted to the testbench due to spatial limitations. The mains voltage cable is directly fed into the case without any connectors in-between. If the cable is not long enough for future use, it may be removed by first taking out the incoming wires from the terminals next to the power supplies on the bottom of the cabinet. It may then be replaced with a longer one. The rest of the interfaces are situated on the top of the cabinet for easy access to connecting sensors and actuators. All sensor and actuator cables are detachable. All ports are labeled accordingly on the cabinet with the sensors' and actuators' respective cables labeled in the same way. The following list shows which sensor/actuator is associated with which of the three different connectors used:

- 4-Pin: Pressure sensors  $P_{1...6}$ , linear potentiometer, BDCV sensor, BDCV1, BDCV2, PRV.
- 24-Pin: RT Interface - including all sensor signals and command signals for PRV, BDCV and Servo valve.
- 8-Pin: Servo Valve, Force gauge.

A list of connectors used with model no. for panel mount and plug is given in table F.5. Manufacturer for the connectors used is **Binder**.

Table F.5: Connerctors: Binder - Ordering Numbers

	<b>Plug</b>	<b>Panel Mount</b>
<b>8-Pin</b>	99 4830 00 08	09 4831 00 08
<b>24-Pin</b>	09 0495 70 24	09 0498 00 24
<b>4-Pin</b>	99 0429 14 04	09 3432 92 04

Pins located in the 4-pin connectors are all wired up the same way. The wiring layouts of the 8-pin connectors differ from each other for the servo valve and force gauge respectively. In the following the connectors' wiring according to the pin layout appearing in Fig. F.5 is listed. The pin layout is mirrored along the vertical axis of the connector depending on the direction from which it is viewed. Pin numbers are also indicated on the respective connector itself. The wiring layout for 4-pin connectors is given in table F.6, wiring layout for the servo valve in table F.7, for the force gauge in table F.8 and for the 24-pin RT interface in table F.9.

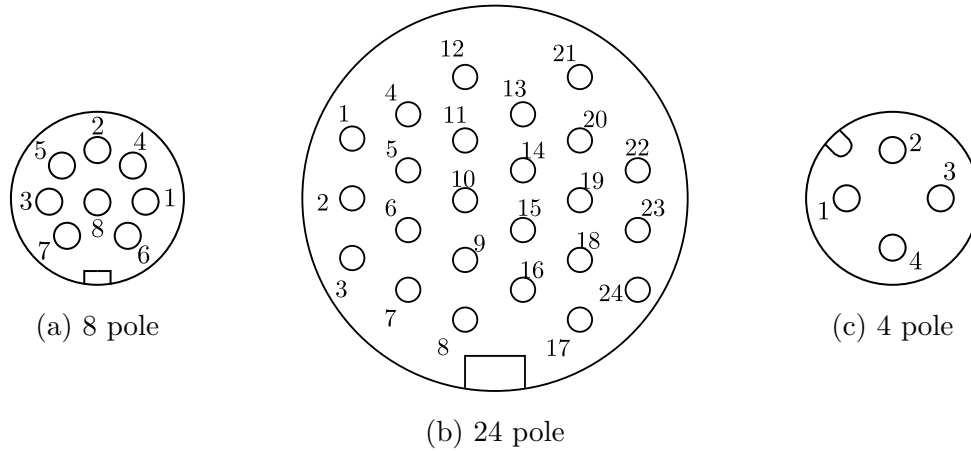


Figure F.5: Connector port layout - cabinet mounted view

Table F.6: 4-pin wiring layout

<b>Pin</b>	<b>Color</b>	<b>Description</b>
1	White	V+
2	Brown	Signal
3	Green	GND
4	n.a.	n.a.

Appendix F. Hydraulic Test Setup

Table F.7: 8-pin wiring layout for servo valve

<b>Pin</b>	<b>Color</b>	<b>Description</b>	<b>Datasheet Indicator</b>
1	White	not used	C
2	Green	V+	A
3	Grey	GND	E
4	Brown	GND	B
5	Yellow	Measure Signal	F
6	Blue	n.a.	n.a.
7	Pink	Command Signal	D
8	Red	GND	G

Table F.8: 8-pin wiring layout for force gauge

<b>Pin</b>	<b>Sensor Color</b>	<b>Cabinet Color</b>	<b>Description</b>
1	White	White	Measure +
2	Green	Green	Sensing +
3	Grey	Grey	Sensing -
4	Black	Brown	Excitation -
5	n.a.	Yellow	Shielding
6	Blue	Blue	Excitation +
7	n.a.	Pink	n.a.
8	Red	Red	Measure -

Table F.9: 24-pin wiring layout for real-time-interface

Pin	Color	Sense/Command	Device	Module	Module Pin
1	White	n.a.	n.a.	n.a.	n.a.
2	White Green	n.a.	n.a.	n.a.	n.a.
3	Brown Green	n.a.	n.a.	n.a.	n.a.
4	White Blue	Sense	Force Gauge	1	12a
5	Red Blue	n.a.	n.a.	n.a.	n.a.
6	Pink Brown	n.a.	n.a.	n.a.	n.a.
7	Pink White	n.a.	n.a.	n.a.	n.a.
8	Pink Grey	n.a.	n.a.	n.a.	n.a.
9	Purple	Sense	$P_6$	2	3a
10	Black	Command	BDCV	2	11a
11	Red	Sense	$P_3$	1	13a
12	Brown Grey	Sense	$P_5$	2	1a
13	Blue	Sense	Linear Pos.	1	11a
14	Pink	Sense	BDCV	1	10a
15	Grey	Sense	$P_4$	1	14a
16	Yellow	Sense	$P_2$	1	9a
17	Green	n.a.	GND	1	6a
18	White Grey	Command	PRV	2	10a
19	Yellow Brown	Sense	Servo Valve	1	7a
20	Brown	Sense	$P_1$	1	8a
21	White Yellow	Command	Servo Valve	2	9a
22	n.a.	n.a.	n.a.	n.a.	n.a.
23	n.a.	n.a.	n.a.	n.a.	n.a.
24	n.a.	n.a.	n.a.	n.a.	n.a.

## F.5 Wiring Schematic

In the following a schematic wiring layout for the components used is shown and can be cross referenced with the information and tables given previously.



